Advances in electrical energy storage using core-shell structures and relaxor-ferroelectric materials

by

James Emery Brown

B.S., Truman State University, 2012

AN ABSTRACT OF A DISSERTATION

submitted in partial fulfillment of the requirements for the degree

DOCTOR OF PHILOSOPHY

Department of Chemistry
College of Arts and Sciences

KANSAS STATE UNIVERSITY
Manhattan, Kansas

2018

Abstract

Electrical energy storage (EES) is crucial in todays' society owing to the advances in electric cars, microelectronics, portable electronics and grid storage backup for renewable energy utilization. Lithium ion batteries (LIBs) have dominated the EES market owing to their wide use in portable electronics. Despite the success, low specific capacity and low power rates still need to be addressed to meet the increasing demands. Particularly, the low specific capacity of cathode materials is currently limiting the energy storage capability of LIBs. Vanadium pentoxide (V_2O_5) has been an emerging cathode material owing to its low cost, high electrode potential in lithium-extracted state (up to 4.0 V), and high specific capacities of 294 mAh g^{-1} (for a 2 Li^+/V_2O_5 insertion process) and 441 mAh g^{-1} (for a 3 Li^+/V_2O_5 insertion process). However, the low electrical conductivities and slow Li^+ ion diffusion still limit the power rate of V_2O_5. To enhance the power-rate capability we construct two core-shell structures that can achieve stable 2 and 3 Li^+ insertion at high rates.

In the first approach, uniform coaxial V_2O_5 shells are coated onto electrospun carbon nanofiber (CNF) cores via pulsed electrodeposition. The materials analyses confirm that the V_2O_5 shell after 4 hours of thermal annealing at 300 °C is a partially hydrated amorphous structure. SEM and TEM images indicate that the uniform 30 to 50 nm thick V_2O_5 shell forms an intimate interface with the CNF core. Lithium insertion capacities up to 291 and 429 mAh g^{-1} are achieved in the voltage ranges of 4.0 – 2.0 V and 4.0 – 1.5 V, respectively, which are in good agreement with the theoretical values for 2 and 3 Li^+/V_2O_5 insertion. Moreover, after 100 cycles, remarkable retention rates of 97% and 70% are obtained for 2 and 3 Li^+/V_2O_5 insertion, respectively.

In the second approach, we implement a three-dimensional (3D) core-shell structure consisting of coaxial V_2O_5 shells sputter-coated on vertically aligned carbon nanofiber (VACNF)

cores. The hydrated amorphous microporous structure in the "as-deposited" V_2O_5 shells and the particulated nano-crystalline V_2O_5 structure formed by thermal annealing are compared. The former provides remarkably high capacity of 360 and 547 mAh g^{-1} in the voltage range of 4.0 – 2.0 V and 4.0 – 1.5 V, respectively, far exceeding the theoretical values for 2 and 3 Li^+/V_2O_5 insertion, respectively. After 100 cycles of 3 Li^+/V_2O_5 insertion/extraction at 0.20 A g^{-1} (~ C/3), ~ 84% of the initial capacity is retained. After thermal annealing, the core-shell structure presents a capacity of 294 and 390 mAh g^{-1}, matching well with the theoretical values for 2 and 3 Li^+/V_2O_5 insertion. The annealed sample shows further improved stability, with remarkable capacity retention of ~100% and ~88% for 2 and 3 Li^+/V_2O_5 insertion/extraction.

However, due to the high cost of Li. alternative approaches are currently being pursued for large scale production. Sodium ion batteries (SIB) have been at the forefront of this endeavor. Here we investigate the sodium insertion in the hydrate amorphous V_2O_5 using the VACNF core-shell structure. Electrochemical characterization was carried out in the potential ranges of 3.5 – 1.0, 4.0 – 1.5, and 4.0 – 1.0 (vs Na/Na^+). An insertion capacity of 196 mAh g^{-1} is achieved in the potential range of 3.5 – 1.0 V (vs Na/Na^+) at a rate of 250 mA g^{-1}. When the potential window is shifted upwards to 4.0 – 1.5 V (vs Na/Na^+) an insertion capacity of 145 mAh g^{-1} is achieved. Moreover, a coulombic efficiency of ~98% is attained at a rate of 1500 mA g^{-1}. To enhance the energy density of the VACNF-V_2O_5 core-shell structures, the potential window is expanded to 4.0 – 1.0 V (vs Na/Na^+) which achieved an initial insertion capacity of 277 mAh g^{-1}. The results demonstrate that amorphous V_2O_5 could serve as a cathode material in future SIBs.

Advances in electrical energy storage using core-shell structures and relaxor-ferroelectric materials

by

James Emery Brown

B.S., Truman State University, 2012

A DISSERTATION

submitted in partial fulfillment of the requirements for the degree

DOCTOR OF PHILOSOPHY

Department of Chemistry
College of Arts and Sciences

KANSAS STATE UNIVERSITY
Manhattan, Kansas

2018

Approved by:

Major Professor
Dr. Jun Li

Copyright

Abstract

Electrical energy storage (EES) is crucial in todays' society owing to the advances in electric cars, microelectronics, portable electronics and grid storage backup for renewable energy utilization. Lithium ion batteries (LIBs) have dominated the EES market owing to their wide use in portable electronics. Despite the success, low specific capacity and low power rates still need to be addressed to meet the increasing demands. Particularly, the low specific capacity of cathode materials is currently limiting the energy storage capability of LIBs. Vanadium pentoxide (V_2O_5) has been an emerging cathode material owing to its low cost, high electrode potential in lithium-extracted state (up to 4.0 V), and high specific capacities of 294 mAh g^{-1} (for a 2 Li^+/V_2O_5 insertion process) and 441 mAh g^{-1} (for a 3 Li^+/V_2O_5 insertion process). However, the low electrical conductivities and slow Li^+ ion diffusion still limit the power rate of V_2O_5. To enhance the power-rate capability we construct two core-shell structures that can achieve stable 2 and 3 Li^+ insertion at high rates.

In the first approach, uniform coaxial V_2O_5 shells are coated onto electrospun carbon nanofiber (CNF) cores via pulsed electrodeposition. The materials analyses confirm that the V_2O_5 shell after 4 hours of thermal annealing at 300 °C is a partially hydrated amorphous structure. SEM and TEM images indicate that the uniform 30 to 50 nm thick V_2O_5 shell forms an intimate interface with the CNF core. Lithium insertion capacities up to 291 and 429 mAh g^{-1} are achieved in the voltage ranges of 4.0 – 2.0 V and 4.0 – 1.5 V, respectively, which are in good agreement with the theoretical values for 2 and 3 Li^+/V_2O_5 insertion. Moreover, after 100 cycles, remarkable retention rates of 97% and 70% are obtained for 2 and 3 Li^+/V_2O_5 insertion, respectively.

In the second approach, we implement a three-dimensional (3D) core-shell structure consisting of coaxial V_2O_5 shells sputter-coated on vertically aligned carbon nanofiber (VACNF)

cores. The hydrated amorphous microporous structure in the "as-deposited" V_2O_5 shells and the particulated nano-crystalline V_2O_5 structure formed by thermal annealing are compared. The former provides remarkably high capacity of 360 and 547 mAh g^{-1} in the voltage range of 4.0 – 2.0 V and 4.0 – 1.5 V, respectively, far exceeding the theoretical values for 2 and 3 Li^+/V_2O_5 insertion, respectively. After 100 cycles of 3 Li^+/V_2O_5 insertion/extraction at 0.20 A g^{-1} (~ C/3), ~ 84% of the initial capacity is retained. After thermal annealing, the core-shell structure presents a capacity of 294 and 390 mAh g^{-1}, matching well with the theoretical values for 2 and 3 Li^+/V_2O_5 insertion. The annealed sample shows further improved stability, with remarkable capacity retention of ~100% and ~88% for 2 and 3 Li^+/V_2O_5 insertion/extraction.

However, due to the high cost of Li. alternative approaches are currently being pursued for large scale production. Sodium ion batteries (SIB) have been at the forefront of this endeavor. Here we investigate the sodium insertion in the hydrate amorphous V_2O_5 using the VACNF core-shell structure. Electrochemical characterization was carried out in the potential ranges of 3.5 – 1.0, 4.0 – 1.5, and 4.0 – 1.0 (vs Na/Na^+). An insertion capacity of 196 mAh g^{-1} is achieved in the potential range of 3.5 – 1.0 V (vs Na/Na^+) at a rate of 250 mA g^{-1}. When the potential window is shifted upwards to 4.0 – 1.5 V (vs Na/Na^+) an insertion capacity of 145 mAh g^{-1} is achieved. Moreover, a coulombic efficiency of ~98% is attained at a rate of 1500 mA g^{-1}. To enhance the energy density of the VACNF-V_2O_5 core-shell structures, the potential window is expanded to 4.0 – 1.0 V (vs Na/Na^+) which achieved an initial insertion capacity of 277 mAh g^{-1}. The results demonstrate that amorphous V_2O_5 could serve as a cathode material in future SIBs.

Table of Contents

List of Figures

List of Tables

Acknowledgements

"John 3:16-For God loved the world so much that he gave his only son so that anyone who believes in him shall not perish but have eternal life"

First and foremost, I would like to express a special thanks to my advisor Professor Dr. Jun Li for his support and guidance throughout my graduate school career. I would also like to thank my supervisory committee member, Dr. Daniel Higgins, Dr. Emily McLaurin, Dr. Keith Hohn, Dr. Bala Natarajan, and former member Dr. Eric Maatta. Special thanks go out to Dr. Judy Wu and Dr. Gary Malek from the University of Kansas, Dr. Chris Sorenson and Dr. Dong Lin of Kansas State University for their guidance and collaboration. I would also like to thank Dr. Christine Aikens for her advising regarding Phi Lambda Upsilon, Dr. Chris Culbertson, Earline Dikeman and Michael Hinton for their help in teaching. Special mention goes to Tobe Eggers, Ron Jackson, Jim Hodgson, Collen Gaur, Ian Andree, and Dr. Dan Boyle for their help over the last five years.

Special thanks go to all former and present group members: Dr. Steven Klankowski, Dr. Gaind Pandey, Dr. Seok-Hwan Park, Dr. Yueping Fang, Dr. Luxi Zhang Swisher, Dr. Foram Madiyar, Yichen Zheng, Tao Liu, Ayyappan Elangovan, and Yang Song. I would also like to thank former summer REU students Emily Campion, Jackelyn Cubalo, Lisa Zhu, and Dorian Sneddon for their help on various projects. Many thanks to my friends: Jay Sibbitts, Caleb Russell, Harrison Schmidt, Nicole Green, Dr. Jordan Woehl, Eric Geanes, Sarah Schuetze, and Ashlyn Lehwald among others for their support throughout graduate school. I would also like to thank all the members of the Beta Rho Chapter of Alpha Chi Sigma fraternity for their support over the years.

I gratefully acknowledge the funding supported by NASA grant NNX13AD42A; ARO contracts AROW911NF-09–1–0295, ARO-W911NF-16-1-0029 and W911NF-12-1-0412, NSF grants NSF-DMR-1105986, NSF-DMR-1508494 and NSF-CBET-1703263; NSF EPSCoR Award EPS-0903806; and the matching support from the State of Kansas through Kansas Technology Enterprise Corporation.

Finally, a heartfelt appreciation goes out to my parents James R. Brown and Susan Robinson; grandparents Robert and Sue McCloud, Jim and Connie Brown, and Mary Brown; sisters Mallory S. Brown, Aubry L. Brown, and Anevay L. Robinson; and loved ones for their support throughout the years. Without them I would not be where I'm at today.

Dedication

"To my parents James R. Brown and Susan V. Robinson; grandparents Robert and Sue McCloud, Jim and Connie Brown, and Mary Brown; sisters Mallory S. Brown, Aubry L. Brown, and Anevay L. Robinson; and loved ones."

Preface

The dissertation comprises of the following major sections:

Chapter 1 – This chapter provides a broad overview of electrical energy storage. Here the basic concepts of electrical energy storage are discussed along with a short comparison between the different technologies in terms of energy density and power density. A thorough introduction to traditional electrical electrostatic capacitors and the emerging field of high dielectric materials is provided. The physical principles and materials of EDLCs, pseudocapacitors, lithium and sodium ion batteries is thoroughly discussed as well. In addition, techniques in optimizing faradaic electrical energy storage performance, electrode formation, and characterization are briefly discussed.

Chapter 2 – An accepted paper, published in *ACS Applied Materials and Interfaces*. High aspect ratio, vertically aligned carbon nanofibers (VACNFs) are conformally coated with aluminum oxide (Al_2O_3) and aluminum-doped zinc oxide (AZO) using atomic layer deposition (ALD) to produce a three-dimensional array of metal-insulator-metal core-shell nanostructures. The conformal core-shell AZO/Al_2O_3/VACNF array structure demonstrated in this work provides a promising three-dimensional architecture toward applications of solid-state capacitors with large surface area having a thin, leak-free dielectric separator.

Chapter 3 - An accepted paper, published in *ACS Applied Materials and Interfaces*. The energy storage properties of $Pb_{0.92}La_{0.08}Zr_{0.52}Ti_{0.48}O_3$ (PLZT) films are evaluated at variable film thickness of 125, 250, 500, and 1000 nm. Cyclic I-V measurements are used to evaluate the dielectric properties, which not only provides the total electric displacement, but also separates contributions from each of the relevant components including electric conductivity (D1), dielectric capacitance (D2), and relaxor-ferroelectric domain switching polarization (P). The results show that the PLZT

films can be optimized for different energy storage applications by tuning the film thickness to optimize between the linear and nonlinear dielectric properties and energy storage efficiency.

Chapter 4 – An accepted paper, published in *Electrochimica Acta*. This study reports an approach to achieving stable 2 and 3 Li^+ insertion into vanadium pentoxide (V_2O_5) as lithium-ion battery (LIB) cathode using a core-shell structure fabricated on electrospun carbon nanofiber (CNF) membranes more suitable for large scale production. The results reveal that the core-shell structure is an effective approach to breaking the intrinsic limits of V_2O_5 and enabling this high-capacity cathode materials for future LIBs.

Chapter 5 – An accepted paper, published in *Advanced Materials Interfaces*. Here we demonstrate an approach to achieving stable 3 Li^+ insertion into V_2O_5 by implementing a three-dimensional (3D) core-shell structure consisting of coaxial V_2O_5 shells sputter-coated on VACNFs. The as-deposited core-shell structure achieves capacities above theoretical values owning to the nature of the amorphous hydrated shell. After thermal annealing, near theoretical values are achieved with superior cycling stability.

Chapter 6 – A manuscript under review. Using the same 3D array core-shell structure discussed in Chapter 5, an approach to achieving high coulombic efficiency and Na^+ insertion/extraction capacity in V_2O_5 at high applied current rates is discussed. Owing to the optimal potential window throughout literature, four different potential windows are investigated to provide insight on tradeoffs between high capacity and coulombic efficiency.

Chapter 7 - A short discussion of future projects and current ongoing projects is provided.

Chapter 8 - A conclusion of the main findings in each of these published reports is provided.

Chapter 1 - Introduction into Electrical Energy Storage

1.1: Basics of Electrical Energy Storage

1.1.1 Motivation for Research

The depletion of fossil fuels coupled with new and innovated technologies has been the motivation for research in renewable electrical energy storage (EES) systems.[1] Renewable energy sources such as wind and solar are intermittent and don't convert electrical energy during down times. To offset these intermittences EES systems are used in conjunction to deliver electrical energy when required.[2-3] Recently, the development of EES technologies has been a major focus in the transportation sector.[4] Mass transportation systems such as buses, subways and trains are making the push to rely solely on renewable energy.[5-7] Hybrid and electric cars require EES technologies to provide additional energy for purposes of acceleration and braking.[8-9] In addition, electric cars must be as convenient as combustible engines to be competitive in the free market. Hence, advancements in the charging rate of the EES systems is required. This also applies to new and innovated technologies like laptops, iPads, and iPhones.[10] As technology advances, the energy requirements will also continue to increase. In addition, the demand for rapid charging is ever more growing.[11] It's clear that EES technologies play a critical part in our daily lives, however, the desirable performance is far from satisfactory.

1.1.2 Commercialized EES Technologies

To meet current demands EES technologies have been developed for a variety of different applications. Commercialized EES devices can be categorized into one of two groups: faradic and non-faradic. Non-faradic technologies include capacitors and electric double layer capacitors (EDLCs) where electrical charge is stored at the electrode surface. On the other hand, faradic based technologies such as Lithium-ion Batteries (LIBs) and pseudocapacitors store electrical

charge within the electrode material through the intercalation of a Li^+ ion or a series of oxidation and reduction reactions between the electrode and electrolyte. It should be noted that LIBs are secondary batteries that can be recharged; and different from primary batteries where electrical charge is provided through a single irreversible electrochemical reaction. Furthermore, EDLCs and pseudocapacitors are both electrochemical capacitors (ECs); a term that will be used to describe both.

1.1.3 Energy and Power

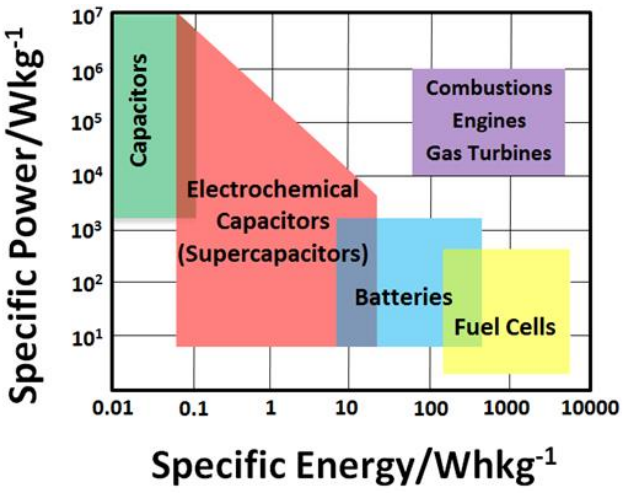

Figure 1.1 Ragone plot for electrical energy storage systems

Tradeoffs are common in EES in terms of the amount of charge that can be stored and the rate at which it's delivered. This relationship is illustrated in the Ragone plot in Figure 1.1. Capacitors are high-power devices that can deliver electrical charge very rapidly. The maximum specific power (P) of an EES system can be calculated using Equation 1.1

$$P_{max} = \frac{V^2}{4 * ESR}$$

Equation 1.1

where V is the operating voltage, and ESR (equivalent series resistance) is the accumulated resistance of the current collector, electrode and electrolyte. The high-power capability of

capacitors originates from a large operating voltage and a low ESR owning to the lack of a current collectors and electrolyte. On the other hand, LIBs are high-energy devices owning to the fact that electrical charge is stored throughout the electrode material. Despite the high operating voltages, the low specific energy of capacitors is due to the charge being stored only at the electrode surface. The specific energy (E) of a EES system can be approximated using Equation 1.2

$$E = \frac{1}{2} C_0 V^2$$

Equation 1.2

where C_0 is the specific capacitance or capacity and V is the operating voltage. It should be noted that this calculation is primarily used for capacitors and only an approximation for LIBs. The specific energy for LIBs is more complex and beyond the scope of this section. However, LIBs possess a high ESR and operate at low voltages (~2-4 volts) thus limiting their specific power capabilities. ECs have bridged the gap between batteries and capacitors with moderate specific energy and power capabilities useful in many niche applications. However, performance is still far from satisfactory. The aim in EES research is to extend the current limits of specific power and energy of LIBs and capacitors, respectively, to be competitive with combustible engines. Thus, our research focuses on increasing 1) the specific energy of capacitors and 2) the specific power LIBs.

1.2: Solid-State Electrostatic Capacitors

Solid-state electrostatic capacitors are modeled after the parallel plate capacitor as illustrated in Figure 1.2a. A dielectric layer physically separates two conductors or electrodes that are connected through an external circuit. When a voltage (V) is applied across the dielectric positive charge (q_+) builds on the surface of one side (which repels the q_+ on the other) allowing a

buildup of negative charge (q_-) on the other. Thus, charge is stored in an electric field (as compared to a magnetic field associated with inductors) as illustrated in Figure 1.2b.

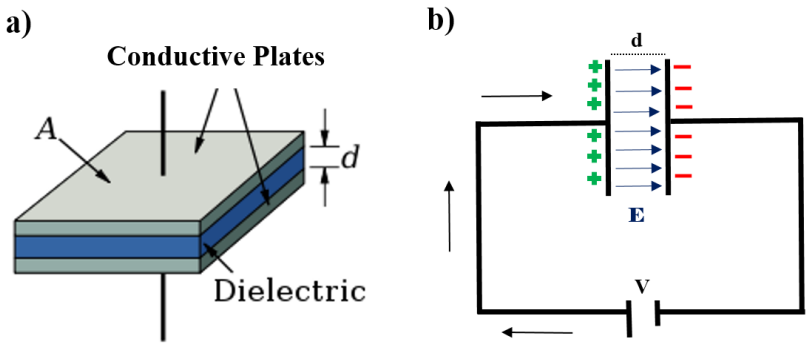

Figure 1.2 a) An illustration of the parallel plate capacitor and b) electric circuit diagram demonstrating the chare storage mechanism of solid-state electrostatic capacitors.

1.2.1 Linear Dielectrics

The amount of electrical charge (q) stored in a capacitor is linearly proportional to the applied voltage (V) as shown in Equation 1.3:

$$q = CV$$

Equation 1.3

where C is the capacitance express in the units of Farads (F). The capacitance can be calculated using the parallel plate capacitor in Equation 1.4

$$C = \frac{A\varepsilon\varepsilon_0}{d}$$

Equation 1.4

where A is the surface area of one electrode, d is the thickness of the dielectric, ε is the permittivity of the dielectric material (or dielectric constant), and ε_0 is the vacuum permittivity constant of air (8.854187×10^{-12} F m^{-1}). Capacitance values in most commercial capacitors ranges from a low as a picofarad (pF) to several millifarad (mF).

To increase the energy density of linear dielectric capacitors, research has focused on increasing the capacitance. According to Equation 1.4 there are three ways to accomplish this: 1)

increase the surface area of the electrode material, 2) use dielectric materials with high permittivity, and 3) decrease dielectric thickness. Increasing the overall surface area has been a point of interest in the field of solid-state electrostatic capacitors. Nanostructured templates such as anodic aluminum oxides templates (AAO)[12-14], silicon entrenched substrates[15-16], and multi layered ceramic capacitors (MLCCs)[17-18] have all been reported. In section 1.5.4.2, we will discuss the use of a vertically aligned carbon nanofiber arrays as a high surface area substrate for linear dielectric capacitors. Dielectric materials with high permittivities such as aluminum oxide (Al_2O_3, ε ~8)[19-21], hafnium oxide (HfO_2, ε ~25)[22-24], tantalum pentoxide (Ta_2O_5, ε ~50)[25-26] have all been explored for linear dielectric capacitors.

Most commercial capacitors have dielectric films on the order of several microns in thickness. To obtain sub-micron thick dielectrics, physical vapor deposition techniques such as reactive ion sputtering and pulse laser deposition have been employed (see section 1.6.1). Moreover, for thicknesses on the order of several nanometers, a chemical vapor deposition technique known as atomic layer deposition (1.6.1.3) has been employed. However, ultra-thin films have several drawbacks such as; 1) low operating voltage due to dielectric breakdown, 2) susceptible to pinholes resulting in short circuiting. If the operating voltage is too high, the electron orbitals within the dielectric material begin to elongate eventually damaging the dielectric material. Once the breakdown threshold is reached electrons are ripped from the orbital shells essentially converting the dielectric material to a conductor. Thus, careful consideration must be taken when designing a new solid-state electrostatic capacitor.

1.2.2 Nonlinear Dielectric Capacitors

Nonlinear dielectric films have attracted the attention of many due to the orders-of-magnitude higher dielectric constants than that of conventional linear dielectric materials. The

nonlinearity originates from the distinctive nonlinear dielectric properties associated with ε (and C_0) significantly dropping at high voltage bias V (or the electric field E). Here, internal polarization states are associated with the orientation of dipole moment of individual domains which can be reversed under an external electric field.[27] Consequently, the energy storage mechanism in nonlinear capacitors is quite different from conventional linear dielectric capacitors. Among them, ferroelectric and relaxor-ferroelectric materials have been leading the way for high-energy density solid-state electrostatic capacitors.

1.2.2.1 Ferroelectric Capacitors

Ferroelectric materials such as poly(vinylidene fluoride) (PVDF)[28-29] and lead zirconate titanate (PZT)[30-31] are promising nonlinear dielectrics for EES technology. However, ceramic films like PZT are particularly attractive due to their high ε value (~1000 vs. ~100 or less for polymers), superior mechanical and thermal properties, larger temperature range for operation, and high breakdown field E_b. The domain switching is represented by the characteristic hysteresis loop in the polarization-electric field (P-E) curve where the polarization P is the total charge involved in the process as shown in Figure 1.3a. For comparison, a representative P-E curve for linear dielectrics is presented in Figure 1.3b.

The energy storage properties of ferroelectric capacitors are schematically illustrated in Figure 1.3c. The total energy stored can be determined by integrating the area between the charging polarization curve and the max polarization (blue and green). However, the shaded region between the vertical axis and the discharge loop from max polarization to zero polarization (green) represents the recoverable electrical energy density, or the energy available for use. Thus, the blue shaded region represents energy that is lost; the energy required for reorientation of the dipole moment of the micron sized domains when electric field is reversed. Therefore, electrical

energy storage efficiency is quite poor and can lower than 50%. In linear dielectric films, the energy lost is negligible due to the atomic size of the domains, which require very little energy for reorientation resulting in electrical energy storage efficiency of ~100%. A comparison between the energy storage mechanisms of ferroelectric and linear dielectric capacitors is illustrated in Figure 1.3d. Therefore, for energy storage purposes, the hysteresis P-E loop needs to be suppressed with low remnant polarization (P_r) and low coersive field (E_c) values to reduce the energy loss and therefore enhance the overall efficiency.

1.2.2.1 Relaxor-Ferroelectric Capacitors

Relaxor-ferroelectric materials are a subclass of ferroelectrics that also present a permanent dipole moment in individual domains. However, their domain sizes are on the order of nanometers instead of micrometers. Thus, it takes much less energy to align the dipole moment with the external electric field, leading to a more suppressed P-E loop as shown in Figure 1.3e. The energy storage properties are like ferroelectrics but with a higher efficiency as illustrated by the ratio of green (available energy) to blue (energy loss) in Figure 1.3f. The increase in efficiency originates from the decreased domain size which requires less energy for realigning in the electric field.

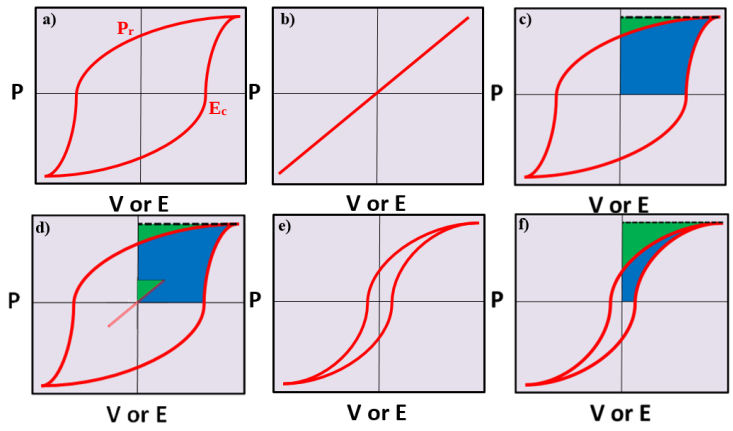

Figure 1.3 Typical P-E loops for ferroelectric a) and linear b) capacitors. A visual representation of the energy storage mechanism in ferroelectric capacitors c) and a visual comparison with linear capacitors d). An illustration of a typical P-E loop for relaxor-ferroelectric capacitors e) and their energy storage mechanism f).

Recently, several tungsten bronze and perovskite compounds have been investigated for relaxor-ferroelectric capacitors. Several of the tungsten bronze compounds of interest include barium strontium niobate [$(Ba_xSr_{1-x})Nb_2O_6$][32-34] and lead barium niobate [$Pb_{1-x}Ba_xNb_2O_6$][35-37]. In perovskites, the nonlinear electrical energy storage properties are associated with mixed cations of different valencies occupying one of the lattice sites in ABO_3 structures. These energy storage materials fall into one of two subclasses; A-site and B-site substitutions. Several of the common B-site substitution compounds include lead magnesium niobate [$(PbMg_{1/3}Nb_{2/3})O_3$ (PMN)][38-39] and lead scandium tantalate [$Pb(Sc_{1/2}Ta_{1/2})O_3$ (PST)][40-41]. One of the most well studied A-site substitution compounds is bismuth strontium titanate $(Bi_{2/3x}Sr_{1-x})TiO_3$ which has shown some moderate success in electrical energy storage.[42-43] However, one of the A-site substitution compounds of interest is lanthanum-doped lead zirconium titanate [$(Pb_{1-x}La_x)(Zr_yTi_{1-y})O_3$ (PLZT)], the A-site substituted form of PZT. It shows great potential in not only EES, but in other applications such as nonvolatile random-access memories, microwave devices, and electro-mechanical or photo-mechanical transducers.[44-46] Research has focused on its energy storage ability owing to its high ε (~1200) and low remnant polarization. In chapter 3 we discuss the energy storage properties of epitaxial PLZT films and observed a transition from linear to nonlinear properties with increasing film thickness.

1.3: Electrochemical Capacitors

ECs also known as Supercapacitors or Ultracapacitors store electrical charge at an electrode/electrolyte interface. Electric double-layer capacitors (EDLCs) and pseudocapacitors, both of which are ECs, differ in their charge storage mechanism. Briefly, ECs are modeled as two capacitors in series where electrodes are electrically connected through an external circuit but physically separated by an electrolyte as illustrated in Figure 1.4a. Here, a brief discussion on the

charge storage mechanisms as well as common electrode and electrolytes for EDLC (section 1.3.1) and pseudocapacitor (section 1.3.2) is included.

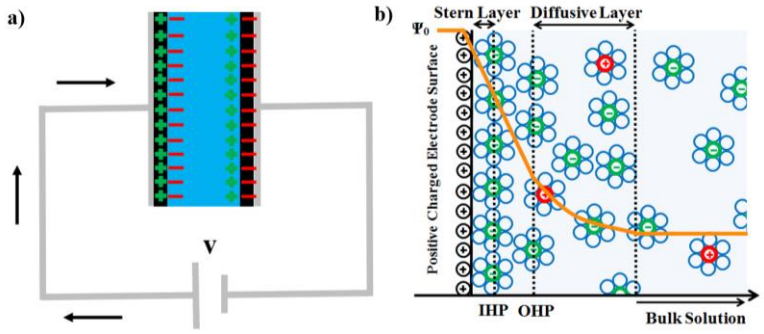

Figure 1.4 a) Circuit model of ECs and b) Guoy-Chapman-Stern Model

1.3.1 EDLCs

EDLCs store electric charge in the form of a double layer governed by the Guoy-Chapman-Stern (GCS) model illustrated in Figure 1.4b. A double layer is formed when positive charge accumulating at the surface of one electrode interact with negatively charged ions in solution forming a stern layer at the interface and a diffusive layer extending to the solution. Meanwhile negative charge accumulates at the surface of the other electrode creating a second double layer with the positive ions in solution as illustrated in Figure 1.5a. Thus, a potential difference arises across the capacitor as illustrated in Figure 1.5b. When fully discharged, the double layers dissipate resulting in a net potential of zero as illustrated in Figures 1.5c and d. The capacitance is analogous to the parallel plate capacitor in Equation 1.5.

$$C = \frac{A\varepsilon\epsilon_0}{d}$$

Equation 1.5

where A is the specific surface area of the electrode, ε is the relative permittivity of the electrolyte, ε_0 is the permittivity of vacuum, and d is the separation distance or Debye length (κ^{-1}) at the electrode/electrolyte interface. The capacitance can be enhanced by increasing the specific surface

area (SSA) of the electrode and the ionic strength of the electrolyte (I); which has an inverse relationship with the Debye length (κ^{-1}) as shown in Equation 1.6.

$$\kappa^{-1} \propto \frac{1}{\sqrt{I}}$$

Equation 1.6

Thus, the capacitance is several orders of magnitude higher than linear dielectric capacitors owing to the high SSA (500-2500 m^2 g^{-1}) and small ion separation at the interface (≤1 nm).

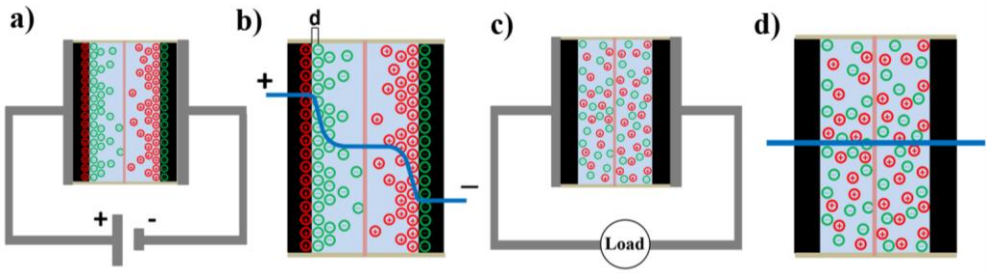

Figure 1.5 a) Fully charged EDLC in a circuit, b) potential profile of a fully charged EDLC, c) fully discharged EDLC, and d) potential profile of EDLC fully discharged

1.3.1.1 Electrode Materials for EDLCs

EDLCs consist of high surface area carbon electrodes such as activated carbon (AC)[47-48], single walled carbon nanotubes (SWCNT)[49-50], multi walled carbon nanotubes (MWCNT)[51-52], templated carbons[53-54], graphene[55-56] and activated carbon nanofibers (ACNFs)[57-58]. Among them, AC has been the most widely studied owning to its high SSA of 500-3000 m^2 g^{-1}, commercial availably, low cost and high specific capacitance values of ~300 F g^{-1}. However, the ultra-high SSA hasn't shown much of an advantage in terms of capacitance due to small pore sizes which are inaccessible to most ions in solution. Efforts have been made to optimize the pore size distribution through adjusting the activation process, however, this results in a loss of material density and electrical conductivity which reduces volumetric density and power capability. SWCNT and MWCNT have attracted a great deal of attention owning to their unique pore structure, electrical

properties and mechanical stability. However, the specific capacitance is limited (100-200 F g^{-1}) due to a low SSA (500 m^2 g^{-1}) which is attributed to their poorly developed microporous volume. Templated synthesis can provide an interconnected network of microporous and mesoporous carbon with tunable pore sizes, large SSA (1000-2000 m^2 g^{-1}) and a capacitance of 200-350 F g^{-1}. However, synthesis is time consuming making them unsuitable for large scale production. Graphene has been of interest owing to its high theoretical SSA (2630 m^2 g^{-1}), robustness, mechanical strength, electrical conductivity and high theoretical capacitance (550 F g^{-1}). However, only moderate success has been achieved owing to the inaccessibility of a large portion of the graphene surface due to aggregation during cycling. ACNFs has gathered a great deal of interest owing to its ultra-high SSA (up to 3000 m^2 g^{-1}) and outer microporous structure (as compared to the interior wall in ACs) which allow fast ion access which is promising for high-power applications. However, their low bulk density (0.2 g mL^{-1}) makes them unsuitable for small volume ECs.

1.3.1.2 EDLC Electrolytes

The specific energy and power of EDLCs are governed by the choice of electrolyte, which can be categorized into three broad groups: 1) aqueous, 2) room temperature ionic liquids (RTILs), and 3) salts dissolved in organic solvents.[59] Aqueous electrolytes such as KOH, NaOH, KCl, Na_2SO_4,and H_2SO_4 are of great interest owning to their low cost and ease of fabrication. Moreover, their high ionic conductivity (0.1-1 S cm^{-1}) makes them very attractive for high-power applications.[59] However, the decomposition of water restricts their voltage range to below 1V ultimately limiting the specific energy. On the other hand, RTILs containing imidazolium or pyrrolidinium cations with small anions such as tetrafluoroborate (BF_4^-) or bis(trifluoromethanesulfonyl)imide ($TFSI^-$) operate in a larger voltage range of 3 - 6 V.[60-61] Thus,

a higher specific energy can be achieved. However, their low ionic conductivity (0.1 – 10 mS cm^{-1}) limits their power capability. Moreover, operation at sub-ambient temperatures drastically increases their viscosity resulting in a loss of ionic mobility and conductivity which leads to a loss in capacitance. Organic based electrolytes such as a 1M tetra-ethylammonium tetrafluoroborate ($TEABF_4$) dissolved in acetonitrile provide moderate energy and power owing to their operating voltage of 2 - 3V and moderate ionic conductivity (10 – 100 mS cm^{-1}).[62] However, fabrication requires an inert atmosphere which is costly for production which has limited their use to niche applications. Moreover, safety concerns such as flammability and corrosion are a major drawback.

1.3.2 Pseudocapacitors

Pseudocapacitors store electrical charge by means of fast oxidation and reduction reactions between the electrode and electrolyte solution. The term pseudo is used because charge is not stored in a true capacitance form due to the faradaic nature. However, some of the electrical charge is stored through the fast surface redox reactions involving redistribution of ions and a double layer as described in the previous section. The term capacitance arises from the fact that the fast reactions mimic the performance of traditional EDLCs.[63] The specific capacitance of pseudocapacitors is generally several orders of magnitude higher than EDLCs due to charge storage within the electrode material. For an electrode to be considered pseudocapacitive, it must be able to exist in multiple oxidation states with no phase changes involving irreversible modifications of a 3-dimensional structure.[63] Pseudocapacitors can be categorized into two subclasses based on electrode material: 1) transition metal oxides, and 2) conductive polymers.

1.3.2.1 Transition Metal Oxides

Transition metal oxides such as RuO_2, MnO_2, NiO, V_2O_5, Co_3O_4, Fe_2O_3 and Fe_3O_4 have all been investigated as potential pseudocapacitors.[64-70] $RuO_2 \cdot xH_2O$ has been most widely studied

owing to its high electrical conductivity (~10^5 S cm^{-1}), high theoretical specific capacitance (2000 F g^{-1}) and three distinct oxidation states.[71] Most of the success is derived from its ability to operate in acid solutions with fast reversible electron transfer with an electroadsortion of protons on the surface shown in Schematic 1.1 where Ru oxidation states can change from (II) up to (IV) in a potential window of 1.2 V.

$$RuO_2 + xH^+ + xe^- \leftrightarrow RuO_2\text{-}x(OH)_x \quad \text{where } 0 \leq x \leq 2.$$

Schematic 1.1

Despite its success, the high cost of Ru makes it unsuitable for large scale production. MnO_2 has been considered a suitable replacement owing to its high theoretical specific capacitance (1380 F g^{-1}) and surface adsorption of electrolyte cations (K^+, Na^+, …) as express in Schematic 1.2.[65]

$$MnO_2 + xC^+ + \gamma H^+ + (x+\gamma)e^- \leftrightarrow MnOOCxHy$$

Schematic 1.2

A schematic of the charge storage mechanism for MnO_2 is shown in Figure 1.6. Here the electrode is represented by the purple and orange circles in oxidation states of Mn(IV) and Mn(III), respectively. The ions in solution are represented by green and red circles as negative and positive, respectively. When fully charged, the two electrodes will exist in different oxidation states with the positive side at the high valence state [Mn(IV)] and the negative side at the lower valence state [Mn(III)]. Thus, a potential difference is observed across the capacitor as shown in Figure 1.6a. During discharging, the electrodes will be in an intermediate state with a mix of valance states where the potential decreases at the positive side and increase at the negative side as illustrated in Figure 1.6b. When fully discharged, both electrodes will have an equal mix of both valence states, thus no potential difference exists as shown in Figure 1.6c. However, the low diffusion coefficients (D_{H^+} = 6 x 10^{-10} cm^2 s^{-1} and D_{Li^+} = 3 x 10^{-10} cm^2 s^{-1}) and poor electrical conductivity (~10^{-5} – 10^{-6}

S cm^{-1}) make it impractical as a stand-alone material.[72-73] Conductive additives such as carbon black and electrically inert polymer binders are needed which limits the specific capacitance to below 200 F g^{-1}.

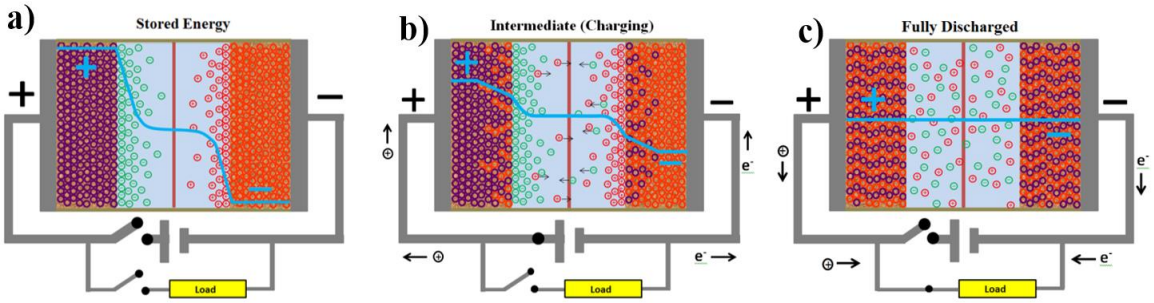

Figure 1.6 a) Illustration of a fully charged, b) intermediate charged state, and c) fully discharged pseudocapacitor system

NiO has been of interest owing to its ease of synthesis and high theoretical specific capacitance (3750 F g^{-1}).[66] However, high resistivity and poor cycling stability currently makes it unsuitable for practical applications. V_2O_5 has been sought after owing to its large number of oxidation states and high theoretical capacitance (>1000 F g^{-1}).[74] However, its low electrical conductivity (~10^{-5} – 10^{-3} S cm^{-1}) has hindered high-power capabilities. Recently, it's been shown that hydrogen thermal treatment of VO_2 increases the conductivity by 3 orders of magnitude due to the synergistic effects of H-doping.[75] Fe_2O_3 and Fe_3O_4 offer the advantage of low cost and high electrical conductivities.[69-70] Moreover, their operation in the negative potential range makes them attractive in hybrid systems (see section 1.3.3). However, their achievable specific capacitance is low and currently inhibits their practical use.

1.3.2.1 Conductive Polymers

Electrically conducting polymers (ECPs) have been of interest owing to their fast-reversible switching between redox states, high charge density, high electrical conductivity (from a 5 S cm^{-1} to 500 S cm^{-1}) and low cost.[76] Electrons are conducted through conjugated bonds along

the polymer backbone. Here, two rapid oxidation reactions occur simultaneously, one is the oxidation of the monomer and the other is the oxidation of the polymer with the insertion of a dopant/counter ion.[73] Electrical energy is stored in ECPs as delocalized π-electrons are accepted and released during electrochemical doping/dedoping as illustrated in Schematic 1.3.

p-doping (with counter anions): (Polymer) + γA^- ↔ [(Polymer)γ^+ γA^-] + γe^-

n-doping (with counter cations): (Polymer) + γC^+ + γe^- ↔ [(Polymer)γ^- γC^+]

Schematic 1.3

ECPs are classified into three types.[77] Type 1 is a symmetric configuration which utilizes p-doping ECPs for both positive and negative electrodes. However, the specific energy is limited due to the operating voltage of ~1V and only half of the total capacitance is achieved. Type II is an asymmetric configuration which utilizes two different p-doping ECPs with distinct electroactivities thus increasing the specific energy. Type III utilizes the same ECP for both electrodes where the positive electrode is p-doped and the negative electrode is n-doped. Thus, the specific energy is enhanced due to the wide operating voltage of 2 - 3 V. However, the develop of n-doping polymers remains a challenge.[73, 76] Moreover, chemical stability remains an issue. Common ECPs include polypyrrole (PPy), polyaniline (PANI), and derivatives of polythiophene.

PPy is one of the most studied ECPs due to its fast charge/discharge kinetics, high energy density, low cost, moderate conductivity (10-50 S cm^{-1}), high theoretical capacitance (620 F g^{-1}).[78-80] However, its high-density limits access to the interior sites of the polymer by dopant ions which in turn reduces its achievable capacitance. PANI or PAN is attractive owing to its high electroactivity and high specific capacitances (400-500 F g^{-1}).[81-82] However, high capacitance is only achievable in highly acidic mediums. Moreover, poor cycling and low power densities due to its low electrical conductivity (0.1-5 S cm^{-1}) limit its applicability. Thiophene-based ECPs such

as poly(3,4-ethylenedioxythiophene) or PEDOT is one of the more popular thiophene derivatives owing to its high electrical conductivity (300-400 S cm^{-1}) and chemical stability.[83] It has the advantage of being an electron rich polymer and consequently has a low oxidation potential which allows it to operate in a large voltage range of 1.2 V.[84] However, due to its large molecular weight only a low specific capacitance of 210 F $g^{-1}$is achieved.

Despite the progress made, pseudocapacitors remain under developed for practical applications. This is largely due to the fact that the pseudocapacitive field is plagued with papers presenting electrode performances that mimic a mediocre secondary battery rather than capacitive performance.[85] Moreover, as a stand-alone technology, pseudocapacitors don't offer much in the way of high specific power or energy owing to their narrow potential window in aqueous solutions.[86] However, they have become very attractive in asymmetric or hybrid systems.

1.3.3 Asymmetric or Hybrid Capacitors

Asymmetric ECs are defined as capacitors with two different electrode materials. The positive electrode has high resistance or overpotential to O_2 evolution, while the negative electrode has a high resistance or overpotential to H_2 evolution in an aqueous solution.[87] There are three types of asymmetric ECs.[88] Type I incorporates a pseudocapacitive material as the positive electrode and an EDLC material as the negative electrode.[89-90] Several studies report the use of RuO_2 or MnO_2 as a positive electrode and AC or graphene as the negative electrode.[91-92] Type II uses a lithium-insertion battery cathode such as $LiCoO_2$ as a positive electrode and a EDLC material as a negative electrode using a Li based aqueous solution.[93-94] This type of capacitor is referred to as a hybrid capacitor with a battery insertion on one side and a double layer formation on the other. Type III is the least studied which uses two different pseudocapacitive materials.[95-97] When compared to Type II, faster rates can be achieved since Type II is limited by the sluggish

Li^+ ion insertion. Moreover, the total cell capacitance or the amount of electrical charge stored is limited by the electrode with the lowest capacitance. Hence the total cell capacitance is usually limited to the capacitance of the EDLC material in Type II.

1.4: Secondary Batteries

1.4.1 Lithium Ion Batteries

LIBs currently dominate the secondary battery market in providing EES for many portable electronics. They are composed of an anode and a cathode that are connected through an external circuit but physically separated by a lithium based organic electrolyte as shown in Figure 1.7. Most commercial LIBs comprise of a Lithium Cobalt Oxide ($LiCoO_2$) cathode and a graphite anode. When fully charged, lithium atoms are stored in between the graphene layers of graphite. Upon discharge lithium atoms are oxidized to their ionic state Li^+ and migrate out of the anode toward the cathode, while the electrons conduct through the external circuit providing electric energy as shown in Schematic 1.4.

$$Li_xC_6 \leftrightarrow XLi^+ + 6C + Xe^-$$

Schematic 1.4

Upon arrival at the cathode, the electrons reduce the valance state of the cathode materials allowing Li^+ ions to intercalate as shown in Schematic 1.5.

$$Li_{(1-x)}MO_2 + XLi^+ + Xe^- \leftrightarrow LiMO_2$$

Schematic 1.5

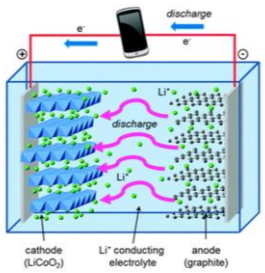

Figure 1.7 Schematic of LIB from Islam and Fisher at Chem. Soc. Rev. 43 (2014)

Discharging is completed when all the available insertion sites are filled. For recharging, the reverse process takes place with the oxidation of the cathode resulting in electrons conducting through the external circuit toward the anode while the Li^+ ions are extracted into the electrolyte. At the anode, Li^+ ions intercalate back into the graphene layers where they are reduced to their metallic state. The overall reaction process is illustrated in Schematic 1.6.

$$Li_{(1-x)}MO_2 + Li_xC_6 \leftrightarrow LiMO_2 + 6C$$

Schematic 1.6

The amount of electric charge an electrode material can store is express as capacity and is defined as milliamp hours per gram (mAh/g) as opposed to Farads per centimeter square or gram (F/cm^2 or F/g) in dielectric capacitors and ECs. The criteria for electrode materials in LIBs are that they must be reversible in the insertion and extraction of Li^+ and have a high potential for Li^+ to insert/extract as a cathode and low potential to serve as an anode.[98] Figure 1.8 maps out LIB electrode materials by their capacities and lithium insertion/extraction potentials.

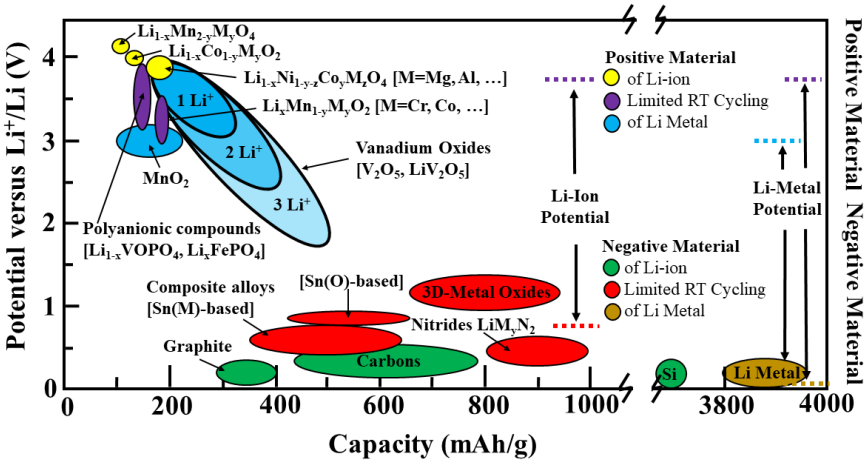

Figure 1.8 Schematic map of LIB materials, their capacities and potentials to Li^+ insertion/extraction (Adopted from Tarascon, J.M; Armond, M.; Nature, 2001, 414, 359-367)

1.4.1.1 Cathodes

Since the commercialization of LIBs by SONY in 1991 Lithium Cobalt Oxide ($LiCoO_2$) has been the leading cathode in EES owing to its high theoretical capacity of 272 mAh/g and high

redox potential of 4.2 V.[99] However, a practical reversible capacity of only ~147 mAh/g is achieved. Despite the advantages, the high cost and poor thermal stability of Cobalt have plagued $LiCoO_2$. Moreover, its stability can be quite poor compared to other materials and can undergo performance degradation or even failure when overcharged. The high charging voltage is advantageous to increase the cell capacity, but fading often negates this advantage. The cause of this has been associated with the dissolution of Co in the electrolyte after full delithiation. These drawbacks motivated the research into new LIB cathode materials. Materials for LIB cathodes can be categorized into three structural groups: 1) Oliviens, 2) Spinel Oxides, and 3) Layered Oxides.[100]

1.4.1.1.1 Oliviens

Olivines ($LiMPO_4$ [M = Fe, Mn, Co]) were once considered the most promising candidates to replace $LiCoO_2$ owing to their cyclability and high specific capacity.[101] Their open 3D framework allows the insertion/extraction of Li^+ ions to move along the conducting channel reducing structural damage over long term cycling.[102] $LiFePO_4$ is the most studied member of the olivine group owing to its low cost, long life, environmental friendliness and high theoretical capacity of 170 mAh g^{-1}. Despite its numerous advantages, its poor electrical conductivity (10^{-9} S cm^{-1}) limits its performance in high-power application. Moreover, its operating voltage is limited to 3.5 V due to the Fe^{3+}/Fe^{2+} redox couple. To overcome these setbacks the substitution of other transition metals such as Mn, Co, Ni has been investigated. $LiMnPO_4$ has an enhanced redox couple potential of 4.1 V providing a 15% increase in gravimetric energy density over $LiFePO_4$.[103] However, the Jahn-Teller effect of Mn^{3+} ions leads to low practical capacities and poor rate performances. $LiCoPO_4$ has an increased redox couple potential of 4.8 V providing an even higher energy density.[104] However, the high cost associated with Co as seen with the $LiCoO_2$ offset any

advantages. Recently, mixtures of $LiMnO_4$ or $LiCoPO_4$ with $LiFePO_4$ have shown an increase in voltage due to the increase in Mn and Co content and an increase in capacity due to the iron content.[105] $LiNiPO_4$ can reach a redox potential upwards of 5.1 V providing some of the highest energy density to date for cathode materials.[106] However, such a high voltage isn't practical due to side reactions with the electrolyte. Recently $Li_3V_2(PO_4)_3$ has been investigated owning to its high theoretical capacity of 197 mAh g^{-1} and a redox potential of ~4.8V.[107] The addition of vanadium enhances the lithium diffusion thus improving the performances at higher current rates leading to higher specific power.[108] Despite the advantage of high redox potentials, the low electrical conductivities associated with Olivines hinder their use in many practical applications.

1.4.1.1.2 Spinel Group

The Spinel compounds (LiM_2O_4 [M = Mn, Ni, Fe, Co]) are known for their robust host structure enabling 3D Li^+ ion diffusion pathways, low cost, and environmental friendliness.[109] One of the most researched members of the group $LiMn_2O_4$ has been sought after owing to its moderate theoretical capacity of 148 mAh g^{-1} and high redox potential of 4.1 V.[110-111] However, a phase change during cycling which has been attributed to the loss of oxygen which results in a loss of capacity. Moreover, the capacity fading has also been attributed to the dissolution of Mn^{2+} into the electrolyte. Transition metals such as Fe, Co, and Ni have been mixed with $LiMn_2O_4$ to overcome these challenges. The addition of iron ($LiFe_xMn_{2-x}O_4$) has resulted in additional discharge plateaus at high voltages (up to 5 V) with a moderate increased the capacity, however, capacity fading is still a major issue.[112] The addition of Co ($LiCo_xMn_{2-x}O_4$) has been shown to improve the capacity retention during cycling by stabilizing the spinel crystal structure.[113] Nickel has become the preferred addition ($LiNi_xMn_{2-x}O_4$) owing to its low cost and enhanced capacity retention capability. $LiMn_{1.5}Ni_{0.5}O_4$ has become quite popular owing to its increased redox

potential (4.7 V), increased capacity and higher capacity retentions.[114] The increased voltage is associated with the high oxidation potential of Ni^{2+} to Ni^{4+}, making it a promising high voltage cathode material. Moreover, the Ni^{2+} pushes all Mn ions to Mn^{4+} which results in a more stable structure thus suppressing the Jahn-Teller distortion. Despite the efforts, the spinel compounds are still plagued with low reversible capacities due to the limitation of 0.5 Li^+ ion per MO_2 formula. Moreover, the high voltages associated with nickel are not compatible with current electrolytes.

1.4.1.1.3 Layered Compounds

Layered compounds ($LiMO_2$ [M = Co, Ni, Mn, V]) are the most studied and successful cathode material for LIBs owing to the successes of $LiCoO_2$.[115] Other materials such as $LiNiO_2$ have been investigated owing to its high capacity (190-210 mAh g^{-1}), low cost, high energy density and similar Li^+ ion insertion mechanism of $LiCoO_2$.[116] However, nickel ions often occupy sites in the lithium plane which impedes lithiation/delithiation thus making the preparation of the appropriate composition a daunting task. $LiMnO_2$ has been sought after owing high obtainable capacity of ~200 mAh g^{-1} and high Mn^{3+}/Mn^{4+} redox potential of 4.5 V.[117] However, the Jahn-Tell distortion continues to result in capacity fading. Various compositions of Ni and Mn ($LiNi_xMn_yO_2$ [x + y = 1]) have also been investigated. The equal mixing ($LiNi_{0.5}Mn_{0.5}O_2$) has been the most successful composition is owning its high retainable capacity of ~200 mAh g^{-1}.[118-119] However, the cation mixing of Ni^{2+} and Li^+ ions leads to poor cycling stability. Cobalt has been introduced to form $LiNi_xCo_yMn_zO_2$ (x + y + z = 1) in effort to reduce the amount of defect Ni^{2+} ions in the Li^+ ion layer. $LiNi_{1/3}Co_{1/3}Mn_{1/3}O_2$ has been the most practical composition owning to its high theoretical capacity of 272 mAh g^{-1} and good stability.[120-121] Li-rich oxides ($xLi_2MO_3 \cdot (1-x)LiMO_3$ [0 < x < 1] [M = Ni, Mn, Co, V]) have recently garnered attention owning to their

enhanced capacity up to 300 mAh g^{-1}.[122-123] However, poor cycling and rapid capacity fading plague the Li-rich oxides.

1.4.1.1.4 Vanadium Pentoxide

Vanadium pentoxide (V_2O_5) is regarded as a promising layered cathode material owing to its high theoretical capacity due to multiple Li^+ insertion/extraction reactions in addition to the low cost, low toxicity, high electrode potential in lithium-extracted state (up to 4.0 V) and easily accessible layered structure for Li^+ ion insertion.[124] Theoretically, crystalline V_2O_5 can achieve a reversible specific capacity of 294 mAh g^{-1} (for a two Li^+/V_2O_5 insertion process) and an irreversible capacity of 441 mAh g^{-1} (for a three Li^+/V_2O_5 insertion process).[125] Achieving reliable capacity with V_2O_5 cathodes close to the theoretical value has been a challenge due to the small Li^+ ion diffusion coefficients (~10^{-15} – 10^{-12} cm^2s^{-1}) and low electrical conductivities (~10^{-3} – 10^{-5} S cm^{-1}), which ultimately hinder the performance of V_2O_5 cathodes in practical EES devices.[126-127] It is well known that the Li^+ intercalation process in crystalline V_2O_5 is accompanied by multiple phase transitions. Trace amounts of Li^+ intercalation results in α-$Li_xV_2O_5$ ($x < 0.01$) structure, which is transformed into ε-$Li_xV_2O_5$ ($0.35 < x < 0.7$) after further lithiation. Insertion of exactly one Li^+ leads to the formation of δ-phase $Li_xV_2O_5$ ($x = 1$). Further lithiation converts the δ-phase to γ-$Li_xV_2O_5$ ($1 < x < 2$).[128] At more than two Li^+ insertions, an irreversible transformation to rock-salt-type ω-$Li_xV_2O_5$ phase ($2 < x < 3$) typically occurs as described in Schematic 1.7.

(1) $V_2O_5 + 0.5Li^+ + 0.5e^- \leftrightarrow Li_{0.5}V_2O_5$ [$\varepsilon - Li_xV_2O_5$ $(0.35 < x < 0.7)$]

(2) $Li_{0.5}V_2O_5 + 0.5Li^+ + 0.5e^- \leftrightarrow LiV_2O_5$ [$\delta - Li_xV_2O_5$ $(x = 1)$]

(3) $LiV_2O_5 + 1Li^+ + 1e^- \leftrightarrow Li_2V_2O_5$ [$\gamma - Li_xV_2O_5$ $(1 < x < 2)$]

(4) $Li_2V_2O_5 + 1Li^+ + e^- \leftrightarrow Li_3V_2O_5$ [$\omega - Li_xV_2O_5$ $(2 < x < 3)$]

Schematic 1.7

Such phase transition processes induce large lattice strains due to different crystal structures and lattice constants in distinct phases mixed within each single particle, which unavoidably causes irreversible structural damage resulting in poor battery life. The larger amount of Li insertion by 3 Li^+/V_2O_5 insertion makes such structural changes even more severe.[67] As a result, practical applications of traditional crystalline V_2O_5 cathodes have been limited to below two Li^+/V_2O_5 insertion/extraction processes.

1.4.1.2 Anodes

Lithium metal was once considered the ideal anode in LIBs owing to its low reduction potential (-3.04 vs S.H.E.) and high theoretical capacity of 3840 mAh g^{-1}. Unfortunately, numerous safety concerns arose when short circuiting occurred after several cycles due to rapid dendrite growth.[129] Thus, graphite has been the leading anode in commercial LIBs since hitting the market in 1991 owing to its electrical conductivity and good Li^+ ion insertion/extraction reversibility. However, despite the success, its low specific capacity of ~372 mAh g^{-1} limits its energy storage capability. Efforts are underway to find alternative materials with high capacity and good stability in or order to be applicable in large scale production. Current researched materials can be categorized into three main groups depending on their electrochemical reaction with lithium; 1) intercalation/de-intercalation, 2) alloy/de-alloy and 3) conversion reactions.[130]

1.4.1.2.1 Intercalation/de-intercalation

Carbon allotropes have been of interest owning to their thermal and chemical stability and electrical conductivity. Moreover, their electrochemical stability at low potentials ($\leq$ 0.01 V Li/Li^+) makes them attractive for next generation LIBs.[130] Carbon based anodes can be categorized into two groups according to their orientation;1) hard carbons (graphitizable carbons) that have a high degree of long range order and 2) soft carbon (non-graphitizable) that have a highly disorder

orientation.[131] Soft carbons have had tremendous success in LIBs in part due to the success of graphite. However, low capacities and high voltage hysteresis during the delithiation process hinders their use in next generation LIBs. Hard carbons on the other hand have not had the same success.[132] They were first investigated by the Kureha Corporation in 1991 as negative electrodes in LIBs. A capacity of 500 mAh g^{-1} was achieved in the potential range of 0-1.5 V (vs Li/Li^+).[133] However, the random alignment of graphene sheets proved to be problematic in lithium diffusion. Moreover, they suffered from low initial coulombic efficiency and tap densities which attributed to their initial downfall in LIBs.

Recently research has been focused on nanosized carbon allotropes such as graphene, SWCNTs and MWCNTs. SWCNTs and MWCNTS have been investigated as owing to their superior electronic conductivity, good mechanical stability and high theoretical capacity estimated to be 1116 mAh g^{-1}.[134-136] The high capacity is attributed to the intercalation of Li^+ ions at the surface of the outer graphitic layers as well as inside the central tube. However, achieving such a capacity has been a major challenge. Moreover, coulombic efficiency is poor due to the presences of large structural defects and high voltage hysteresis. Research has focused on optimizing wall thicknesses, tube diameters, porosity and shape to overcome these drawbacks.[136] Graphene on the other hand, has been considered an alternative owing to its high electrical conductivity, surface area and charge mobility.[137-138] However, the theoretical capacity has been a point of debate which has been reported as either 780 or 1116 mAh g^{-1}.[139] These values are based on different interactions where former assumes adsorption of Li^+ ions on both faces of graphene, while the latter assumes Li^+ ions are is trapped at the benzene ring in a covalent bond (LiC_2 stoichiometry).[140] Other allotropes such as carbon nano onions (CNOs), carbon nanofibers (CNFs) and hollow carbon

spheres have been investigated as well.[141-143] However, most of these allotropes currently have a high production cost making them unsuitable for commercial LIBs.

Recently titanium based oxides have attracted a lot of attention owing to their excellent intercalation/de-intercalation of Li^+ ions along with low cost, low toxicity, minimal volume changes and excellent cycling life.[144] Spinel $Li_4Ti_5O_{12}$ (LTO) has been sought after owing to its excellent reversibility at high operating potentials (~1.5 V vs Li/Li^+).[145] Upon Li^+ ion insertion, the rock salt type $Li_7Ti_5O_{12}$ forms yielding an almost unchanged structure which is beneficial in terms of safety.[145] However, its low theoretical capacity (175 mAh g^{-1}),electrical conductivity (~10^{-13} S cm^{-1}), and relatively high Li insertion/extraction potential limit its practical use.[146] Titanium dioxide (TiO_2) or titania has gained a lot of attention in recent years owing to its large-scale producibility and moderate theoretical capacity of 330 mAh g^{-1}.[147] In addition, its excellent stability at high potentials (~1.5 V vs Li/Li^+) provides advantages over many other materials.[148] Moreover, its high electrochemical activity, good chemical stability and structural diversity provides many additional benefits. However, achieving the full capacity remains a challenge.

1.4.1.2.2 Alloy/De-alloy

Some of the most promising anodes for next generation LIB anodes form an alloy with lithium and have the highest theoretical capacities to date. Among them, silicon has been the most widely studied owing to its ultra-high theoretical capacity of 4200 mAh g^{-1}.[149] Moreover, it's the second most abundant element in the earth's crust making it inexpensive and environmentally friendly. The high specific capacity is due to the formation of intermetallic Li-Si binary compounds such as $Li_{12}Si_7$, Li_7Si_3, $Li_{13}Si_4$, and $Li_{22}Si_5$ or the fully lithiated alloy $Li_{4.4}Si$. However, large volumetric expansion (up to 400%) has hindered its development in current LIBs.[150-151]

Silicon monoxide (SiO) has been considered a good alternative owing to its minimal volume change and respectable theoretical capacity (>1600 mAh g^{-1}).[152] However, its atomic structure has been a source of controversy over the past century and has yet to be solved. Thus, the electrochemical reactions happening during the charge-discharge process are yet to be fully understood. Most reports suggest that SiO is converted to Si and lithium oxides ($SiO + xLi \leftrightarrow Si + Li_xO$), followed by the possibly Si-Li formation ($xLi + Si \leftrightarrow Li_xSi$).[153] Alternatively, the direct formation of Si-Li alloy and lithium silicates ($xLi + SiO \leftrightarrow Li_{x-y}Si_z + Li_xSiO_z$) has also been suggested.[154] Despite the progress, its low electric conductivity currently inhibits its applicability.

Germanium (Ge) has been extensively studied owing to its high theoretical capacity (1623 mAh g^{-1}) and electrical conductivity which is ~10^4 times that of silicon providing a great advantage for high-power applications.[155-156] However, its high cost and dramatic volume changes (~300 %) limit its applicability. Tin oxide (SnO_2) has been sought after owing to its current mass production capability.[144] The electrochemical lithium alloying reactions can be summarized in two steps. The first step involves an irreversible step where SnO_2 is reduced into Sn and lithium oxides ($SnO_2 + 4Li \leftrightarrow Sn + 2Li_2O$) providing an initial theoretical capacity of 1491 mAh g^{-1}. The second step involves a reversible Sn-Li alloying/dealloying reaction ($Sn + 4.4Li^+ \leftrightarrow Li_{4.4}Sn$) resulting in the commonly considered theoretical capacity of 783 mAh g^{-1}.[157] However, the large volumetric change associated with alloy/dealloy materials continues to limit its practical LIB application.

1.4.1.2.4 Conversion materials

Anodes based on a conversion mechanism are composed of transition metal compounds such as oxides, phosphides, sulfides and nitrides (M_xN_y; M = Fe, Co, Cu, Mn, Ni and N = O, P, S and N) where the transition metal compound is reduced and a lithium compound (Li_xN_y; N = O, P, S and N) is formed upon lithiation as described in Schematic 1.8.[130]

$$M_xN_y + zLi^+ + ze^- \leftrightarrow Li_zN_y + xM$$

Schematic 1.8

Among the oxides haematite (α-Fe_2O_3) and magnetite (Fe_3O_4) are some of the most well studied owing to their high abundancy, low cost, non-toxicity and high theoretical capacities of 1007 (α-Fe_2O_3) and 926 (Fe_3O_4) mAh g^{-1}.[158-159] Moreover, the relatively high electrical conductivity of Fe_3O_4 (10^2 S cm^{-1}) makes it advantageous for high-power applications. However, low Li^+ diffusion coefficients, volume expansion and high electrode potential ($\geq$ 1.0 V vs Li/Li^+) has hindered their applicability. Cobalt oxides such as Co_3O_4 and CoO have been sought after owing to their relatively high capacities 890 and 715 mAh g^{-1}, respectively.[160-161] However, the high cost of cobalt makes their applicability unlikely in next generation LIBs. Extensive research has also been focused on a variety of other transition metal oxides such as NiO, MnO_x, CuO_x, MoO_x, and CrO_x for a variety different advantages.[162] Despite intense efforts, low capacities (~500-800 mAh g^{-1}), poor electrical conductivities and slow Li^+ ion diffusion need to be addressed.

1.4.2 Sodium Ion Batteries

Despite the success of LIBs, they're not adequate for large-scale production in the transportation and energy sectors due to the high cost of lithium. Lithium is a rare Earth metal (<<< 0.9% of the Earth's crust) bringing the cost of lithium-containing precursors such as lithium carbonate to $5000/ton.[163] Sodium on the other hand makes up about 2.6% of the earth's crust, bringing estimations down to about $115-165/ton for sodium-containing precursors such as torna.[164] Sodium is an attractive alternative owning to its similar chemical properties to that of lithium. However, the production of sodium ion batteries (SIBs) has been hindered by sodium's large ionic radius (1.02 Å) compared to lithium's (0.59 Å) making the choice of electrode materials challenging.[165]

1.4.2.1 Anodes

Like lithium, sodium metal was also once considered an ideal anode. However, its low melting point (97.7 C) raised many safety concerns making it unsuitable for any realistic applications. Moreover, at room temperature it suffers from poor reversibility during long-term plating and stripping due to formation of nonuniform solid electrolyte interphase as well as dendritic growth.[166] Despite the enormous success of graphite, attempts to replicate the performance in SIBs has resulted in rapid capacity fading and ultimately cell failure after several cycles owing to the small d-spacing (3.43 Å) between the graphene sheets. Efforts have been made to modify the d-spacing of graphite through various synthesis. Wen et al. reported the expansion of oxidized graphite using a thermal annealing procedure. A high capacity of 284 mAh g^{-1} was achieved at a current density of 20 mA g^{-1}.[167] Moreover, a capacity of 136 mAh g^{-1} was maintained at 100 mA g^{-1} after 1000 cycles. Interestingly the Na^+ insertion mechanism into the expanded graphite is similar to the Li^+ insertion, which is different from other carbon materials.[168]

1.4.2.1.1 Carbon Materials

Carbon has been of interest owning to its high natural abundancy and renewability. Of all the carbon allotropes previously mentioned, graphene and hard carbons have been the most studied. Graphene has been sought after owing to its high electrical conductivity and chemical stability. Wang el al. achieved a reversible specific capacity of 217 mAh g^{-1} at a current density of 40 mA g^{-1} using reduced graphene oxide.[169] It has been shown that performance can be significantly enhanced by the addition of a heteroatom doping or synthesizing a hierarchically porous structure. Xu et al. reported a nitrogen-doped graphene foam that reached an ultra-high specific capacity of 2600 mAh g^{-1} in the initial cycle and stabilized at 1050 mAh g^{-1} in fifth cycle at a current density of 100 mA g^{-1}.[164] Hard carbons have been of interest owing to their highly

disordered structure and large interlayer distances.[170] They have exhibited reversible capacities up to 300 mAh g^{-1} at higher current rates.[171] Other carbon allotropes such as CNFs, MWCNT and SWCNT have been investigated, but often have poor cyclic stability and rate capability.[172-174]

1.4.2.1.2 Alloy/De-alloy

As in the case of LIBs, alloy-based anodes exhibit some of the highest theoretical capacities to date. Unfortunately, the ultra-high capacity of silicon can't be replicated due its inactivity with the Na^+ ion. As an alternative, Indium has been explored but has only reached a capacity of ~100 mAh g^{-1}.[175] Sn and Ge have been heavily researched owing to their high theoretical capacities of 847 and 369 mAh g^{-1}.[176-177] However, the high cost, sluggish kinetics and poor cycling stability have proven to be problematic. Among all the alloy-based anodes, phosphorous has the highest theoretical capacity of 2596 mAh g^{-1}.[174] However, its low electrical conductivity (1 x 10^{-14} S cm^{-1}) limits its high-power capability. Antimony (Sb) is one of the more promising with a theoretical capacity of 660 mAh g^{-1}.[178] Despite the progress, large volume expansion continues to be a hurdle for the SIB community.

1.4.2.1.3 Metal Oxides

Metal oxides store Na^+ ions through conversion reactions and have become of interest in recent years owing to their low cost. They fall into one of two categories according to the electrochemical activity of the metal.[168] The first category contains electrochemically inactive metals such as Fe, Co, Ni, Cu, Mn, and Mo, where the metal oxides react with Na^+ ions through a one-step conversion reaction shown in Schematic 1.9.

$$MO_x + 2xNa^+ + 2xe^- \leftrightarrow xNa_2O + M$$

Schematic 1.9

Iron oxide (Fe_2O_3) has been of great interest owning to its ultra-high theoretical capacity (1007 mAh g^{-1}).[179] Spinel $NiCo_2O_4$ and CuO have recently been investigated not only for their high theoretical capacities (890 and 674 mAh g^{-1}, respectively) but rather for their relatively high electrical conductivities (0.1 - 1.0 S cm^{-1}) which makes them much more suitable for high-power applications.[180-181] Titanium oxides such as TiO_2, $Na_2Ti_3O_7$, $Na_4Ti_5O_{12}$, $Li_4Ti_5O_{12}$, and $Na_2Ti_6O_{13}$ have also been explored due to their nontoxicity, low operating voltage, low strain and excellent cyclability.[182] However, the performance depends on their morphology, as well as electrolyte and binder composition. Moreover, due to the low number of Na^+ ion storage sites, capacity is often limited to below 200 mAh g^{-1}. Other metal oxides such as Co_3O_4, NiO, MoO_3, and MnO_x have also been investigated, however, their capacities rarely reach above 500 mAh g^{-1}.[183-186]

For higher capacity, category two metal oxides with electrochemically active metals such as Sn and Sb have been explored.[168] Here, metal oxides first react with Na^+ via a conversion reaction (schematic 1.9) followed by an alloying reaction as shown in Schematic 1.10.

$$M + yNa^+ + ye^- \leftrightarrow Na_yM$$

Schematic 1.10

SnO_2 and Sb_2O_3 have been extensively studied owing to their theoretical capacities of 782 and 1102 mAh g^{-1}, respectively.[187-188] Despite the higher capacity retentions, the high-volume expansion associated with alloying has been proven to be problematic

1.4.2.1.4 Metal Sulfides

Layered metal sulfides (MS_x) such as MoS_2, SnS_2, SnS, WS_2 and TiS_2 have been investigated as potential anodes owing to their large interlayer spacing which can accommodate the Na^+ ion.[168] The large interlayer spacing originates from the orientation of the metal and sulfur atoms where the metal atoms (M) are sandwiched between two sulfur layers (S). A strong covalent

bond exists between the M-S interactions, while weak van der Waal interactions hold together the S-M-S single-layers.[168] Among them molybdenum disulfide (MoS_2) has been the most widely studied. The mechanism of Na-MoS_2 formation occurs through a two-step process as shown in Schematic 1.11:

$$1)\ \ MoS_2 + xNa^+ + xe^- \leftrightarrow Na_xMoS_2\ (x < 2)$$

$$2)\ \ Na_xMoS_2 + (4-x)Na^+ + (4-x)e^- \leftrightarrow 2Na_2S + Mo$$

Schematic 1.11

The Na^+ ion first intercalates into MoS_2 to form an intermediate (Na_xMoS_2), which decomposes to Na_2S and Mo through a conversion reaction.[189] It should be noted that a similar mechanism is proposed for all the layered MS_x. Unfortunately, the second step usually causes severe volume expansion and sluggish kinetics for Na^+ intercalation which results in rapid capacity fading. To overcome this issue the second step can be restricted by limiting the cut voltage to ~0.4 V vs Na/Na^+. However, this strategy often limits the available capacity to ~300 mAh g^{-1}.[190] The synthesis of unique MoS_2 architectures and the incorporation of carbon additives have allowed the low voltage limit to be extended to 0.01 V vs Na/Na^+ with stable capacities of 600 mAh g^{-1}.[191]

1.4.2.2 Cathodes

Like LIBs, the cathode continues to be the bottleneck for SIBs with respect to the low capacity compared to many of the proposed anodes. The success of CoO_2 is yet to be replicated in SIBs, however, research has shown some promising results.[191] Most of the cathode proposed currently being investigated fall into one of three groups; 1) polyanionic compounds, 2) metal hexacyanometalates and 3) metal oxides.[192]

1.4.2.2.1 Polyanionic Compounds

Polyanionic compounds have been pursued extensively as Na^+ ion intercalation cathodes owing to their structural diversity, stability and high operating voltages which are crucial for future technologies.[192] Olivine $NaFePO_4$ has been one of the most pursued owing to the success of its $LiFePO_4$ analogue and its high theoretical capacity of 154 mAh g^{-1}.[193] NASICON $Na_3V_2(PO_4)_3$ is another phosphate compound that has been investigated owing to its unique ion-diffusion channels, however, theoretical capacity is limited to 117 mAh g^{-1} since only two thirds of the Na^+ ions can be extracted below 4.5 V (vs Na/Na^+).[194] Pyrophosphates such as $Na_2MP_2O_7$ (M = Fe, Co, Mn) and $Na_4M_3(PO_4)_2P_2O_7$ (M = Co, Fe) have been of interest owing to their structural diversities which offer different advantages in terms of thermal stability and Na^+ ion accessibility.[195-196] Fluorophosphates such as Na_2MPO_4 (M =Fe, Co, Mn) and $Na_3(VO_x)_2(PO_4)_2F_{3-2x}$ ($0 \leq x \leq 1$) as well as sulfates like $Na_2Fe_2(SO_4)_3$ have also been investigated owing to their relatively high operating voltages which is advantageous for high energy density.[197-199] However, despite the advantages of polyanionic compounds, the practical capacities are often limited to below 100 mAh g^{-1} which currently hinder their applicability in future technologies.

1.4.2.2.2 Metal Hexacyanometalates

Metal hexacyanometalates have been of interest owing to their rigid open framework with interstitial sites suitable for Na^+ ion accommodations and simple synthesis with nontoxic precursors which is required for large scale production. Hexacyanometalates can be categorized into two kinds, $KM[Fe(CN)_6]$ and $Na_xM[M'(CN)_6]$.[192] In the $KM[Fe(CN)_6]$ group, $KFe[Fe(CN)_6]$ also known as Prussian Blue has been of interest owing to its high operating voltage and theoretical capacity 126 mAh g^{-1}.[200] Other metals (M = Mn, Ni, Cu, Co, and Zn) have been substituted for the Fe with achievable capacities ranging from 50 – 100 mAh g^{-1}.[201] $Na_xM[M'(CN)_6]$ on the other

hand is a Prussian Blue analogue that can reach a high theoretical capacity of 170 mAh g^{-1} [based on $Na_2FeFe(CN)_6$].[202] Several other analogues such as $Na_xMn[Fe(CN)_6]$ and $Na_xCo[Fe(CN)_6]$ have also been pursued.[203] Moreover, $Na_2Mn[Mn(CN)_6]$ has been shown to provide a high capacity of 209 mAh g^{-1}, however rapid capacity fading ensues likely due to Mn dissolution.[204] Despite the efforts, most of the reported metal hexacyanometalates based SIB cathodes rarely reach above 120 mAh g^{-1} which is not suitable for practical applications.

1.4.2.2.3 Metal Oxides

Transition-metal oxides have attracted a lot of interest owing to their controllable synthesis and high electrochemical activity. Among them single-metal layered oxides such as Na_xCoO_2 and Na_xMnO_2 have been considered. Na_xCoO_2 was once considered a potential cathode owing to its good ionic diffusivity and the success of it analogue $LiCoO_2$.[205] However, electrochemical performance is still far from satisfactory with practical capacities rarely reaching 100 mAh g^{-1}.[206] On the other hand, Na_xMnO_2 appears to be more attractive owing to its low cost and high theoretical capacity of 243mAh g^{-1}.[207] However, structural collapse has been a major drawback. $NaFeO_2$ is of interest owing to the abundancy of iron and the highly active $Fe^{4+/3+}$ couple, but stability above 3.5V (vs Na/Na^+) still limits its applicability.[208] Several other single-metal oxides such as $NaCrO_2$ and $NaNiO_2$ have been investigated which show promising results.[209-210] As standalone cathodes, these materials show promising results but with some major drawbacks. However, to capitalize on the synergistic contributions each of these metals offer, multi-metal oxides such as $Na[Ni_xMn_y]O_2$, $Na[Ni_xMn_yCo_z]O_2$ and $Na[Ni_xMn_yFe_z]O_2$ have been investigated.[192] Tradeoffs between high capacity, high voltages, and stability can all be modulated by varying the composition of each of the metals.

1.4.2.2.4 Vanadium Pentoxide

Among the metal oxides, V_2O_5 has been investigated as a potential SIB cathode owing its low cost, low toxicity, high electrode potential in lithium-extracted state (up to 4.0 V) and accessible layered structure for ion insertion.[124] It has been reported that V_2O_5 can achieve a theoretical capacity of 236 mAh g^{-1} ($Na_xV_2O_5$ (x~1.6)).[211] Orthorhombic V_2O_5 has an interlayer d-spacing of 4.4 Å and has been the gold standard for LIB research. Su et al. achieved an insertion capacity of 230 mAh g^{-1} in the first cycle at a rate of 20 mA g^{-1}, however, capacity dropped to 159 mAh g^{-1} in the second cycle.[212] Despite the moderate success, the small d-spacing results in structural collapse leading to rapid capacity fading. On the other hand, bilayered V_2O_5 is reported to have a d-spacing of ≥10 Å which is much more suitable for Na^+ insertion.[213-214] Tepavcevic et al. achieved a reversible insertion capacity of 250 mAh g^{-1} with significantly improved cycling stability.[215] Several reports have suggested that amorphous V_2O_5 can outperform crystalline due to the disordered nature of the lattices which can aid in pseudocapacitive contribution.[216-218]

1.5: Techniques in Optimizing Faradaic EES Performance

One of the major emphases in research has been to improve the charge-discharge rates for high-power applications. To achieve high rates two major issues that need to be addressed are 1) poor ion diffusion coefficients (D_o) and 2) low electrical conductivities of electrode materials**.**

1.5.1 Ion Diffusion Coefficient

Many of the proposed electrodes are plagued with poor D_o which is defined as $L = (D_o t)^{1/2}$ where L is the length of diffusion and t is the time required to diffuse through the respective length. Thus, a smaller D_o results in longer charging and discharging duration. Tables 1.1 and 1.2 list the Li^+ and Na^+ diffusion coefficients of many of the commonly proposed materials with the diffusion lengths achieved in 60 and 10 seconds. [73, 159, 219-225]

	Li^+ diffusion ($cm^2\ s^{-1}$)	Dif. Length 1 min (Li^+)	Dif. Length 10 Sec (Li^+)
MnO_2	3×10^{-10}	1341 nm	547 nm
V_2O_5	10^{-12}–10^{-13}	75-25 nm	32-10 nm
VO_2	10^{-9}–10^{-10}	2450-775 nm	1000-316 nm
TiO_2	$(3\text{-}5)\times10^{-15}$	4.24 – 5.48 nm	1.73 – 2.24 nm
Si	$(5\text{-}7)\times10^{-11}$	548–648 nm	224–265 nm
$LiFePO_4$	$(0.024\text{-}2.2)\times10^{-13}$	3.83–36.4 nm	1.56–14.9 nm
$LiCoO_2$	10^{-9}–10^{-8}	2450 – 7750 nm	1000 – 3160 nm
Fe_3O_4	7.15×10^{-14}	20.71 nm	8.46 nm
SnO_2	$(3\text{-}5)\times10^{-6}$	$(1.3\text{-}1.7)\times10^5$ nm	$(5.5\text{-}7.1)\times10^5$ nm

Table 1.1 Li^+ diffusion coefficients values of various electrode materials

	Na^+ Diffusion ($cm^2\ s^{-1}$)	Dif. Length 1 min (Na^+)	Dif. Length 10 Sec (Na^+)
MnO_2	5×10^{-10}	1732 nm	707 nm
V_2O_5	$(9\text{-}0.05)\times10^{-12}$	232-11 nm	95-7 nm
$NaFePO_4$	10^{-14}	7.75 nm	3.2 nm

Table 1.2 Na^+ diffusion coefficients of values of various electrode materials

To overcome low D_o, the synthesis of low-dimensional nanostructures such as nanorods, nanofibers, nanoribbons, nanobelts, nanowires, nanosheets, nano/microspheres, nanoflowers, and 3D porous nanosheets assembly has been employed. This strategy increases the overall SSA and provides short diffusion pathways for Li^+ and Na^+ ions, which in turn offers more electrochemically active sites for enhanced performance. Low-dimensional nanostructures can also partially relieve any large lattice strain during the phase transition processes of many materials which significantly extends the battery life. However, the poor electrical contact between the nanoparticles becomes a dominant factor that limits the power rate capabilities.

1.5.2 Electrical Conductivity

In conjunction with low D_o, the electrical conductivity of many of the proposed electrode materials further inhibits any real high-power applicability. The reported electrical conductivity values for some common electrode materials are listed in Table 1.3.[72-73, 222]

	MnO_2	V_2O_5	TiO_2	Si	$LiFePO_4$	$LiCoO_2$	Fe_3O_4	SnO_2
Conductivity σ ($S\ cm^{-1}$)	10^{-5} – 10^{-6}	10^{-3} – 10^{-5}	10^{-10}	1.56×10^{-5}	10^{-7}–10^{-10}	~10^{-3}	10^2	10^{-3}

Table 1.3 Electrical conductivity values for common electrode materials

It is clear as to why $LiCoO_2$ has had a lot of success in commercialized LIBs when you compare its values in Tables 1.1 and 1.3 with other electrode materials. Unfortunately, many of the other electrode materials still fall into either the semiconductor or insulator range as shown in Figure 1.9.

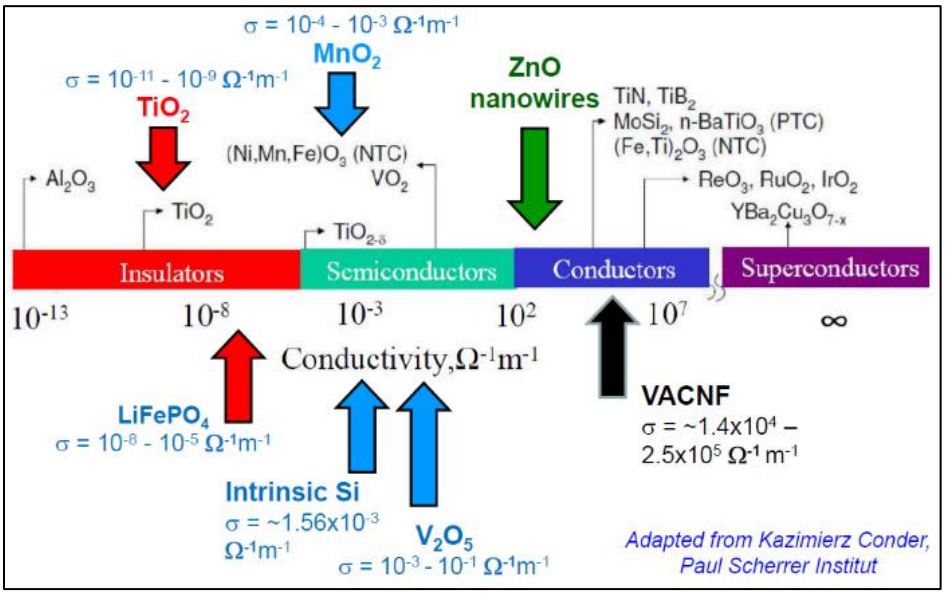

Figure 1.9 Electrical conductivity comparison for various materials. (Adopted from Kazimierz Conder, Paul Scherrer Institute)

The incorporation of low dimensional conductive carbon allotropes such as MWCNTs, graphene, and rGO has been the avenue for many of the proposed electrodes.[67, 179, 226] The addition of these conductive allotropes enhances the electrical conductivity throughout the electrode by providing electrical pathways to and from the active material. Moreover, these additives also prevent aggregation between the active particles leading to long battery life. An in-depth discussion covering the synthesis of low dimensional nanostructures and the incorporation of carbon additives for all the electrode materials previously discussed is beyond the scope of this thesis. Instead we opt to focus on several synthetic strategies for carbon additive in section 1.5.3 and current state-of-the-art core-shell structures in section 1.5.4.

1.5.3 Addition of Carbon Additive Strategies

The addition of carbon additives has been the gold standard for overcoming the low electrical conductivity. Here three techniques used to synthesize carbon additives-active material composites include; 1) simple mixing, 2) hydrothermal synthesis, and 3) microwave-assisted synthesis are briefly discussed.

1.5.3.1 Simple Mixing

The simple mixing of active nanoparticles and carbon additives was one of the first techniques to show significant improvements in battery performance. Here, mass percentages of 60-90% active material, 5-35% carbon and 5-15% binder (PVDF) are mixed together in an organic solvent (usually N-Methyl-2-pyrrolidone(NMP)) and casted onto a metal current collector. The resulting slurry is then dried in a vacuum oven for 12 to 24 hours. It is considered the easiest and perhaps the quickest method for composite formation. However, the poor electrical contact at the active nanoparticle-carbon interface still limits their ability to reach desired power rates.

1.5.3.2 Hydrothermal Methods

To improve the electrical contact at the interface hydrothermal synthesis has been employed to grow single crystals directly (active material) on the carbon surface. Here, rGO has been used extensively due to the broken carbon bonds and function groups on the basal plane of the graphene sheet. Synthesis is done at high temperatures in a stainless-steel autoclave under pressure through a conduction process and has been accomplished in both organic (solvothermal synthesis) and aqueous solutions. Pandey et al. showed improved battery and electrochemical capacitor performance with near theoretical capacity using a two-step hydrolysis of vanadium oxytriisopropoxide (VTIP) in isopropyl alcohol onto rGO sheets.[67] Despite the success, synthesis often requires up to 18 hours to complete which makes it unsuitable for large scale production.

Moreover, the resulting product often needs to be mixed with a conductive additive (carbon black or super p) and a binder in NMP and casted onto a current collector as describe in section 1.5.3.1.

1.5.3.3 Microwave-Assisted Synthesis

Microwave-assisted synthesis is a modern technique that is used to synthesize inorganic nanoparticles such as nanorods and quantum dots. Traditionally, solvents with strong microwave absorption capabilities (represented by a value of loss tangent [tanδ]) in the range of 0.25 – 1.25 tanδ are heated up rapidly by microwave radiation which provides the energy needed to drive the synthesis of the nanoparticles from added precursor(s).[227] For EES purposes, low absorbing solvents are used in conjunction with strong microwave absorbing carbon additives in the range of 0.5 – 1.0 tanδ which can drive the synthesis of the nanoparticle growth directly on the surface. The synthesis requires several minutes to complete which is a huge leap forward for large scale production. However, microwave-assisted deposition is still in its infancy and many parameters still need to be investigated before any real applicational uses can be considered.

1.5.4 Core-Shell Structures

Core-shell structures are defined as structures with an inner core that have one or more shells or outer layers of a different material surrounding it. Recently they have become state-of-the-art for EES research owing to their high-power capabilities. Though numerous strategies have been employed for many of the electrode materials previously discussed, we can place all of them into two broad categories. In the first category, the active materials are coated with a thin conductive shell such as carbon or a conductive polymer. Liu et al. reported a yolk-shell design with a carbon coating on Si nanoparticles that reached a Li^+ ion insertion capacity of ~2800 mAh g^{-1} at a rate of 0.1C.[228] The yolk-shell like core-shell structure allowed the Si nanoparticles to expand during lithiation without severe structural collapse as illustrated by the 74% capacity

retention after 1000 cycles. Wang et al. reported a $LiFePO_4$-carbon nanocomposite core-shell that achieved a capacity of 90 mAh g^{-1} at a rate of 10 A g^{-1} or about 60C further illustrating the high-power performance.[229] Chao et al. reported a V_2O_5-conductive-polymer core-shell nanobelt array that achieved a capacity of ~300 mAh g^{-1} at 1C which dropped to 115 mAh g^{-1} at an ultra-high rate of 80C.[230] However, these strategies have several drawbacks; 1) a reduction in the available surface area of the active material, 2) a large EDLC contribution from the outer shell which can be beneficial but exaggerates the true charge storage capacity if the mass of the outer shell is not considered, and 3) the electrical connection between the nanoparticles is likely quite poor and often requires a conductive additive and binder as previously discuss. These drawbacks can be overcome in the second category where the core-shell approached is reversed, hence a conductive core with an active shell. Here only the outer shell is exposed to the electrolyte with minimal contribution from the inner core which can provide a more reliable assessment of the material properties. More importantly, this strategy allows for the coating on continuous carbon networks as shown by Chen et al. where V_2O_5 was deposited onto a MWCNT sponge like network which achieved a high areal capacity of 1300 μAh cm^{-2} at a rate of 1C.[231] Here, we will only focus on electrospun carbon nanofibers and vertically aligned carbon nanofibers in sections 1.5.4.1 and 1.5.4.2, respectively, which are vital to this thesis.

1.5.4.1 Electrospun Carbon Nanofibers

Electrospun carbon nanofibers (CNFs) are cylindrical shaped allotropes with a high-aspect ratio; diameters varying from 50-500 nm and lengths ranging from 1-1000 μm. The internal structure is composed of different modified graphene sheet arrangements varying from disordered to hard carbon.[232] CNFs are synthesized using various electrospinning methods to form self-supported membrane networks. Briefly, polymers such as polyacrylonitrile (PAN) are dissolved in an

organic solvent and loaded into a syringe. A high voltage (≥ 10 kV) is applied between the syringe needle and the collector which pulls the polymer out to form a Taylor cone. The polymer string flows from the end of the cone which spins through the applied field until it is deposited onto the rolling current collector. The resulting polymer membrane is thermally stabilized in air followed by carbonization at a high temperature (≥1000 °C) under nitrogen, forming a continuous CNF network. SEM images of bare CNFs at low (a and b) and high (c and d) magnification are shown in Figure 1.10.

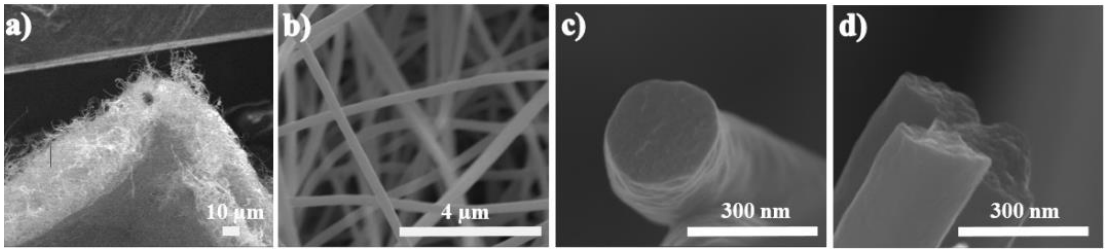

Figure 1.10 Low (a and b) and high (c and d) magnification SEM images of bare CNFs

1.5.4.2 Vertically Aligned Carbon Nanofibers

Vertically aligned carbon nanofibers (VACNFs) are a special type of MWCNT with a high-aspect ratio comprised of small graphene cups or cones (ranging from 100 to 300 nm in diameter) stacked on top of one another forming a fiber-like structure.[233] The cup shaped form is referred to as "bamboo-like structures" while the cone shaped is referred to as herringbone (or fishbone). VACNFs are grown on a nickel coated (catalyst) conductive substrate using a DC-biased plasma chemical vapor deposition (PECVD) procedure.[234] Fiber height is controlled by growth time and typically ranging from 3-10 µm. A schematic of bamboo and herringbone VACNFs along with SEM and TEM images of bare fibers are presented in Figure 1.11.

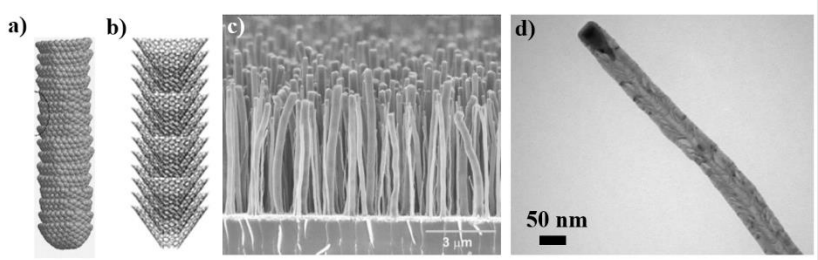

Figure 1.11 A schematic of bamboo a) and herringbone b) VACNFs. SEM image of bare VACNFs c), and a TEM of a bare VACNF d). (Reprinted with permission from ACS Appl. Mater. Interface 2014, 6, 6865-6871)

VACNFs are unique in the fact that the side walls are composed entirely of graphitic carbon containing numerous dangling bonds which allows for coating without the need of activation or etching. Moreover, the dangling bonds allow for a good electrical connection at the fiber-shell interface. They are an ideal substrate for core-shell structures owing to their high electrical conductivity, large surface area, and robustness. In addition, the fibers are well separated from one

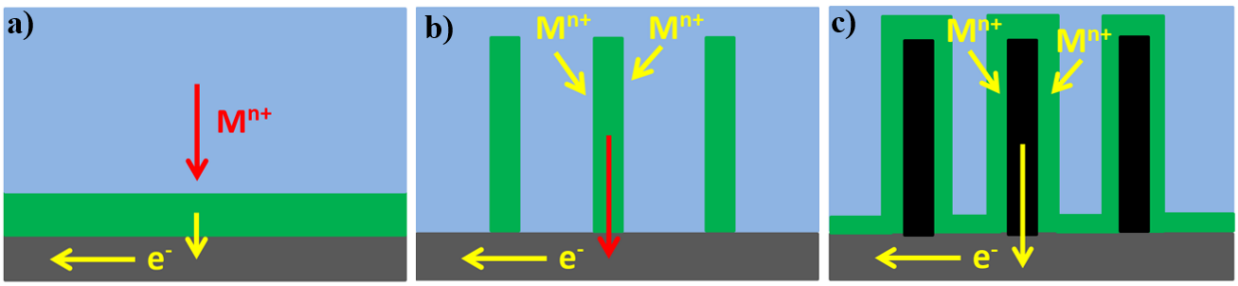

Figure 1.12 An illustration demonstrating the advantage of VACNFs with active material casted as a thin film a), grown as vertically aligned wires b), and deposited on VACNFs c).

another on the order ~100-400 nm when grown as a random array which allows for a wide variety of deposition techniques to be employed. The illustration in Figure 1.12 demonstrates the advantage of VACNFs with a low surface area film (a), high surface area vertical nanowires with poor electrical conductivity (b), and a high surface area film coated on the VACNFs with M^{n+} representing ions (Li^+ or Na^+) in solution.

Previously we deposited Si on VACNFs to form a core-shell structure to be used as an anode in LIBs.[150-151] The large separation between the fibers allowed the volume expansion

associated with Si to occur. MnO_2 has also been deposited using both electrochemical and vapor phase deposition techniques for pseudocapacitive applications.[72, 235] Here we deposit Al_2O_3 as a dielectric material for high energy electrostatic capacitors and V_2O_5 as a cathode for both LIB and NIBs.

1.6: Deposition Techniques for Core-Shell Structures

One of the major challenges in constructing core-shell structures is the choice of an appropriate deposition technique. Several things need to be considered such as material cost, time required for deposition, deposition uniformity and scalability. There are numerous deposition techniques that can be employed, however, the choice depends on the nature of the core substrate and the desired application. Here we briefly discuss the techniques used in the following chapters.

1.6.1 Vapor Phase Deposition

Vapor phase deposition techniques are classified as either physical vapor deposition (PVD) or chemical vapor deposition (CVD). PVD is characterized as a high vacuum deposition where the target (desired material for deposition) is in a condensed phase that goes to a vapor phase then back to a condensed phase in the form of a thin film on a substrate. In CVD one or more precursors either react or decompose on the substrate surface to form a thin film. Here we briefly discuss two PVD techniques (ion sputtering and pulsed laser deposition) and one CVD technique (atomic layer deposition).

1.6.1.1 Sputtering

In a typical sputtering process, a voltage is applied between the target material (cathode) and the substrate (anode). An inert gas such as argon is introduced to the system at a pressure of ~0.1 Torr. Using an external power source, the argon atoms are ionized to create a plasma. Depending on the conductivity of the target material, DC and RF sources are used for metals and

dielectrics, respectively. The Ar^+ ions are accelerated toward the target causing atoms to be sputtered off.[236] Some of these atoms will deposit on the substrate as shown in Figure 1.13a. In reactive ion sputtering, a reactive gas such as oxygen is introduced to the chamber to react with ejected target atoms to form an oxide materials such as metal oxides as shown in Figure 1.13 (b). Ion sputtering has several advantages over other PVD techniques such as low cost and higher film uniformity.

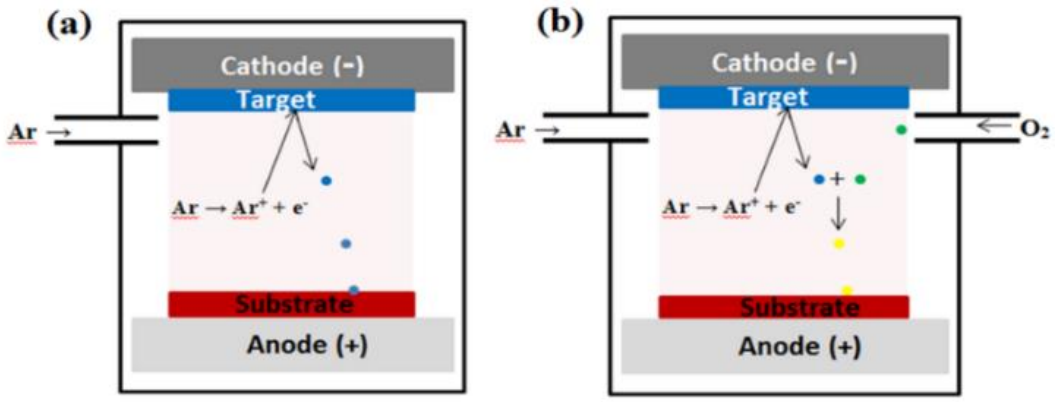

Figure 1.13 Schematic of ion sputtering a) and reactive ion b)

1.6.1.1 Pulsed Laser Deposition

Pulsed laser deposition (PLD) is a PVD technique that uses a high-power pulsed laser beam to eject target atoms for deposition. Briefly, the target material is evaporated when the laser pulse is absorbed through a series of energy conversion steps where the energy is first converted to electronic excitation and then into thermal, chemical and mechanical energy resulting in evaporation, ablation, and plasma formation or plume. The plasma plume containing many energetic species such as molecules, atoms, electrons, ions and molten globules is deposited directly onto a heated substrate as shown in Figure 1.14.[237] This process can be done in an ultra-high vacuum or in the presence of a gas such as oxygen for metal oxide deposition.

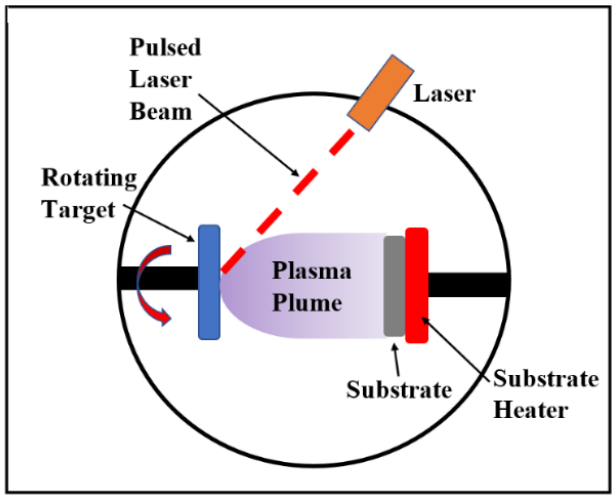

Figure 1.14 Schematic of a Pulsed Laser Deposition Setup

1.6.2.1 Atomic Layer Deposition

Atomic layer deposition (ALD) is a CVD technique where atomic scaled layers can be deposited. Briefly two gases enter the deposition chamber one at a time. The first gas will either chemically or physically bond to the substrate surface depending on its nature. Once full coverage is achieved, the excess gas is pumped out. The second gas is then introduced where it chemically bonds to the gas molecules on the surface to form a single atomic layer. Excess gas along with any byproducts is pumped out. The process is repeated for every atomic layer; hence thickness is controlled by the number of deposition cycles.[238] ALD has several advantages such as: 1) deposition is self-limiting where only one atomic layer can be deposited at a time, 2) film thickness is controlled, and 3) conformal deposition can be achieved over uneven topography. However, the major drawbacks are the time required to complete deposition, thus it is limited to ultrathin films.

1.6.2 Electrochemical Deposition

Electrochemical deposition or electrodeposition (EDP) covers a broad range of deposition techniques such as electroless deposition and electroplating. Electroless deposition dates back over 2000 years, where decorative gold plating was done, which occurs when a copper surface is

exposed to gold ions.[239] More recently electroplating has become a common technique for coating thin metal films onto an electrode surface. Briefly, a cathode is electrically connected to an anode whose composition is made up of the metal to be coated. Both are immersed in an electrolyte containing one or more dissolved metal salts as well as other ions that permit the flow of electricity. An external power supply directs current to the anode, oxidizing the metal atoms that it comprises allowing them to dissolve in solution. The dissolved metal ions are reduced or "plated out" at the surface-electrolyte interface of the cathode forming a film thin. The most common form of electroplating is used for creating pennies, which are small zinc plates covered in a layer of copper.[240] More modern techniques utilize non-consumable anodes such as platinum and stainless steel as current sources in a three-electrode setup to drive the electrochemical reaction onto a substrate using ions in solution. EDP has the advantage of offering control over film uniformity, however, the mass to be deposited is limited to the concentration of the electrolyte solution. Moreover, EDP offers several advantages such as low cost (no vacuum system) and accomplished at low temperatures. However, the EDP of complex films such as superlattices and perovskites is still in its infancy; limiting deposition to simple films such as metals, polymers, and metal oxides.

1.6.2.1 Amperometry

Amperometry is a EDP technique where the potential is fixed and the current response is measured as a function of time as shown in Figure 1.15. In a three-electrode setup the voltage can either be positive or negative with respect to the reference electrode to drive either a reduction or oxidation at substrate surface.[241] One of the advantages of this technique is that mass of the deposited film can be estimated using Equation 1.6:

$$n_a = \frac{1}{nF}\int_{t=0}^{t} i dt$$

Equation 1.6

where n_a are the moles of analyte deposited, n is the number of electrons transferred in the reaction, F is Faraday constant, t is the deposition time, and i is the measured current response. Moreover, the duration of the deposition is often quite short depending on the conductivity of the deposited material and the desired film thickness.

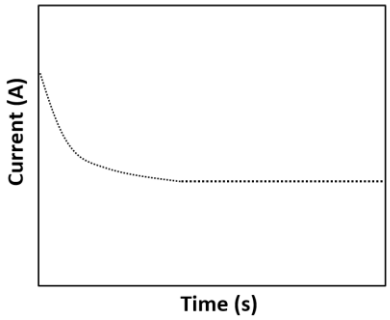

Figure 1.15 A schematic of an amperometric curve with a current response measured as a function of time

Despite the advantages, this method is often inadequate for the formation of many core-shell structures. For example, substrates such as VACNFs and CNF membranes have many voids and uneven topographies where unwanted pH gradients and electrolyte depletion in localized areas disrupts deposition. After a short duration, a thick film will form on top of the VACNFs (as opposite to around individual fibers) or on the outside of the CNF membrane leaving most of the interior bare, thus limiting the method to flat substrates.

1.6.2.2 Pulsed Electrodeposition

Pulsed electrodeposition can be employed for core-shell formation where two different voltages designated as "on" and "off" are applied. The "on" voltage is the potential required for deposition to occur, while the "off" voltage terminates deposition and is usually set at either 0V or open circuit potential (OCP).[235] The cycling between the two potentials allows for the deposition to occur in between pulses as shown in Figure 1.16.

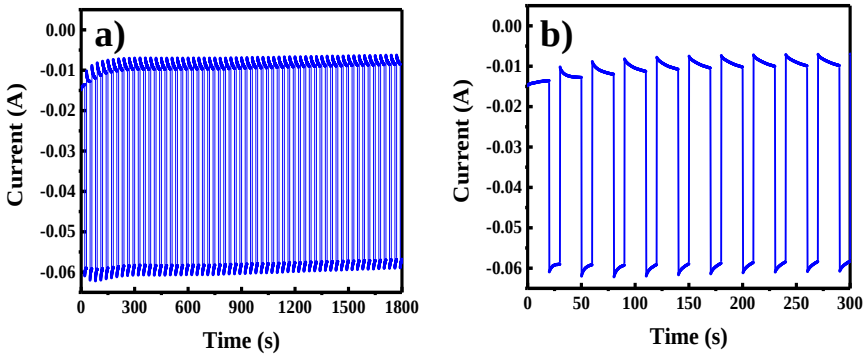

Figure 1.16 a) A schematic of a 60-cycle pulsed electrodeposition with a 10 second on time and a 20 second off time. The first 300 seconds are expanded in b) to clearly show the pulses.

A short "on" time allows for a thin layer to be deposited along the core structure. A longer "off" time allows for any unwanted concentration gradients to dissipate while replenishing localized areas with fresh electrolyte. Once completed, the system is ready for the next cycle. The technique has been shown to be beneficial for several core-shell structures. However, potential drift in the reference electrode remains a concern and care must be taken for long durations.

1.7 Teflon and Coin Cell Assembly for Electrochemical Characterization

Testing cells for electrochemical characterization can be assembled either in the open atmosphere or in an inert system depending on the nature of the electrolyte. Aqueous based EC cells are often assembled in the open atmosphere using apparatus such as Swagelok's or various Teflon cells as shown in Figures 1.17a-c. In a typical Swagelok (Figure 1.17a), a porous separate along with an electrolyte solution are sandwiched between two electrodes inside a hollow Teflon tube. Two stainless steel caps are screwed onto each end of the Teflon tube holding the cell together. A two-electrode setup is used for characterization where no reference electrode is required. Other Teflon cells utilize a three-electrode setup where the working electrode can be compressed at the bottom (Figure 1.17b) or inside (Figure 1.17c) depending on the design. For the cell in Figure 1.17b the counter and reference electrodes are suspended in an electrolyte

solution inside the Teflon chamber above the working electrode. The Teflon cell in Figure 1.17c is typically immersed in an electrolyte solution with counter and references electrodes suspended nearby. It should be noted that these are just three of the many possible apparatus that can be used for aqueous based EC cells.

For organic based electrolytes cells must be assembled inside an inert atmosphere due to the rapid degradation of the electrolyte in the presence of oxygen. The Swagelok and Teflon cells can be utilized inside an inert atmosphere for characterization, however, it is often the case that the cells need to be tested outside of the enclosed environment. For this purpose, coin or button cells (Figure 1.17d) are assembled inside a glove box prior to removal. To limit the discussion, only LIB and NIB assembly will be discussed. Briefly, working electrode disks of ~18 mm in

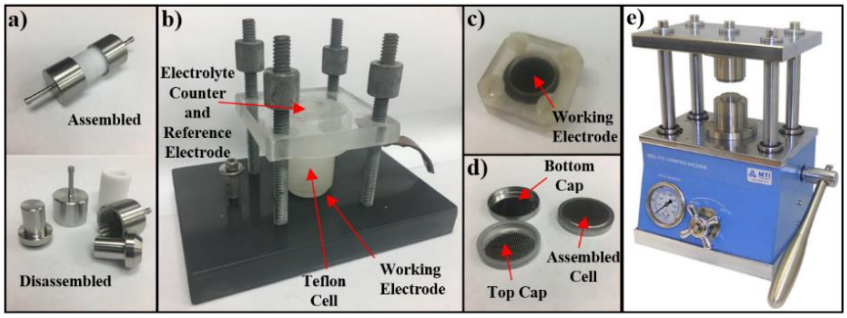

Figure 1.17 Swagelok cell a), two different Teflon cell apparatus b) and c). Coin cells d) and a hydraulic crimping press for coin cell assembly from MTI Corporation.

diameter are placed in the bottom cap while anode disks (Li or Na foil) placed in the top cap. A porous glass fiber separator is soaked in electrolyte and placed on top of the working electrode. The top cap is then inverted and placed on top. The coin cell is then sealed using a hydraulic crimper shown in Figure 1.17e. It should be noted that other cell designs such as the cylinder, pouch and prismatic cells can be used, but are beyond the scope of this discussion.

1.8: Characterization Techniques

To evaluate the EES capability, electrochemical characterization techniques such as cyclic voltammetry (CV), galvanostatic charge discharge (CD), and electrochemical impedance

spectroscopy (EIS) are employed. To conduct these techniques instruments such as potentiostats and bipotentiostat (single and multi-working electrodes) as well as multi-channel battery analyzers are used. Several of the instruments shown in Figure 1.18 include a CHI Electrochemical Workstation a), Princeton Applied Research PARSTAT 2273 Advanced Electrochemical System b), Ivium-n-Stat Multichannel potentiostat c), and an MTI 8-Channle Battery Analyzer d).

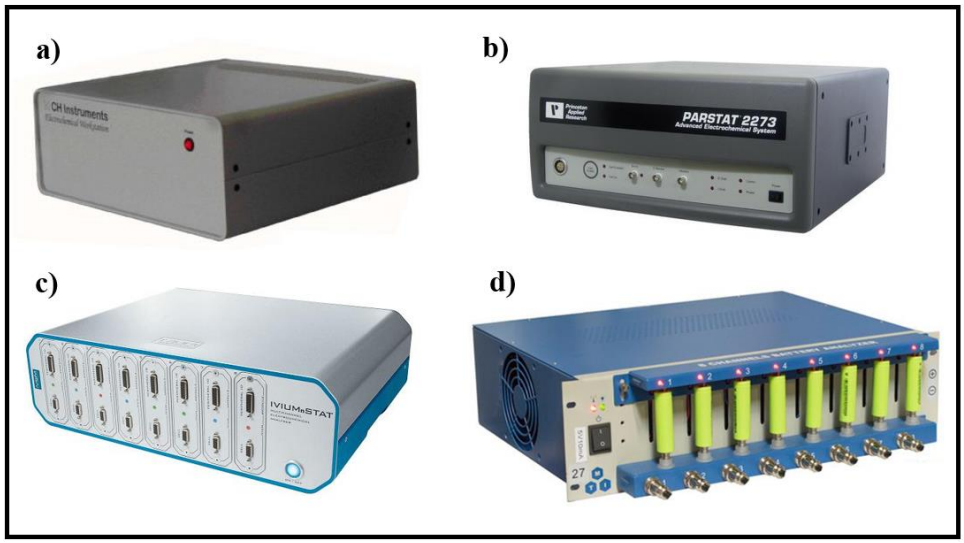

Figure 1.18 Instruments used for testing include a) CHI Electrochemical Workstation from CHI inc, b) Princeton Applied Research PARASTAT 2273 Advance Electrochemical System, c) 8 channel Ivium-n-Stat Potentiostat, and d) 8 channel Battery Analyzer MTI cooperation.

1.8.1 Cyclic Voltammetry

Voltammetry encompasses a wide variety of characterization techniques where a current response is measured by varying an applied voltage respect to time (scan rate) at the working electrode. Common types of voltammetry include linear sweep (LSV), staircase, squarewave, stripping, differential pulse, and CV. CV utilizes this technique by cycling the applied voltage between defined voltages where the analyte or electrode is repeatedly oxidized and reduced and the current responses are recorded. Here, a repeated triangular waveform is applied at the working electrode as shown in Figure 1.19.

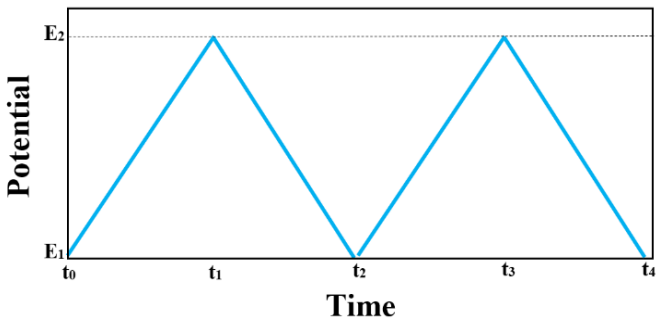

Figure 1.19 A schematic of a triangular waveform for cyclic voltammetry

1.8.1.1 Capacitors (Electrostatic, EDLCs, Pseudocapacitors)

The CV curve for an ideal capacitor can be described as boxed shaped curve with perfect corners at the high and low potentials where the voltage waveform is reversed as shown in Figure 1.20a. However, real capacitors have a RC time constant (τ) and when the waveform is reversed, rounding occurs as shown in Figure 1.20b.[242] The rounding originates from two sources; 1) the voltage drop in real systems due to the contribution of the ESR, and 2) the time required for charge at the electrode surface to begin discharging. For electrostatic capacitors, this rounding is often minimal due to a low ESR and the small charge storage capability. However, this rounding often becomes much more dominating in ECs due to a higher ESR and a larger charge storage capacity as shown in Figure 1.20c. The capacitance C, can be estimated using Equation 1.7

$$C = \frac{i_c - i_d}{2} * v^{-1}$$

Equation 1.7

where i_c and i_d are the current responses of the charging and discharge curves (usually at the midway point), respectively, and v is the scan rate. It should be noted that Equation 1.3 only provides the true capacitance of an ideal capacitor, and the more the deviation from ideal behavior, the less reliable Equation 1.7 is. For true capacitance, the CV curve can be integrated which is discussed in more detail in Chapter 3.

1.8.1.2 Lithium and Sodium Ion Batteries

For LIB and NIB, the CV curve is distinctively different as shown in Figure 1.20d. Here, the insertion of Li^+ or Na^+ ions into crystalline materials results in a pair of oxidation and reduction peaks. The curve in Figure 1.20d depicts the insertion and extraction involving a single-phase transition. However, depending on the number of phase transitions, multiple pairs of insertion and extraction peaks can often be observed. The capacity can be calculated by integrating the CV curves, however, these curves are often used as a qualitative assessment rather than a quantitative measurement. It should be noted that the incorporation of low dimension nanostructures provides a much larger SSA over that of traditional battery materials which results in more pseudocapacitive features. Hence, there is often an overlap or a merge between the CV curves in Figure 1.20c and 1.20d. Moreover, nano sized amorphous materials have a much larger pseudocapacitance contribution than crystalline materials which results in many of the traditional peaks being superimposed, thus curves begin to appear as EC curves in Figure 1.20c.[243] This phenomenon will be observed and discussed more thoroughly in Chapters 4, 5, and 6.

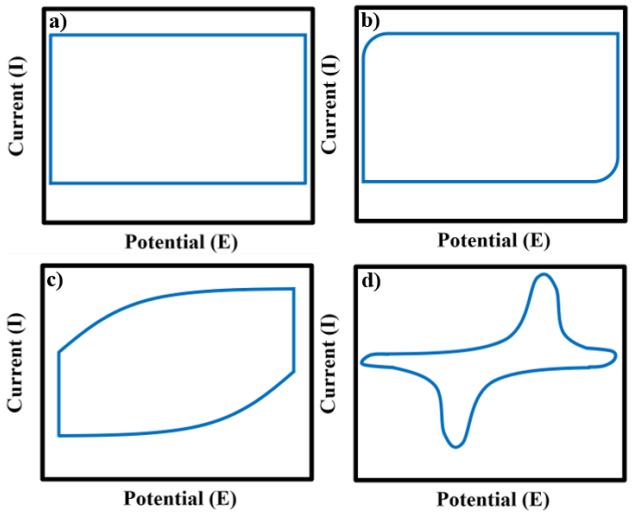

Figure 1.20 A representative CV curve for an ideal capacitor a), a realistic CV curve for an electrostatic capacitor b), electrochemical capacitor c), and crystalline electrode materials for secondary batteries d).

1.8.2 Chronopotentiometric Galvanostatic Charge-Discharge

In galvanostatic charge-discharge (CD) a fixed current is applied to the working electrode to charge or discharge the system until a set potential is reached. Once the potential limit is reached, the current is reserved and the opposite process occurs. The slope of the curve is governed by the amount of charge that can be stored per volt (i.e. capacitance). A cycle is accomplished once a full charge and discharge process is completed. The applied current must be chosen carefully as it depends on either the SSA (in electrostatic capacitors) or the mass (in ECs, LIBs, and NIBs) of the electrode.

1.8.2.1 Capacitors (Electrostatic Capacitors and ECs)

The CD curve for an ideal capacitor can be described as a perfectly linear line extending the entirety of the fixed potential range as shown in the charging (solid blue line) and discharging (dashed blue line) curves in Figure 1.21a. However, the voltage drop in real capacitors causes a drop in the curve when the direction of the current is reversed as indicated by the bracket in Figure 1.21b. In electrostatic capacitors, the drop is quite small due to the low ESR, whereas in ECs its more dramatic drop. As previously mentioned pseudocapacitors are not true capacitors and only mimic the performance. Thus, the CD curves will only have some small curvatures or plateaus due to ion insertion at the electrode surface as shown in Figure 1.21c. The capacitance C, can be calculated using Equation 1.8

$$C = \frac{i * t}{V}$$

Equation 1.8

where *i* is the applied current, *t* is the time required to complete a charge or discharge cycle, and *V* is the voltage range. Several things to note: 1) the capacitance is only calculated with either the charging or discharging curve, and 2) the voltage drop (V^1) can be accounted for by subtracting it

from the voltage window (V) to give a corrected voltage range (V^*) where ($V^* = V - V^1$). As previously stated the applied current is important. In electrostatic capacitors, the surface area dictates the current and the normalized the applied current ranges from 1 to 100 μA cm^{-2}. Though ECs can be normalized by the surface area, mass specific current is typically used with a current range of 1 to10 A g^{-1}. It should be noted that these ranges are commonly seen throughout literature. With state-of-the-art core-shell structures, higher applied currents can be used.

1.8.2.2 Lithium and Sodium Ion Batteries

The CD curves for LIB and NIB are described as long flat plateaus due to the slow ion insertion mechanisms in crystalline materials as shown in Figure 1.21d. The voltage at which the plateau arises is dependent on the insertion potential. Charge storage is calculated by multiplying the applied current (in the unit of mA) by the time required to complete one charge or discharge cycle. For battery purposes, the time is converted to hours and capacity is determined by normalizing the charge storage with the electrode mass to give mAh g^{-1}. Owing to low D_o, the applied current is significantly lower than ECs with a range of 10 to 1000 mA/g. Recently this range has been extended to 10 A g^{-1} in several reports owing to the improved electrical conductivity of the electrode material. The incorporation of low dimensional crystalline materials has resulted in a merge between the curves in Figure 1.21c and d. Moreover, amorphous materials nearly resemble the curve seen in Figure 1.21c due to the lattice disorder of the electrode material.

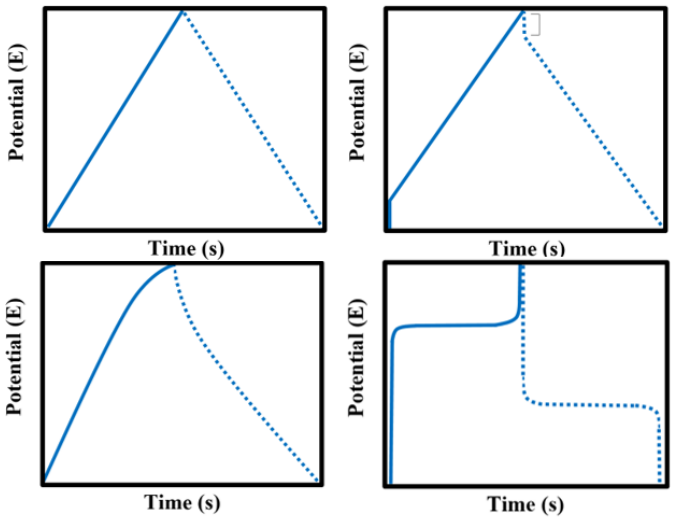

Figure 1.21 Representative CD curves for an ideal capacitor a), realistic CD curves for an electrostatic capacitor b), ECs c), and crystalline materials for secondary batteries d).

1.8.3 Electrochemical Impedance Spectroscopy

So far resistance has only been discussed as a linear property governed by Ohms Law (V = IR) as shown in Figure 1.22a. In real electrochemical systems, a complex nonlinear resistance or impedance is encountered when current flows through a circuit as shown in Figure 1.22b. Electrochemical Impedance Spectroscopy (EIS) is used to probe the electrochemical features of electrode materials to understand reactions rates, insertion mechanisms, measure the impedance and model complex systems as a simple circuit.[242] Briefly, a sinusoidal potential wave is applied to the system and the responding current wave is measured. Though the impedance is nonlinear, it's expected that at a small potential the system does behave linearly as shown in the insert in Figure 1.22 b. Thus, the amplitude of the applied potential wave is usually kept below 15 mV. By measuring the phase shift of the responding current wave and using a Euler equation, a real and imaginary resistance (or impedance) is determined. However, to model the electrochemical system, the potential wave is applied at various frequencies and the resulting resistances are plotted

in what is called a Nyquist plot shown in Figure 1.22c. Here each point represents the real (x-axis) and imaginary (y-axis) resistance at a single frequency. Using advanced computer software, the shape of the Nyquist plot can be modeled as a simple circuit. In an ideal capacitor, the shape would be a straight-line right along the y-axis. However, real systems have an x-intercept (R_s) at the high frequency range originating from the ESR. The semicircle originates from charge transfer resistance (R_{et}) which can be minimized using nanosized particles and conductive cores. The Warburg diffusion element (Z_w) at the low frequencies can be used to study mass transport phenomena. It should be noted that the Nyquist plot in Figure 1.22c is a simple plot and depending on the design and type of electrochemical system, the shape of the plot can vary dramatically. An in-depth derivation of EIS is beyond the scope of this discussion, but the brief description above should provide enough details for the following chapters.

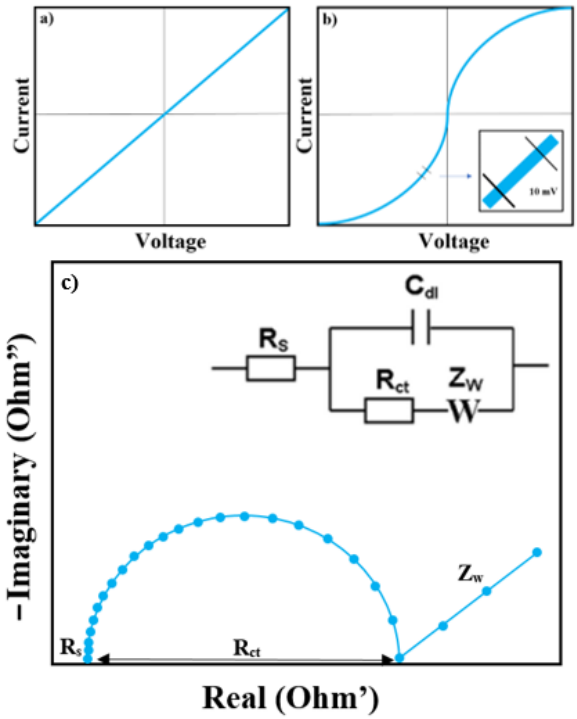

Figure 1.22 A representative I-V curve governed by Ohms Law a), and for a real electrochemical system b). A representative Nyquist plot for an electrochemical system c).

Chapter 2 - Atomic Layer Deposition of Al-Doped ZnO/Al_2O_3 Double Layers on Vertically Aligned Carbon Nanofiber Arrays

2.1 Introduction

Three-dimensional (3D), carbon-based nanostructures have unique advantages for energy applications due to their desirable electrical properties, large surface-to-volume ratio, low specific mass, and relatively large abundance.[244-246] Among the 3D, carbon-based nanostructures, VACNFs grown on conductive substrates provide an ideal 3D electrode that are most desirable for many energy device applications including dye-sensitized solar cells[247], hybrid supercapacitors[235], and lithium-ion batteries.[150] The VACNFs can be easily grown to tens of microns in length, vary from 50 to 150 nm in diameter (~100:1 aspect ratio), and have an areal density of 10^9 CNFs/cm^2 providing a significantly enhanced electrode surface area.

Conformal coating of functional materials on VACNF arrays is required for applications that take advantage of the large surface area. However, for high aspect ratio vertical structures, conformal coating can be quite challenging due to shadow effects from most deposition techniques. ALD provides an ideal method for solving this problem. In particular, ALD allows atomic-scale thickness control of the conformal coating due to its self-terminating, layer-by-layer growth mechanism.[248] Progress has been made recently in coating 3D structures using ALD. For example, Banerjee *et al.* reported successful ALD coating of anodized aluminum oxide (Al_2O_3) nanotubes with a 200:1 aspect ratio in order to fabricate TiN/Al_2O_3/TiN metal-insulator-metal capacitors.[12] In addition, Kemell *et al.* utilized ALD to conformally coat Si micropores with a 25:1 aspect ratio in order to fabricate Si/Al_2O_3/Al-doped ZnO (AZO) capacitor arrays.[15] The atomic-scale thickness control provided by ALD in these examples was advantageous in achieving

extremely thin dielectric layers on the order of several nanometers as illustrated by the high capacitances reported.

ALD is a chemical process and requires well-defined surface functional groups for atomic layer nucleation during alternating exposures of chemical precursors. When these functional groups are not readily available, such as the case with carbon nanotubes (CNTs) that have chemically inert sidewalls[249], ALD coating cannot be carried out unless the CNT sidewalls are covalently or noncovalently functionalized beforehand. Covalent functionalization requires the formation of defect sites where nucleation occurs, but with this process the electrical transport properties of the CNTs are seriously degraded due to charge carrier scattering by the generated defects. Additionally, ALD growth after covalent functionalization will not be completely uniform since the defect site locations are randomly distributed throughout the CNTs.[250] Noncovalent functionalization does not create defect sites, but it does require additional procedural steps and chemicals leading to higher cost and longer fabrication time.[251] Unlike CNTs, VACNFs consist of conically stacked graphitic cups with dangling carbon bonds on the outer rims which are distributed along the sidewalls of the fiber.[233, 252] These dangling bonds along the graphitic edges are quickly converted into C-H and C-OH bonds once exposed to air and can serve as ideal nucleation sites for coating of functional materials by ALD which eliminates the need for covalent or noncovalent functionalization.[253-255] In addition, VACNFs have highly conductive metallic properties (with a resistivity of (6.3±1.7) $x10^{-4}$ Ω cm) in contrast to the mixed metallic and semiconductor properties of CNTs, and thus serve well as a current collector.[256]

In this work, we explore ALD fabrication of 3D, metal-insulator-metal core-shell nanostructures using pristine VACNF arrays as one of the metallic electrodes. The obtained conformal core-shell AZO/Al_2O_3/CNF structures represent the first successful double-layer ALD

coatings on vertically aligned, 3D CNF arrays and are promising candidates for high-performance, solid-state capacitors.

2.2 Experimental Details

VACNF arrays were grown on 1 cm by 2 cm silicon substrates coated with a 100-nm thick chromium barrier layer and a 22.5-nm thick nickel catalyst film. VACNF growth was accomplished using a DC-biased PECVD system (Black Magic PECVD System, AIXTRON) at 800 °C with a flowing mixture of C_2H_2 (at 63 sccm) and NH_3 (at 250 sccm) gas precursors at a processing pressure of ~4.1 Torr following a previously published procedure.[150, 235, 247] The VACNF samples used in this study have an average areal density of ~109 CNFs/cm^2, with a diameter in the range of 50-150 nm and a length of 3-5 μm controlled by 20 to 30 minutes of growth time.

Figure 2.1 shows a schematic for the complete Al_2O_3 ALD growth cycle, including reaction by-products, on a CNF sample. The Al_2O_3 ALD growth procedure and ALD reactor design are discussed extensively in previously published materials.[257-260] ALD Al_2O_3 films were grown using high-purity H_2O (optima grade, Fisher Scientific) and trimethylaluminum (TMA, $Al(CH)_3$; semiconductor grade, Akzo Nobel) as precursors. Ultrahigh purity (99.9999%) N_2 was used as the carrier and purging gas with a maintained flow rate of 5 sccm throughout all ALD cycles. The VACNF array substrates were heated to 200 °C for Al_2O_3 growth. ALD cycling began with a one-second H_2O exposure to further prepare the graphitic edges with hydroxyl groups for reaction with TMA. After the initial H_2O exposure, the ALD chamber and gas feeding lines were purged with N_2 for 30 seconds to prevent chemical vapor deposition occurrence during the TMA exposure. Following the N_2 purge, a one-second TMA exposure provided the aluminum atoms that bonded to the hydroxyl group oxygen atoms on the VACNF sidewalls. Another 30-second N_2 purge was

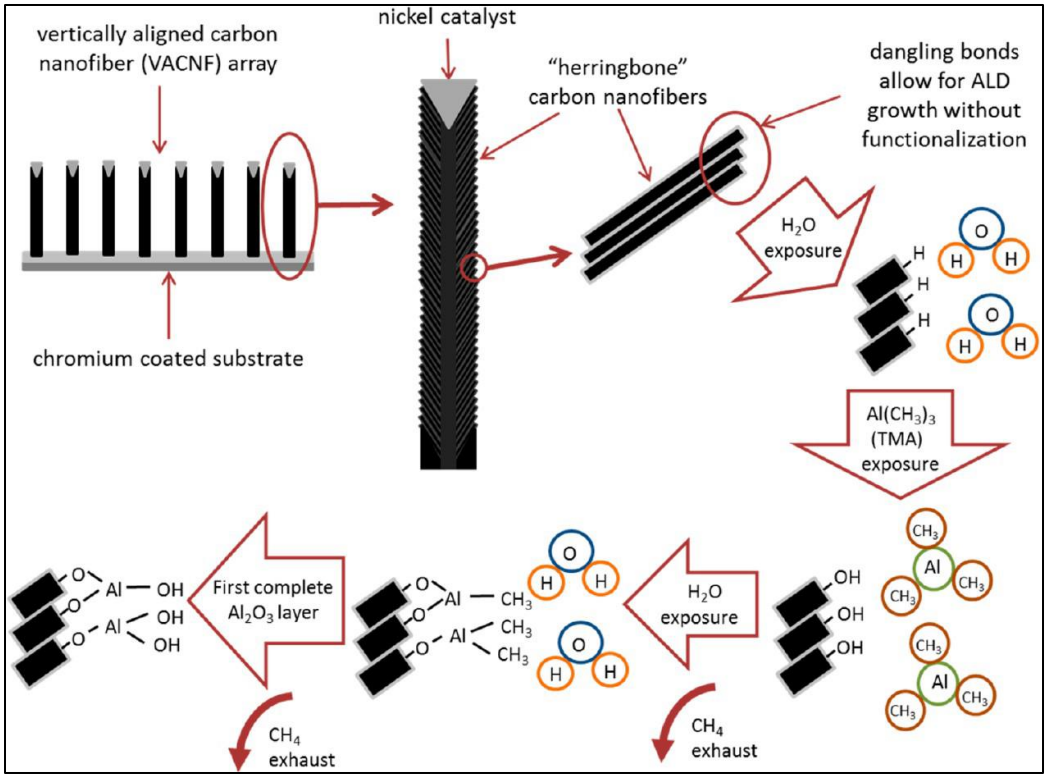

Figure 2.1 Schematic of one complete Al_2O_3 ALD cycle along the sidewall of a CNF. (Reprinted with permission from ACS Appl. Mater. Interface, 2014, 6, 6865-6871)

then performed to clear the chamber and gas lines of any residual TMA. This process was repeated for a total of 200 cycles with a final exposure of H_2O to end with hydroxyl groups along the sidewalls. The as-grown Al_2O_3 is typically amorphous,[261] therefore, to improve the crystallinity of the Al_2O_3 layer, a coated VACNF array was thermally annealed in a tube furnace at 450 °C for 30 minutes and then cooled to room temperature.

To verify the integrity of the ALD Al_2O_3 film, a planar capacitor was fabricated. The base electrode comprised of an n-doped silicon substrate coated with a 100-nm chromium layer on top. A 20-nm Al_2O_3 dielectric layer was grown on the chromium surface utilizing the ALD method mentioned previously. A top electrode was provided by sputtering 600 nm of palladium on a portion of the Al_2O_3 surface. Another planar sample, fabricated under the same conditions, was annealed in a tube furnace using the same conditions as the VACNF array sample except at a

temperature of 400 °C. The lower temperature was utilized to eliminate cracking of the film that appeared at the higher temperature. The top electrode for the thermally annealed sample was applied after annealing was performed.

ALD AZO was grown with the same precursors as before but with the addition of diethylzinc (DEZ, $(C_2H_2)_5Zn$; research grade, SAFC Hitech) while utilizing the 19:1 Zn/Al ratio as published by Kong et al.[262] in order to achieve the desired electrical conductivity. The Al_2O_3/VACNF array substrate was heated to 200 °C for AZO growth. The 200 ALD cycles consisted of 10 supercycles where each supercycle contained 19 cycles of alternating H_2O and DEZ for every one doping cycle of H_2O and TMA. Each precursor exposure was one second with a 30-second N_2 purge in between. The resistivity of the AZO film was determined by growth on a glass slide that was placed alongside the Al_2O_3/VACNF array during fabrication.

The structure and morphologies of the samples were examined using field-emission scanning electron microscopy (FESEM, FEI Nova SEM 430) at an electron beam accelerating voltage of 3.5 keV. High-resolution transmission electron microscopy (HRTEM) images and selected area electron diffraction patterns were obtained using an FEI Tecnai F20 XT field-emission transmission electron microscope at 200 kV. The chemical composition and distribution of the core-shell structures were analyzed using energy dispersive X-ray spectroscopy (EDX). Electrical characterization was conducted on the planar capacitor using a 760D Bipotentiostat (CH Instruments Inc., TX). The specific capacitance was measured by cycling the bias voltage between -0.1 to +0.1 V at various scan rates, and the Galvanostatic charge-discharge at selected current densities. The Ohmic resistance across the 20-nm thick Al_2O_3 dielectric layer was measured using AC impedance spectroscopy for further insight.

2.3 Results and Discussion

The growth rate for Al_2O_3 on silicon oxide (SiO_2) for our system was previously determined to be approximately 0.11 nm/cycle by spectroscopic ellipsometry[259-260] and follows closely to other published results.[257-258] HRTEM images revealed that the inner shell of the ALD double-layer coated on a VACNF was ~20 nm thick which is in agreement with the thickness anticipated from 200 ALD cycles of Al_2O_3 growth. This verified the assumption that nucleation of Al_2O_3 would occur directly along the graphitic edges of the VACNFs without need for functionalization. This confirmation is important since covalent functionalization of CNTs degrades charge mobility as well as conductivity of the CNTs, and noncovalent functionalization requires additional time and cost. Direct atomic layer bonding to VACNF surfaces using ALD growth has advantages in maintaining the high conductivity of the electrode, simplifying the device fabrication procedure, and generating cleaner interfaces between electrode surface and ALD materials with minimized surface defects and chemical contaminants. These advantages are critical towards fabrication of high-performance, 3D nanostructured devices utilizing VACNF arrays as part of the 3D electrode.

Additional HRTEM images also revealed that the outer 19:1 AZO layer of the ALD double-layer coating on the VACNFs was ~33 nm thick. The corresponding growth rate of 0.17 nm/cycle is comparable to, but slightly less than, that reported by J. W. Elam et al. using similar conditions.[263-264] The resistivity of the 19:1 AZO on glass was approximately 4.2×10^{-3} Ω cm as was expected according to previously published results.[262-263, 265] This resistivity corresponds to a sheet resistance of 1.3×10^{3} Ω/□. In addition, this result suggests that aluminum doping of ZnO during the ALD supercycles was sufficient. Since AZO is a transparent conducting oxide, ALD

of AZO will allow in situ fabrication of metal-insulator-metal multilayers on various substrates, especially to conformally coat VACNFs.

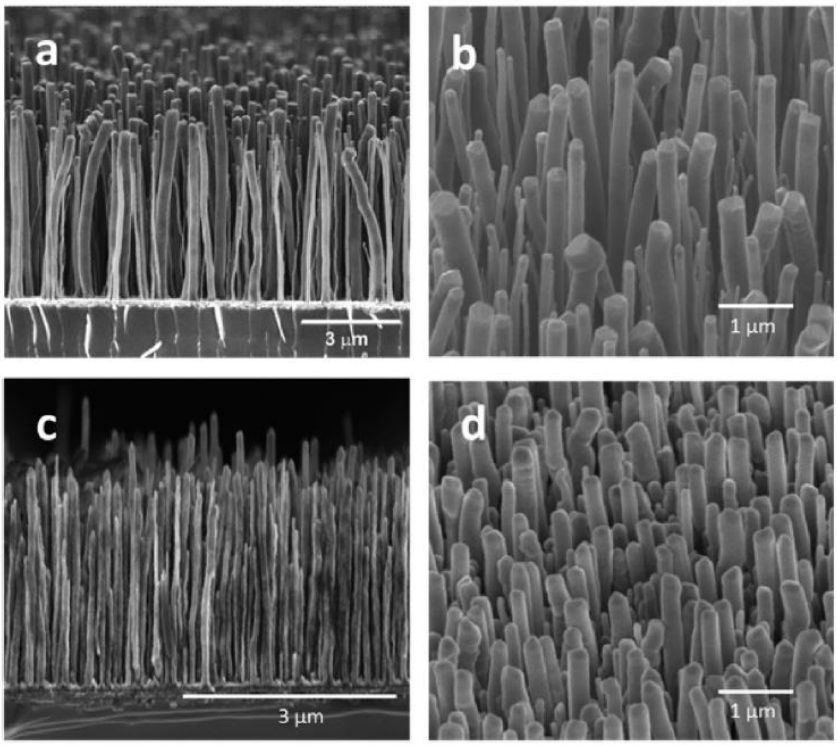

Figure 2.2 FESEM images of VACNF arrays. (a) Side view of an as grown VACNF array on Si after cleavage. (b) 45° perspective view from top of an as-grown VACNF array with the Ni catalyst tip clearly visible. (c) Side view and (d) 45° perspective view from top of an AZO/Al_2O_3 coated VACNF array. (Reprinted with permission from ACS Appl. Mater. Interface, 2014, 6, 6865-6871)

As depicted in Figures 2.2a (side view) and b (45° perspective view), the FESEM images of as-grown CNFs reveal their vertically aligned nature with an approximate density of 10^9 CNFs/cm^2. The images also verify that the VACNF diameters are in the range of 50-150 nm with heights ranging from 3 to 5 μm. The nickel catalyst for each VACNF is clearly noticeable in Figure 2.2b as a bright spot on the fiber tip. After growth of the ALD AZO/Al_2O_3 double layer coatings, the nickel nanoparticles become less visible. The vertically aligned nature of each VACNF is still apparent in both side view (Figure 2.2c) and 45° perspective view (Figure 2.2d).

Additionally, Figure 2.2d clearly reveals an increase in VACNF thickness due to the ALD coatings. In particular, the AZO/Al_2O_3 double-layer coating appears highly uniform and conformal as expected for ALD.

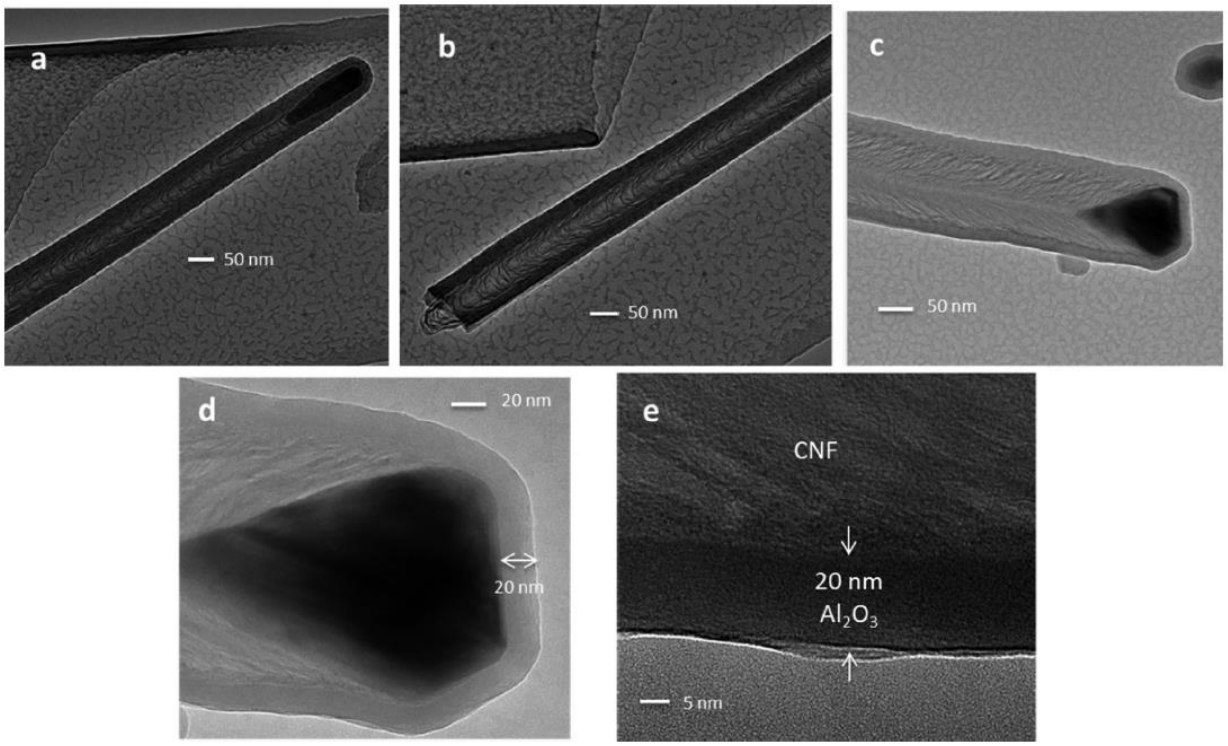

Figure 2.3 TEM images of (a) conformal Al_2O_3 coating along a CNF including the Ni catalyst tip. (b) Conformal Al_2O_3 coating continues down the shaft of the CNF up until the point where it was broken off from the base. (c) Conformal Al_2O_3 coating along another CNF which also shows the "herringbone" nature of the CNF. (d) Close-up of the conformal coating around the Ni tip. (e) Extreme close-up image of CNF core and Al_2O_3 shell. (Reprinted with permission from ACS Appl. Mater. Interface, 2014, 6, 6865-6871)

To further confirm the conformal nature of the ALD core-shell structure, HRTEM images were taken of individual Al_2O_3/VACNF samples. Figures 2.3a and b show the 20-nm Al_2O_3 conformal coating extending down the entire length of a VACNF to the point where it broke off of the metal base. As mentioned previously, this thickness is in agreement with spectroscopic ellipsometry data taken of ALD Al_2O_3 growth on SiO_2 coated silicon substrates. More importantly, the resulting Al_2O_3 thickness verifies the assumption that pre-functionalization of the

VACNF surface is not required for ALD growth to occur. The graphitic edges on the VACNF sidewalls were sufficient nucleation sites for initiating ALD growth. Examining the scale bars of Figures 2.3a and b reveals that the outer diameter of the Al_2O_3/VACNF core-shell structure is increased accordingly to a value of approximately 110 nm. The stacked cone-like nature of a "herringbone" VACNF is apparent in each of the TEM images of Figure 2.3, and a closer examination of Figure 2.3b reveals the cone shape of the VACNF where it was pulled from the base. In addition to the type of VACNF core present, the 20-nm conformal shell coating around the nickel catalyst tip is clearly shown in Figures 2.3a, c, and d. A close-up image of the VACNF transitioning to the amorphous Al_2O_3 shell is shown in Figures 2.3e which again verifies the 20-nm thickness.

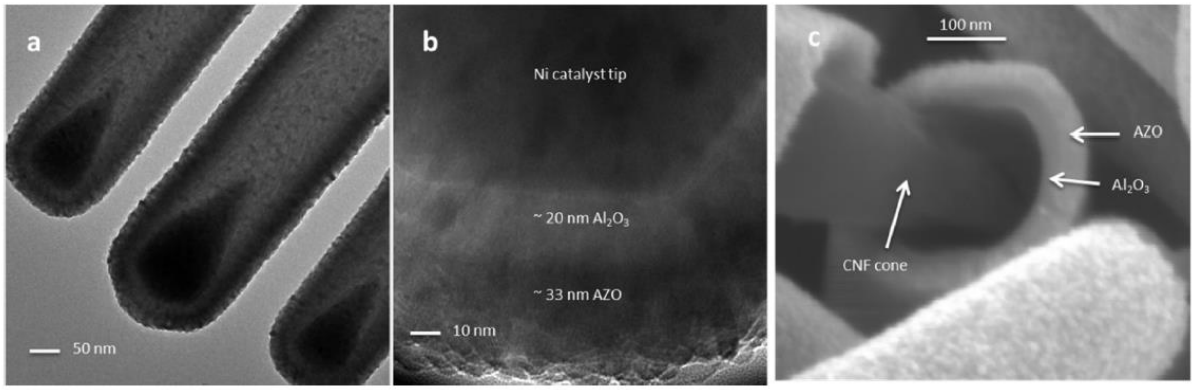

Figure 2.4 HRTEM images of multilayer ALD growth on VACNFs. (a) Multilayer Al_2O_3/AZO conformal coatings transition without problem from CNF to Ni catalyst tip. (b) HRTEM close-up of Ni/Al_2O_3/AZO layering. (c) FESEM image showing core−shell multilayer structure. (Reprinted with permission from ACS Appl. Mater. Interface, 2014, 6, 6865-6871)

The HRTEM images of AZO/Al_2O_3 double-layer coated VACNFs are depicted in Figures 2.4a and b. These images reveal the expected growth of 20-nm Al_2O_3 on which a 33-nm AZO layer can be seen in a conformal shell along a portion of the VACNF with a complete capping of the nickel catalyst tip. A cross section FESEM image of an AZO/Al_2O_3/VACNF sample (Figure 2.4c) verified the core-shell structure of the AZO/Al_2O_3 coating at the point that a coated VACNF

was broken off by mechanical force. In addition to the conformal coating surrounding the VACNF, the cone-like nature of the VACNF core is also apparent.

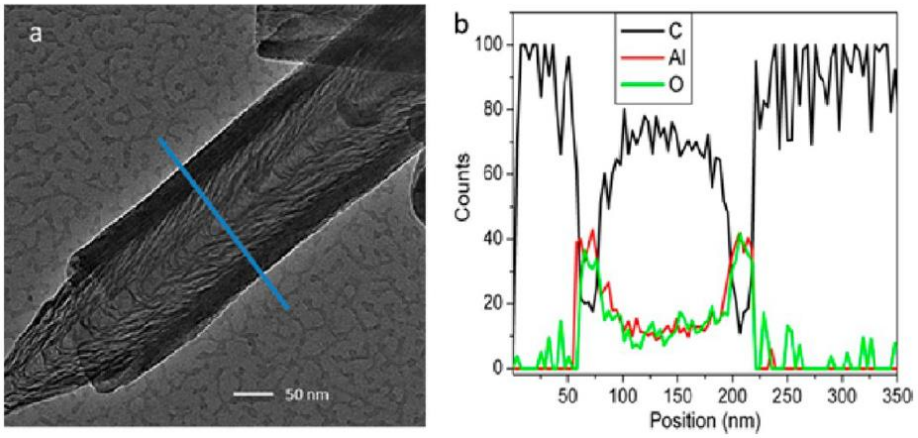

Figure 2.5 EDX elemental analysis. (a) HRTEM image of Al_2O_3/CNF with blue line showing scan region. (b) Elemental count vs position graph. (Reprinted with permission from ACS Appl. Mater. Interface, 2014, 6, 6865-6871)

To further confirm that Al_2O_3 was indeed the material grown by ALD to form the inner shell, EDX data was obtained along a portion of a coated VACNF (Figure 2.5a). The elemental counts vs. position graph indicate that the VACNF core has a diameter of ~125 nm while the whole core-shell structure after ALD coating has an outer diameter of ~165 nm. The elemental analysis further revealed significant counts of aluminum and oxygen along the 20-nm thick sidewalls (Figure 2.5b). Furthermore, the carbon count is significantly larger inside the Al_2O_3 shell which is expected due to the presence of the CNF.

It has been shown that annealing an amorphous film can induce crystallization and convert an amorphous structure into a polycrystalline form.[266] To confirm this process, electron diffraction patterns were obtained from the selected area under TEM for pre-annealing (Figures 2.6a and b) and post-annealing (Figures 2.6c and d) samples of Al_2O_3 coated CNFs. Only a ring-

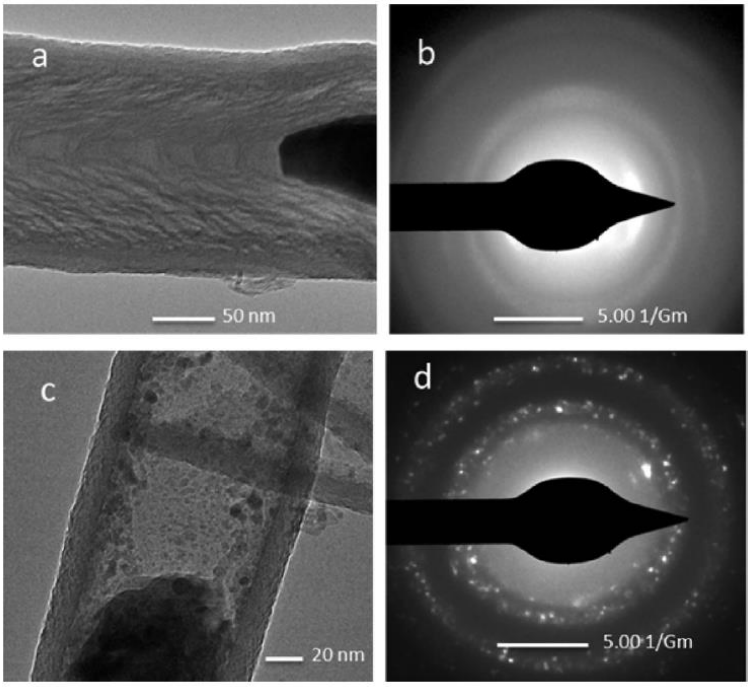

Figure 2.6 (a) Al_2O_3 coated CNF before annealing. (b) No diffraction pattern is present before annealing. (c) Al_2O_3 coated CNF after annealing. (d) Apparent diffraction pattern is present after annealing. (Reprinted with permission from ACS Appl. Mater. Interface, 2014, 6, 6865-6871)

like diffusive diffraction pattern was produced for the pre-annealed sample (Figures 2.6b), confirming the as-made ALD Al_2O_3 to be amorphous. After annealing the same sample in air, a diffraction pattern with sharp spots on the diffusive rings formed (Figure 2.6d), verifying that the Al_2O_3 layer was now polycrystalline. This transformation may change the properties of the Al_2O_3 layer, which could be beneficial for some applications.

To assess the dielectric properties of ALD deposited Al_2O_3, we constructed two electrostatic planar capacitors were constructed with one using an unannealed Al_2O_3 layer and another with an annealed Al_2O_3 layer. Both capacitors had 2 mm x 2 mm lateral size with 20-nm Al_2O_3 dielectric layer deposited by ALD that was sandwiched between a 600-nm palladium top electrode and a 100-nm chromium bottom electrode on an n-doped silicon substrate. Electrostatic measurements were conducted to determine their specific capacitance and dielectric constants.

Comparable dielectric constants as well as nearly identical capacitive behaviors were observed for both capacitors. Therefore, discussion is limited to only the annealed capacitor.

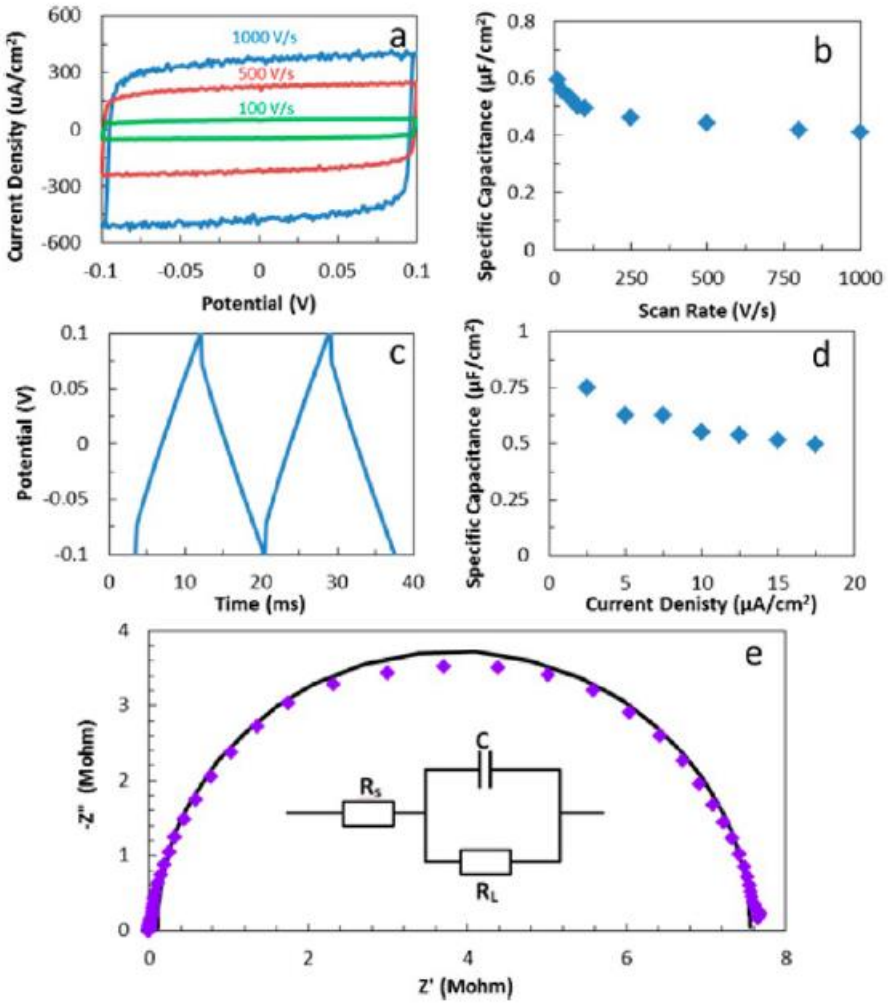

Figure 2.7 Electrical characterization of a planar capacitor. (a) I−V curves measured by cycling the bias voltage between −0.1 to +0.1 V at the rates of 100, 500, and 1000 V/s, respectively. (b) The area-specific capacitance vs the scan rate derived from the cycling I−V measurements. (c) Galvanostatic charge−discharge curve at a constant current density of 12.5 μA/cm^2. (d) Area-specific capacitance vs current density calculated from charge−discharge curves. (e) Nyquist plot of the AC impedance spectrum of a 2 mm × 2 mm planar capacitor and the fitting curve with a Randles circuit. The AC frequency was varied from 100 kHz to 10 mHz and the amplitude was fixed at 5 mV. The fitted series resistance (RS) and leaking current resistance (RL) were 94 Ohm and 7.5 MOhm, respectively, and the capacitance was 1.64 × 10^{-8} F (i.e., 0.41 μF/cm^2). (Reprinted with permission from ACS Appl. Mater. Interface, 2014, 6, 6865-6871)

An ideal electrostatic capacitor has perfect rectangular shaped I-V curves when the bias voltage is cycled between two voltage settings. Figure 2.7a shows the cycling I-V curves of an annealed planar capacitor. The rectangular shapes indicate the near perfect capacitive behavior. Both the charging and discharging curves are nearly horizontal indicating high Ohmic resistance across the thin Al_2O_3 dielectric film. The small rounded corners, along with the nearly vertical I-V curves at the voltage limits, indicate a low RC time constant and low equivalent series resistance (ESR), which is expected for an electrostatic capacitor.

The area-specific capacitance (C_0) was approximately calculated at each cycling rate using the following Equation 2.1:

$$\boldsymbol{C_0 = \frac{I_c - I_d}{2v}\, x\, \frac{1}{A}}$$

Equation 2.1

where I_c is the charging current and I_d the discharging current at 0 V, v the cycling rate, and A the geometric area of the sandwiched dielectric capacitor. A plot of the area-specific capacitance vs. the cycling rate is depicted in Figure 2.7b. The value is nearly constant for scan rates from 100 V/s to 1000 V/s, indicating the capability of a high-power density, which is essential for an electrostatic capacitor.

The area-specific capacitances of the planar capacitors were also determined by Galvanostatic charge-discharge study at constant current densities. An ideal capacitor shows perfectly symmetric charging and discharging curves with identical time duration. A charge-discharge curve for the annealed planar capacitor at a current density of 12.5 $\mu A/cm^2$ is shown in Figure 2.7c with duration of ~9 milliseconds. A small IR drop can be seen at the beginning of each curve due to ESR (< 1 kΩ, mostly due to contact resistance) in the circuit.

The area-specific capacitance was further determined by Galvanostatic charge-discharge measurements at each current density using the following Equation 2.2:

$$C_o = \frac{I \, x \, \Delta t}{\Delta V} x \frac{1}{A}$$

Equation 2.2

where *I* is the applied current density, *Δt* the time to reach the full charge or discharge, *ΔV* the voltage window, and A the geometric area of the sandwiched dielectric capacitor. The slowly decreasing trend of the area-specific capacitance vs. current density in Figure 2.7d is consistent with good dielectric capacitive behaviors revealed by cycling I-V measurements in Figures 2.7a and b.

A Nyquist plot of the annealed planar capacitor and the fitted curve using a Randles circuit are shown in Figure 2.7e. The frequency of the AC voltage bias was varied from 100 kHz to 10 mHz with a fixed amplitude of 5 mV. The fitted series resistance (RS, or ESR) and leaking current resistance (RL) were 94 Ohm and 7.5 MOhm respectively. An RL of 7.5 MOhms indicates very high Ohmic resistance across the annealed Al_2O_3 dielectric film. The semicircle symmetry of the spectrum indicates near perfect electrostatic capacitive behavior. The capacitance was calculated to be 1.64 $x10^{-2}$ μF which translates to a specific capacitance of 0.41 μF/cm^2.

Banerjee et al. reported on a state-of-the-art metal−insulator−metal capacitor using anodic aluminum oxide nanopores coated with a thin layer of TiN (5.5 nm) followed by a thin layer of Al_2O_3 (6.7 nm) and a second layer of TiN (12.6 nm), all via ALD.[248] Two capacitors were constructed at pore depths of 1 μm (A1) and 10 μm (A10) with reported equivalent planar capacitances (EPCs) of 9.9 and 96.0 μF/cm^2, respectively. The corresponding area-specific capacitances for planar dielectric layers derived from their study are 0.72 and 0.74 μF/cm^2, respectively. Although the annealed planar capacitor reported here has a lower area-specific capacitance of 0.41 μF/cm^2, the dielectric constant, k, of the ALD Al_2O_3 layer in this study is actually higher considering the difference in the dielectric thicknesses (20 nm in this work vs 6.7

nm by Banerjee et al.). This work achieved a value of ~9.3 vs ~5.5 by Banerjee et al. as calculated following Equation 1.4 where ε_0 is the vacuum permittivity and d the thickness of the dielectric layer. Clearly, the quality of Al_2O_3 layer deposited by ALD in this experiment is close to the theoretical value of 9.34 for alumina.[267] In addition, the EPC values reported by Banerjee et al. were obtained using an LCR meter operating at 20 Hz. However, when frequencies of 100 Hz or greater were applied, noticeable dispersion was observed, which greatly decreased the overall capacitance. In this report, the planar capacitor was characterized in great detail using cyclic voltammetry (CV), galvanostatic charge−discharge, and electrical impedance spectroscopy (EIS). CV results (Figure 2.7a) showed a maximum voltage ramp of 1000 V/s (the high limit of the instrument) in a potential window of 0.2 V in which one full cycle is equivalent to 2500 Hz. For applications that utilize a larger voltage window from −2 to 2 V, it should still have a working frequency of 250 Hz when the same voltage ramp rate is applied. The galvanostatic charge−discharge measurements had a maximum applied current density of 17.5 $\mu A/cm^2$ with a charge−discharge duration of ~5 ms (or 200 Hz). Neither CV, nor the charge−discharge results in panels b and d in Figure 2.7, showed any evidence of significant dispersion. The EIS in the full frequency range from 100 kHz to 10 mHz was nicely modeled with the Randles circuit as shown in Figure 2.7e. Therefore, it is likely that the working frequency could be as high as 100 kHz indicating a large power density. This is the main advantage of a solid-state capacitor over an electrochemical capacitor which is not able to operate at such high working frequencies. The fabrication and characterization of the planar capacitor in this work established a critical step toward our next goal of fabricating a 3D, solid-state VACNF array capacitor. Utilizing the area-specific capacitance from this planar capacitor, and optimizing the growth conditions of the

VACNFs and Al_2O_3 dielectric layer, a predicted theoretical capacitance of 83 μF per cm^2 CNFs is possible.

2.4 Conclusions

3D VACNF arrays were used as conducting, high aspect ratio substrates for ALD coating of AZO/Al_2O_3 double layers. HRTEM imaging revealed that the ALD AZO/Al_2O_3 double layers can form a smooth and conformal shell on VACNF arrays without any pre-functionalization. This uniform growth was achieved along the entire length of the VACNFs from the nickel catalyst tip down to the base. The elemental make-up of the Al_2O_3 core-shell was verified using EDX analysis. Electron diffraction images obtained with pre- and post-annealed samples revealed that the Al_2O_3 originally grew in an amorphous state on the CNFs, and changed to a polycrystalline state after thermal annealing. FESEM images were also obtained in order to show the vertically aligned state of the CNFs uniformity across the substrate. Electrical characterization utilizing planar capacitors confirmed that the Al_2O_3 dielectric deposited by ALD matched the ideal theoretical behavior. This result is important toward the development of high-performance, solid-state capacitors for energy storage.

2.5 Acknowledgments

The authors acknowledge support in part by NASA contract No. NNX13AD42A, ARO contract No. AROW911NF-09–1–0295, W911NF-12-1-0412, and NSF contracts Nos. NSF-DMR-1105986 and NSF EPSCoR-0903806, and matching support from the State of Kansas through Kansas Technology Enterprise Corporation. We thank Dr. Gaind P. Pandey for his assistance in manuscript preparation.

Chapter 3 - Controlling Dielectric and Relaxor Ferroelectric Properties for Energy Storage by Tuning $Pb_{0.92}La_{0.08}Zr_{0.52}Ti_{0.48}O_3$

1.3 Introduction

EES devices are critical for powering portable electronics and supporting renewable energy technologies. Current commercial EES devices include batteries, dielectric capacitors, and supercapacitors. Among them, solid-state dielectric capacitors have distinctly high-power density, very large operation voltage and long cycle life. The simple structure, small footprint, low package volume and ease in fabrication make them particularly suitable for integration into microelectronics which requires fast charge-discharge (in milliseconds or smaller timescale) for short-term power regulation. Conventional dielectric capacitors are based on linear properties, i.e. the stored charge *Q* is proportional to the product of the capacitance *C* and the applied voltage V by $Q = CV$ with C being a constant over the applied voltage range. However, the energy density of such linear dielectric capacitors is low (~10^{-2} to 10^{-1} W·h/kg) compared with other EES technologies.[268] One solution to this problem is employing materials with higher dielectric constant ε_r to achieve higher areal specific capacitance C_0 as defined by $C_0 = \varepsilon_0\varepsilon_r/d$ with ε_0 being the vacuum permittivity and *d* the dielectric film thickness. Among possible candidates, ferroelectric materials have attracted extensive attention due to the orders-of-magnitude higher dielectric constant ε_r than that of conventional dielectric materials.[268-270] Interestingly, they present distinctive nonlinear dielectric properties with ε_r (and C_0) significantly dropping at high voltage bias *V* (or the electric field *E*). Consequently, the energy storage mechanism in ferroelectric capacitors is quite different from conventional dielectric capacitors.[268, 270]

Common ferroelectric films used for capacitors include polymers such as poly(vinylidene fluoride) (PVDF)[268, 271-273] and ceramics,[268-270, 274-275] whose internal polarization states associated with the orientation of dipole moment of individual domains can be reversed under an external electric field. The domain switching is represented by the characteristic hysteresis loop in the polarization-electric field (*P*-*E*) curve where the polarization *P* is the total charge involved in the process. The term *P* is simplified as *Q* in earlier discussion on linear dielectric capacitors. Ceramic films are particularly attractive due to their higher ε_r value than polymers (~1000 vs. ~100 or less), superior mechanical and thermal properties, larger temperature range for operation, and high breakdown field E_b. However, for energy storage, the hysteresis *P*-*E* loop needs to be suppressed in order to reduce the energy loss and therefore enhance the overall efficiency. The need for increased efficiency has motivated efforts of exploring relaxor-ferroelectric materials, a subclass of ferroelectrics.[27] Like normal ferroelectrics, relaxor-ferroelectric materials present a permanent dipole moment in individual domains.[27, 274, 276] However, their domain sizes are on the order of nanometers instead of micrometers like those of typical ferroelectric materials. Thus, it takes much less energy to align the dipole moment with the external electric field, leading to smaller coercive field E_c and lower remnant polarization P_r in the typical *P*-*E* loop.[268, 270, 276]

One type of particularly interesting ceramic relaxor-ferroelectric material is lanthanum-doped lead zirconium titanate (PLZT),[277-278] an A-site substituted form of lead zirconate titanate (PZT). It is a well-known member of the perovskite family and shows great potential in applications such as nonvolatile random-access memories, microwave devices, and electro-mechanical or photo-mechanical transducers.[44-46] In particular, research has been focused on its energy storage ability owning to its high permittivity and low remnant polarization.[270, 278-279] Hao *et al* reported an energy density up to 28.7 J/cc and with an aerial capacitance density of 925

nF/cm^2 for 1 μm thick $Pb_{0.91}La_{0.09}(Ti_{0.65}Zr_{0.35})O_3$ (PLZT 9/65/35) films on platinum-buffered silicon substrates.[278] Tong *et al* obtained comparable results with a maximum energy density of 22 J/cc with an electrical energy storage efficiency of 77% for a 3 μm $Pb_{0.92}La_{0.08}(Zr_{0.52}Ti_{0.48})O_3$ (PLZT 8/52/48) film deposited on a lanthanum nickel oxide buffer layer covered nickel substrate (LNO/Ni).[270] These results show very high energy storage capabilities approaching that of electrochemical capacitors. However, the PLZT films in both studies were produced via sol-gel methods which often introduce defects during the fabrication process, such as residual fine pores, hydroxyls, and cracking during the drying stage. Moreover, many sol-gel methods require long fabrication time, large amounts of precursors, and high cost for materials which may make them inadequate for large scale production.

Here we report the study of energy storage properties of high-quality epitaxial PLZT (8/52/48) thin films (from ~100 nm to 1000 nm) grown by pulsed laser deposition (PLD) – a potential scalable technique. These PLZT films contain much less crystallographic defects, especially reduction in the number of large-angle grain boundaries.[280-282] However, since the thickness is near the scale of grain boundaries, the current passing through these PLZT films contains significant leakage current due to the finite electric conductivity[275, 283-284] and capacitive charge-discharge current due to the linear dielectric permittivity,[285-286] which are superimposed with the conventional polarization measurement due to relaxor-ferroelectric domain switching as observed in thicker films. The relative contributions from each component should depend on the film thickness. The leakage current and linear dielectric charge-discharge current should decrease when the film thickness is increased, and the complicated non-linear ferroelectric current should begin to dominate. It is difficult, perhaps even impossible, to separate the three components of leakage, charge-discharge, and nonlinear ferroelectric current using conventional *P-E*

measurements. Therefore, we adapt a method based on cyclic current-voltage (*I-V*) measurements by applying triangular voltage waveforms using simple potentiostat. The contributions of three components are extracted based on their characteristic *I-V* features as described by Yan et al.[285] Our results reveal for PLZT thickness increasing from 125 to 250, 500, and 1000 nm, PLZT transitions from an approximately linear dielectric to a largely non-linear relaxor-ferroelectric behavior. Accordingly, the energy storage density and efficiency are significantly altered. This result is important toward understanding the energy storage properties of the PLZT thin films and to the best of our knowledge, this is the first work to use the cyclic *I-V* method to investigate the energy storage capability of a relaxor-ferroelectric thin film.

3.2 Experimental Details

PLZT films were grown at 650 ^{o}C under 225 mTorr oxygen partial pressure on (001) Nb doped STO (Nb:STO) or (100) $LaNiO_3$ (LNO), which also serves as the bottom electrode, on $LaAlO_3$ substrate using a pulsed laser deposition (PLD) system with KrF excimer laser (wavelength of 248 nm and pulse width of 25 ns) as described before.[282] The average laser pulse energy density was 2 J/cm^2 with laser repetition rate of 10 Hz. After deposition, the films were *in-situ* annealed at 600 Torr oxygen and 650 ^{o}C for half an hour to reduce oxygen vacancies before cooling down to room temperature. Top electrodes were formed using 10 nm Pt followed by 80 nm Au deposited by electron-beam evaporation through a shadow mask to define 400-µm-diameter circular electrode area. X-ray diffraction (XRD) profiles were taken using a Bruker AXS D8 diffraction system. The topography of the PLZT film was measured with an atomic force microscope in tapping mode (WiTec Alpha300, Germany).

For validation of the ferroelectric properties, the PLZT films were first measured using the conventional method with a Radiant Premier II tester (Albuquerque, NM) at 100 Hz and an applied

electric field of -160 to 160 kV/cm. The data are presented in the form of a typical *P-E* hysteresis loop in Figure B.1a. Permittivity and dielectric loss, as shown in Figure B.1b were measured at 10 kHz with an Agilent E4980A Precision LCR Meter.

Cyclic *I-V* measurements of 125 and 250 nm PLZT films were conducted using a 760E Bipotentiostat (CH Instruments Inc., Austin, TX) and those for the thicker PLZT films (500 nm and 1 um) using a PARSTAT 2273 Analyzer (Princeton Applied Research Corporation, Oakridge, TN). The voltage range for each instrument above is about ±6 V and ±10 V, respectively. All measurements were conducted in two-electrode setup with the bottom electrode connected through a copper plate underneath the sample. A tungsten microprobe was brought into contact with the top electrode using a XYZ Micromanipulator (Quarter Research, Bend, OR). The voltage ramping rate υ of the triangular waveform was fixed at a value between 100 and 2000 V/s. The electric displacement D was calculated by dividing the integrated area under the *I-V* curve with υ and present in D-E loops.

3.3 Results and Discussion

X-ray diffraction confirmed the PLZT films are (001)-oriented epitaxial with the in-plane (100) and (010) axes aligned with that of Nb:STO or LNO electrode layers, as shown in Figure 3.1a. The XRD θ-2θ profile was measured with a tilt angle at 45° with respect to the normal of the film. The average surface roughness of PLZT film is around 10 nm over an area of 10×10 μm^2 from atomic force microscopy measurement as shown in Figure 3.1b. A TEM image of the lateral view of a representative 500 nm PLZT film sample in Figure 3.1c shows the exact thickness and columnar structure.

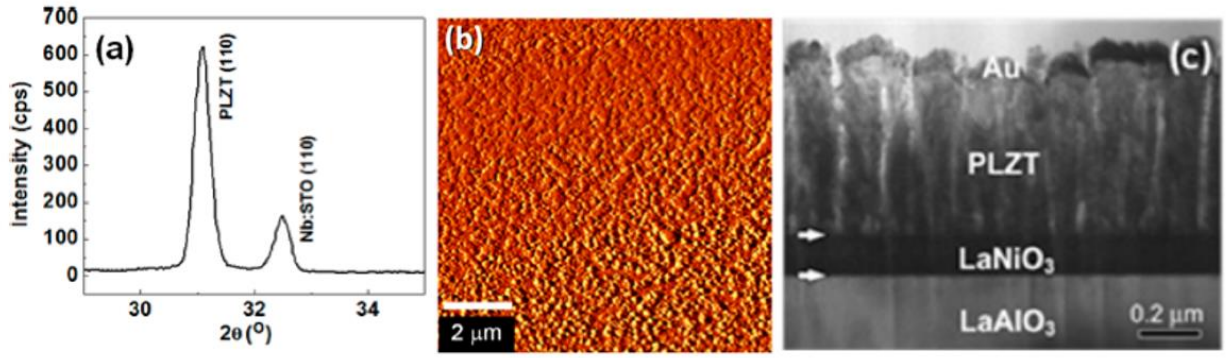

Figure 3.1 (a) X-ray diffraction pattern of PLZT deposited by pulsed laser deposition on Nb:STO substrate measured with a 45° tilt angle. (b) Topographic image by atomic force microscope of the PLZT film. (c) A transmission electron microscopy image of the cross-sectional view of the PLZT film. (Reprinted with permission from ACS Appl. Mater. Interface, 2014, 6, 22417-22422)

Figure 3.2a shows a typical *P-E* loop for the 500 nm PLZT film measured with the conventional Radiant Premier II tester at 100 Hz between an applied field of -160 to 160 kV/cm (i.e. E_{max} = 160 kV/cm). The shape of the hysteresis loop validates that the PLD grown PLZT film behaves as a relaxor-ferroelectric material under such unsaturated polarization conditions, as

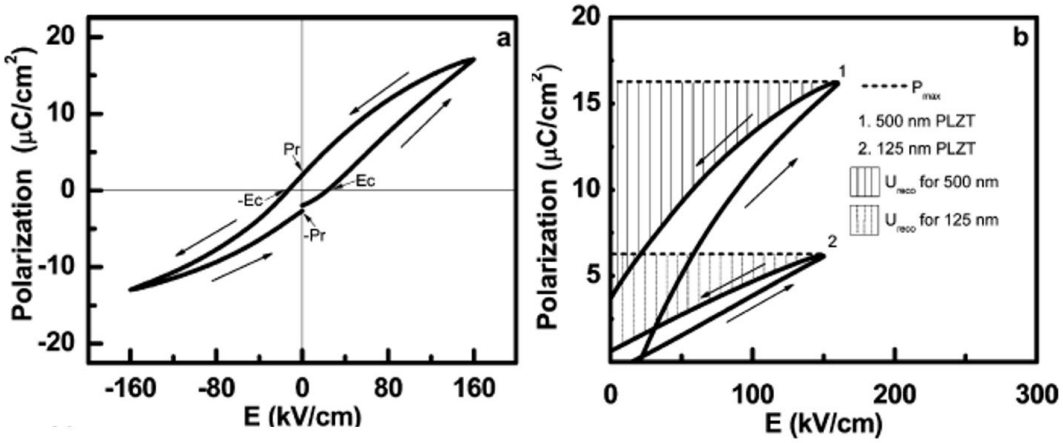

Figure 3.2 (a) P−E hysteresis loop of the 500 nm PLZT film measured using the conventional method and a Radiant Premier II tester shows the representative relaxor-ferroelectric behavior with characteristic coercive field (E_c and $-E_c$) and remnant polarization (P_r and $-P_r$). (b) Schematic illustration of the energy storage characteristics obtained using the P−E hysteresis loops of a 500 nm PLZT film (curve 1) in comparison with a 125 nm PLZT film (curve 2). (Reprinted with permission from ACS Appl. Mater. Interface, 2014, 6, 22417-22422)

described within previous publications.[270, 276] The values of the coercive field E_c and remnant polarization P_r are 24 kV/cm and 3.6 μC/cm^2, slightly smaller than those reported values of 1-μm-thick PLZT film by a sol-gel process under the similar E_{max}.[278] The observed higher nonlinearity is attributed to the high domain mobility in epitaxial PLZT thin films.[282]

The energy storage properties of the thin-film PLZT are schematically illustrated in Figure 3.2b with quadrant I of the *P*-*E* loops for the 500 nm (1) and 125 nm (2) PLZT films. The shaded region between the discharge loop and the line at max polarization P_{max} represents the recoverable electrical energy density U_{reco} in units of *J/cc*, which can be calculated by integrating the area between P_r and P_{max} as shown in Equation 3.1:[268, 270, 276-277]

$$\boldsymbol{U_{reco} = \int_{P_r}^{P_{max}} E \mathrm{d} P}$$

Equation 3.1

The total energy stored U_{store} can be determined in a similar way by integrating the area between the charging polarization curve and the P_{max} line, which consists of the shaded region plus the area inside the loop. The electrical energy storage efficiency η is thus determined Equation 3.2:

$$\eta = \frac{U_{reco}}{U_{store}} \mathrm{X}\ 100\%$$

Equation 3.2

Since the permittivity is defined by the general relationship $\varepsilon_0\varepsilon_r = \mathrm{d}P/\mathrm{d}E$, the recoverable electrical energy density in Equation 3.3 can be defined as:

$$\boldsymbol{U_{reco} = \int_{0}^{E_{max}} \varepsilon_0 \varepsilon_r \mathrm{E} \mathrm{d} E}$$

Equation 3.3

For a relaxor-ferroelectric material, ε_r is a function of *E*. As shown in Figure B.1b, the 500 nm PLZT film presents a very high ε_r (~1300) peaked at the electric field around E_c and quickly drops

to ~650 at E = 100 kV/cm. The permittivity curves shift in opposite direction in correlation with the *P-E* loop in Figures 3.2a and B.1a. In contrast, in a linear dielectric capacitor, the *P-E* loop diminishes and thus the stored energy can be completely recovered. In addition, the polarization curve superimposes onto a straight line with $P = C_0V = C_0Ed = \varepsilon_0\varepsilon_rE$, where $C_0 = (\varepsilon_0\varepsilon_r)/d$ is the area-specific capacitance. Incorporating this result within Equation 3.3 gives the simple and commonly known formula for volume-specific energy density of linear dielectric capacitors in Equation 3.4:

$$\boldsymbol{U = (\frac{1}{2} C_0 V^2)/d = (\frac{1}{2} C_0 E^2) \times d.}$$

Equation 3.4

Unfortunately, the linear dielectric capacitor is limited in energy storage, which is typically several orders of magnitude smaller than batteries, due to the much lower ε_r. It is of interest to investigate how the dielectric properties of the PLZT films can be tailored by tuning the film thickness so that optimum energy storage properties can be achieved within the material system as it transitions from a linear dielectric to relaxor ferroelectric.

It should be noted that the polarization *P* in the *P-E* curves shown in Figures 3.2 and B.1a should be more precisely referred to as electric displacement *D*, which consists of three contributions: electric conductivity *D1*, dielectric capacitance *D2*, and domain switching ferroelectric polarization *P*.[285] In conventional thick ferroelectric films, *D1* and *D2* are negligible and thus only *P* is presented. For thin relaxor-ferroelectric films with the thickness less than 1000 nm, the leakage current (*D1*)[275, 283-284] and dielectric capacitive current (*D2*)[285-286] become significant since both are inversely proportional to the film thickness. For relaxor-ferroelectric thin films, the nanoscale grain structure and defects make them highly susceptive to leakage current and high ε_r values make the dielectric capacitance significant (with $C_0 = (\varepsilon_0\varepsilon_r)/d$). However,

conventional *P-E* measurements only record the total *D* and are inadequate for providing insights into the individual factors.

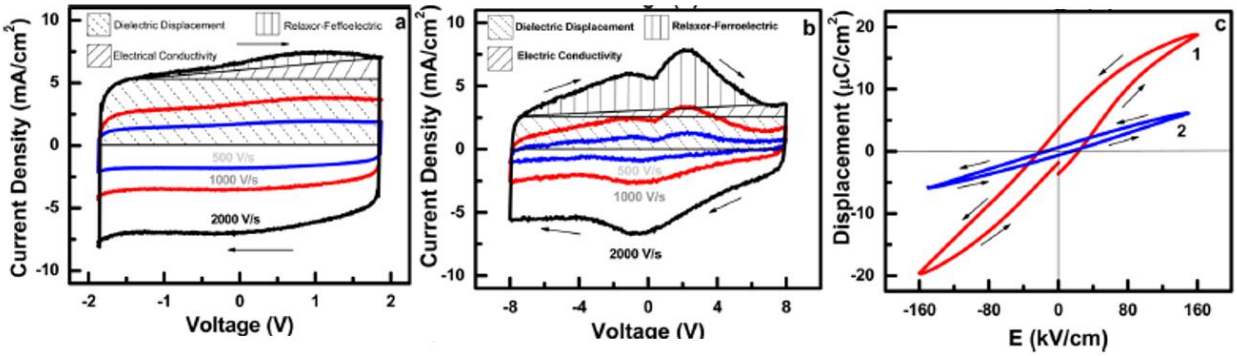

Figure 3.3 Cyclic I−V curves for the 125 nm (a) and 500 nm (b) PLZT films, depicting the contributions to the total dielectric displacement by electric conductivity D1, linear dielectric capacitance D2, and relaxor-ferroelectric domain switching polarization P. The measurements were performed by applying triangular waveforms at a constant cycling rate of 500, 1000, and 2000 V/s, respectively. (c) The electric displacement to electric field (D−E) loops for the 500 nm (curve 1) and 125 nm (curve 2) PLZT films derived by integrating the charges under the I−V curves. (Reprinted with permission from ACS Appl. Mater. Interface, 2014, 6, 22417-22422)

This issue can be resolved with cyclic *I-V* measurements using a triangular voltage waveform, as described by Yan et al.[285] The contributions of all three components can be separated by their characteristic *I-V* features illustrated in Figure 3.3. Figures 3.3a and 3.3b show the *I-V* curves at scan rate υ of 500, 1000, and 2000 V/s from two representative PLZT films with 125 nm and 500 nm thickness, respectively. I-V characteristics for all four-film thickness (125, 250, 500 and 1000 nm) are shown in Figure B.2 for direct comparison. The measurements were conducted at about ±2 V and ± 8 V, respectively, to maintain the same maximum electric field E_{max} at ±160 kV/cm (below the breakdown field E_b as shown in Figure B.3). Clearly, the *I-V* curve from a completed cycle of the 125-nm PLZT film presents a shape close to a rectangular box, which is characteristic of simple linear dielectric capacitors. In contrast, the *I-V* curve of the 500-nm PLZT film is dominated by a pair of broad waves peaked at ~2.0 V in forward scan and at ~0.5 V in reverse scan. The electric displacement *D* can be calculated by integrating the area under the *I-V*

curve and then dividing by the scan rate υ. For clear view, the contributions of *D1*, *D2*, and *P* are marked by different shaded areas under the forward scan curve at 2000 V/s for both samples.

The *I-V* curve of an ideal linear dielectric capacitor should be a rectangular box except small rounding at the two voltage limits due to the RC delay when the polarity is reversed. The magnitude of the current density is a constant during the scan and is proportional to the scan rate (i.e. $i_0 = C_0 \times \upsilon$). Indeed, the baseline current density in both Figures 3.3a and b linearly increase with the scan rate. The *D2* contribution is much larger in 125-nm PLZT film than that in 500-nm one. For both PLZT samples, the baseline has a slope. The slope of the line can be extrapolated from the two ends of the I-V curve to add a triangular area attributed to *D1* on top of the dielectric boxes. The straight line is simply the Ohmic effect due to the electric conductivity of the PLZT film. From the slope of the baseline, the resistivity ρ of the PLZT film can be calculated to be 1.6 $x10^8$ and 2.9 $x10^8$ Ω-cm for 125-nm and 500-nm, respectively. These values are smaller than ~8.3 $x10^{10}$ Ω-cm resistivity of the sol-gel deposited 1-μm PLZT film derived from the stable leakage current in a previous study. It is worth noting that the dynamic current at high scan rate (2000 V/s) is expected to be nearly 10 times higher.[278] The high crystallinity of the PLZT film by PLD may also give higher conductivity.[282]

The remaining area under the *I-V* curve is from the wave feature attributed to domain switching polarization *P*. This area is rather small in the 125-nm PLZT film but becomes prominent in the 500-nm PLZT film. The shape and peak voltage of the *I-V* waves in the 500-nm sample is sensitive to the history and the voltage bias conditions V_{max} but its peak area remains about the same and proportionately increases with the scan rate υ. The domain switching peaks in the charging and discharging cycles, however, are not symmetric to zero voltage with values of ~2.0 V and -0.5 V, respectively, indicating an asymmetrical pull of domain switching between the

charging and discharging cycles. This is likely due to voltage and charge offsets by effects of strain gradient as a result of epitaxial stresses when sandwiched between two different substrates or electrode materials.[287-288] The asymmetrical *I-V* feature is even more prominent with the 1000-nm PLZT film showing peak at ~7.0 V and 0 V, respectively (see Figure B.2d).

The total electric displacements derived from one *I-V* cycle of both 125-nm and 500-nm samples are presented in Figure 3.3c in the form of *D-E* curves. The *D-E* loop of the 500-nm PLZT film is very similar to the conventional *P-E* loop shown in Figure 3.2a, with comparable P_r (3.6 μC/cm^2), E_c (24 kV/cm) and P_{max} (~18 μC/cm^2). Interestingly, the *D-E* loop of the 125-nm PLZT film is significantly suppressed, showing smaller values for P_r (0.63 μC/cm^2), E_c (15 kV/cm) and P_{max} (~6.1 μC/cm^2). The forward and reverse curves come close to forming a straight line. The small loop is attributed to the small ferroelectric waves and the small leakage current in the *I-V* curve superimposed on the dominant dielectric box. Clearly, the 125-nm PLZT film behaves closer to a linear dielectric capacitor while the 500-nm PLZT film is dominated by relaxor-ferroelectric properties. The P_r and E_c values at the same E_{max} show approximately a linear relationship with the PLZT film thickness (see Figure B.4).

As shown in Figure 3.4a, the total electric displacement value *D* per unit of lateral area derived from the *I-V* measurements at the E_{max} = 160 kV/cm monotonically increases from ~12 to ~52 μC/cm^2 as the PLZT film thickness is increased from 125 to 1000 nm. The rate of increase reduces as the thickness becomes larger. Furthermore, the contributions by *D1*, *D2*, and *P* show very different dependence on the film thickness. In theory, the leakage displacement *D1* at the same E_{max} (=160 kV/cm) should linearly increase with the film thickness *d* due to the Ohmic relationship $D1 = (E_{max}^2/\rho\upsilon)d$ if the resistivity ρ is a constant for each thickness. The data for the films is consistent with this assumption with the exception of the 1000-nm PLZT film. The

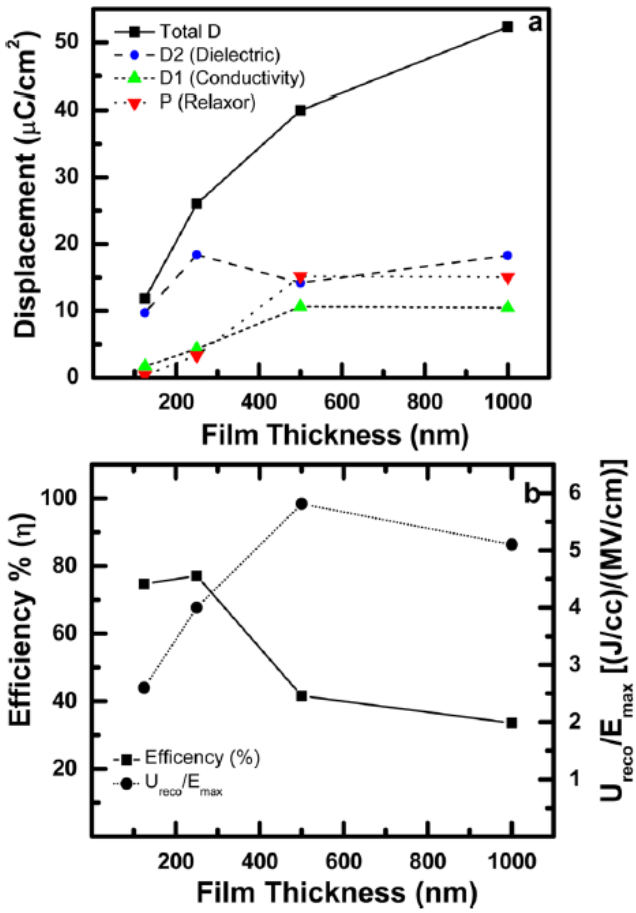

Figure 3.4 (a) Total electric displacement D and the contributions from electric conductivity D1, linear dielectric capacitance D2, and relaxor-ferroelectric domain switching polarization P versus the film thickness. (b) The energy storage efficiency and volumetric density (J/cc) normalized with the max electric field strength E_{max} (MV/cm) for different PLZT film thicknesses. (Reprinted with permission from ACS Appl. Mater. Interface, 2014, 6, 22417-22422)

dielectric displacement *D2*, on the other hand, is expected to be independent of the film thickness as defined by $D2 = C_0V_{max} = \varepsilon_0\varepsilon_r E_{max}$ if the dielectric permittivity ε_r is a constant over all thicknesses. This assumption appears valid for the observed *D2* values which randomly vary within ±4 μC/cm^2 from an average value of ~15 μC/cm^2. The relaxor-ferroelectric polarization *P* shows the largest change vs. film thickness in concert with the *D1* value. At 125 nm, there is minimum domain switching and negligible *P* value. This may be attributed to two factors: (1) suppression of domain wall motion by the mechanical strain/stress from substrate clamping and

pinning of grain boundaries; and, (2) the effects from an interfacial layer, as reported in a thickness dependence study of $BiFeO_3$ ferroelectric films.[275] The *P* value jumps to 15.2 μC/cm^2 for the 500-nm PLZT film and slightly drops to 14.9 μC/cm^2 for the 1000-nm PLZT film. These values correlate well with the area under the broad *I-V* wave curves in Figures 3.3a-b and Figure B.2. Overall, the 1000-nm PLZT film shows the highest total displacement *D*.

For energy storage applications, the high displacement value needs to be supported through high volumetric recoverable density U_{reco} and high energy storage efficiency η, which can be calculated with Equation 3.1 and 3.2, respectively. Due to the film thickness, the E_{max} in this study was set at ~160 kV/cm, just below the breakdown field E_b as shown in Figure B.3. Since it is known that U_{reco} is linearly proportional to E_{max}, the normalized value U_{reco}/E_{max} (i.e. the proportional coefficient) is plotted in Figure 3.4b for ease of comparison with previous studies using much higher E_{max} on thicker films.[270, 278] The 500 and 1000 nm PLZT films show much higher U_{reco}/E_{max} values than those at 125 and 250 nm, at 5.8 and 5.1, (J/cc)/(MV/cm), respectively. These values are not far from 11.9 and 13.3 [(J/cc)/(MV/cm)] with sol-gel deposited PLZT films of 3 μm and 1 μm thickness, respectively.[270, 278] On the other hand, the thinner films show much higher energy storage efficiency at 75% (125 nm) and 77% (250 nm) compared to thicker films at 42% (500 nm) and 34% (1000 nm). There is a clear transition in energy storage efficiency from 250 nm to 500 nm thickness in correspondence with changing from close-to linear dielectric properties to nonlinear relaxor-ferroelectrics.

3.4 Conclusion

It has been shown that the energy storage properties of the thin PLZT films deposited using pulsed laser deposition can be optimized by tuning the film thickness. Cyclic *I-V* measurements were used to determine the electric displacement and evaluate the contributions from electric

conductivity, linear dielectric displacement and non-linear relaxor-ferroelectric domain switching. The *D-E* hysteresis loops constructed by integrating the charge under the *I-V* curves show consistent features with conventional *P-E* loops with characteristic coercive field and remnant polarization of relaxor-ferroelectric materials. As the film thickness increases from 125 nm to 1000 nm, the PLZT film shifts from the behavior close to that of a linear dielectric to relaxor-ferroelectric properties. The thicker PLZT films at 500 and 1000 nm thickness show much higher recoverable energy storage density, but thinner films (at 125 and 250 nm) present higher energy efficiency. There is a tradeoff between the linear dielectric properties and non-linear relaxor-ferroelectric properties for electrical energy storage. Future work on temperature dependence of the PLZT thin films and study of larger film thickness will be used to further optimize this material system for solid-state energy storage system.

3.5 Acknowledgments

This work was supported by NASA grant NNX13AD42A and NSF EPSCoR Award EPS-0903806 (including the matching support from the State of Kansas through Kansas Technology Enterprise Corporation).

Chapter 4 - Facilitating High-Capacity V_2O_5 Cathodes with Stable Two and Three Li^+ Insertion Using a Hybrid Membrane Structure Consisting of Amorphous V_2O_5 Shells Coaxially Deposited on Electrospun Carbon Nanofibers

4.1 Introduction

Electrical energy storage (EES) technologies play a major role in todays' society owing to the advances in hybrid and electric cars,[289] the ever-growing demand for portable electronic devices,[290] and grid-leveling for energy generated by intermittent renewable sources.[2] Lithium ion batteries (LIBs) have dominated the EES market for the past several decades.[1, 291] However, there are growing demands to improve LIBs for higher energy and power densities. These critically depend on electrode materials and architectures. Particularly, the low specific capacity of cathode materials is currently the bottleneck limiting the energy storage capability of LIBs.[292] Most commercial LIBs can achieve a near theoretical specific capacity of 372 mAh g^{-1} with a graphite anode and even higher values with emerging anode materials such as Si,[150, 293-294] while only ~140 – 170 mAh g^{-1} can be achieved with the cathode (such as $LiCoO_2$, $LiFePO_4$, etc).[292] Hence, developing novel cathode materials with higher charge storage capacity is one of the top priorities in LIB research.[295-296]

Vanadium pentoxide (V_2O_5) had been studied as a candidate of high-capacity cathode material owing to its low cost, low toxicity, high delithiated electrode potential (up to 4.0 V), and easily accessible layered structure for Li^+ ion insertion.[124] Crystalline V_2O_5 can achieve a reversible specific capacity of 294 mAh g^{-1} for a two Li^+/V_2O_5 insertion process. However, three Li^+/V_2O_5 insertion was found to be highly irreversible even though a high insertion capacity of

441 mAh g^{-1} was observed in the first cycle.[125, 297-298] It is well known that the Li^+ intercalation process in crystalline V_2O_5 is accompanied by multiple phase transitions.[125, 297] Trace amounts of Li^+ intercalation results in α-$Li_xV_2O_5$ ($x < 0.01$) structure, which is transformed into ε-$Li_xV_2O_5$ ($0.35 < x < 0.7$) after further lithiation. Insertion of one Li^+ leads to the formation of δ-phase $Li_xV_2O_5$ ($x = 1$). Further lithiation converts the δ-phase to γ-$Li_xV_2O_5$ ($1 < x < 2$). At more than two Li^+ insertions, an irreversible transformation to rock-salt-type ω-$Li_xV_2O_5$ phase ($2 < x < 3$) occurs.[125, 297] Even below 2 Li^+/V_2O_5 insertion, such phase transition processes induce large strains in the particles, causing irreversible structural damage and quick capacity fading.[125, 297] Insertion up to 3 Li^+/V_2O_5 makes such structural changes even more severe. As a result, practical applications of crystalline V_2O_5 cathodes have been hindered.[125, 297] In recent years, V_2O_5 gained renewed interests due to the evidence that the lattice strains and structural collapse can be largely circumvented with nanostructured morphology.[297, 299-300] Particularly, the traditionally neglected amorphous V_2O_5 has shown potential for better stability and higher Li^+ insertion capacity than crystalline V_2O_5, even possible to exceed 3 Li^+/V_2O_5 insertion.[243, 301]

Besides the complicated phase transitions, lithium insertion/extraction in V_2O_5 cathodes has also been limited by the intrinsic properties of V_2O_5. Crystalline V_2O_5 materials have small Li^+ ion diffusion coefficients (~10^{-15} – 10^{-12} cm^2 s^{-1}) and low electrical conductivities (~10^{-5} – 10^{-3} S cm^{-1}).[126, 302] Amorphous V_2O_5 may provide a higher Li^+ diffusion coefficient, but at the price of sacrificing the electrical conductivity and mechanical strength. Two strategies have so far been employed to overcome the intrinsic limits of V_2O_5, mostly with crystalline materials. The first one is to mitigate the low Li^+ ion diffusion coefficients by using low-dimensional nanostructures.[126, 297, 303-307] This strategy increases the overall specific surface area (SSA) and provides shorter diffusion pathways for Li^+ ions. In addition, low-dimensional nanostructures can also partially

relieve the large lattice strain during the phase transitions and significantly extend the battery life. However, the electrical contact between V_2O_5 nanoparticles may degrade and become a dominant factor. The second strategy (often combined with the first one) is to incorporate low dimensional conductive carbon materials such as multiwall carbon nanotubes (MWCNTs),[226, 308-311] graphene, [126, 312] and reduced graphene oxide (rGO)[67, 219, 313-316] to form nanocomposite materials. The addition of these conductive additives prevents aggregation and enhances the effective electrical conductivity throughout the electrode material. However, the poor electrical contact at the interface of the V_2O_5 nanoparticles and carbon additives and the lack of a continuous carbon framework still limit these materials from reaching high capacity at higher power rates.

Recently continuous core-shell structures have been investigated by depositing V_2O_5 thin shells using atomic layer deposition (ALD)[231] or ion sputtering[317] onto preformed three-dimensional (3D) nanostructured carbon templates. In such binder-less 3D core-shell structures, the highly conductive carbon framework has been retained as a continuous electrical pathway to effectively collect electrons from the active materials in the thin shells. The robust carbon core also improves the mechanical stability of the electrode. Here we extend this concept into a potentially scalable process based on electrodeposition of V_2O_5 shells onto a self-supported carbon nanofiber (CNF) membrane fabricated by electrospinning. The pulsed electrodeposition process enables formation of a uniform coaxial V_2O_5 shell of 30-50 nm in thickness on the CNF surface throughout the entire mesoporous membrane. With proper thermal treatment, the V_2O_5 shell was converted into a partially hydrated amorphous structure. The core-shell structure was found to be effective in overcoming the poor mechanical stability and low electrical conductivity of the disordered V_2O_5 shell. The lithium storage capability of such core-shell materials was found superior to traditional crystalline V_2O_5 materials. The half-cell characterization in the potential

range of 4.0 – 2.0 V (vs. Li/Li^+) showed a capacity up to 291 mAh g^{-1}, matching the theoretical value for 2 Li^+/V_2O_5 insertion/extraction with a remarkable capacity retention rate of 97% after 100 cycles. When extending the lower potential limit to 1.5 V (vs. Li/Li^+), reversible 3 Li^+/V_2O_5 insertion/extraction up to 429 mAh g^{-1} was achieved, with 70% of the capacity retained after 100 cycles. These results demonstrate that the core-shell structure may enable the traditionally unfavored amorphous V_2O_5 material to surpass crystalline V_2O_5 for future high-capacity LIB cathodes.

4.2 Experimental Details

4.2.1 CNF formation and pulsed electrodeposition V_2O_5

CNFs were prepared using a simple electrospinning method followed by post thermal annealing as reported before.[318-319] Briefly, 0.8 g of polyacrylonitrile (PAN) was dissolved in 8.0 g of N, N-dimethylformamide (DMF) at 120 °C under vigorous stirring for one hour. The resulting solution was cooled to room temperature and loaded into a syringe and electrospun into polymer fibers on a Spraybase® system (Profector Life Sciences, Cambridge, MA). After continuous electrospinning for 5 hours at a flow rate of 1 mL/hour at an applied electric field strength of 1 kV/cm (with 18 kV voltage bias at a nuzzle-collector distance of 18 cm), a letter paper sized membrane is collected on an aluminum foil wrapped on the rotating drum. The resulting polymer membrane was stabilized in air at 280 °C for two hours followed by carbonization at 1000 °C for one hour under nitrogen, forming a continuous CNF membrane. The CNF membrane was then used as a working electrode during pulsed electrodeposition in a three-electrode electrochemical cell, where a Pt foil and a Ag/AgCl (4M KCl) were used as the counter and reference electrodes, respectively, under control by a Parstat 2273 Analyzer (Princeton Applied Research Corporation, Oak Ridge, TN). The composition of the V_2O_5 sol electrolyte was modified from a previous

report,[216] with 0.91 g of V_2O_5 powder dissolved in 50 mL of deionized (DI) water and 4.5 mL of 30% hydrogen peroxide by vigorous stirring at room temperature for one hour. To achieve uniform V_2O_5 shells across the entire 60 μm thick CNF membrane, a novel pulsed electrodeposition was implemented. The electrode potential was first set at 0 V for 20 seconds to establish electrolyte equilibrium and then followed by -2.0 V for 10 seconds for electrophoretic deposition of V_2O_5. This sequence was repeated for 60 cycles. The resulting CNF-V_2O_5 core-shell membrane was dried in air for one hour at 70 °C followed by thermal annealing at 300 °C for four hours in air. Several samples were further annealed for an additional 20 hours in air at 300 °C to burn out the carbon and leave only the hollow crystalline V_2O_5 shell for the purpose of materials characterization.

4.2.2 Materials Characterization

The surface morphology of the bare CNFs and the thin V_2O_5 shells was examined with a Helios NanoLab 660 (FEI, Hillsborro, OR) field emission scanning electron microscope (FESEM) which was equipped with a focused ion beam apparatus to create cross sections of the sample. High resolution transmission electron microscopy (HRTEM) and scanning transmission electron microscopy (STEM) with high-angle annular dark-field (HAADF) images were obtained using a FEI Tecnai Osiris (S)TEM system (FEI, Hillsborro OR) to further evaluate the crystal structure of the outer V_2O_5 shell. Elemental analysis and mapping were carried out using energy-dispersive X-ray spectroscopy (EDS) in the TEM to show uniformity of the V_2O_5 shell along the CNF. Raman spectra were obtained using a Renishaw inVia confocal Raman microscope (Gloucestershire, UK) with a laser wavelength of 532 nm. The crystallinity was evaluated using a Rigaku SmartLab (The Woodlands, TX) X-ray diffractometer. Diffraction analysis was conducted from 10° to 60° using a Cu Kα source with a wavelength of 1.541 Å. Brunauer–Emmett–Teller (BET) measurements were carried out with a ASAP 2460 Surface Area and

Porosity Analyzer (Norcross, GA) to determine the specific surface area (SSA) and porosity. Thermal gravimetric analyses (TGA) were carried out using a TA Instrument Q50 (New Castle, DE) from room temperature to 800 °C in air at a rate of 5 °C/min.

4.2.3 Electrochemical Characterization

To evaluate the electrochemical performance of the CNF-V_2O_5 cathode, half-cells were assembled into stainless steel coin cells (CR2016, MTI Corporation, Richmond, CA). The CNF-V_2O_5 core-shell porous membrane was used as a self-supported binder-less cathode against a 16-mm dia. lithium disk anode electrode which were separated by a 0.65 mm thick glass fiber separator (El-Cell, Hamburg, Germany). The cell was assembled in an argon filled M-Braun LabStar50 stainless steel glovebox (Garching, Germany) with water and oxygen contents less than 0.5 ppm. The CNF-V_2O_5 core-shell membrane (2.4 mg) was adhered to an aluminum current collector using a thin layer of inert "glue" made of ~0.1 mg Super P and ~0.1 mg polyacrylic acid (PAA) in ~0.5 mL solution of N-Methyl-2-pyrrolidone (NMP). The mass of the applied "glue" was only 2-5% of the CNF-V_2O_5 core-shell membrane and serve only for the purpose to retain the membrane in place during cell assembly. The adhered CNF-V_2O_5 core-shell membrane was then dried for 1 hour at 70 °C under vacuum prior to cell assembly. The contribution of the inert glue to the overall capacity is negligible. The electrolyte consisted of 1.0 M lithium hexaflourophosphate ($LiPF_6$) in a mixture of 1:1:1 volume ratio ethylene carbonate (EC), ethyl methyl carbonate (EMC), and dimethyl carbonate (DMC) with a 2% vinylene carbonate additive (Novolyte, Ohio). Galvanostatic charge-discharge cycles were performed using a MTI 8 channel battery analyzer (MTI Corporation, Richmond CA). All gravimetric capacities were calculated relative to the mass of V_2O_5 that was determined by TGA. Cyclic voltammetry (CV) and

electrochemical impedance spectroscopy (EIS) measurements were performed using a CHI760D potentiostat (CH Instruments, Austin, TX).

4.3 Results and Discussion

4.3.1 SEM/TEM characterization of the CNF-V_2O_5 core-shell structure

A low-magnification SEM image of the bare CNF membrane is shown in Figure 4.1a. Clearly, CNFs form an entangled network with random stacking and large inter-CNF pores (varying from ~1 to 3 μm). Two high-magnification SEM images of the side and cross-sectional views of bare CNFs are shown in Figures C.1a and C.1b, respectively. From these images, the majority of the bare CNFs have the diameter spreading between ~100 nm to ~400 nm with the average value at ~250 nm. The thickness of the CNF membrane was estimated to be 50-60 μm as shown in the SEM images in Figures C.1c and C.1d. A high-magnification SEM image of the cross-section of a single CNF deposited with a V_2O_5 shell is shown in Figure 4.1b. It is clear that the V_2O_5 (illustrated by the white arrow) forms an intimate interface with the CNF core, showing no visible boundaries at the cross section. A SEM image at a low accelerating voltage (3 kV) in Figure 4.1c shows that the V_2O_5 shell is a continuous porous layer with slightly larger outer surface roughness than the original CNF cores. Additional SEM images in Figure C.2 further illustrate the uniform coaxial deposition of V_2O_5 shells throughout the CNF membrane. Furthermore, the SEM image at a higher accelerating voltage (10 kV) in Figure 4.1d shows better contrast between the outer V_2O_5 layer and the CNF cores. Particularly, the area inside the red circle where fiber 1 crosses atop fiber 2 clearly shows about 30-50 nm thin conformal V_2O_5 coating on the CNF cores.

To further evaluate the V_2O_5 shell, the sample was annealed at 300 °C in air for a prolonged time of 24 hours. SEM images in Figures 4.1e-f confirm that the CNF cores were burnt out, leaving only the crystalized V_2O_5 shells as hollow tubes. The polycrystalline V_2O_5 tube is apparently rougher than the 4-hour annealed sample in which V_2O_5 shells retain the as-deposited morphology. The digital photographs show that the membrane changes from the black color similar to the bare CNFs (Figure 4.1g) to the bright yellow color reminiscent of orthorhombic crystalline V_2O_5 (Figure 4.1h).

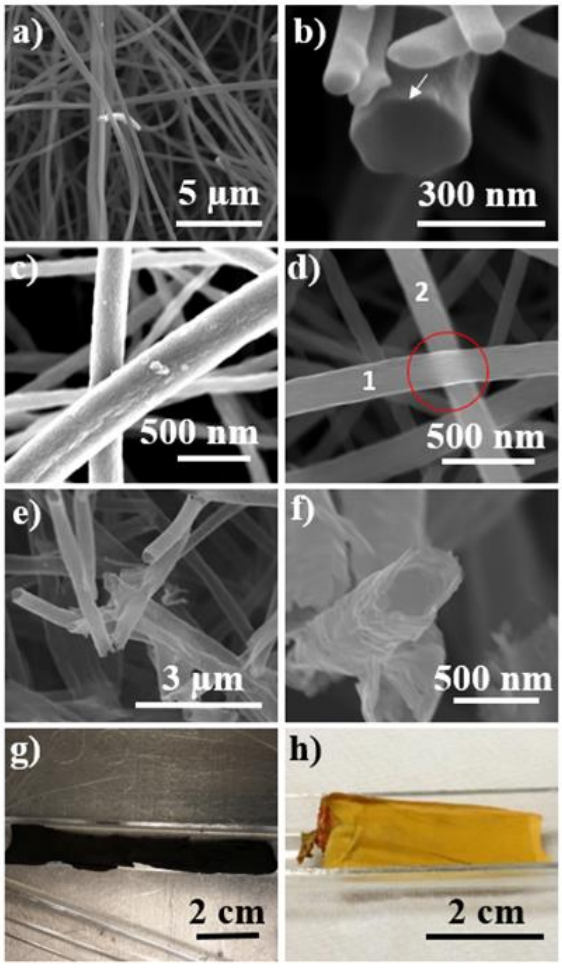

Figure 4.1 Low-magnification SEM images of a) a bare CNF membrane and b) the cross-section of a single CNF-V_2O_5 core-shell nanofiber. SEM images at accelerating voltages of c) 3 kV and d) 10 kV showing the thin coating of V_2O_5 at the surface of CNFs. e) Low- and f) high- magnification SEM images of hollow V_2O_5 shells after burning out CNF cores by the prolonged thermal annealing. Digital photograph images of g) a bare CNF membrane and h) a hollow V_2O_5 shell membrane.

A HRTEM image of the 4-hour annealed CNF-V_2O_5 core-shell structure is shown in Figure 4.2a. The outer V_2O_5 layer is visible along the CNF core as highlighted by the white brackets. Additional HRTEM images are shown in Figure C.3a with white dash lines added in Figure C.3a as visual guides to differentiate the inner CNF core and the outer V_2O_5 shell. A TEM image of the hollow V_2O_5 shell after carbon burnout is shown in Figure 4.2b. A high-angle annular dark-field (HAADF) STEM image of the 4-hour annealed CNF-V_2O_5 core-shell structure is shown in Figure 4.2c. The lack of sharp diffraction spots in the selective area electron diffraction (SAED) pattern in the inset of Figure 4.2c confirms that both CNF and V_2O_5 are amorphous or highly disordered. In contrast, the SAED of the hollow V_2O_5 shell after prolonged annealing in inset of Figure 4.2d shows sharp diffraction spots, which indicates the formation of a crystalline V_2O_5 structure. Due

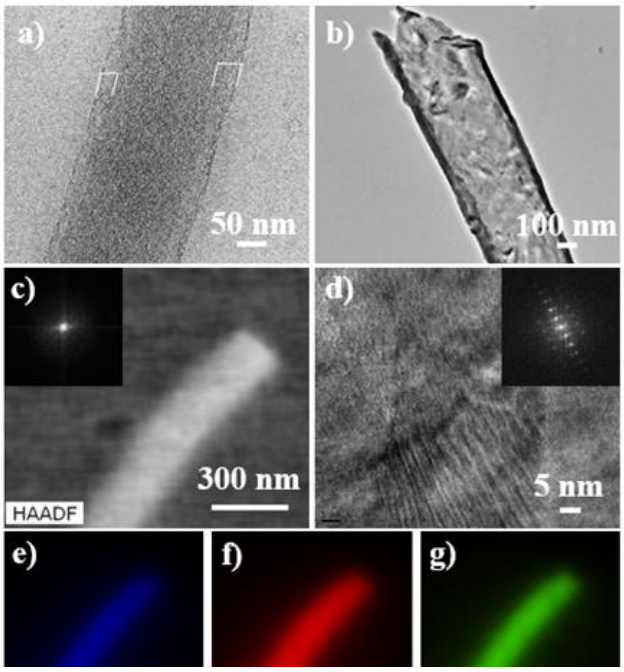

Figure 4.2 TEM images of a) a CNF-V_2O_5 core-shell structure and b) a hollow V_2O_5 shell after burning out the CNF core. c) A HAADF STEM image of a CNF-V_2O_5 core-shell structure. d) A HRTEM image of a hollow V_2O_5 shell. EDS mapping of the single CNF-V_2O_5 nanofiber in panel (c) showing the presence of e) carbon, f) oxygen, and g) vanadium. The scale bars in panel (e) to (g) are 300 nm. The insets in panels (c) and (d) are selected area electron diffraction patterns.

to the large V_2O_5 tube diameter and shell thickness, the HRTEM image (Figure 4.2d) only shows the texture of the crystalline V_2O_5 structure but not the atomic lattices. The EDS in Figure C.4 shows that the CNF-V_2O_5 core-shell material is dominated by C, O, N, and V elements. The N atoms are likely residue from the starting PAN precursors in electrospinning. Elemental mapping in Figures 4.2e-g and the line profiles in Figure C.5 confirm the uniform distribution of C, O and V elements in the core-shell nanofibers.

It is noteworthy that the observed uniform coaxial V_2O_5 coating on each CNFs throughout the membrane is highly desired for effective current collection. Due to the high density and heavy entanglement of the CNF membrane (as shown in Figures C.1c-d), V_2O_5 deposition is limited by mass transport. Materials opt to deposit much faster at the outer surface of the membrane in normal continuous electrodeposition at a constant potential or current, leading to capping the outer surface and insufficient deposition inside the CNF membrane. Such uneven deposition was avoided in this study by adopting a unique pulse electrodeposition method similar to our previous studies.[78, 320] Figures C.6a and C.6b show the experimental setup and a CV curve of the CNF membrane in the V_2O_5 sol solution. During electrodeposition, the electrode potential was first set at -2.0 V for 10 seconds (the "on" time) to deposit a sub-nanometer thick V_2O_5 layer throughout the CNF network. A longer "off" time of 20 seconds then followed, with the electrode potential at 0 V, which stopped V_2O_5 deposition and allowed fresh electrolyte to diffuse into the membrane and re-establish the concentration equilibrium. These two steps alternatively repeated 60 times to obtain the desired V_2O_5 quantity. The current profiles in Figures C.6c and C.6d indicate that the pulsed electrodeposition process is highly reproducible except the first few cycles. The quantity of V_2O_5 deposition can be controlled by varying the number of cycles. The schematic diagram in Figure

C.7 illustrates the effects on the deposition uniformity across the CNF membrane by the common constant voltage vs. the pulsed electrodeposition.

4.3.2 Materials characterization of the CNF-V_2O_5 core-shell structure

The Raman spectra of the CNF-V_2O_5 core-shell structure in Figure 4.3a shows the characteristic peaks of V_2O_5 (at 140, 282, 403, 513, 696, and 993 cm^{-1}) which match well with pure α-V_2O_5 nanopowders.[321] The peak at 990 cm^{-1} corresponds to the stretching mode of the vanadyl V=O double bond, which does not exist in the lower oxidation states of vanadium oxides. The stretching mode of V-O-V corresponds to the peak at 696 cm^{-1}. The peaks located at 513 and 403 cm^{-1} are assigned to the bending vibration of V_2-O and the V=O bonds of α-V_2O_5, respectively. The well-defined peak at 282 cm^{-1} corresponds to the bending vibration of V=O bonds of α-V_2O_5. The peak at 143 cm^{-1} corresponds to the long range external mode α-V_2O_5, suggesting pockets of long range order in the mostly disordered structure. These results suggest that the 4-hour annealed samples are dominated by the chemical bonds of V_2O_5,[322-323] even though the crystal structure was highly disordered (or amorphous). The peaks at 1351 and 1614 cm^{-1} correspond to the D and G bands of the CNF core. Clearly, both disordered sp^3 and graphitic sp^2 carbon present in the CNFs.

The XRD analysis of the 4-hour annealed CNF-V_2O_5 core-shell structure (blue) and 24-hour annealed hollow V_2O_5 shells (red) in Figure 4.3b show the dramatic effects of annealing time on the crystal structure. The CNF-V_2O_5 core-shell structure shows a very broad asymmetric peak which can be de-convoluted into a small peak at 17.15° and a large peak at 20.77°, respectively. The d-spacing values are 5.17 and 4.27 Å, respectively, corresponding to the interlayer distance of

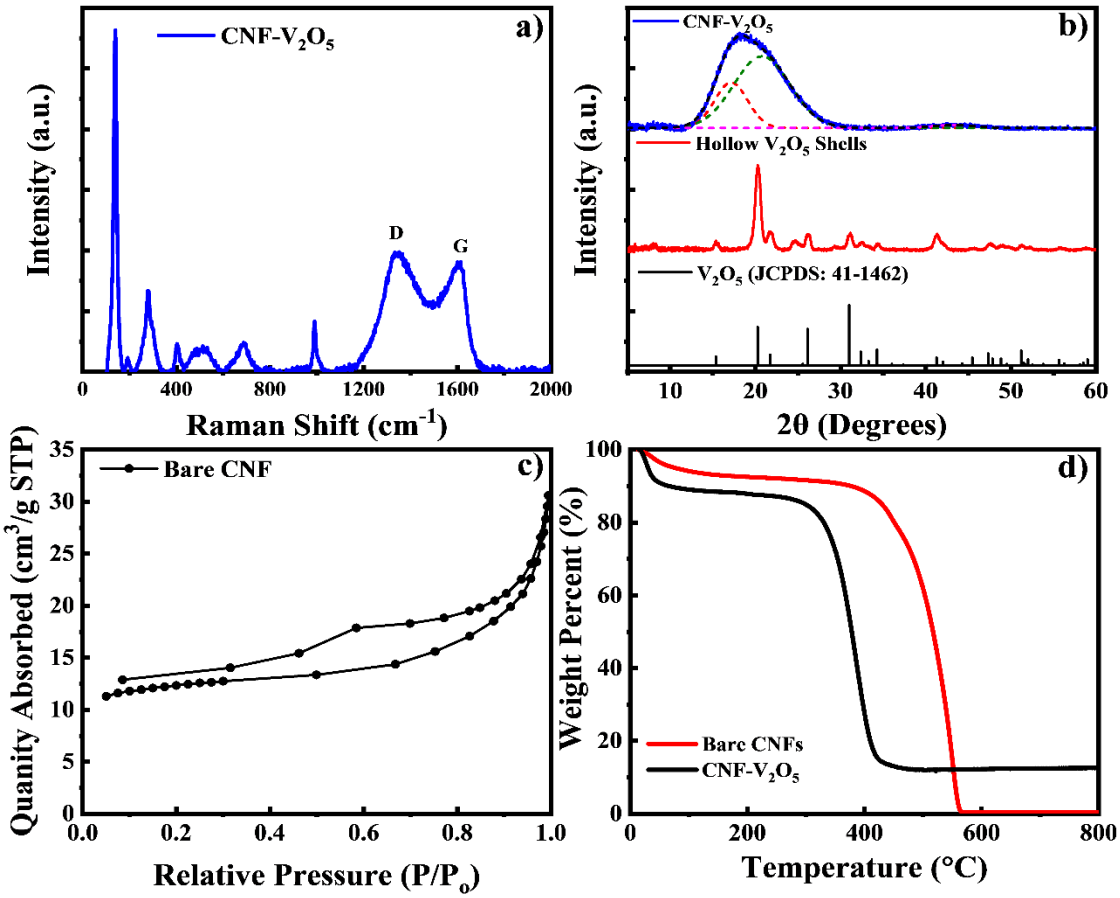

Figure 4.3 a) Raman spectrum of the CNF-V_2O_5 core-shell structure. b) XRD patterns of the CNF-V_2O_5 core-shell structure (blue) and hollow V_2O_5 shells (red). c) BET measurements of bare CNFs. d) TGA measurements of bare CNFs and the CNF-V_2O_5 core-shell material.

V_2O_5 shell and the disordered graphitic carbon core. The d-spacing of 5.17 Å is larger than the 4.37 Å inter-layer spacing of orthorhombic α-V_2O_5 crystals, which is likely due to the presence of a certain degree of hydration in V_2O_5.[324] The coherent length calculated from the de-convoluted XRD peak width is 1.96 nm (about a stack of only 5 V_2O_5 atomic layers), consistent with amorphous properties observed with SAED of TEM. It's worth noting that the d-spacing of CNF (4.27 Å) is significantly larger than that of graphite (3.43 Å), and in conjunction with a coherent length of only 1.16 nm (about a stack of ~4 carbon layers). The high degree of disorder is consistent with the Raman spectroscopy. A zoom-in plot of the deconvoluted XRD peak of the CNF-V_2O_5 core-shell structure is presented in Figure C.8. The weak peak at 2θ of 43.3° can be attributed to

the (002) peak of graphitic layers. In contrast, the hollow V_2O_5 shells after prolonged annealing show sharp diffraction peaks that can be attributed to the highly crystalline orthorhombic phase of α-V_2O_5, which is consistent with the pattern of JCPDS: 41-1426 database. It should be noted that a weak peak at 24.74° was observed after the prolong annealing, which is attributed to residual graphitized carbon with a smaller d-spacing of 3.60 Å.

The N_2 adsorption/desorption isotherm for the bare CNFs is shown in Figure 4.3c, indicating a mesoporous structure. The BET surface area was determined to be 38.5 $m^2 g^{-1}$. After V_2O_5 deposition, the BET isotherm showed similar features and a BET surface area of 42 $m^2 g^{-1}$, but the pore radius distribution shifted from the range of 2-8 nm to 6-12 nm (see Figure C.9). The small increase in surface area after V_2O_5 deposition is attributed to the porosity of the disordered V_2O_5 and outer surface roughness. The composition and thermal stability of the samples were investigated with TGA shown in Figure 4.3d, at a rate of 5 °C/min. For both bare CNFs and the CNF-V_2O_5 core-shell structure, a loss of 5% and 10%, respectively, was observed below 100 °C, due to desorption of physisorbed gas molecules (mostly water due to the high humidity in the environment). Such water sorption in the porous materials is unavoidable since the samples were stored and transported in the air prior to TG measurements. Bare CNFs started to be burnt at ~400 °C and were completely gone at ~560 °C. In contrast, the CNF-V_2O_5 core-shell structure started to lose the carbon materials near ~300 °C and the mass rapidly dropped to ~12 % at ~450 °C and then maintained stable at this value up to ~800 °C. As indicated by the SEM and TEM images in Figures 4.1 and 4.2, the main CNF core was retained for thermal annealing at ~300 °C for 4 hours while the quality of both CNF core and V_2O_5 shell is improved. The mass above 450 °C can be attributed entirely to crystalline V_2O_5. The shift in the initial carbon burning temperature can be attributed to the proximity oxygen source from metal oxides which are in direct contact with

carbon as well as possible catalysis by vanadium, which deserve further study in the future. The V_2O_5 percentage varied from ~10% to 30% in samples prepared in different days which were mainly due to slow drift of the reference electrode potential (by about 20 to 40 mV). Thus, all specific capacities in later LIB tests were calculated using the actual V_2O_5 mass determined by the TGA analyses of each sample

4.3.3 Assessment of 2 Li^+/V_2O_5 insertion/extraction between 4.0 – 2.0 V

The Li-ion storage properties of the above described CNF-V_2O_5 core-shell structure was systematically characterized in the half-cell configuration using CR2016 coin cells. An 18-mm diameter disk was punched out from the CNF-V_2O_5 membrane and glued onto an Al disk of the same diameter as the cathode (see Figure C.10). The as-assembled cell is in the charged state with a cell voltage in the range of 2.3 - 3.3 V. A galvanostatic discharge process was carried out first and followed by alternating charge/discharge measurements at different current rates at fixed potential windows. Columbic efficiency was calculated as the percentage ratio of the discharge (Li^+ insertion) capacity to the charge (Li^+ extraction) capacity in the prior step. Typically, C rates (rather than current densities) are used in literature for battery characterization. To avoid confusion, in this paper, all referred C rates are based on the actual time to complete a full charge or discharge process at the specific current density, with a rate of C/n corresponding to the condition to complete charge or discharge in n hours. For $n \leq 1$, an alternative notation (1/n)C is used for simplicity. To better assess the materials properties and compare them with the theoretical values, only the mass of V_2O_5 is used for calculating the gravimetric capacity in this study. The contribution of the CNF network to Li storage is negligible in the studied potential range.

The CNF-V_2O_5 core-shell structure was first investigated for 2 Li^+ insertion per V_2O_5 formula with galvanostatic charge-discharge measurements in the voltage range of 4.0 – 2.0 V (vs.

Li/Li$^+$) as shown in Figure 4.4a. Cells were discharge/charged for 25 cycles each at 5 different current densities (100, 250, 500, 750, and 1000 mA g^{-1}) before returning to the initial current rate (100 mA g^{-1}) at cycle 26. The first five cycles at 100 mA g^{-1} (~ C/3 rate) were unstable with an insertion capacity of 291 mAh g^{-1} and a coulombic efficiency of 94% at cycle 5. The insertion (discharge) capacity at this low rate matches well with the theoretical capacity of 294 mAh g^{-1} for 2 Li$^+$/V_2O_5 insertion process.[297] When the rate was increased to 250 mA g^{-1} (~1C rate), the cell was stabilized with an insertion capacity of 242 mAh g^{-1} and a higher coulombic efficiency to 97%. High insertion capacities of 217, 207, and 198 mAh g^{-1} were obtained at rates of 500 (2.3C), 750 (3.6C), and a 1000 (5.1C) mA g^{-1}, respectively. Interestingly, as the rate was increased to

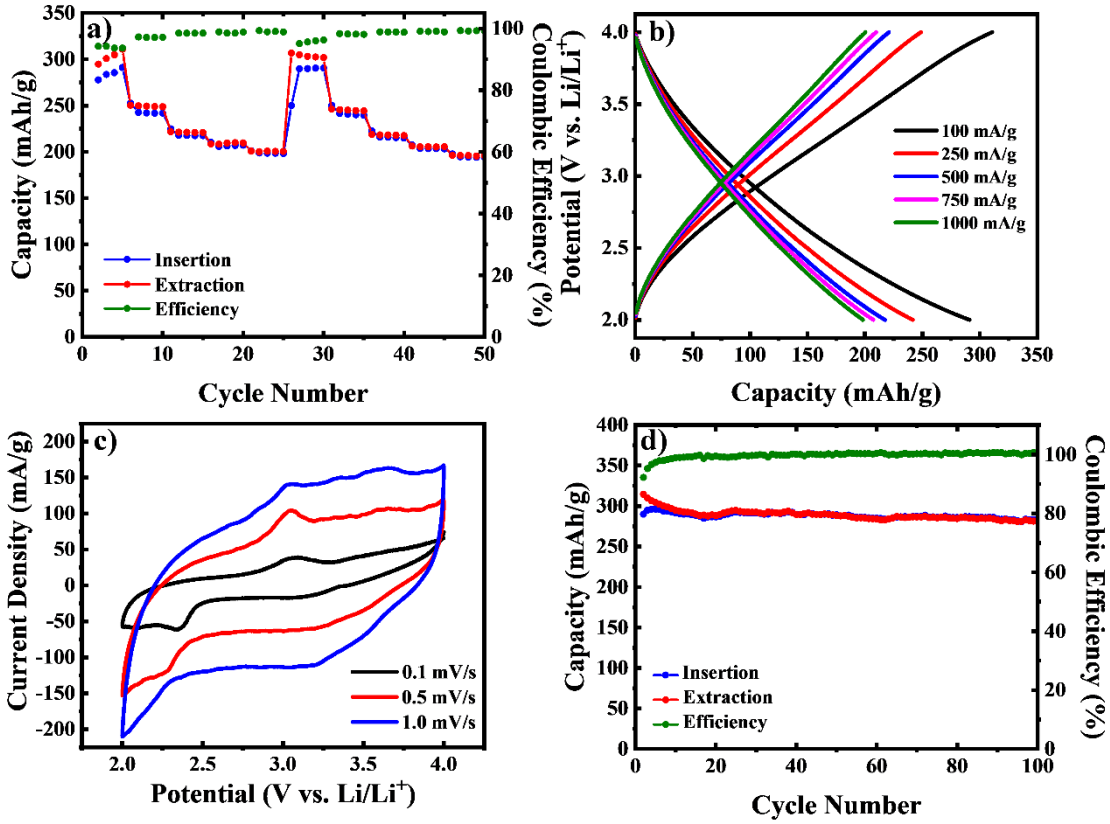

Figure 4.4 Electrochemical characterization of the 2 Li$^+$/V_2O_5 insertion/extraction. a) Rate performance of the CNF-V_2O_5 core-shell structure in the potential range of 4.0 – 2.0 V (vs Li/Li$^+$) at 5 different current density values (100, 250, 500, 750, and 1000 mA g^{-1}), each with 5 charge-discharge cycles. b) The galvanostatic charge-discharge profiles of the last cycle at each current density in the rate-performance tests. c) Cyclic voltammetry curves at 0.1 (black), 0.5 (red) and 1.0 (blue) mV s^{-1} in the potential range of 4.0 – 2.0 V (vs Li/Li$^+$). d) Long-term cycling at a rate of 100 mA g^{-1}.

1000 mA g^{-1}, the coulombic efficiency increased to ~99%. Generally, the coulombic efficiency decreases at higher current rates in literature. Here the coulombic efficiency increases with increasing current rates which can be attributed to the better current collecting capability and faster reaction kinetics with the core-shell structure. It is also likely that a high pseudocapacitance contribution aids in the high coulombic efficiency at the high rates. When the current was reduced back to 100 mA g^{-1} in cycles 26-30, a stable insertion capacity of 290 mAh g^{-1} was achieved, resulting in a capacity retention of ~99% comparing to cycle #5. Insertion capacities of 240, 215, 203, and 194 mAh g^{-1} were obtained at current rates of 250, 500, 750, and 1000 mA g^{-1}, respectively, in cycles 31-50. These values are all comparable to those in cycles 6-25 of the first set of rate-performance tests, demonstrating the high stability of the CNF-V_2O_5 core-shell structure. It is notable that the capacity only dropped by ~32% as the charge-discharge current was increased 10 times from 100 to 1000 mA g^{-1}.

A representative Nyquist plot of electrochemical impedance spectroscopy (EIS) measurements at the charged state (~4.0 V) was obtained after 5 cyclic voltammetry cycles (1 mV/s) as shown in Figure C.11. An equivalent series resistance of 53.33 Ohm (R_1) and a charge transfer resistance of 170.8 Ohm (R_3) was derived from the fitted circuit, which are a little bit high and expected for amorphous V_2O_5 materials. The capacitance value of the constant phase element (CPE, represented by Q_2) corresponding to the CNF-V_2O_5 electrode was derived to be only 4.6 μF, indicating a low EDLC contribution from the CNF framework. The R_3 value of 80.18 Ohm and the capacitance value 8.8 μF in the first CPE (Q1) are likely originated from the Li counter electrode. The cell performance likely can be further improved in the future by optimizing the electrical contact in the core-shell nanofiber membrane.

The galvanostatic charge-discharge curves of the last cycle at current rates of 100 (black), 250 (red), 500 (blue), 750 (magenta), and 1000 (green) mA g^{-1} in the rate-performance tests are presented in Figure 4.4b. All profiles show nearly linear curves without clear flat plateaus that are commonly seen for Li^+ insertion/extraction in crystalline V_2O_5, indicating that the system behaved like a pseudocapacitor. These properties explain the high stability and high coulombic efficiency at the high applied current rates. The high degree of pseudocapacitance contribution is also seen in the CV curves in Figure 4.4c. Only a small reduction peak was observed between 3.2 - 3.0 V corresponding to the crystalline phase transformation from α-V_2O_5 to ε-$Li_xV_2O_5$ ($0.35 < x < 0.7$) and δ-LiV_2O_5. The two reduction peaks commonly observed in crystalline V_2O_5[297] were superimposed in this study owing to the amorphous nature of V_2O_5. A larger reduction peak was observed at 2.3 V at a scan rate of 0.1 mV s^{-1} corresponding to the phase transformation from δ-LiV_2O_5 to γ-$Li_2V_2O_5$. During the extraction process, only a single oxidation peak was observed at 3.0 V corresponding to the phase transformation of γ-$Li_2V_2O_5$ back to δ-LiV_2O_5. Two small oxidation peaks followed at ~3.4 and 3.6 V corresponding to the phase transformation from δ-LiV_2O_5 to ε-$Li_xV_2O_5$ ($0.35 < x < 0.7$) and α-V_2O_5, respectively. Compared with the CVs of crystalline V_2O_5 materials, the CNF-V_2O_5 core-shell structure present a large baseline separation between the charge and discharge currents, reflecting the dominant pseudocapacitive properties associated with the amorphous V_2O_5 shells. Figure 4.4d further demonstrates the remarkable stability of the CNF-V_2O_5 core-shell structure in 100 charge/discharge cycles at 100 mA g^{-1} (~C/3 rate). A stable capacity of 292 mAh g^{-1} was obtained at cycle 10 which only slightly decreased to 282 mAh g^{-1} in cycle 100, resulting in a high capacity retention of 97%.

It is noteworthy that current LIBs are mainly focused on ordered crystalline materials due to ordered Li^+ ion pathways and well-defined redox reactions. Even though enhanced capacity was

obtained with disordered oxide materials[325] (including hydrated V_2O_5 [299, 326-327]), these materials are limited by the poor mechanical stability, low electrical conductivity and tortuous ion pathways. Using core-shell hybrid structures in which thin V_2O_5 shells coated on stable nanostructured carbon cores has been demonstrated as an effective approach to overcoming these issues.[231] Particularly, we have previously demonstrated that partially hydrated amorphous V_2O_5 shells deposited on vertically aligned carbon nanofiber (VACNF) arrays provided over 30% higher capacity than crystalline V_2O_5 shells in highly stable 2 Li^+/V_2O_5 processes.[317] The results of the electrospun CNF-V_2O_5 core-shell structure in this study further validate the effectiveness of the core-shell hybrid approach. Furthermore, electrospinning is a potentially scalable technique which can be adapted for future LIB production.

4.3.4 Assessment of 3 Li^+/V_2O_5 insertion/extraction between 4.0 – 1.5 V

To explore the potential for even higher capacity, we further investigated the 3 Li^+/V_2O_5 insertion/extraction properties by lowering the low voltage limit to 1.5 V (vs. Li/Li^+). Similar to the earlier study, cells were discharged/charged for 5 cycles each at 5 different current densities (100, 250, 500, 750, and 1000 mA g^{-1}) before returning to the initial current rate (100 mA g^{-1}) at cycle 26 to repeat the sequence. The galvanostatic charge-discharge rate performance is summarized in Figure 4.5a. Similar to the 2 Li^+/V_2O_5 insertion/extraction performance, the first five cycles at 100 mA g^{-1} (C/4.3) were somewhat unstable with an insertion capacity of 429 mAh g^{-1} and a coulombic efficiency of 103% in cycle 5. The capacity is close to the theoretical capacity of 441 mAh g^{-1} for 3 Li^+/V_2O_5 insertion/extraction in crystalline V_2O_5. When the rate was increased to 250 mA g^{-1} (C/1.4), the cell was stabilized with an insertion capacity of 338 mAh g^{-1}

and a coulombic efficiency of 100%. High insertion capacities of 280, 250, and 236 mAh g^{-1} were obtained at rates of 500 (1.8C), 750 (3.0C), and a 1000 (4.2C) mA g^{-1}, respectively, with coulombic

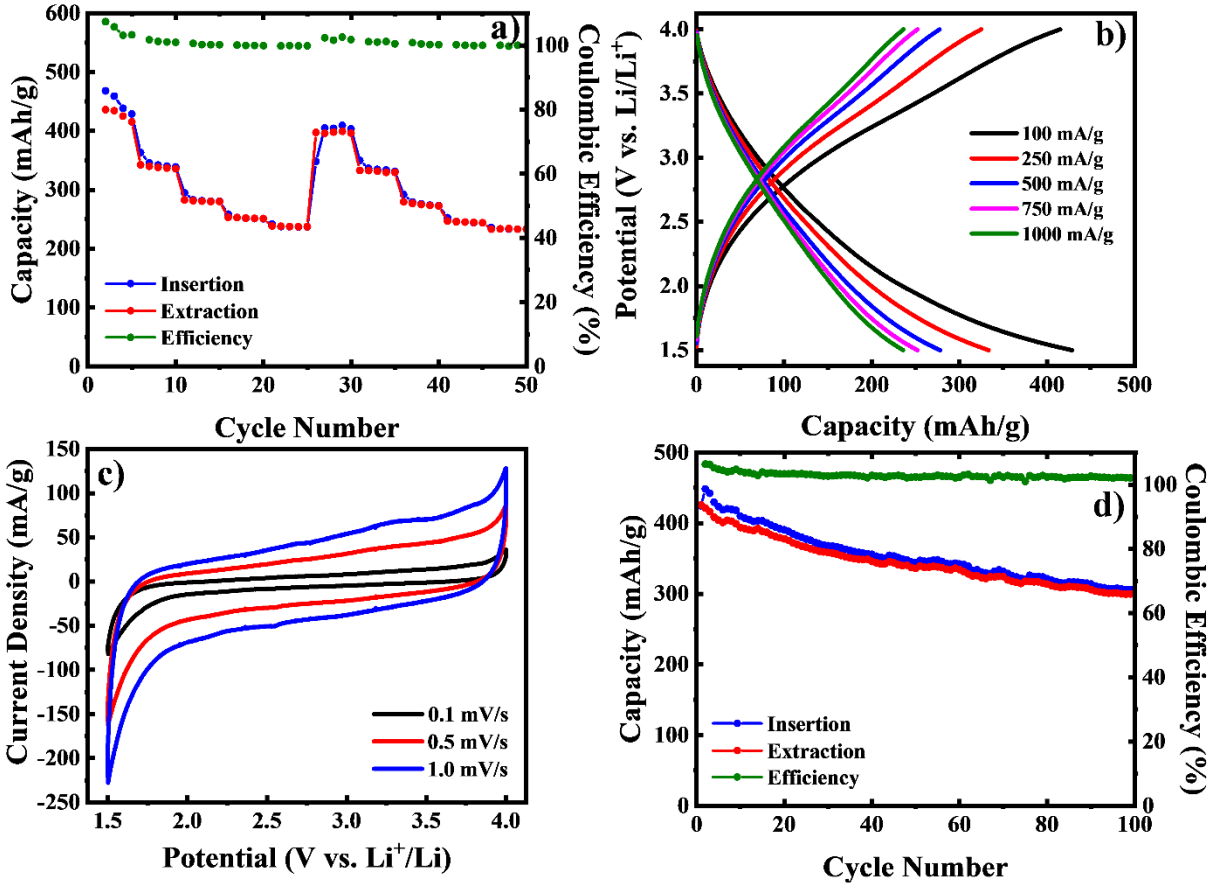

Figure 4.5 Electrochemical characterization of the 3 Li^+/V_2O_5 insertion/extraction. a) Rate performance of the CNF-V_2O_5 core-shell structure in the potential range of 4.0 – 1.5 V (vs Li/Li^+) at 5 different current density values (100, 250, 500, 750, and 1000 mA g^{-1}), each with 5 charge-discharge cycles. b) The galvanostatic charge-discharge profiles of the last cycle at each current density in the rate performance. c) Cyclic voltammetry curves at 0.1 (black), 0.5 (red) and 1.0 (blue) mV s^{-1} in the potential range of 4.0 – 1.5 V (vs Li/Li^+). d) Long-term cycling at a rate of 100 mA g^{-1}.

efficiencies of ~100%. When the current was returned to 100 mA g^{-1} in cycle 26-30, an insertion capacity of 405 mAh g^{-1} was achieved. Comparing to cycle #5, the capacity retention was ~94%. Insertion capacities of 330, 273, 244, and 233 mAh g^{-1} were obtained at current rates of 250, 500, 750, and 1000 mA g^{-1}, respectively, in cycles 31-50, retaining ~98% of the corresponding capacities in cycle 6-25.

Charge-discharge curves at current rates of 100 (black), 250 (red), 500 (blue), 750 (magenta), and 1000 (green) mA g^{-1} are presented in Figure 4.5b. All profiles retain the nearly linear feature as those in the 2 Li^+/V_2O_5 insertion/extraction processes. The shape of the charge-discharge curves is consistent with those of rGO/V_2O_5-$LiBO_2$ glass composite materials in the same potential range [301]. The stabilized CV curves in Figure 4.5c show nearly ideal pseudocapacitive features with flat baselines and a large separation between the forward and backward scans. In addition, the first negative scan in Figure C.12 showed similar CV features as Figure 4.4c, with a large reduction peak at ~2.3 V corresponding to the phase transformation from α-LiV_2O_5 to γ-$Li_2V_2O_5$ with the intermediate phase superimposed. A further downward dip was observed at 1.5 V corresponding to the phase transformation from γ- $Li_2V_2O_5$ to rock-salt-type ω-$Li_xV_2O_5$ ($2 < x < 3$). However, the oxidation peaks in the reversed positive scan overlapped into a broad wave spreading from 2.0 to 3.5 V. Both the large reduction peak at 2.3 V and the broad oxidation wave disappeared in the 2nd cycle (red), showing only the smooth capacitive features. This behavior is consistent with literature [297], showing that the transformation into the rock-salt structure by 3 Li^+/V_2O_5 insertion irreversibly damages the crystal structure and converts it into a fully amorphous structure. Notably, the CV curves after the 1st cycle became stabilized. Both Figures 4.5c and 4.5d indicate that Li storage is dominated by the large pseudocapacitance. Figure 4.5d demonstrates that a decent stability can be obtained with this mechanism in long cycling at 100 mA g^{-1}. The capacity slowly dropped from 442 mAh g^{-1} in cycle 3 to 310 mAh g^{-1} in cycle 100, retaining 70% of the original value. The results in Figure 4.5c is a great leap from the extensive studies seeking using crystalline V_2O_5 materials for 3 Li^+/V_2O_5 processes [297]. It is attributed to the novel properties of the CNF-V_2O_5 core-shell hybrid structure. The scalable

capability of electrospinning and electrodeposition may provide a viable method to push the core-shell concept involving amorphous V_2O_5 materials [231, 317] closer to LIB applications.

4.3.5 Discussion on the novel properties of amorphous V_2O_5 cathodes

Table C.1 and Table C.2 compare the performance of the CNF-V_2O_5 core-shell structure in 2 Li^+/V_2O_5 and 3 Li^+/V_2O_5 insertion/extraction, respectively, with an extensive list of studies in literature. For 2 Li^+/V_2O_5 insertion/extraction, the CNF-V_2O_5 core-shell structure is among the top judging by both the specific capacity and current density (or C rates). For 3 Li^+/V_2O_5 insertion/extraction, the advantages of CNF-V_2O_5 core-shell structure in specific capacity and current density (or C rates) is more evident. In addition, the improved stability and the potential for scalable production of the CNF-V_2O_5 core-shell structure by electrospinning and pulsed electrodeposition make it attractive for future LIB developments.

So far extensive efforts are being made to attain the high capacity at high power rates by improving ion diffusion using nanostructured V_2O_5 materials, particularly 2D nanosheets [300]. Interestingly, the rate-performance curves of the 2 Li^+/V_2O_5 process (Figure 4.4a) and 3 Li^+/V_2O_5 process (Figure 4.5a) in this study show a common phenomenon, i.e. a high specific capacity was retained at a relatively high current density of 1,000 mA g^{-1}, which is not obtainable with traditional micron-sized V_2O_5 materials. As demonstrated in a study by Rui et al [328], the rate-performance curve of few-layer V_2O_5 nanosheets (2.1-3.8 nm thick) shift upward by ~100 mAh g^{-1} comparing to that of bulk V_2O_5 crystals (1-4 μm in size). Here we have obtained a stable high capacity of 198 mAh g^{-1} at a high rate of 1,000 mA g^{-1} (~5C) for 2 Li^+/V_2O_5 process, comparable to the reports with few-layer V_2O_5 nanosheets[328] and V_2O_5 nanoparticles anchored on CNTs.[329] More importantly, we were able to obtain a relatively stable high capacity of 236 mAh g^{-1} at the high rate of 1,000 mA g^{-1} (~4C) for the 3 Li^+/V_2O_5 process, which have not been obtained with

nanostructured V_2O_5 alone. In our previous study using the hybrid structure of V_2O_5 shells on vertically aligned carbon nanofiber cores,[317] we have observed that the rate-performance curve of the amorphous V_2O_5 shells shift up by ~60 mAh g^{-1} in 2 Li^+/V_2O_5 process and by ~150 mAh g^{-1} in 3 Li^+/V_2O_5 process comparing to the crystalline V_2O_5 shells. Those observations are consistent with the results in this study, which demonstrate that the core-shell hybrid structure is effective to facilitate the high-capacity and high-power capability of amorphous V_2O_5 materials. It is particularly attractive for future batteries involving larger ions such as Na^+ or polyvalent ions such as Mg^{2+}, which may benefit from the more open structure of amorphous V_2O_5 materials.

4.4 Conclusion

In summary, self-sustained CNF membranes fabricated by carbonizing electrospun PAN nanofibers were used as 3D porous LIB electrodes. A thin V_2O_5 layer was coated onto the CNFs using a pulsed electrodeposition from a V_2O_5 sol solution. SEM, HRTEM and XRD analysis confirmed that the CNF-V_2O_5 core-shell structure consisted of a uniform coaxial V_2O_5 layer on the continuous CNF core throughout the whole membrane. After 4 hours of thermal annealing at 300 °C in the air, the V_2O_5 shell presents as a partially hydrated amorphous material. Electrochemical characterization in the potential range of 4.0 – 2.0 V (vs Li/Li^+) revealed that the V_2O_5 shell in this core-shell structure present reversible 2 Li^+/V_2O_5 insertion/extraction with a near theoretical capacity of 291 mAh g^{-1} and excellent stability even at high rates. There was nearly no capacity fading after 100 cycles. Moreover, when the potential range was extended to 4.0 – 1.5 V (vs Li/Li^+), a high capacity of 429 mAh g^{-1} was obtained corresponding to reversible 3 Li^+/V_2O_5 insertion/extraction. A relatively high capacity retention of 70% was obtained after 100 cycles. These results demonstrated that the CNF-V_2O_5 core-shell structure is an effective approach to

breaking the intrinsic limits of crystalline V_2O_5 and enabling amorphous V_2O_5 materials to be used as a promising scalable high-capacity LIB cathode.

4.5 Acknowledgments

We would like to thank Jacob Hughes at Kansas State University (KSU) for the Raman Spectroscopy analysis, Shah Valloppilly at the University of Nebraska Center for Materials and Nanoscience (NCMN) for XRD analysis, Steve Michalski at NCMN for BET measurements, Xingzhang Li and Anand Sarella at NCMN for TEM imaging, and Dan Boyle of KSU for helping with SEM imaging. We would also like to give a special thanks to Manomi Perera, Chamara Gunawardana, and Christer Aakeröy of KSU for their help in the TGA analysis and Dr. Changsang Yun of Seoul National University for assistance in electrospinning nanofibers. This work was supported by a NASA grant NNX13AD42A and NSF grants CBET-1703263 and DMR 1707585.

Chapter 5 - Highly Stable Three Lithium Insertion in Thin V_2O_5 Shells on Vertically Aligned Carbon Nanofiber Array for Ultrahigh-Capacity Lithium Ion Battery Cathodes

5.1 Introduction

Advanced EES systems are becoming increasingly important in supporting energy conversion systems utilizing intermittent renewable sources such as wind and solar energy[2], powering hybrid and electric cars[289], and enhancing the performance of today's portable electronics.[290] LIBs currently dominate the EES market owing to their high-energy storage capabilities.[290, 330] Despite of this success, the LIBs' specific capacity and power rates still need to be raised to meet the increasing demands. Particularly, the low specific capacity of cathode materials is currently the key factor limiting the energy storage capability of LIBs.[292] For example, in the most common commercial LIBs, a near theoretical specific capacity of 372 mAh g^{-1} can be achieved with the graphite anode while only ~ 140 mAh g^{-1} specific capacity with $LiCoO_2$ cathode.[292] Hence, the current LIB research has put an extensive emphasis on improving the charge storage capacity and power delivery capability of the cathode materials.[295-296]

V_2O_5 is regarded as a promising cathode material owing to its high theoretical capacity due to multiple Li^+ insertion/extraction reactions in addition to the low cost, nontoxic chemical properties, high electrode potential in lithium-extracted state (up to 4.0 V) and easily accessible layered structure for Li^+ ion insertion.[124] Theoretically, crystalline V_2O_5 can achieve a reversible specific capacity of 294 mAh g^{-1} (for a two Li^+/V_2O_5 insertion process) and an irreversible capacity of 441 mAh g^{-1} (for a three Li^+/V_2O_5 insertion process),[125] which are significantly higher than today's commercial cathode materials such as $LiCoO_2$ (140 mAh g^{-1}), $LiMn_2O_4$ (148 mAh g^{-1}) and

$LiFePO_4$ (170 mAh g^{-1})[298] that are limited to only one Li^+ insertion/extraction. A few reports have even suggested that amorphous V_2O_5 in supercritically dried xerogels and aerogels can achieve extremely high capacities up to 560 and 650 mAh g^{-1}, respectively (equivalent to 4 and 5.8 Li^+ insertion/extraction per V_2O_5), owing to their highly porous network, high surface area, and short Li^+ diffusion paths.[218, 326] Unfortunately, these materials suffer from poor mechanical/chemical stability and rapid capacity fading, making realizing the predicted high capacity in practical LIBs difficult.

Achieving reliable capacity with V_2O_5 cathodes close to the theoretical value has been a challenge due to the small Li^+ ion diffusion coefficients (~10^{-15} – 10^{-12} cm^2s^{-1}) and low electrical conductivities (~10^{-3} – 10^{-5} S cm^{-1}) in this material, which ultimately hinder the performance of V_2O_5 cathodes in practical EES devices.[126-127] Also, it is well known that the Li^+ intercalation process in crystalline V_2O_5 is accompanied by multiple phase transitions. Trace amounts of Li^+ intercalation results in α-$Li_xV_2O_5$ ($x < 0.01$) structure, which is transformed into ε-$Li_xV_2O_5$ ($0.35 < x < 0.7$) after further lithiation. Insertion of exactly one Li^+ leads to the formation of δ-phase $Li_xV_2O_5$ ($x = 1$). Further lithiation converts the δ-phase to γ-$Li_xV_2O_5$ ($1 < x < 2$). At more than two Li^+ insertions, an irreversible transformation to rock-salt-type ω-$Li_xV_2O_5$ phase ($2 < x < 3$) typically occurs.[128] Such phase transition processes induce large lattice strains due to different crystal structures and lattice constants in distinct phases mixed within each single particle, which unavoidably causes irreversible structural damage resulting in poor battery life.[67] The larger amount of Li insertion by 3 Li^+/V_2O_5 insertion makes such structural changes even more severe. As a result, practical applications of traditional crystalline V_2O_5 cathodes have been limited to below two Li^+/V_2O_5 insertion/extraction processes.

Two strategies have so far been employed to overcome these intrinsic limitations. The first one is to overcome the low Li^+ ion diffusion coefficients through synthesis of low-dimensional nanostructures such as nanorods,[331] nanofibers,[332] nanoribbons,[333] nanobelts,[334] nanowires,[335] nanosheets,[336] nano/microspheres,[128, 337-339] nanoflowers,[340] and 3D porous nanosheets assembly.[341-343] This strategy increases the overall SSA and provides short diffusion pathways for Li^+ ions, which in turn offers more electrochemically active sites for enhanced LIB performance. Low-dimensional nanostructures can also partially relieve the large lattice strain during the phase transition processes and significantly extend the battery life. However, the poor electrical contact between nanoscale V_2O_5 nanoparticles becomes a dominant factor that limits the power rate capabilities. Moreover, the low surface energy of V_2O_5 often leads to aggregation of the nanostructures, resulting in capacity fading and ultimately structural collapse. The second strategy (combined with the first strategy) is to incorporate low dimensional conductive carbon materials such as MWCNTs,[226, 308-309] graphene,[126, 312, 344] and rGO[67, 219, 313-315] to form composite materials. The addition of these conductive additives prevents aggregation and enhances the electrical conductivity throughout the electrode material. However, the poor electrical contact at the interface of the V_2O_5 nanoparticles and carbon additives still limits these materials to reach higher power rates required for many practical applications.

Coating thin V_2O_5 shells on continuous three-dimensional (3D) conductive frameworks was found to be an effective approach to resolving the above issues for higher lithium storage capacity. The concept has been demonstrated with ultrathin V_2O_5 coatings by electrochemical deposition on a vertically aligned Ni nanorod array[345] and a vertically aligned carbon nanotube array,[346] and by atomic layer deposition (ALD) on a 3D MWCNT sponge network.[231] Stable 2 Li^+/V_2O_5 insertion/extraction in the voltage range of 4.0 – 2.1 V (vs. Li/Li^+) has been

demonstrated, with only < 0.1% decay per cycle over 100 charge-discharge cycles.[231] More importantly, high-capacity 3 Li^+/V_2O_5 insertion/extraction was achieved in the initial 20 cycles when the voltage range was expanded to 4.0 – 1.5 V, though the capacity dropped by 49% after 100 cycles.[231] However, the very thin V_2O_5 coatings (≤10 nm) in these hybrid structures made it difficult to accurately assess the small V_2O_5 mass. Thus, it was difficult to accurately assess the gravimetric capacities and correlate them with the theoretical values at different stages of the multi-Li^+ insertion/extraction processes. Further studies are needed to explore better core-shell structures that can stabilize V_2O_5 during deep Li^+ insertion for practical high-capacity V_2O_5 cathodes.

Here, we report a study using V_2O_5 shells sputter-coated on vertically aligned carbon nanofibers (VACNFs) with an aim to address on the above-discussed issues. VACNFs can be described as a robust brush-like array of high-aspect-ratio carbon nanofibers (~50 - 150 nm in diameter and 3 – 10 μm in length) consisting of conically stacked graphitic structures.[233] They offer a distinctive advantage over other carbon allotropes owing to their abundancy of graphitic edges along the sidewall, which provide an excellent electrochemical interface leading to strong interactions with shell materials. Previously we have reported the ability to obtain over 3,200 mAh g^{-1} capacity with remarkable power rates and cycling stability using silicon shells of the radial thickness up to ~ 200 nm on VACNF cores as a LIB anode material.[150-151] Here, a similar 3D core-shell architecture was prepared by radio frequency (RF) sputtering of thick V_2O_5 shells (up to ~100 nm radial thickness) on VACNFs, which was investigated as a LIB cathode material both with and without thermal annealing. The annealed sample consisting of nanocrystalline V_2O_5 shell has illustrated the full theoretical capacity of 2 Li^+/V_2O_5 insertion/extraction (~294 mAh g^{-1}, relative to V_2O_5 mass) in the voltage range of 4.0 – 2.0 V and is able to retain 100% capacity after 100 cycles. In deeper discharging to 1.5 V, the annealed sample delivers ~390 mAh g^{-1} in the initial

cycles, about 88.4% of the full 3 Li^+/V_2O_5 insertion/extraction capacity, and shows only ~12% fading after 100 cycles at 0.20 A g^{-1} (C/2) rate. In contrast, the as-deposited sample with disordered V_2O_5 shells provides a capacity of ~547 mAh g^{-1} at 4.0 – 1.5 V, equivalent to 3.7 Li^+/V_2O_5 insertion/extraction, and is able to retain ~84% of the initial capacity after 100 cycles. To our knowledge, the VACNF-V_2O_5 core-shell structure at deep discharge in 4.0 – 1.5 V shows the highest stabilities and capacity retentions for a 3 (and more) Li^+/V_2O_5 insertion/extraction process reported to date.[126, 301, 333, 347] These results confirmed the recent finding that disordered oxides may be able provide excess lithium storage beyond the theoretical stoichiometric limit due to sublattice intermixing of Li/metal cations and formation of a percolation network.[325] The core-shell structure in this study provides a potential strategy to overcome the drawback of low electrical conductivity in amorphous V_2O_5. This concept is highly promising for developing stable nonconventional high-capacity cathode materials for LIB and future sodium-ion batteries

5.2 Experimental Details

5.2.1 VACNF Array Growth

Graphite sheets (0.4 mm thick; Fiber Materials Inc., USA) were coated with 30 nm nickel films using a high-vacuum Perkin Elmer 4400 series magnetron sputtering system at UHV Sputtering Inc. (Morgan Hill, CA). VACNFs with an average length of ~5 μm were grown on the 20-nm Ni coated graphite disks of 17.5 mm in diameter using a DC-biased PECVD system (AIXTRON, CA) following a previously published procedure.[150-151, 233-234] A pre-treatment procedure was applied first by thermally heating the Ni/graphite substrate to 500 °C in 250 sccm NH_3 at a pressure of 3.9 Torr and then applying plasma at 40 Watts for 30 seconds. The combined effects of thermal dewetting and NH_3 plasma etching broke the Ni film into randomly distributed nanoparticles that catalyzed the growth of VACNFs in a tip growth mode.[233-234] The diameter and

distribution of the VACNFs were mostly determined by these Ni nanoparticles. After pre-treatment, a mixture of acetylene (at 63 sccm) and ammonia (at 250 sccm) was used as the precursors for VACNF growth at substrate temperature of 750 °C and a pressure of 4.6 Torr. The plasma power was kept at 45 Watts for 30 minutes to grow the ~5.0 μm long VACNFs.[151]

5.2.2 V_2O_5 Deposition

V_2O_5 was deposited on the VACNFs using RF sputtering of a high purity (99.99%) V_2O_5 target of 50 mm in diameter. The V_2O_5 target was kept at a distance of 30 mm from the VACNF substrate maintained at room temperature during the deposition. The sputtering gun was inclined toward the V_2O_5 target at a 45° angle for optimal deposition. The processing chamber was evacuated to 3×10^{-6} Torr prior to deposition. During deposition, a power of 150 W was applied to the sputtering gun at a working pressure of 10 mTorr (92% Ar + 8% O_2 by volume). A ten-minute pre-sputtering was applied in order to obtain a fresh V_2O_5 surface. After a 120-minute deposition, the amount of V_2O_5 deposited onto the VACNF substrate was found to be equivalent to a uniform film thickness of 425 nm on a flat surface, i.e. a nominal thickness of 425 nm. This was confirmed by repeating the sputtering deposition on a polished Si substrate in place to the VACNF substrate. Following deposition, the substrate was allowed to cool for at least 30 minutes prior to removal from the chamber. Some VACNF-V_2O_5 core-shell structures were subjected to post-growth annealing in air at 450 °C for two hours, which facilitated crystallization of the V_2O_5 shells on the VACNFs. A schematic of the fiber growth and deposition process is illustrated in Figure D.1a. Digital images of the core-shell structure at various processing steps are shown in Figures D.1b-e.

5.2.3 Materials Characterization

The surface morphology of the VACNF-V_2O_5 core-shell structures were investigated using a Versa 3D Dual Beam (FEI, Hillsborro, OR) field emission scanning electron microscope (SEM).

The microstructure of the sample was examined using a Tecnai F20 XT (FEI, Hillsborro, OR) high resolution transmission electron microscope (HRTEM). Elemental analysis was carried out using the energy dispersive X-ray spectroscopy (EDS) in the SEM. In conjunction with SEM. The crystallinity was evaluated using a PANalytical Empyrean (PANalytical, Almelo, The Netherlands) x-ray diffractometer (XRD). Diffraction analysis was conducted from 10° to 60° using a Cu source. Raman spectra were obtained using a Thermo Scientific DXR system at a laser wavelength of 532 nm. X-ray photoelectron spectroscopy (XPS) spectra were obtained using a PHI 5000 Versa system with a monochromated Al K_α (1486.7 eV) source to further evaluate the valance state of the vanadium oxide near the surface.

5.2.4 Electrochemical Characterization

To evaluate electrochemical performance of the VACNF-V_2O_5 cathode, half-cells were assembled into stainless steel coin cells (CR2032, MTI Corporation, Richmond, CA). The VACNF-V_2O_5 core-shell structures were used as working electrodes against a 16-mm dia. lithium disk counter electrode which were separated by a 0.65 mm thick glass fiber separator (El-Cell, Hamburg, Germany). The cell was assembled in an argon filled M-Braun LabStar50 stainless steel glovebox (Garching, Germany). The electrolyte consisted of 1.0 M lithium hexaflourophosphate ($LiPF_6$) in a mixture of 1:1:1 volume ratio ethylene carbonate (EC), ethyl methyl carbonate (EMC), and dimethyl carbonate (DMC) with a 2% vinylene carbonate additive (Novolyte, Ohio). Galvanostatic charge-discharge cycles were performed using a MTI 8 channel battery analyzer (MTI Corporation, Richmond CA). All gravimetric capacities were calculated relative to the mass of V_2O_5. Cyclic voltammetry (CV) measurements were performed using an Ivium-n-Stat (Ivium Technologies, Eindhoven, The Netherlands) and a CHI760D potentiostat. (CH Instruments, Austin, TX).

5.3 Results and Discussion

5.3.1 SEM/TEM Characterization of Materials Morphology

The SEM image of the as-deposited VACNF-V_2O_5 core-shell structure in Figure 5.1a shows uniform coaxial V_2O_5 coating along the VACNFs. A high-magnification SEM image in Figures 5.1b and D.2a-b shows a rough texture extending across the shell surface with a distinctive feature of the nanocolumn-like microstructure (as detailed further later) that commonly formed in thick sputtered films. A morphology change occurred after annealing resulting in clustering of the core-shell structures (Figure 5.1c). The nanocolumnar V_2O_5 shells appear to be converted into non-uniform nanoparticles as indicated in Figure 5.1d. These changes are consistent over the entire sample, as further illustrated in Figures D.2c-d.

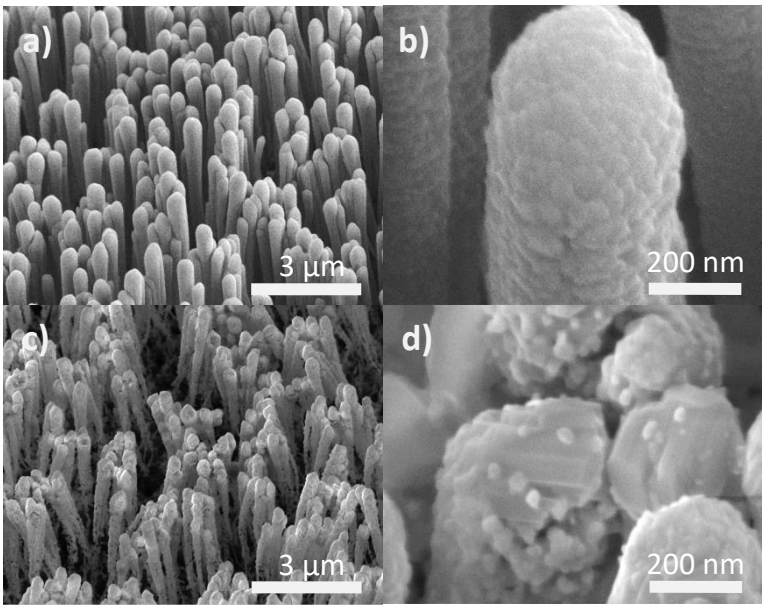

Figure 5.1 Low-magnification a) and high-magnification b) SEM images of the as-deposited VACNF-V_2O_5 core-shell structures. Low-magnification c) and high-magnification d) SEM images of the annealed VACNF-V_2O_5 core-shell structures. (Reprinted with permission from Adv. Mater. Interfaces 2016, 3, 1600824)

A TEM image of the as-deposited V_2O_5 on a single CNF is shown in Figure 5.2a. A thick coating can be seen at the top of the sample which tappers off down the nanofiber forming a cotton

swab like structure. This phenomenon can be described as a snow fall effect which is a common theme in sputtering deposition on non-flat surfaces. The dark tear shaped region in the center is the nickel catalyst embedded in the tip of the VACNFs. About 425 nm thick V_2O_5 film can be seen directly above the Ni catalyst tip. The VACNF shaft is embedded in the V_2O_5 as the light gray column below the Ni catalyst particle, whose contour is visually highlighted with the white dashed lines. The nanocolumnar structure of the V_2O_5 shell can be seen along the shaft of the nanofiber, forming a secondary brush-like structure which is anchored at an oblique angle of ~40° from the tip direction. This type of structure follows the Thornton's Structural Zone Model which is common when the substrate temperature is held well below the melting point of the depositing material during deposition which is 690 °C for V_2O_5.[151, 348] This model predicts that at such conditions the deposited shell material tends to form arrays of vertical nanocolumns separated by voids or low-density boundaries but strongly anchored on the surface of VACNFs, forming a well-defined porous shell. Moreover, the layered graphitic edges at the VACNF sidewall may further facilitate the growth of such nanocolumns. This type of structure can enhance the electrochemical performance of V_2O_5 by providing short Li^+ diffusion paths in solid V_2O_5 and maximizing diffusion through liquid electrolytes penetrating into the voids similar to the highly porous network in aerogel materials.

Figures D.3a-b further reveal that the nanocolumnar structure in the as-deposited V_2O_5 shell is uniform along the shaft of the fiber. The high-magnification TEM image in Figure 5.2b reveals that the V_2O_5 is a highly porous amorphous structure, which is further confirmed by the selective area electron diffraction (SAED) pattern in the insert of Figure 5.2b. Upon thermal

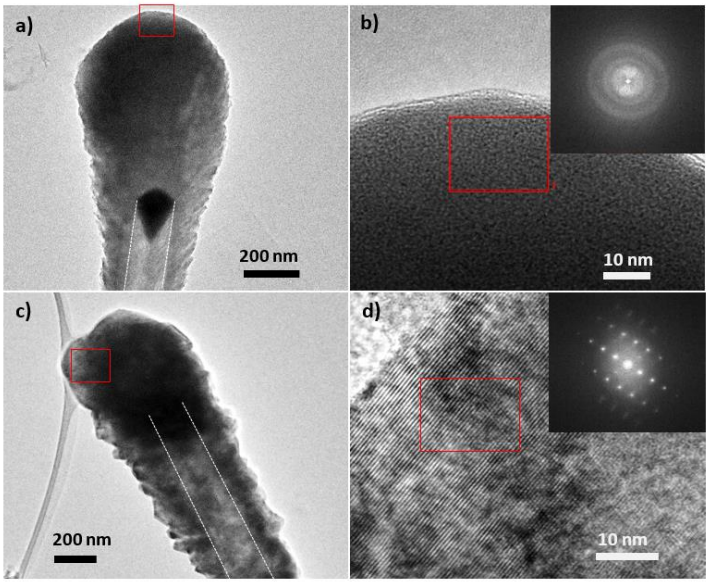

Figure 5.2 Low-magnification a) and high-magnification b) TEM images of the as-deposited VACNF-V_2O_5 core-shell structures. Low-magnification c) and high-magnification d) TEM images of the annealed VACNF-V_2O_5 core-shell structures. The white dashed lines have been inserted to indicate the contour of the VACNF surface. SAED patterns are presented in the insert of b) and d) for the as-deposited and annealed, respectively. (Reprinted with permission from Adv. Mater. Interfaces 2016, 3, 1600824)

annealing, the nanocolumnar V_2O_5 structure is converted into denser nanocrystalline domains of ~ 50 to 100 nm in size, as illustrated in Figure 5.2c. The annealed core-shell structure tends to cluster into small bundles as revealed by SEM image (Figure 5.1c) and TEM images (Figures D.3c-d). The HRTEM image in Figure 5.2d shows the highly ordered crystalline lattices of the annealed V_2O_5 with sharp diffraction spots in the SAED pattern. The nature of the thermal annealing processes will be discussed later with supports from spectroscopic data.

5.3.2 Spectroscopy Characterization of Materials Composition

EDS maps in Figure D.4 show that both the as-deposited and annealed structures consist of primarily vanadium oxides. Carbon and nickel peaks originating from the VACNFs and the catalyst, respectively, are also present. XRD patterns of the sputtered V_2O_5 films are presented in Figure 5.3a. To avoid the high background from the graphite substrate (to be used in LIB tests), the XRD study used V_2O_5 films directly deposited on a polished silicon substrate, which were

annealed in the same conditions as for the VACNF-based samples. The as-deposited film shows only a single peak at ~33° which is attributed to silicon, indicating that the as-deposited V_2O_5 film is likely an amorphous structure. In contrast, the annealed film shows sharp diffraction peaks that can be attributed to the highly crystalline orthorhombic phase of V_2O_5 and is consistent with the JCPDS: 41-1426 database.

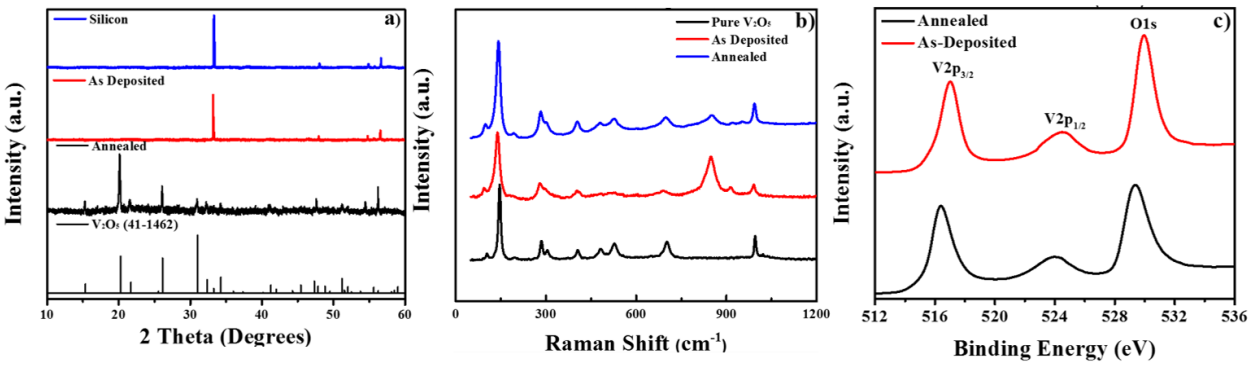

Figure 5.3 XRD patterns a) of as-deposited and annealed V_2O_5 films on a silicon chip. Raman spectra b) of the as-deposited and annealed core-shell structures grown on graphite paper (to be used for LIB tests) compared with pure V_2O_5 powder. High-resolution XPS spectra c) of the as-deposited and annealed structures on graphite paper at binding energies of $V2p_{1/2}$, $V2p_{3/2}$, and O1s. (Reprinted with permission from Adv. Mater. Interfaces 2016, 3, 1600824)

The Raman spectra of the as-deposited and annealed V_2O_5 samples are shown in Figure 5.3b. The typical peaks of V_2O_5 (146, 283, 304, 405, 475, 524, 685, and 993 cm^{-1}) are observed in both spectra and match well with pure V_2O_5 nanopowder.[321] The peak at 993 cm^{-1} is characteristic of α-V_2O_5 corresponding to the stretching mode of the vanadyl V=O double bond, which does not exist in the lower oxidation states of vanadium oxides. The peaks located at 475 and 405 cm^{-1} are assigned to the bending vibration of V_2-O, and the V=O bonds of α-V_2O_5, respectively. The partially resolved peak at 305 cm^{-1} is due to the bending vibration of the triply bonded V_3-O bond in V_2O_5, but is mostly overlapped with the peak at 286 cm^{-1} which corresponds to the bending vibration of V=O bonds of α-V_2O_5. These results suggest that the as-deposited and annealed films indeed contain characteristic Raman peaks for V_2O_5.[322-323]

However, an anomalous peak appears at 850 cm^{-1} in the as-deposited spectrum which doesn't match any of the known V_2O_5 peaks in literature. At first glance, this peak appears to indicate a mixed phase with other VO_x. However, to the best of our knowledge, the closest match to this peak in literature is the monoclinic VO_2 insulating phase with a peak at 826 cm^{-1}.[349] But it is still 25 cm^{-1} off from our observation. Such a large shift that only occurs to this single peak but no other peaks makes it unlikely attributed to the presence of large amount of VO_2 phases. Therefore, we attribute this peak mainly to the hydration of the V_2O_5 surface originated from moisture in the air which matches well with previous Raman spectroscopy studies by Bell et al. on supported V_2O_5 catalyst.[350-351] The water content was not quantified in this work; however, it is not expected to exceed more than one mole of H_2O per mole of V_2O_5, possibly with a chemical formula $V_2O_5 \bullet H_2O$. In terms of battery safety, it is expected that such a low H_2O content does not pose risks in practical applications. Interestingly, the hydrated or hydrogenated mesoporous metal oxides have been reported in several studies to facilitate higher electrical conductivity and generate larger pseudocapacitance.[352-354] The peak intensity at 850 cm^{-1} in the annealed structure significantly decreases correlating well with the formation of crystalline V_2O_5 phases. The dehydration and crystallization processes during thermal annealing convert the initial porous amorphous structure of hydrated V_2O_5 material into a heterogeneous film consisting of denser V_2O_5 nanocrystals. The non-uniform stress associated with such phases transitions may have caused the core-shell nanofibers to bend and clustering with neighbors (as revealed in Figure 5.1).

To further understand the annealing effects, XPS was used to investigate the change in chemical bonding and elemental compositions between the as-deposited and annealed VACNF-V_2O_5 core shell structures. Figure D.5a shows the wide-scan XPS survey spectra of both as-deposited and annealed structures with almost the same features. For example, the C1s peak

originated from either VACNFs or the graphite substrate appears at ~ 284.3 eV for the as-deposited and 284.4 eV for the annealed samples. However, the binding energies of $V2p_{3/2}$, $V2p_{1/2}$, and O1s appear at 517.0, 524.6 and 530.0 eV, respectively, in the as-deposited sample, but downshift by 0.6 eV to 516.4, 524.0, and 529.4 eV in the annealed sample, as shown in Figure 3c. The downshift in these XPS peaks serves as an indication of the degree of dehydration, as reported in a previous study.[216] In addition, more detailed information can be extracted from the peak shapes. Figure D.5c shows the deconvoluted peaks of the XPS O1s peaks for both as-deposited and annealed samples, which consist of a V-O peak (~ 529.4 - 530 eV) and a V-OH peak (~ 531 - 532 eV). Quantitative analysis shows that the ratio of the peak area between V-OH and V-O decreases after annealing, confirming that the as-deposited sample is hydrated. Meanwhile, the $V2p_{3/2}$ peaks of the as-deposited sample can be resolved into two contributions, V^{4+} and V^{5+} (Figure D.5d). A quantitative analysis indicates that about 90 % of the vanadium are in V^{5+} state (i.e., corresponding to V_2O_5). The results from XRD, Raman spectra and XPS suggest that the as-deposited structure is a hydrated amorphous V_2O_5 mixed with a small amount of VO_2 at the surface. After annealing, the hydration is removed, the VO_2 at the surface is oxidized to V_2O_5, and the amorphous V_2O_5 is converted into connected crystalline nanoparticles.

5.3.3 Assessment of 2 Li^+/V_2O_5 Insertion between 4.0 – 2.0 V

The SEM image in Figure D.6a reveals that the average thickness, i.e. the nominal thickness, of the same amount of V_2O_5 deposited on a flat Si substrate is 425 nm in the as-deposited sample. From this, the mass of V_2O_5 on each 2.40 cm^2 VACNF disk electrode can be estimated to be 0.343 mg based on the density of bulk V_2O_5 (3.36 g cm^{-3}). In order to better assess the materials properties and compare them with the theoretical values, only the mass of V_2O_5 is used for gravimetric capacity calculations in this study. It needs to be noted that we may have slightly

overestimated the V_2O_5 mass since the micro-porosity and hydration may lower the density of the deposited V_2O_5 film. But it is sufficient to provide a conservative estimation of the gravimetric capacities. The accurate gravimetric capacity may be slightly higher. Interestingly, the thermal annealing treatment converts the uniform amorphous V_2O_5 film into a porous particulated film with slightly larger film thickness, higher porosity and rougher surface.

The Li^+ insertion/extraction properties of the VACNF-V_2O_5 core-shell structures were first investigated with CV from 2.0 to 4.0 V (vs. Li^+/Li). Figure D.7a shows the first four cycles at a scan rate of 0.1 mV s^{-1} for the as-deposited structure. Two reduction peaks are observed in the first cycle at ~3.2 and ~2.5 V corresponding to the phase transformation from α-V_2O_5 to δ-LiV_2O_5 and γ-$Li_2V_2O_5$, respectively. However, these peaks quickly decrease and almost disappear in cycle 3. The CV curves become stabilized and overlapped after the 3rd cycle, showing only weak redox waves superimposed on flat pseudocapacitive features. Importantly, insertion/extraction of the initial 0.50 Li^+ in V_2O_5 in the first cycle is abnormal in both samples, with a large unstable oxidation (extraction) peak and a poorly defined reduction (insertion) peak. Both oxidation and reduction peaks disappear after 3 cycles and become nearly flat baselines. The quick conversion of the commonly observed redox waves to the flat pseudocapacitive feature reflects the unique properties of these core-shell structures which are significantly different from those of bulk crystalline V_2O_5 in literature.[128, 309] The annealed structure shows similar characteristics (Figure D.7b). In addition, both as-deposited and annealed samples show stable CV curves at higher scan rates in later cycles (Figures D.7c and d), which are consistent with pseudocapacitive properties observed in V_2O_5 shells on VACNTs.[346]

Galvanostatic charge-discharge measurements were then used to study the rate performance of the VACNF-V_2O_5 core-shell structures in the voltage range of 4.0 – 2.0 V. Cells

were discharge/charged for 10 cycles at 10 different current densities (0.20, 0.35, 0.50, 0.60, 0.75, 0.90, 1.00, 1.20, 1.35, and 1.50 A g^{-1}) before returning to the initial current rate (0.20 A g^{-1}). In this paper, all referred C rates are based on the time required to complete the last stable charge/discharge cycles at a specific current density, with a rate of 1C (or C/1) corresponding to the condition to complete charge or discharge in 1 hour. The rate performance of the as-deposited structure is presented in Figure 5.4a. A reversible insertion/extraction capacity of ~390 mAh g^{-1} was observed at a rate of 0.20 A g^{-1} (~C/2) in the 2nd cycle but dropped to 360 mAh g^{-1} in cycle 10. This extraordinarily high capacity can be attributed to the open amorphous structure similar to the V_2O_5 aerogel which has been shown to reach 650 mAh g^{-1} owing to its high degree of porosity.[126, 218] The capacity dropped to 294 mAh g^{-1} when the rate was increased to 0.35 A g^{-1} (~1.2C) in cycle 20. Last cycle insertion capacities of 247, 201, 157, 137, and 113 mAh g^{-1} were achieved at the current density of 0.50, 0.75, 1.00, 1.20, and 1.50 A g^{-1}, respectively, corresponding to about 2C, 3.7C, 6.4C, 8.8C and 13.3C. It should be noted that a high capacity of 113 mAh g^{-1} at a rate of ~13.3C is rarely reported in literature. When the current density was returned to 0.20 A g^{-1} (~C/2) in cycle 101, a capacity of 331 mAh g^{-1} was achieved, resulting in a high capacity retention of ~92%. For all measurements, the Coulombic efficiencies, i.e. the ratio of the discharge (insertion) capacity to the previous charge (extraction) capacity, were about 99% to 100% except for a few points when the current densities were changed. Those disrupted points were taken out from the figures to avoid confusion.

The last cycle charge-discharge profiles at rates of 0.20, 0.35, and 0.50 A g^{-1} in Figure 5.4b exemplify the high capacity of the as-deposited structure. All profiles show nearly linear curves

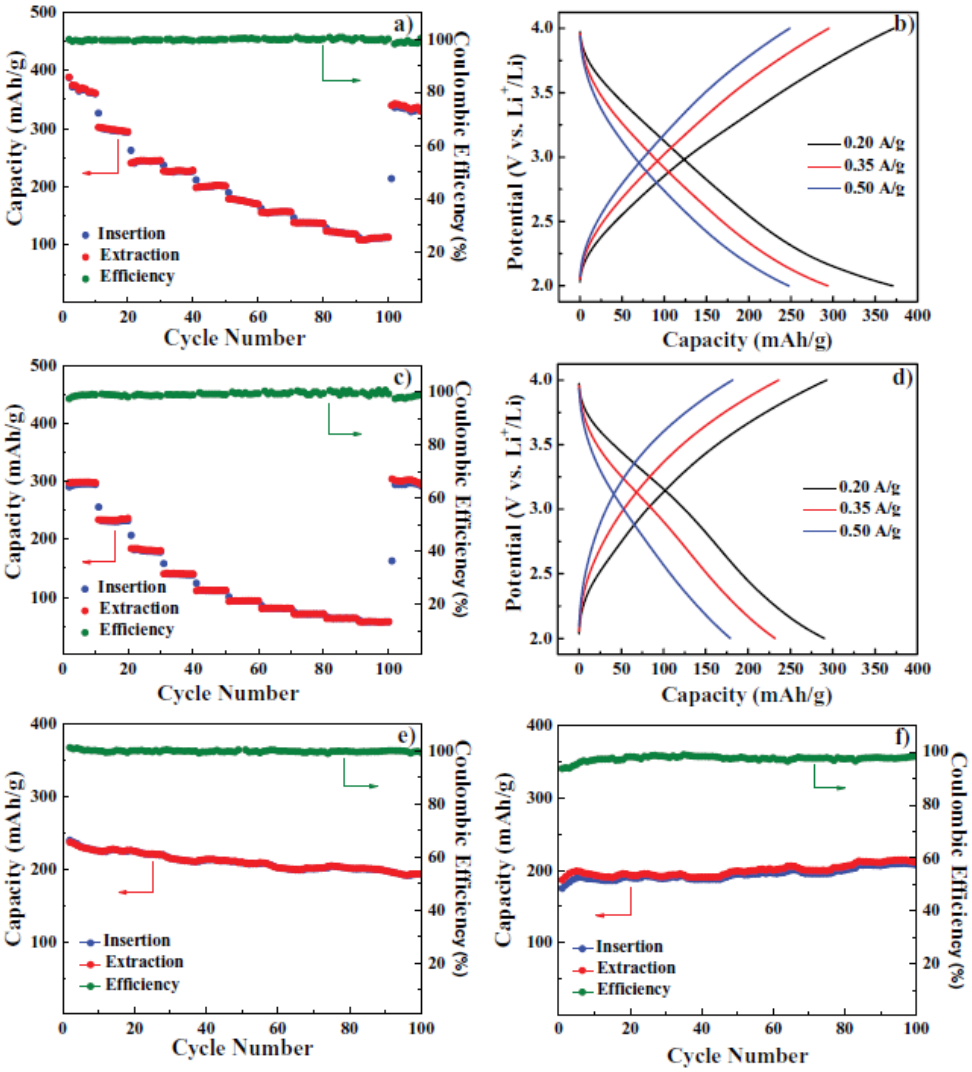

Figure 5.4 Two Li^+/V_2O_5 insertion/extraction. Rate performance of the as-deposited a) and annealed c) VACNF-V_2O_5 core-shell structures in the potential range of 4.0 – 2.0 V at 10 different current density values (0.20, 0.35, 0.50, 0.60, 0.75, 0.90, 1.00, 1.20, 1.35, and 1.50 A g^{-1}), each for 10 charge-discharge cycles. Galvanostatic charge-discharge profiles of the as-deposited b) and annealed d) structures at 0.20, 0.35, 0.50 A g^{-1}. Long-term cycling at a rate of 0.50 A g^{-1} for the as-deposited e) and annealed f) structures. (Reprinted with permission from Adv. Mater. Interfaces 2016, 3, 1600824)

without the flat plateaus commonly seen for Li^+ insertion/extraction in crystalline V_2O_5,[128, 309] indicating similar pseudocapacitive properties as V_2O_5 shells on CNT cores.[231, 346] These properties are also consistent with the CV features. The long-term stability is illustrated in Figure D.8a on the as-deposited sample with three repeating rate testing sequences up to a total of 300 cycles. A capacity of 313 mAh g^{-1} was achieved when the rate was returned to 0.20 A g^{-1} (~C/2) in cycle

201, resulting in a capacity retention of ~87% from that of cycle 10. It is worth noting that rather high capacities of 103 and 102 mAh g^{-1} were achieved at a high current density of 1.50 A g^{-1} (~13.3C) in cycles 190 and 290, respectively. The as-deposited VACNF-V_2O_5 core-shell structure not only presents a remarkably high capacity but also excellent rate capability and impressive stability exceeding the literature on crystalline V_2O_5.

The annealed VACNF-V_2O_5 core-shell structure presents the similar rate performance in the voltage range of 4.0 – 2.0 V, as shown in Figure 5.4c. A capacity of 294 mAh g^{-1} was achieved at a current rate of 0.20 A g^{-1} (~C/1.5) which is consistent with the theoretical capacity of 2 Li^+ insertion/extraction in crystalline V_2O_5. Last cycle insertion capacities of 232, 137, 111, 93, 71, 63, and 57 mAh g^{-1} were achieved at other seven discrete current densities of 0.35, 0.60, 0.75, 0.90, 1.20, 1.35, and 1.50 A g^{-1}, respectively, corresponding to the variation of C-rates from ~1.3C to ~26C. When the rate was returned to 0.20 A g^{-1} (~C/1.5) in cycle 101, a capacity of 292 mAh g^{-1} was achieved, demonstrating a capacity retention of ~99%. Last cycle charge-discharge profiles at rates of 0.20, 0.35, and 0.50 A g^{-1} are shown in Figure 5.4d. Small plateaus can be seen in the potential ranges of 3.5-3.0 V and 2.5-2.2 V in the discharge profile at 0.20 A g^{-1}, owing to the improved crystalline domains by thermal annealing. But the dominating feature is still the pseudocapacitive behavior. At higher rates, the plateaus quickly diminish. The rate performance tests were repeated three times up to 300 cycles as shown in Figure S8b. When the rate was returned to 0.20 A g^{-1} in cycle 201, the cell retained a capacity of 282 mAh g^{-1}, with an astounding retention rate of ~96%. Moreover, when the current rate was increased to 1.50 A g^{-1} (~26C) in cycles 190 and 290, stable capacities of 52 and 54 mAh g^{-1}, respectively, can still be obtained. Figures 5.4e-f demonstrate the high degree of stability for the as deposited and annealed structures

with long term cycle at 0.5 A g^{-1} for 100 cycles resulting in capacity retentions of ~80% and ~100%, respectively.

5.3.4 Assessment of 3 Li^+/V_2O_5 Insertion between 4.0 – 1.5 V

Inspired by the high capacity and excellent stability of 2 Li^+/ V_2O_5 insertion/extraction in both the as-deposited and annealed VACNF-V_2O_5 core-shell structures, we further investigated their electrochemical performance in the voltage range of 4.0 – 1.5 V in order to assess the 3 Li^+/ V_2O_5 insertion/extraction properties. CV measurements of the as-deposited and annealed structures are presented in Figure D.9a-c. A large reduction peak at ~1.80 V can be seen in the first cycle at a rate of 0.1 mV s^{-1} with the annealed structure corresponding to conversion of previously formed γ- $Li_2V_2O_5$ to rock-salt-type ω-$Li_xV_2O_5$ ($2 < x < 3$). However, the CV curve in the second cycle quickly changes to pseudocapacitive features with only small redox waves which are stabilized in later cycles. The as-deposited sample shows similar CV behaviors but the current was much noisier and unstable in the first few scans (data not shown). The 3 Li^+/V_2O_5 insertion/extraction was reversible and stable in later cycles for both structures, as revealed by further CV measurements at faster scan rates of 0.5 and 1.0 mV s^{-1} (Figures D.9b-c).

Similar rate-performance tests as seen in Figure 5.4 were applied in the voltage range of 4.0 – 1.5 V. The as-deposited structure achieved an astonishing initial capacity of 547 mAh g^{-1} at a rate of 0.20 A g^{-1} (~C/3) as shown in Figure 5.5a. After completing the 1st and 2nd rate testing sequences, the current density was returned to 0.20 A g^{-1} (~C/3) in cycles 101 and 201. The capacity slightly dropped to 524 and 486 mAh g^{-1}, respectively, demonstrating the ability to retain ~96% and 89% of the initial capacity. Last cycle insertion capacities of 477, 441, 369, 292, and 257 mAh g^{-1} were achieved at the current densities of 0.35, 0.50, 0.75, 1.20, and 1.50 A g^{-1}, respectively, corresponding to varying the C-rate from ~C/1.4 to ~5.8C. Figure 5.5b shows the

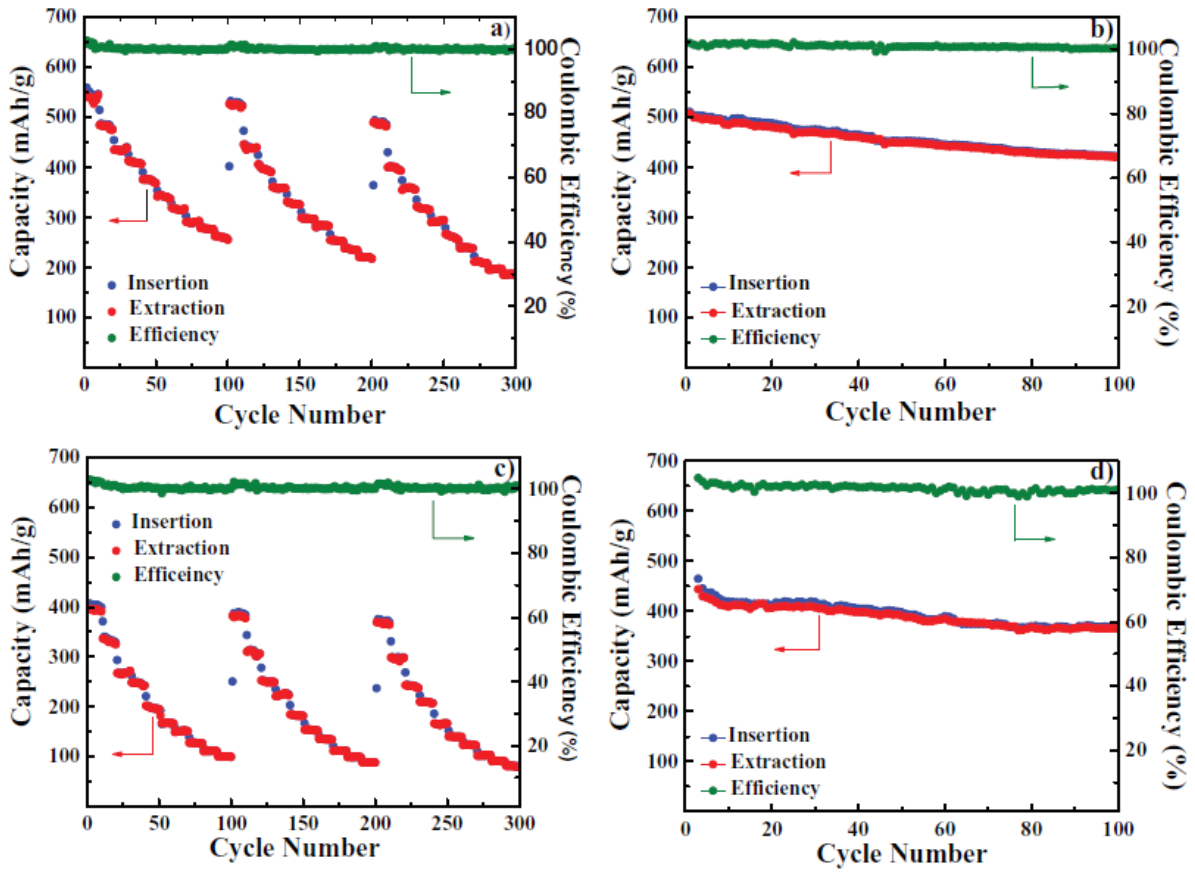

Figure 5.5 Three Li^+/V_2O_5 insertion/extraction. Rate performance a) and long-term cycling test b) at a rate of 0.20 A g^{-1} for the as-deposited VACNF-V_2O_5 core-shell structure in the voltage range of 4.0 – 1.5 V. Rate performance c) and long-term cycling test d) at a rate of 0.20 A g^{-1} for the annealed VACNF-V_2O_5 core-shell structure in the voltage range of 4.0 – 1.5 V. The rate performance is measured at 10 different current density values (0.20, 0.35, 0.50, 0.60, 0.75, 0.90, 1.00, 1.20, 1.35, and 1.50 A g^{-1}), each for 10 charge-discharge cycles. (Reprinted with permission from Adv. Mater. Interfaces 2016, 3, 1600824)

long cycling results of another half-cell of the as-deposited structure at a fixed rate of 0.20 A g^{-1} (~C/2.5). A capacity value of ~500 mAh g^{-1} was achieved at cycle 10, which dropped to ~422 mAh g^{-1} after 100 cycles, resulting in a capacity retention of ~84%. Such a capacity retention rate for 3 Li^+/ V_2O_5 insertion/extraction far exceeds the current state-of-the-art value of 51% after 100 cycles using thin V_2O_5 coatings on 3D MWCNT sponge networks.[231] Over the whole cycling tests, the average Coulombic efficiency was at a remarkable value of >99%.

Figure 5.5c shows the rate performance of the annealed VACNF-V_2O_5 core-shell structure in the voltage range of 4.0 – 1.5 V with similar rate sequences as those in Figure 5.5a. An initial insertion capacity of 395 mAh g^{-1} was achieved at a rate of 0.20 A g^{-1} (C/2), ~90% of the theoretical capacity (441 mAh g^{-1}) for 3 Li^+/V_2O_5 insertion/extraction. When the rate was returned to 0.20 A g^{-1} in cycles 101 and 201 after completing the first and 2nd testing sequences, the capacity slightly dropped to 384 and 369 mAh g^{-1}, resulting in capacity retentions of ~97% and ~93%, respectively. The insertion capacities of 328, 227, 196, 152, 127, and 100 mAh g^{-1} were achieved in the last cycle at the current densities of 0.35, 0.50, 0.75, 1.00, 1.20 and 1.50 A g^{-1}, respectively, corresponding to the variation from ~1.1C to 15C in the first 100 cycles. It is worth noting that a capacity of 100 mAh g^{-1} was achieved at 1.50 A g^{-1} (15C) in cycle 90 which only dropped to 89 and 81 mAh g^{-1} when returned to 1.50 A g^{-1} in cycles 190 and 290, respectively. It is noted that the capacities of the as-deposited structure at 1.50 A g^{-1}, i.e. 257, 218 and 186 mAh g^{-1} in cycles 90, 190 and 290 are significantly higher than those in the annealed sample. But the retention rate between cycle 90 and cycle 290 is higher in the annealed sample than the as-deposited sample (81% vs. 76%). The long-term cycling results in Figure 5.5d at lower current density of 0.20 A g^{-1} (C/2) further illustrate the improved stability of the annealed sample with only a small capacity drop from ~410 mAh g^{-1} in cycle 10 to 360 mAh g^{-1} in cycle 100, exhibiting a capacity retention of ~88%.

The results from the above LIB studies in the voltage range of both 4.0 – 2.0 V and 4.0 – 1.5 V suggest that there are tradeoffs between the as-deposited and annealed structures. The as-deposited structure in both voltage ranges offers higher capacities exceeding the respective theoretical values for both two and three Li^+ insertion/extraction in crystalline V_2O_5. On the other hand, the annealed structure exhibits slightly lower than theoretical capacities but with superior

long cycling stability. Figures D.10a-b provide additional long-cycling results to illustrate the differences between the as-deposited and annealed structures in both voltage ranges. The first 100 cycles were done in the voltage range of 4.0 – 2.0 V at 0.50 A g^{-1}. Note that these cycles are also presented in Figures 5.4e-f. The voltage range was then extended to 4.0 – 1.5 V for the next 200 cycles at the same current density. In the extended voltage range, the as-deposited structure shows a steady declination in capacity from 304 mAh g^{-1} at cycle 120 to 227 mAh g^{-1} in cycle 300, resulting in a capacity retention of ~75%. In contrast, the annealed structure exhibited a high capacity retention of ~95% with a capacity of 304 mAh g^{-1} at cycle 120 and 290 mAh g^{-1} in cycle 300. It is noteworthy that 0.50 A g^{-1} is a rather high current density (~1.6C). Higher capacity can be obtained at lower current density as we demonstrated earlier

5.3.5 Correlation between Materials Structure and Multiple Li^+/V_2O_5 Processes

Figure 5.6 further illustrates the tradeoff between the long-term stability and high capacity between the as-deposited and annealed structures using the data from the three rate testing sequences reported in Figures D.8, 5.5a and 5c. The discharge (insertion) capacity of the last cycle at each rate is plotted against the logarithm of the applied current density. Figure 5.6a demonstrates the high degree of stability for the annealed structure in the voltage range of 4.0 – 2.0 V. Each of the three curves corresponds to the cycle ranges of 1-100 (black), 101-200 (red), and 201-300 (blue). Here all three curves nearly overlap, indicating almost no change in capacity and the excellent stability. When the voltage range is extended to 4.0 – 1.5 V, a small downward shift is observed in later cycles (Figure 5.6b). At the lowest current density (0.20 A g^{-1}, ~C/1.5), the capacity matches the theoretical value for 2 Li^+/V_2O_5 and 3 Li^+/V_2O_5 insertion, respectively. To the best of our knowledge, such a high degree of stability has not been reported in literature for reliable 3 Li^+/ V_2O_5 insertion/extraction.

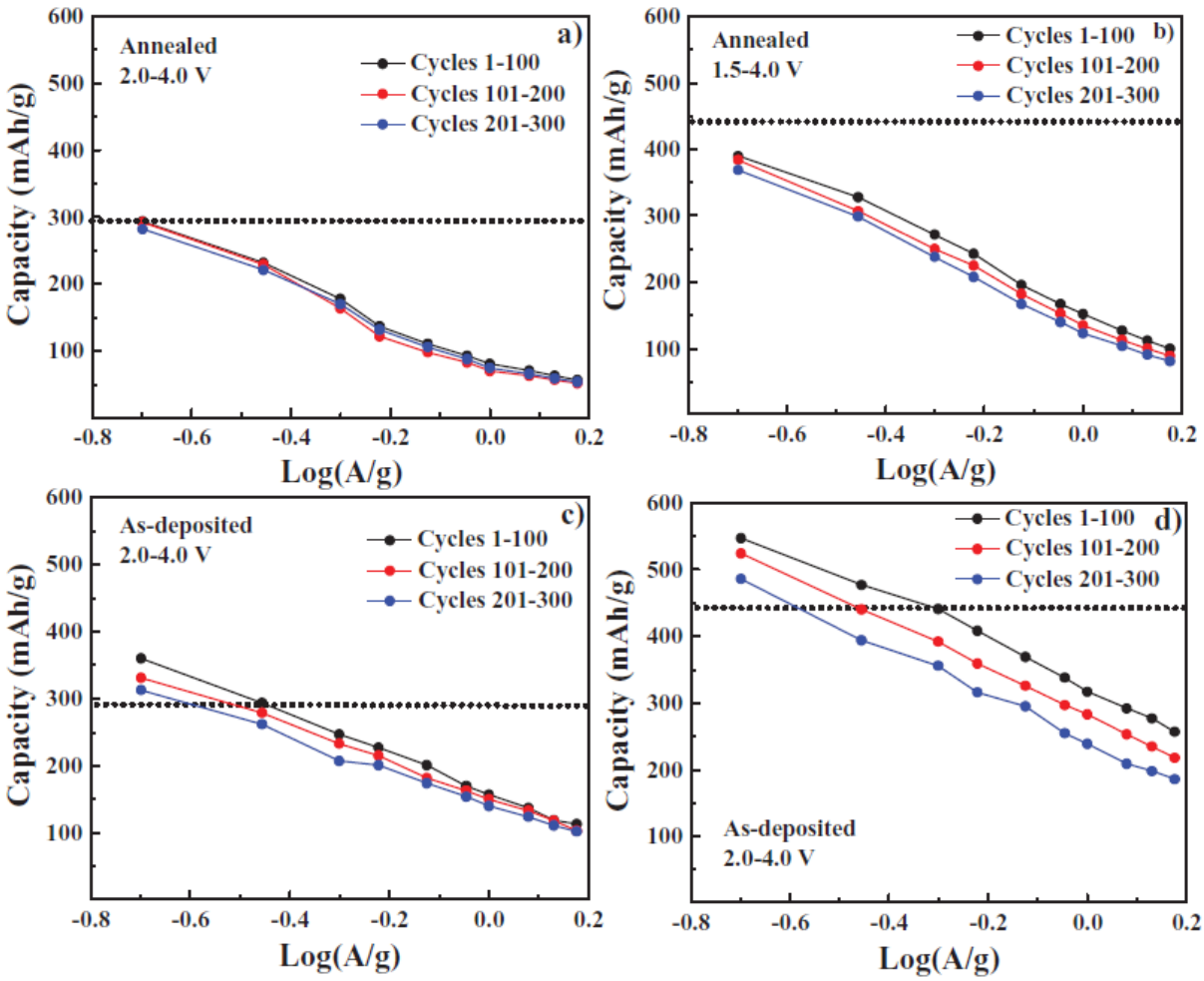

Figure 5.6 Comparison of the capacity and stability. The specific capacity from the last cycle at each specific rate is plot versus the logarithm of the applied current density. Data are from the above discussed 3 sets of rate performance tests with cycles 1-100 (black), 101-200 (red), 201-300 (blue). The annealed structure in the potential ranges of a) 4.0 – 2.0 V and b) 4.0 – 1.5 V and as-deposited structure in the potential ranges of c) 4.0 – 2.0 V and d) 4.0 – 1.5 V are shown in four panels. Dashed lines are placed at the theoretical capacities in both potential ranges, respectively. (Reprinted with permission from Adv. Mater. Interfaces 2016, 3, 1600824)

The most interesting results are from the as-deposited structure in Figure 5.6c. In the voltage range of 4.0 – 2.0 V, the capacity at each current density is clearly higher than the annealed structure. Particularly, the capacity at the lowest current density in the initial cycles clearly exceeds the theoretical value for 2 Li^+/V_2O_5 insertion into crystalline materials. However, this comes at a price in terms of stability, as illustrated by the modest downward shift of the curves

taking in later cycles with respect to earlier ones. Interestingly the curves tend to converge at higher current densities, indicating that better stability can be obtained by taking advantages of surface reactions at higher charge-discharge rates. The as-deposited structure in the extended voltage range of 4.0 – 1.5 V in Figure 5.6d shows the highest capacities in Figures 5.6a-d. At the lowest current density (0.20 A g^{-1}, ~C/2.7), the capacity far exceeds the theoretical value of 441 mAh g^{-1} for 3 Li^+/V_2O_5 insertion into crystalline V_2O_5. However, the stability degrades as illustrated by the larger separation between the curves.

From the above results, we can conclude that: (1) the as-deposited VACNF-V_2O_5 structure provides much higher capacity than theoretical values for both 2 Li^+/V_2O_5 and 3 Li^+/V_2O_5 insertion/extraction in respective voltage ranges; and (2) the annealed VACNF-V_2O_5 structure shows highly stable capacity matching the theoretical values. The first observation can be attributed to the disordered microporous structure of the as-deposited V_2O_5 shells due to the presence hydrated amorphous V_2O_5 in the VACNF-V_2O_5 core-shell structures. Our TEM and XRD data clearly show the amorphous morphology while Raman and XPS data clearly indicate the presence of hydration in the as-deposited V_2O_5 shells on VACNFs. Although ordered materials are generally thought to provide better Li^+ flows, enhanced capacity by disordered hydrated V_2O_5 can be tracked back to early studies in V_2O_5 aerogels and thin hydrated V_2O_5 shells coated on vertically aligned Ni nanorod arrays.[326-327] Recent computational and experimental studies indicate that disordered metal oxides may provide higher storage capacities exceeding the theoretical limit defined by stoichiometry in crystalline material for both LIBs[325] and SIBs.[211] This can be attributed to more surface reactions, sublattice intermixing of metal cations and Li^+ ions, and formation of percolation networks for Li^+ transport through the disordered phases. The problem is how to overcome the poor mechanical stability and low electrical conductivity of the disordered metal

oxides. Besides inducing the amorphous microporous V_2O_5 structure, the hydration contents (in the form of H_2O or OH^- group) may react with Li to form Li_2O_2 or Li_2O which are quite irreversible in bulk V_2O_5 materials. Using thin V_2O_5 shells in core-shell structures on CNTs has shown the ability to make such side reactions more reversible.[231, 346] The core-shell structure on VACNFs in this study demonstrates further enhanced stability, particularly with 3 Li^+/V_2O_5 insertion/extraction. After removing hydration and converting the amorphous V_2O_5 shell into connected V_2O_5 nanocrystals, the Li^+ insertion/extraction is dominated by the common intercalation mechanism in crystalline V_2O_5 and thus matches the theoretical values. But the unique core-shell structure using VACNF templates enables the remarkable stability in long cycling for both 2 Li^+/V_2O_5 and 3 Li^+/V_2O_5 insertion/extractions. Optimizing the amorphous and crystalline structure of V_2O_5 using this core-shell hybrid concept is not only promising for developing high-capacity LIB cathodes but also emerging batteries using Na^+, Mg^{2+} and Al^{3+}.

5.4 Conclusions

In summary, V_2O_5 has been deposited on VACNF arrays by RF sputtering to form three-dimensional VACNF-V_2O_5 core-shell structures and explored as LIB cathodes for deep Li^+ insertion. The amorphous hydrated V_2O_5 shell in the as-deposited sample has shown a remarkably high Li storage capacity of 360-390 mAh g^{-1} in the voltage range of 4.0 – 2.0 V, well exceeding the theoretical value of 294 mAh g^{-1} for 2 Li^+/V_2O_5 insertion/extraction in crystalline V_2O_5. In contrast, the crystallized V_2O_5 shell after thermal annealing presents a capacity of 294 mAh g^{-1}, matching the theoretical values for 2 Li^+/V_2O_5 insertion/extraction. High capacity retention rates of ~82% for the as-deposited structure and ~100% for the annealed structure were obtained after 100 cycles. More importantly, these core-shell structures were able to exhibit stable 3 Li^+/V_2O_5 insertion/extraction when the voltage range is extended to 4.0 – 1.5 V, which are rarely reported.

The as-deposited amorphous V_2O_5 structure achieved a remarkable capacity of 547 mAh g^{-1}, well above the theoretical value of 441 mAh g^{-1} for 3 Li^+/V_2O_5 insertion/extraction in crystalline V_2O_5, and was able to retain ~84% of the capacity after 100 cycles at varied rates. The annealed crystallized V_2O_5 structure exhibited a capacity of 390 mAh g^{-1}, slightly below the theoretical value, but with a better retention rate of ~88% after 100 cycles. Both the as-deposited and annealed core-shell structures well exceed the stability of both 2 and 3 Li^+/V_2O_5 insertion/extraction in literature, which are attributed to the ability to improve the mechanical stability of the disordered microporous V_2O_5 structure and the current collecting capability using the core-shell structure built on VACNFs. This three-dimensional hybrid structure is promising in enabling traditionally unstable high-capacity battery materials for future high-performance batteries.

5.5 Acknowledgments

We would like to thank Ronald Rojeski of Catalyst Power Technologies Inc. for providing materials for this work, Prem Thapa and Maogang Gong of the University of Kansas for help in taking the TEM images, Qingfeng Liu for beneficial discussions of the XPS spectra, and Colleen Gura and Ian Andree of Kansas State University for their help with the XRD analyses. This work was supported by NASA grant NNX13AD42A and NSF EPSCoR Award EPS-0903806 (including the matching support from the State of Kansas through Kansas Technology Enterprise Corporation). JW also acknowledges support from NSF-DMR-1508494 and ARO-W911NF-16-1-0029.

Chapter 6 - Enabling Stable Sodium Ion Battery Cathodes with a Hybrid Structure of Disordered Bilyared $V_2O_5 \cdot nH_2O$ Shells Deposited on Vertically Aligned Carbon Nanofiber Arrays

6.1 Introduction

LIBs have dominated the EES sector for nearly two decades owing to their high-energy storage capabilities.[330, 355] However, the high cost of lithium-containing precursors (about $5000/ton for lithium carbonate in 2010) owing to its low abundancy in the Earth crust makes it undesirable for large-scale applications such as grid-storage backup systems and electric cars.[356-357] Sodium-containing precursors, on the other hand, are much more abundant, which drives down their cost. For example, trona, the precursor for sodium carbonates, costs only $115-165/ton.[357] Moreover, both lithium (Li) and sodium (Na) are members of the alkali metal family and have very similar chemistry, which makes sodium an attractive alternative for lithium. For these reasons, sodium-ion batteries (SIBs) have received extensive attention as an EES system for future large-scale applications in which the cost and sustainability are critical concerns.

However, the electrode materials for SIBs encounter bigger challenges compared to their LIB counterparts. Most prominently, the larger ionic radius of Na^+ ions (1.02 Å) as compared to that of Li^+ (0.76 Å) makes intercalation of Na^+ ions into electrode materials much more difficult.[213, 358] For instance, graphite is the material of choice for anodes in most commercial LIBs with a theoretical capacity of 372 mAh g^{-1}. The d-spacing of 3.35 Å between the graphitic carbon sheets needs to be expanded by ~10% to 3.70 Å upon full lithiation to LiC_6 (with a specific capacity of 372 mAh g^{-1}) to accommodate intercalation of Li^+ ions, which causes some mechanical stress but remains reversible after many cycles.[359] In contrast, using graphite as anodes for SIBs requires

expanding the interlayer spacing to 4.3 Å to achieve an initial reversible capacity of only 284 mAh g^{-1}, which involves ~28% volume expansion.[360] This large volume change has resulted in rapid capacity fading and hence cell failure after only several cycles. Efforts have been made to expand the d-spacing of graphite through various synthesis methods and using various carbon allotropes, which have generated a moderate success towards to high specific capacities of 300 – 600 mAh g^{-1} and good cycling stability.[361-363] So far cathode materials are the bottleneck for SIBs, which are limited by the low energy density, short cycling life and insufficient power density.[364] Among the state-of-the-art SIB cathode materials, Na_xCoO_2 and Na_xFePO_4 ($x \leq 1$) have been investigated owing to the success of their lithium analogues in commercial LIBs.[365-368] Other materials such as polyanionic NASICON-type $Na_2V_3(PO_4)_2$,[224] tunnel-structured metal oxides $Na_{0.61}Ti_{0.48}Mn_{0.52}O_2$,[369] layered metal oxides Na_xMO_2 (x = 0.44-1, M = 3d transition metals)[370-371] and Prussian blue analogs[372-373] have also been explored. However, the insertion/extraction capacities of these cathode materials are only ~100-200 mAh g^{-1} at relatively low operating potentials of 2.6–3.2 V (vs. Na/Na^+), which limits the overall energy density of SIBs.[364] In addition, the cycling stability and lifetime of all these cathode materials are insufficient for practical applications.[364]

In this study, we explore a cathode material of vanadium pentoxide (V_2O_5), for potential high-capacity SIBs. V_2O_5 has been extensively investigated as a potential LIB cathode owing to its high theoretical Li^+ insertion/extraction capacity, as well as its low cost, relatively low chemical toxicity, high electrode potential in delithiated states (up to 4.0 V vs. Li/Li^+) and the readily accessible layered structure for Li^+ ion insertion.[124] Orthorhombic α-V_2O_5 has an interlayer d-spacing of 4.36 Å which can achieve a reversible insertion capacity of 294 mAh g^{-1} (for a two Li^+/V_2O_5 insertion process) and an irreversible capacity of 441 mAh g^{-1} (for a three Li^+/V_2O_5

insertion process).[125] For applications as the SIB cathodes, it's been reported that V_2O_5 can achieve a theoretical reversible capacity of 236 mAh g^{-1} in the form of $Na_xV_2O_5$ with $x \leq \sim 1.6$.[211-212, 374-376] Su *et al.* achieved an insertion capacity of 230 mAh g^{-1} in the first cycle at a rate of 20 mA g^{-1}, however, the capacity dropped to 159 mAh g^{-1} in the second cycle.[212] Despite the moderate success with crystalline α-V_2O_5, its small d-spacing cannot accommodate Na^+ ions and the structure tends to collapse after Na^+ ion intercalation, leading to rapid capacity fading. On the other hand, hydrated V_2O_5 is reported to have an ordered bilayer structure with a large d-spacing of 8-12 Å depending on the degree of hydration, which is much more suitable for Na^+ insertion.[211, 213-215] Tepavcevic *et al*. achieved a reversible insertion capacity of 250 mAh g^{-1} with significantly improved cycling stability using a thin film of nanostructured ordered bilayered V_2O_5 prepared by electrochemical deposition.[215] However, the current rate of 20 mA g^{-1} was rather low. When it was increased to 630 mA g^{-1}, the capacity dropped to 120–140 mA g^{-1} and the value significantly decreased after 80 cycles. Several other reports suggested that amorphous V_2O_5 can outperform crystalline structures due to better accommodation of Na^+ ions in the disordered interlayer lattices and the additional pseudocapacitive contributions.[217-218, 377] Liu *et al*. reported that amorphous V_2O_5 gave a higher capacity of ~250 mAh g^{-1} than the crystalline V_2O_5 at the low rates (40-640 mA g^{-1}) but it was strangely inversed at high current densities (>6,400 mA g^{-1}).[217] Wei *et al.* reported that a hydrated $V_2O_5 \cdot nH_2O$ (n=~0.55) xerogel composed of interconnected nanowire networks gave an even higher reversible capacity of 336 mAh g^{-1} at 50 mA g^{-1} attributed to the large pseudocapacitive contributions associated with fast surface reactions.[378] However, the capacity dropped below 60% after only 30 cycles at 0.1 A g^{-1}.

Despite the encouraging success, the current studies on V_2O_5 SIB cathodes are limited by the intrinsic properties of V_2O_5, such as low sodium ion diffusion coefficients (~10^{-14} – 10^{-12} cm^2

s^{-1}) and poor electrical conductivity (~10^{-3} – 10^{-5} S cm^{-1}), which lead to low power density.[225, 302] Low-dimensional nanoparticles and nanostructured hydrated bilayered structures have been employed to overcome the low Na^+ diffusion coefficients. This strategy increases the overall specific surface area (SSA) and provides short diffusion pathways for Na^+ ions, which in turn offers more electrochemically active sites for enhancing SIB performance. However, the electrical conductivity becomes even lower. The incorporation of low dimensional conductive carbon materials such as multiwall carbon nanotubes (MWCNTs),[308, 379] graphene,[126, 380] and reduced graphene oxide[314, 381] to form composite materials has been a common practice to increase the overall electrical conductivity. Coating thin V_2O_5 shells on continuous three-dimensional (3D) conductive frameworks was found to be a more effective approach to resolving both the ion diffusion and electrical connection issues for higher lithium storage performance.[345, 382-384] However, to the best of our knowledge, this approach has not been well investigated for Na^+ storage.

Here, we report a study using amorphous V_2O_5 shells sputter-coated on vertically aligned carbon nanofibers (VACNFs) as a SIB cathode with an aim to address on the above-discussed issues. VACNFs can be described as a robust brush-like array of high-aspect-ratio carbon nanofibers consisting of conically stacked graphitic structures.[385] The areal density is ~1x10^9/cm^2 with the average diameter variable from ~50 to 150 nm and the length tunable from 3 to 10 μm. VACNFs offer a distinctive advantage over other carbon allotropes owing to their abundancy of graphitic edges along the sidewall, which provide an excellent electrochemical interface leading to strong interactions with shell materials. Previously we have reported that the as-deposited amorphous V_2O_5 shells have the ability to provide a stable capacity of 547 mAh g^{-1} as a LIB cathode in traditionally irreversible 3 Li^+/V_2O_5 processes, which is about 25% higher than the

theoretical value of crystalline V_2O_5 cathodes.[386] In addition, the core-shell structure provided remarkable power rates and cycling stability. Clearly, the nanostructured core-shell architecture provided the desired structural support and efficient electron pathway to enable the use of metastable amorphous V_2O_5 shells. Notably, our recent study shows that the as-deposited amorphous V_2O_5 shell in fact consists of a highly disordered stack of hydrated $V_2O_5{\cdot}nH_2O$ bilayers. The large interlayer spacing (~11.0 Å) would serve well as a host material for the larger Na^+ ions. This study reveals the potentials of such 3D core-shell architecture as stable high-capacity SIB cathodes by systematically comparing properties of the disordered $V_2O_5{\cdot}nH_2O$ bilayer shells and crystalline V_2O_5 shells at various charge-discharge rates and potential windows. The disordered bilayered $V_2O_5{\cdot}nH_2O$ structure indeed shows higher capacity and better stability, particularly at high charge-discharge rates. Depending on the needs, one can trade Na insertion capacity with the stability and reversibility by selecting proper potential windows. These results provide insights into new directions to overcome the bottleneck of current SIB cathode materials.

A schematic of the sample preparation process is illustrated in Figure 6.1a. Digital optical images of the sample at various processing steps are presented in Figures 6.1b-d. The as-deposited VACNF-V_2O_5 core-shell structure in Figure 6.1c shows a blue-green color attributed to the formation of disordered $V_2O_5{\cdot}nH_2O$ bilayers with an interlayer distance of 11.0 Å (see Figure 6.1e and discussion in later sections). The annealed sample in Figure 6.1d gives the characteristic bright yellow color representing the orthorhombic α-V_2O_5 crystal structure with an interlayer spacing of 4.36 Å (see Figure 6.1f).

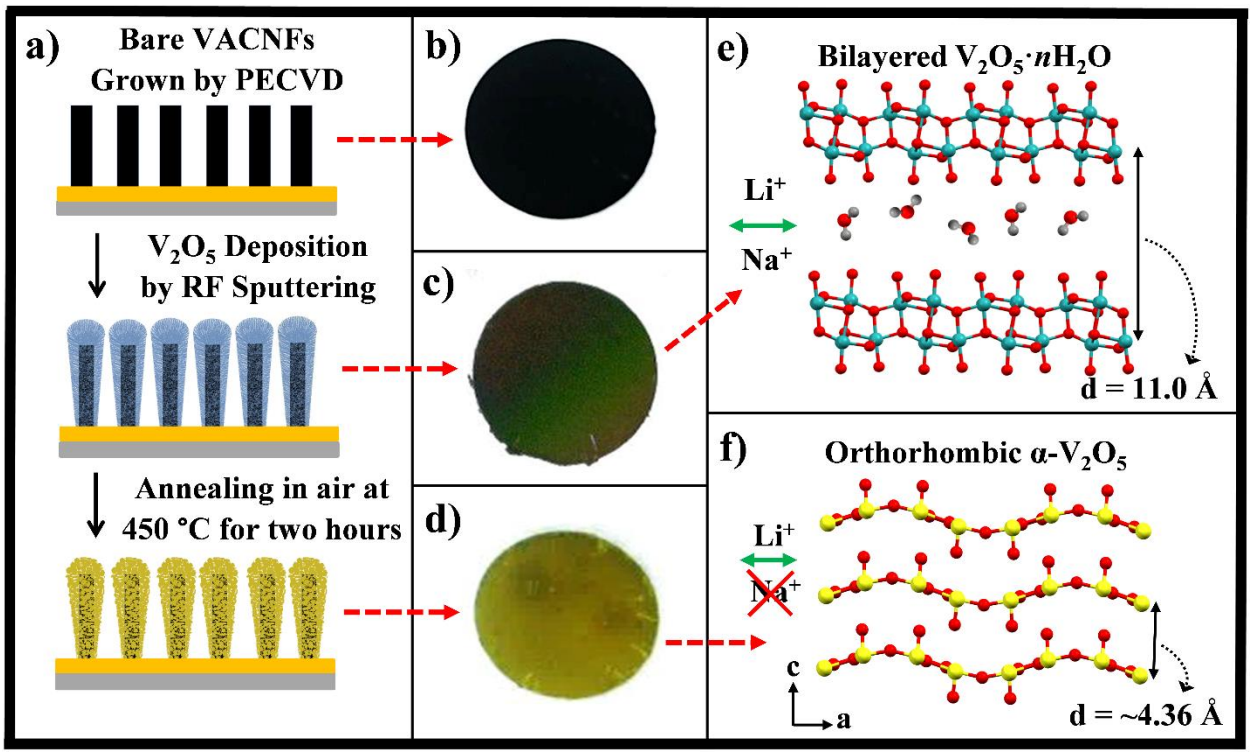

Figure 6.1 a) Schematic illustration of the processes to prepare the hybrid structure of V_2O_5 shells on VACNF cores. Digital photographs of b) bare VACNFs grown on the titanium foil covered with 100 nm Cr barrier layer, c) the "as-deposited" V_2O_5 on VACNFs, and d) after annealing in the air at 450° C for 2 hours. e) The large interlayer spacing of the disordered bilayered $V_2O_5 \cdot nH_2O$ shell in the "as-deposited" sample allowing reversible insertion/extraction of both Li^+ and Na^+ ions and f) the crystalline α-V_2O_5 in the thermal annealed sample only allowing insertion/extraction of smaller Li^+ ions.

6.2 Experimental Details

6.2.1 VACNF Growth

Titanium disks of 17.5 mm in diameter were cut from a 0.25 mm thick Ti foil (Alfa Aesar, Haverhill, MA) and coated with a 100 nm Cr barrier layer followed by a 22 nm Ni film using an ion beam sputtering system (Model 681, Gatan, Pleasanton, CA). VACNFs with an average length of ~5 μm were grown on the Ti/Cr/Ni disks using a DC-biased PECVD system (AIXTRON, Santa Clara, CA) following a previously published procedure.[234, 385, 387-388] A pre-treatment procedure was applied first by thermally heating the Ti/Cr/Ni disks to 500 °C in 250 sccm NH_3 at a pressure

of 3.9 Torr and then applying plasma at 40 Watts for 60 seconds. The combined effect of thermal dewetting and NH_3 plasma etching broke the Ni film into randomly distributed nanoparticles that catalyzed the growth of VACNFs in a tip growth mode.[234, 385] The diameter and distribution of the VACNFs were mostly determined by these Ni nanoparticles. After pre-treatment, a mixture of acetylene (at 70 sccm) and ammonia (at 250 sccm) was used as the precursors for the VACNF growth at substrate temperature of 740 °C and a pressure of 4.6 Torr. The plasma power was kept at 45 Watts for 30 minutes to grow ~5.0 μm long VACNFs.[387]

6.2.2 V_2O_5 Deposition and Annealing

V_2O_5 was deposited on the VACNFs using RF sputtering of a high purity (99.99%) V_2O_5 target of 50 mm in diameter. The V_2O_5 target was kept at a distance of 30 mm from the VACNF substrate that was maintained at room temperature during the deposition. The sputtering gun was inclined at a 45° angle toward the V_2O_5 target for optimal deposition. The processing chamber was evacuated to $< 3\times10^{-6}$ Torr prior to deposition. During deposition, a power of 150 W was applied to the sputtering gun at a working pressure of 10 mTorr (92% Ar + 8% O_2 by volume). The V_2O_5 target was pre-sputtered for ten-minutes in order to obtain a fresh V_2O_5 surface. The amount of V_2O_5 deposited onto the VACNF substrate was found to be equivalent to a uniform film thickness of 425 nm, which was confirmed using flat Si/SiO_2 substrate placed in the same place, i.e. a nominal thickness of 425 nm after 120-minute of deposition. Following the deposition, the substrate was allowed to cool for at least 30 minutes prior to removal from the chamber. Some VACNF-V_2O_5 core-shell structures were subjected to post-growth annealing in air at 450 °C for two hours, which facilitated crystallization of the V_2O_5 shells on the VACNFs.

6.2.3 Materials Characterization

The surface morphology of the VACNF-V_2O_5 core-shell structures were investigated using a Versa 3D Dual Beam (FEI, Hillsborro, OR) field emission scanning electron microscope (SEM). The microstructure of the sample was examined using a Tecnai F20 XT (FEI, Hillsborro, OR) high resolution transmission electron microscope (HRTEM). The crystallinity was evaluated using a PANalytical Empyrean (PANalytical, Almelo, The Netherlands) x-ray diffractometer (XRD). Diffraction analysis was conducted from 10° to 60° using a Cu K_α source (8,979 eV). Raman spectra were obtained using a Thermo Scientific DXR system at a laser wavelength of 532 nm. X-ray photoelectron spectroscopy (XPS) spectra were obtained using a PHI 5000 Versa system with a monochromated Al K_α source (1,486.7 eV) to further evaluate the valance state of the vanadium oxide near the surface.

6.2.4 Electrochemical Characterization

To evaluate electrochemical performance, the VACNF-V_2O_5 cathodes were assembled against 16-mm dia. sodium disk anodes into stainless steel coin cells (CR2032, MTI Corporation, Richmond, CA). A 0.65 mm thick glass fiber disk (El-Cell, Hamburg, Germany) was used as the separator. The cell was assembled in an argon filled M-Braun LabStar50 stainless steel glovebox (Garching, Germany) with < 1 ppm of O_2 and H_2O contents. The electrolyte consisted of 1.0 M sodium perchlorate ($NaClO_4$) in propylene carbonate (PC). Galvanostatic charge-discharge cycles were performed using a MTI 8 channel battery analyzer (MTI Corporation, Richmond CA). All gravimetric capacities were calculated relative to the mass of V_2O_5. Cyclic voltammetry (CV) measurements and electrochemical impedance spectroscopy (EIS) were performed using a CHI760D potentiostat (CH Instruments, Austin, TX).

6.3 Results and Discussion

6.3.1 SEM/TEM Characterization of Materials Morphology

The low-magnification SEM image in Figure 6.2a shows the formation of a uniform coaxial V_2O_5 coating onto the VACNFs. The high-magnification image in Figure 6.2b shows a rough texture extending across the shell surface representing a distinctive feature of the nanocolumnar microstructure that commonly forms in thick sputtered films on unheated substrates.[348] A TEM image of the as-deposited VACNF-V_2O_5 core-shell structure is shown in Figure 6.2c. A thick coating can be seen at the top of the VACNF which tappers off down the shaft forming a cotton swab like structure. This phenomenon can be described as a snow fall effect which is a common theme in sputtering deposition on non-flat surfaces. The dark tear shaped region in the center is the nickel catalyst embedded at the tip of the VACNF whose shaft is embedded in the V_2O_5 as the light gray column below the Ni catalyst particle. The contour of the VACNF surface is visually highlighted with the white dashed lines. The high-resolution TEM (HRTEM) image in Figure 6.2d reveals that the V_2O_5 is porous and amorphous at atomic scales, which is further confirmed by the diffusive pattern of the selective area electron diffraction (SAED) in the insert. As we discussed above, the amorphous open porous structure is advantageous to insertion of sodium ions with a large ionic radius. Upon thermal annealing, the nanocolumnar V_2O_5 structure is converted into denser nanocrystalline domains of ~ 50 to 100 nm in size, as illustrated in Figure 6.2e. The HRTEM image in Figure 6.2f shows the highly ordered crystalline lattices of the annealed V_2O_5 with sharp diffraction spots in the SAED pattern shown in the inset.

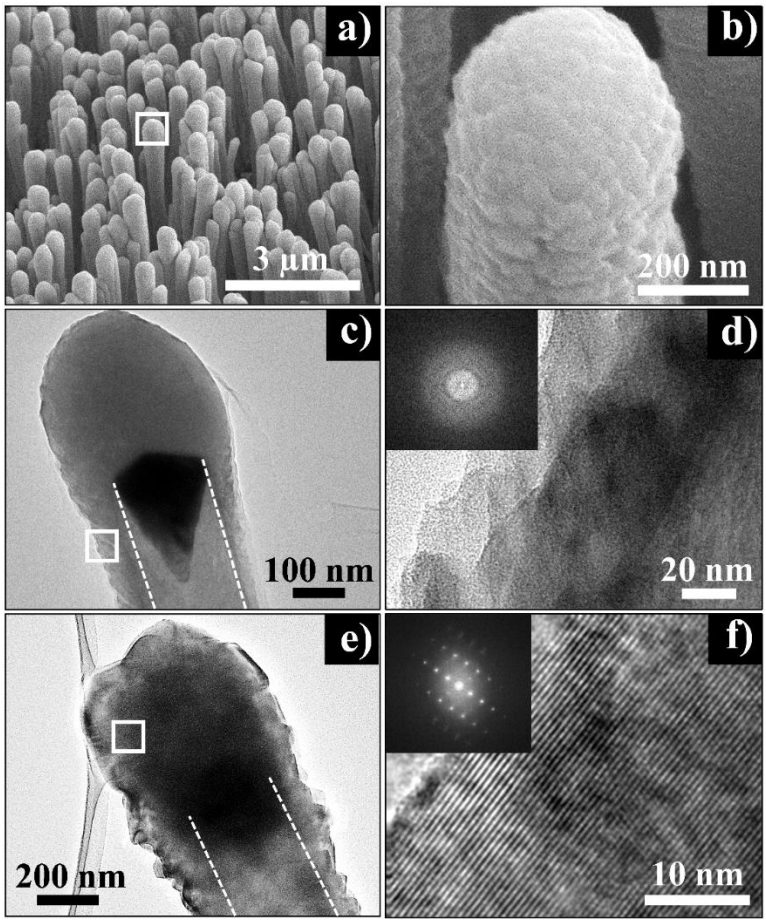

Figure 6.2 SEM images of the as-deposited VACNF-V_2O_5 core-shell structures at a) low magnification and b) high magnification. TEM images of the as deposited VACNF-V_2O_5 core-shell structures at c) low magnification and d) high magnification. The white dashed lines have been inserted to indicate the contour of the VACNF surface. TEM images of the annealed VACNF-V_2O_5 core-shell structure at e) low magnification and f) high magnification. SAED patterns of the as-deposited and annealed samples are presented in the insert of d) and f), respectively.

6.3.2 Spectroscopy Characterization of Materials Composition

The XRD patterns of the VACNF-V_2O_5 samples are presented in Figure 6.3a. The as-deposited core-shell structures (blue) show only a single peak at 7.86° corresponding to a d-spacing of 11.0 Å, which can be attributed to (001) diffraction of hydrated $V_2O_5{\cdot}nH_2O$ bilayers. The coherent length calculated from the fitted Gaussian peak width is 3.87 nm (about a stack of only 4 to 5 V_2O_5 bilayers). The low intensity and the large width of the (001) diffraction peak as well as

the absence of in-plane diffraction peaks indicate that the bilayered structure is highly disordered with only short-range stacking order, which is consistent with the amorphous nature revealed by the diffuse SAED pattern in the inset of Figure 6.2d. Thus, the as-deposited V_2O_5 shell is more appropriately referred to as metastable disordered $V_2O_5 \cdot nH_2O$ bilayers. In contrast, the annealed film (red) shows sharp diffraction peaks that match well with the JCPDS: 41-1426 database (black) and thus can be attributed to the highly ordered orthorhombic α-V_2O_5 crystals.

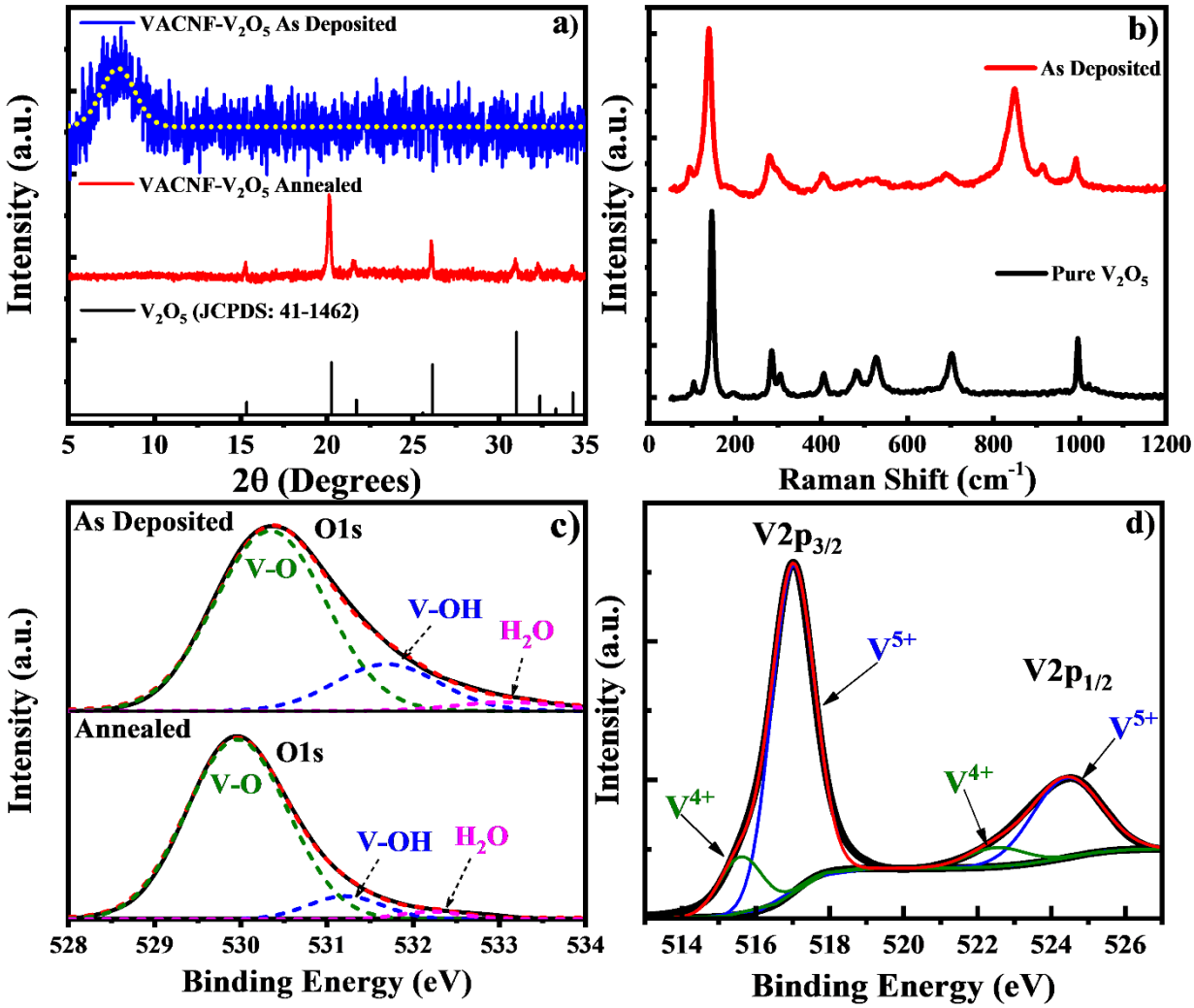

Figure 6.3 a) XRD patterns of the as-deposited and annealed VACNF-V_2O_5 core-shell structures. b) Raman spectra of the as-deposited VACNF-V_2O_5 core-shell structures in comparison with a pure V_2O_5 powder. Deconvoluted XPS core level spectra of c) O1s c) of both structures and d) V2$p_{3/2}$ of the as-deposited VACNF-V_2O_5 core-shell structure.

The Raman spectra of the as-deposited VACNF-V_2O_5 core-shell structures is shown in Figure 6.3b. The typical peaks of V_2O_5 (146, 283, 304, 405, 475, 685, and 993 cm^{-1}) are observed and match well with the pure V_2O_5 nanopowder.[389] The peak at 993 cm^{-1} is characteristic of α-V_2O_5 corresponding to the stretching mode of the vanadyl V=O double bond, which does not exist in the lower oxidation states of vanadium oxides. The stretching mode of V-O-V corresponds to the peak at 685 cm^{-1}. The peaks located at 475 and 405 cm^{-1} are assigned to the bending vibration of V_2-O, and the V=O bonds of α-V_2O_5, respectively. The partially resolved peak at 305 cm^{-1} is due to the bending vibration of the triply bonded V_3-O bond in V_2O_5, but is mostly overlapped with the peak at 286 cm^{-1} corresponding to the bending vibration of V=O bonds of α-V_2O_5. The peak at 146 cm^{-1} corresponds to the long-range external mode of α-V_2O_5, suggesting formation of extended α-V_2O_5 bonding. These results suggest that the as-deposited films indeed contain characteristic Raman peaks for V_2O_5.[390-391]

However, an anomalous peak appears at 850 cm^{-1} which doesn't match any of the common V_2O_5 peaks in literature.[332] In our previous study, we attribute this peak mainly to the hydration of the V_2O_5 surface originating from moisture in the air which matches well with previous Raman spectroscopy studies by Bell *et al.* on supported V_2O_5 catalyst.[351] This assumption is consistent with a report by Marx *et al* that described Raman peaks in the range 750-950 cm^{-1} corresponding to short-range order vibrations of metastable V_2O_5.[392] It should be noted that the hydration peak significantly decreases in intensity in the annealed structure with no other significant differences. The water content was not quantified in this work, however, the 11.0 Å d-space indicates that it likely contains no more than one mole of H_2O per mole of V_2O_5, i.e. with a chemical formula $V_2O_5 \cdot nH_2O$ ($n < 1$).[378, 393] In terms of battery safety, it is expected that such a low H_2O content, particularly embedded in V_2O_5 bilayers, does not pose risks in practical applications. Interestingly,

the hydrated or hydrogenated mesoporous metal oxides have been reported in several studies to facilitate higher electrical conductivity and generate larger pseudocapacitance.[352-354]

XPS was used to investigate the chemical bonding and elemental compositions of the VACNF-V_2O_5 core-shell structures. The wide-scan XPS survey and the expanded $V2p_{3/2}$, $V2p_{1/2}$, and O1s spectra are shown in Figure E.1. The binding energies of the $V2p_{3/2}$, $V2p_{1/2}$, and O1s peaks appear at 517.0, 524.4 and 530.4 eV, respectively, in the as-deposited metastable core-shell structure. After annealing, a downshift by 0.4 - 0.6 eV to 516.4, 523.9, and 530.0 eV is observed. The downshift in these XPS peaks serves as an indication of the degree of dehydration, as reported by Uchaker *et al*.[377] In addition, more detailed information can be extracted from the peak shapes. Figure 6.3c shows the deconvolution of the XPS O1s peaks from both the as-deposited and annealed samples, which consist of a V-O peak (~ 529.4 - 530 eV) and a V-OH peak (~ 531 - 532 eV). The very weak peak above 532 eV is likely due to physisorbed H_2O molecules. A quantitative analysis shows that the ratio of the peak area between V-OH and V-O decreases after annealing, confirming that the as-deposited sample is hydrated. Meanwhile, both the $V2p_{3/2}$ and $V2p_{1/2}$ peaks of the as-deposited sample can be resolved into two contributions, V^{4+} and V^{5+} as shown in Figure 6.3d. Noting that the $V2p_{1/2}$ peak is overlapped with the O1s satellite peak, we used only the $V2p_{3/2}$ peak for quantitative analysis, which indicates that about 82.5% of the vanadium are in V^{5+} state in the as-deposited samples (Figure 6.3d) and it increased to ~94% in the annealed sample (see Figure E.1c). The results from XRD, Raman and XPS altogether suggest that the as-deposited material is mainly hydrated amorphous metastable V_2O_5 bilayer structure mixed with a small amount of VO_2 at the surface. After thermal annealing, the hydration is removed, the VO_2 at the surface is oxidized to V_2O_5, and the metastable V_2O_5 is converted into stable connected crystalline nanoparticles.

6.3.3 Assessment of Na^+/V_2O_5 Insertion between 3.5 – 1.0 V

The nominal thickness of V_2O_5 deposition was measured to be 425 nm using a flat Si substrate as reference.[386] From this, the mass of V_2O_5 deposited on each 2.40 cm^2 VACNF disk electrode can be estimated to be 0.343 mg based on the density of bulk V_2O_5 (3.36 g cm^{-3}). To better assess the materials properties and compare them with the theoretical values, only the mass of V_2O_5 is used for gravimetric capacity calculations in this study. It needs to be noted that we may have overestimated the V_2O_5 mass since the micro-porosity and hydration may lower the density of the deposited V_2O_5 film. The accurate gravimetric capacity may be slightly higher.

The Na-ion storage properties of the above described metastable VACNF-V_2O_5 core-shell structures in the as-deposited samples were systematically characterized in half-cell configuration using CR2016 coin cells. The as-assembled cell was in the charged state with a cell voltage in the range of 1.7 – 2.7 V. A galvanostatic discharge process was carried out first and followed by alternating charge/discharge measurements at different current densities in fixed potential windows. Coulombic efficiency was calculated as the percentage ratio of the discharge (Na^+ insertion) capacity to the charge (Na^+ extraction) capacity in the prior step. C rates (rather than current densities) are commonly used in literature for battery characterization. To avoid confusion, in this paper, all referred C rates are based on the actual time to complete a charge/discharge process at the specific current density, with a rate of C/n corresponding to the condition to complete charging or discharging in n hours. For $n \leq 1$, an alternative notation (1/n)C is used for simplicity.

The Na^+ insertion/extraction properties of the metastable VACNF-V_2O_5 core-shell structures were first investigated using two galvanostatic charge-discharge rate performance sequences in the commonly used voltage range of 3.5 – 1.0 V (vs. Na/Na^+) as shown in Figure E.2. Cells were discharged/charged for 10 cycles at 5 different current rates (250, 500, 750, 1000, and

1500 mA g^{-1}) before returning to the initial rate (250 mA g^{-1}) in cycle 51. An insertion capacity of 196 mAh g^{-1} was observed at a rate of 250 mA g^{-1} in the 2nd cycle but dropped to 152 mAh g^{-1} (1.6C) in cycle 10. Insertion capacities of 122, 105, 93, and 78 mAh g^{-1} were achieved at the last cycle at rates of 500, 750, 1000, and 1500 mA g^{-1}, respectively, corresponding to C-rates of 4.1C, 7.1C, 10.9C, and 19.5C. It should be noted that a stable insertion capacity of 122 mAh g^{-1} at rate of 500 mA g^{-1} is comparable to the performance of commercialized $LiCoO_2$ in LIBs. Moreover, the ability to retain a high capacity of 78 mAh g^{-1} at the large current density of 1500 mA g^{-1} is rarely reported in literature. Interestingly, the extract capacity was about 70 to 50 mAh g^{-1} higher than the insertion capacity in the initial 10 cycles at the lowest current density (250 mA g^{-1}). The difference was dramatically reduced as the current density was increased. Accordingly, even though the coulombic efficiency was only 80-85% initially at the lowest charge/discharge rate, it quickly increased as the rate was increased and reached ~95% at the highest rate of 19.5C (1500 mA g^{-1}). This is in contrast to the LIBs whose coulombic efficiencies typically decrease at higher rates. When the rate sequence was repeated a second time, an insertion capacity of 115 mAh g^{-1} was achieved at the beginning in cycle 52 and more stable insertion capacities of 85, 72, 63, and 53 mAh g^{-1} were achieved at rates of 500, 750, 1000, and 1500 mA g^{-1}, respectively, in cycles 60-100. The stability and reversibility (as indicated by the coulombic efficiency) were steadily improved with the cycle number.

6.3.4 Assessment of Na^+/V_2O_5 Insertion between 4.0 – 1.5 V

The reversibility of Na^+ insertion/extraction in the metastable VACNF-V_2O_5 core-shell structures can be significantly improved by raising the voltage range to 4.0 – 1.5 V (vs. Na/Na^+) as shown in the three galvanostatic charge-discharge rate performance sequences in Figure 6.4a. An insertion capacity of 145 mAh g^{-1} was observed at a rate of 250 mA g^{-1} in the 2nd cycle but

dropped to 122 mAh g^{-1} in 10th cycle. The extraction capacity was ~54.7 mAh g^{-1} higher than the insertion capacity in the 2nd cycle but the difference dropped to only ~14.4 mAh g^{-1} in the 10th cycle, with the coulombic efficiency increased from ~73% to ~89%. The insertion capacity dropped to 94 mAh g^{-1} when the rate was increased to 500 mA g^{-1} (~5C) in cycle 20. Last cycle insertion capacities of 80, 70, and 58 mAh g^{-1} were achieved at rates of 750, 1000, and 1500 mA g^{-1}, respectively, corresponding to the C-rate of about 9C, 14C, and 25.7C. Moreover, the coulombic efficiency steadily increased from 95% in cycle 20 to 98% in cycle 50 (1500 mA g^{-1}). When the current density was returned to 250 mA g^{-1} in cycle 52 an insertion capacity of 97 mAh g^{-1} was achieved resulting in a capacity retention of ~80%. Last cycle insertion capacities of 90, 70, 60, 52, and 43 mAh g^{-1} were achieved at rates of 250, 500, 750, 1000, and 1500 mA g^{-1}, respectively, in cycles 60-100. Moreover, the coulombic efficiency was further improved in the 2nd and 3rd rate sequences and reached ~99% at the rate of 1500 mA g^{-1}. Even the lowest rate gave a coulombic efficiency above 94%. It should be noted that the Na^+ insertion/extraction in literature commonly showed low coulombic efficiency with the extraction capacity higher than insertion value.[215, 217] The reason for larger extraction capacity was not well understood but was presumably attributed to side oxidation reaction of electrolytes. This has been a bottleneck for stable NIB cathode materials. In this study, as shown in Figure 6.4a, a capacity retention of over ~75% was retained at all respective rates in the 2nd rate sequence consisting of 50 total cycles, comparing to the stabilized values in the first rate sequence. The last cycle insertion capacities were 74, 58, 49, 43, and 35 mAh g^{-1} in the third-rate performance sequence at the rate of 250, 500, 750, 1000, and 1500 mA g^{-1}, respectively, able to retain >95% of capacity comparing to the 2nd rate sequence

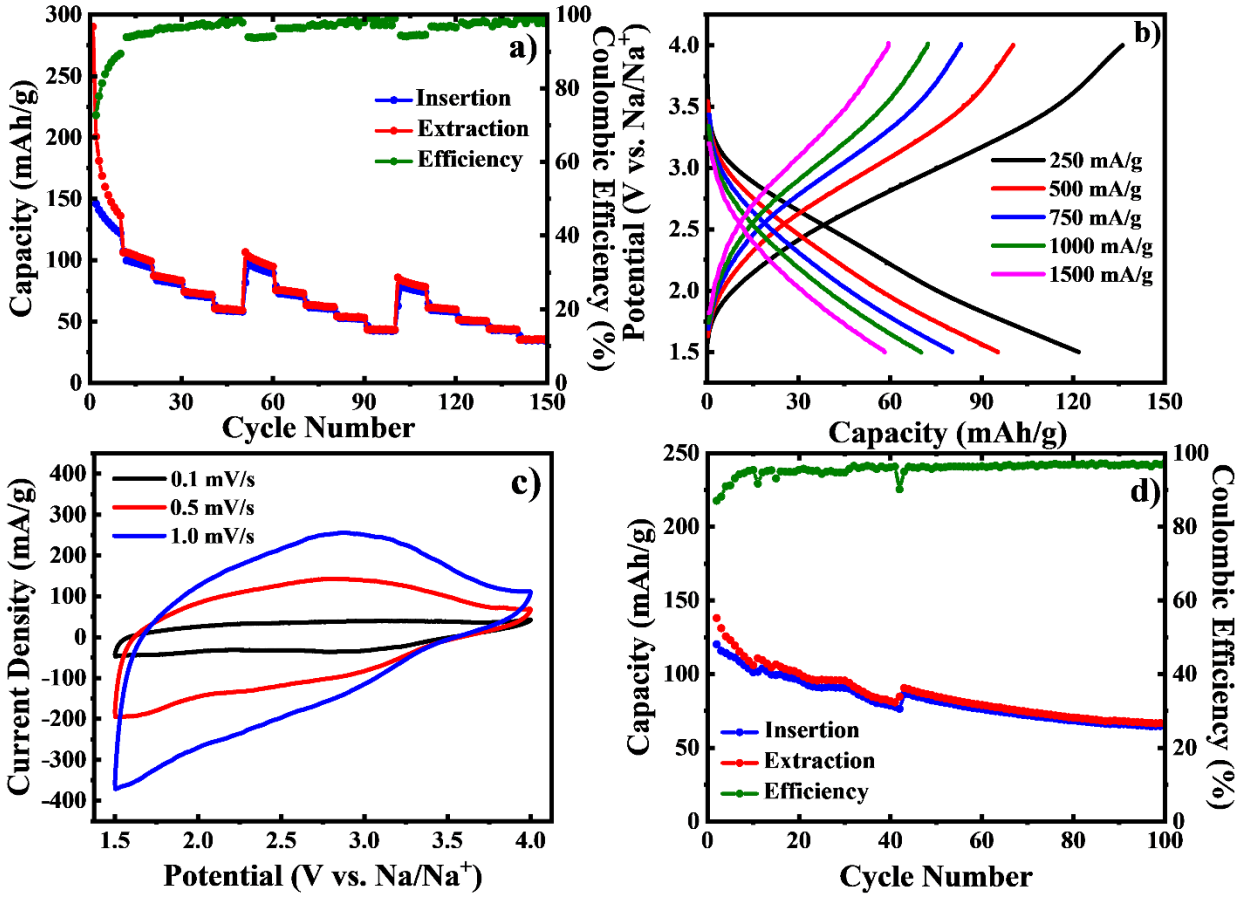

Figure 6.4 Electrochemical characterization of the Na^+/V_2O_5 insertion/extraction of the as-deposited VACNF-V_2O_5 core-shell structure in the potential range of 4.0 – 1.5 V (vs. Na/Na^+). a) Rate performance at 5 different current density values (250, 500, 750, 1000, and 1500 mA g^{-1}), each for 10 charge-discharge cycles. b) The galvanostatic charge-discharge profiles at the last cycle at each current density in the rate performance. c) Cyclic voltammetry curves at 0.1 (black), 0.5 (red) and 1.0 (blue) mVs^{-1}. d) Long-term cycling at the rate of 625 mA g^{-1}. Note: the jump at cycle 42 was due to a power surge that interrupted the long cycling.

The galvanostatic charge-discharge curves in the last cycle at current rates of 250 (black), 500 (red), 750 (blue), 1000 (magenta), and 1500 (green) mA g^{-1} in the first rate-performance sequence are presented in Figure 6.4b. All profiles showed nearly linear curves without any clear flat plateaus that are commonly observed in crystalline materials, indicating that the system behaved like a pseudocapacitor similar to the study on $V_2O_5 \cdot nH_2O$ xerogel composed of interconnected nanowire networks.[378] These properties explain why we were able to obtain the

high stability and coulombic efficiency, especially at the high current rates. The high degree of pseudocapacitance contribution is also seen in the CV curves in Figure 6.4c. Only a single broad reduction peak was observed between 2.0 – 3.3 V (vs. Na/Na^+) on top of a high continuous capacitive background current at scan rates of 0.1 to 1.0 mV s^{-1}. The peak shifted to 2.5 – 3.5 V (vs. Na/Na^+) in oxidation direction. It's likely that the redox peaks accompanying the multiple phase transitions during Na^+ insertion/extraction are broadened and superimposed due to the high degree of disorder in the as-deposited VACNF-V_2O_5, which is better illustrated in the CV curve at the scan rate of 0.1 mV s^{-1} in Figure E.3. It is clear that the sample was dominated by the pseudocapacitive features. Furthermore, the long-term cycling stability at 625 mA g^{-1} is presented in Figure 6.4d. A reversible insertion capacity of 120 mAh g^{-1} was achieved in the 2nd cycle. The capacity dropped quickly in the initial cycles but became stabilized at ~100 mAh g^{-1} after 10 cycles while the coulombic efficiency increased from 87% to ~97%. After 100 cycles an insertion capacity of 65 mAh g^{-1} was observed resulting in a capacity retention of 65% from cycle 10 to 100. Though the capacity retention is not ideal, it's among the best of current SIB cathodes. The cycling was continued up to 300 cycles as shown in Figure E.4 with a final insertion capacity of 36 mAh g^{-1} and a remarkable coulombic efficiency of ~99%.

6.3.5 Assessment of Na^+/V_2O_5 Insertion between 4.0 – 1.0 V

From the results in Figure 6.4 (in 4.0 – 1.5 V) and Figure E.2 (in 3.5 – 1.0 V), it is clear that the potential window critically affects both the capacity and coulombic efficiency. To find the optimal conditions, the three galvanostatic charge-discharge rate sequences were applied in the expanded potential window of 4.0 – 1.0 V (vs. Na/Na^+), as shown in Figure 6.5. An insertion capacity of 277 mAh g^{-1} was observed at a rate of 250 mA g^{-1} in the 2nd cycle but dropped to 207 mAh g^{-1} (0.9C) in cycle 10. It should be noted that a capacity of 277 mAh g^{-1} corresponds to

1.9Na^+ per V_2O_5, which is higher than the reported theoretical value of 236 mAh g^{-1} (1.6Na^+).[211-212, 374-376] This capacity is even higher than the state-of-the-art study based on $V_2O_5{\cdot}nH_2O$ xerogel networks at the similar current density[378] and the same potential window, which can be attributed to the VACNF-V_2O_5 core-shell structure with the disordered bilayered $V_2O_5{\cdot}nH_2O$ shell. Last cycle insertion capacities of 118, 87, 69, and 52 mAh g^{-1} were achieved at rates of 500, 750, 1000, and 1500 mA g^{-1}, respectively, corresponding to 4.3C, 8.5C, 14.5C, and 29C. However, though it showed a similar trend that higher coulombic efficiency can be obtained at higher rates, the highest value is only ~94%. Overall, by expanding the potential window to 4.0 – 1.0 V (vs Na/Na^+) as used in most literature, we can get higher Na^+ insertion capacity. But the coulombic efficiency and cycling stability are sacrificed.

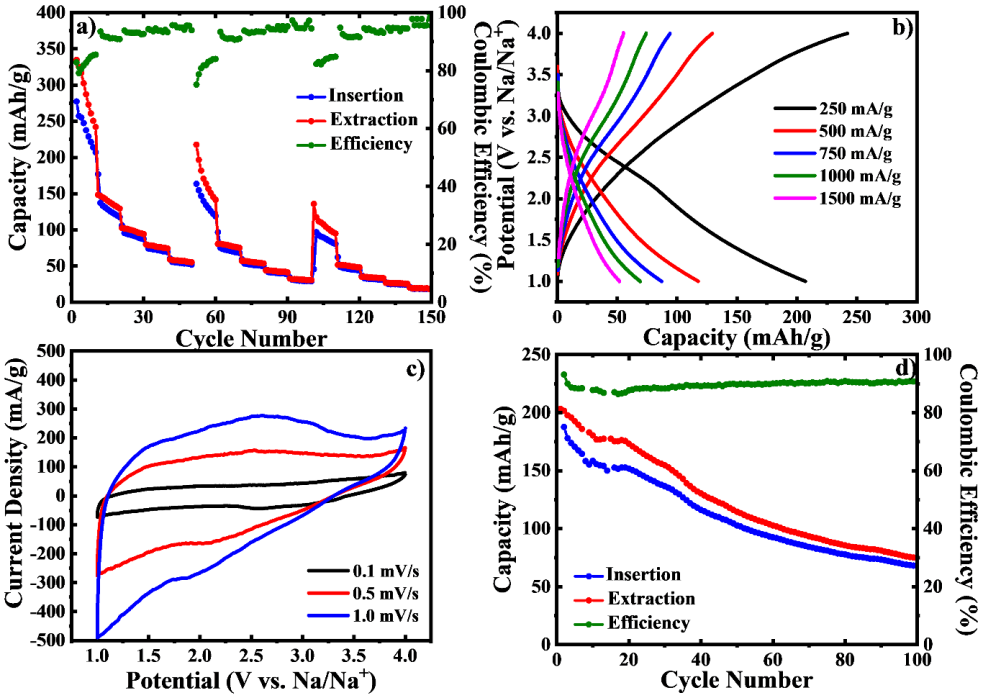

Figure 6.5 Electrochemical characterization of the Na^+/V_2O_5 insertion/extraction of the as-deposited VACNF-V_2O_5 core-shell structure in the potential range of 4.0 – 1.0 V (vs. Na/Na^+). a) Rate performance at 5 different current density values (250, 500, 750, 1000, and 1500 mA g^{-1}), each for 10 charge-discharge cycles. B) The galvanostatic charge-discharge profiles at the last cycle at each current density in the rate performance. c) Cyclic voltammetry curves at 0.1 (black), 0.5 (red) and 1.0 (blue) mV s^{-1}. d) Long-term cycling at the rate of 625 mA g^{-1}.

The galvanostatic charge-discharge curves at different current rates (Figure 6.5b) and CVs in the potential range of 4.0 to 1.0 V (Figure 6.5c) are similar to those in 4.0 to 1.5 V shown Figure 6.4. Interestingly, the first five CV curves at a scan rate of 0.1 mV s^{-1} in Figure E.5 show better resolved redox peaks that quickly decreased and merged into the broad pseudocapacitive feature similar to Figure E.3. It's likely that these peaks were originated from Na^+ ion insertion/extraction into short-range ordered V_2O_5 domains that were disrupted after several cycles. The disappearance of these peaks could explain the rapid capacity fading at the low rates in the initial cycles of the rate performance tests. The core-shell structures provide the capability that even the fully disordered V_2O_5 shell is accessible for the fast surface redox reactions. The long-term cycling at a rate of 625 mA g^{-1} is presented in Figure 6.5d, which further shows the lower coulombic efficiency and fast capacity fading even though the initial capacities are higher than in the narrower potential range of 4.0 to 1.5 V.

6.3.6 Assessment of Na^+/V_2O_5 Insertion between 4.0 – 2.0 V

To further evaluate the properties of the Na^+ insertion in the as-prepared VACNF-V_2O_5 core-shell structures, similar measurements were carried out in the potential window of 4.0 – 2.0 V (vs Na/Na^+) as shown in Figure E.6. While the insertion capacity dropped to 91 mAh g^{-1} (2.7C) in cycle 10 at 250 mA g^{-1}, it out-performed those in the potential window of 4.0 – 1.0 V (vs Na/Na^+) at higher rates in later cycles. Moreover, the coulombic efficiency improved to ~94% at the rate of 250 mA g^{-1} in the second and third rate performances and remained steady at > ~99% at all other rates. The charge-discharge and CV curves showed similar features as those in the wider potential windows, indicating a large pseudocapacitance contribution of the disordered bilayered $V_2O_5 \cdot nH_2O$ structure.

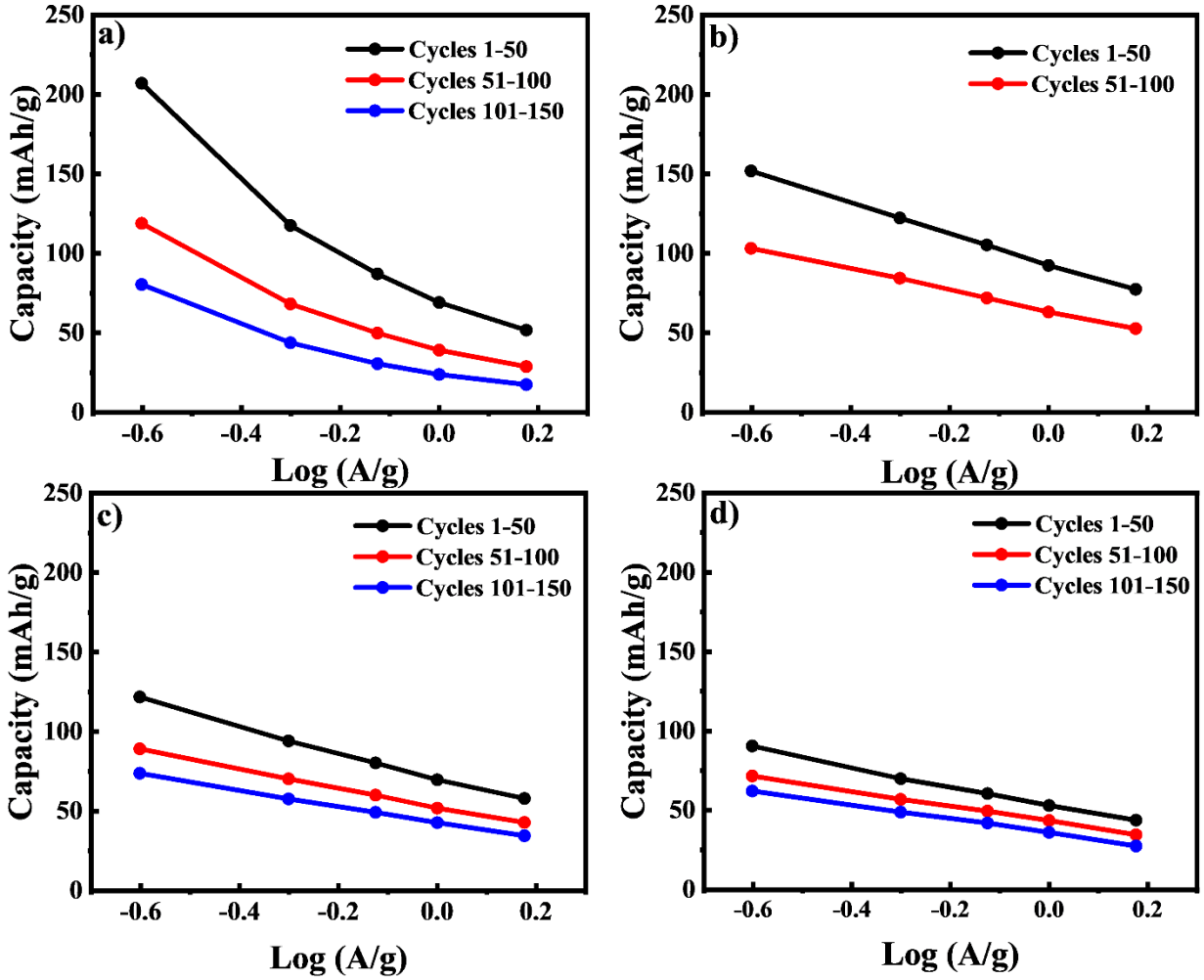

Figure 6.6 Comparison of the capacity and stability in the potential ranges of a) 4.0 – 1.0 V, b) 3.5 – 1.0 V, c) 4.0 – 1.5 V, and d) 4.0 – 2.0 V (vs. Na/Na^+). The specific capacity from the last cycle at each specific rate is plot versus the logarithm of the applied current density. Data are from the above-discussed rate performance tests with cycles 1-50 (black), 51-100 (red), 101-150 (blue).

6.3.7 Correlation between Potential Window and Cycling Performance

Figure 6.6 illustrates the Na^+ insertion capacity and stability of the as-deposited VACNF-V_2O_5 core-shell structures in the four potential windows using the data from the rate testing sequences reported in Figures E.2, 6.4a, 6.5a and E.6a. The discharge (insertion) capacity of the last cycle at each rate is plotted against the logarithm of the applied current density. The highest insertion capacity of the as-deposited metastable VACNF-V_2O_5 core-shell structures can be observed in the potential range of 4.0 – 1.0 V (vs Na/Na^+) as shown in Figure 6.6a. Each of the

three curves corresponds to the cycle ranges of 1-50 (black), 51-100 (red), and 101-150 (blue). Here all three curves have a large separation, indicating a rapid capacity fading over 150 cycles. Figure 6.6b demonstrates a higher insertion capacity at the high rates when the potential window is restricted to 3.5 – 1.0 V (vs Na/Na^+) even though capacity is lower at the lowest rate. Figure 6.6c shows the decrease in separation between the three curves, indicating the higher capacity retention and coulombic efficiency in the potential window of 4.0 – 1.5 V (vs Na/Na^+), even though the insertion capacity is lower. Figure 6.6d shows three nearly overlapping curves when the potential window is restricted to 4.0 – 2.0 V (vs Na/Na^+), which further illustrates the tradeoff between capacity and stability.

6.3.8. Impedance Spectroscopy of Bilayered $V_2O_5 \cdot nH_2O$ as a NIB and LIB Cathode

All the above CVs and charge-discharge curves indicate that the as-deposited VACNF-V_2O_5 electrode is dominated by pseudocapacitive properties due to the large surface reactions of the disordered $V_2O_5 \cdot nH_2O$ bilayer structure. This is further supported by the EIS data shown in Figure 6.7. The Nyquist plot of the SIB half-cell measured at the open circuit voltage of ~2.4 V (vs. Na/Na^+) shows a clear semicircle at high AC frequencies, indicating the presence of faradaic reactions represented by a charge transfer resistance (R_{ct}), instead of the nearly vertical straight lines corresponding to true capacitors. Interestingly, the LIB half-cell using the same as-prepared disordered $V_2O_5 \cdot nH_2O$ bilayer shows a similar shaped Nyquist plots but with a much smaller semicircle. Both these two EIS spectra can be fitted with the equivalent circuit consisting of two RC branches shown in the inset of Figure 6.7. The two capacitors are replaced with the constant phase elements (CPEs) to account for the inhomogeneity of charge transfer reaction and a Warburg element is included to account for the slow diffusion at low frequencies. Apparently, the 2nd RC branch accounts for the main differences between the LIB and SIB. The value of R_{ct2} in SIB (573

Ω) is much larger than that in the LIB (106.2 Ω), which indicates that Na^+ insertion/extraction reactions in the as-prepared disordered $V_2O_5 \cdot nH_2O$ bilayer is more difficult than Li^+ ions and why the SIB is much less reversible and less stable than LIBs made of the same cathode, even with the larger interlayer spacing. Further, all the capacitance values of CPE1 and CPE2 in both the LIB and SIB are very small, only about $7x10^{-6}$ F to $2.8x10^{-3}$ F. Thus, the electrical double layer capacitance is negligible. The measured Na^+ or Li^+ insertion capacity is indeed due to surface faradaic reactions as reported by Wei et al.[378]

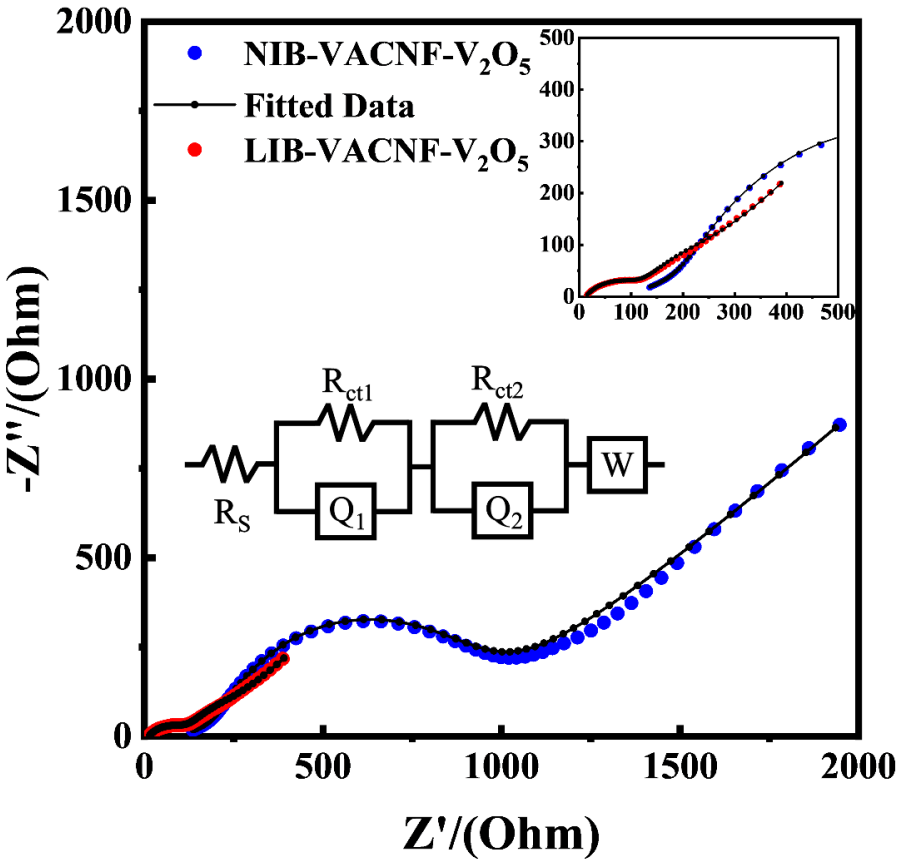

Figure 6.7 The Nyquist plots of electrochemical impedance spectroscopy of half-cell coin cells with an as-deposited VACNF-V_2O_5 electrode as the cathode and a Na disk anode for the SIB study (blue dots) and a Li disk anode for the LIB study (red dots). The EIS was measured at an open circuit voltage of 2.4 V (vs. Na/Na^+) for the SIB and at an open circuit voltage of 3.0 V (vs. Li/Li^+) for the LIB. The black dots are fitting data based on inset equivalent circuit. The inset at the upper-right corner shows the enlarged view in the low-impedance region.

6.3.9 Optimization of the Electrochemical Performance in the Range of 4.0 – 1.0 V

Since the potential range of 4.0 – 1.0 V (vs Na/Na^+) gave the highest capacity, we employed five strategies to explore the possibility of improving the stability of the VACNF-V_2O_5 core-shell structure in this potential range. In the first strategy, the electrolyte (1.0 M $NaClO_4$ in PC) was substituted with 1.0 M $NaClO_4$ in EC/DEC 1:1 (v/v). However, no significant improvements were observed as shown in Figure E.7. In the second strategy, the VACNF-V_2O_5 core-shell structures were annealed at 450 °C in air for two hours as was done in our previous study to form an orthorhombic crystalline shell.[386] The first few cycles were very unstable due to irreversible side reactions. An insertion capacity of ~315 mAh g^{-1} in the 3rd discharge with a long plateau at ~3.0 to 3.5 V was observed (Figure E.8), reflecting the behavior of crystalline electrodes. However, the capacity quickly faded and severe structural collapse was observed after 10 cycles. Clearly, the small interlayer d-spacing of orthorhombic V_2O_5 cannot accommodate reversible intercalation of large Na^+ ions, as reported in literature.[215, 217, 377] In the third strategy, annealing temperature was reduced to 250 °C to maintain partial hydration and the amorphous porous structure. When compared to the metastable as-deposited core-shell structure without annealing, the capacities increased at the higher rates, but the coulombic efficiency and stability degraded as shown in Figure E.9. Following the work of Tepavcevic *et al.*,[215] the fourth strategy was based on annealing the VACNF-V_2O_5 core-shell structure at 120 °C under vacuum for 20 hours to form an ordered bilayered $V_2O_5 \cdot nH_2O$ structure without losing hydration. However, no improvement was observed as shown in Figure E.10. In the fifth strategy, a 5.5 nm thick Al_2O_3 film was deposited on the as-deposited VACNF-V_2O_5 core-shell structure using atomic layer deposition (ALD) in order to create a barrier layer to suppress potential side reactions with the electrolyte during charging to 4.0 V.[394-397] Again, no significant improvements were observed as shown in Figure E.11. An in-

depth discussion of these strategies is provided in Appendix E to provide insights for future studies. At this stage, the as-deposited VACNF-V_2O_5 core-shell structure with highly disordered bilayered $V_2O_5{\cdot}nH_2O$ shell gave the best results.

6.4 Conclusions

In summary, V_2O_5 has been deposited on VACNF arrays by RF sputtering to form a unique three-dimensional VACNF-V_2O_5 core-shell structured SIB cathode. The as-deposited metastable V_2O_5 shell present a highly disordered bilayered $V_2O_5{\cdot}nH_2O$ structure with a large interlayer spacing of 11.0 Å that can facilitate Na^+ insertion. A high initial insertion capacity of 277 mAh g^{-1} was achieved in the potential window of 4.0 – 1.0 V (vs Na/Na^+) at the current density of 250 mA g^{-1}. However, such low current density yielded a significantly higher extraction capacity and low coulombic efficiency, which are part of the reason for rapid capacity fading. As the charge-discharge rate was increased (with the higher current density of 500, 750, 1000 and 1500 mA g^{-1}), the electrode became more reversible with the coulombic efficiency reaching ~94%. In fact, the coulombic efficiency can be increased to over 99% accompanying with clear improvements in cycling stability by lowering the upper limit to 3.5 V or increasing the lower limit to 1.5 or 2.0 V, but at the expense of losing some capacity. The optimal operation needs to balance the tradeoff of these properties. Higher reversibility and stability can be obtained at higher charge-discharge rates, which is attributed to the large pseudocapacitive contributions due to the fast surface reactions in the disordered bilayered $V_2O_5{\cdot}nH_2O$ structure, as supported by the CV and EIS results. At the current stage, the as-deposited VACNF-V_2O_5 structure with the disordered bilayered $V_2O_5{\cdot}nH_2O$ shell has shown superior performance at high charge-discharge rates ($\geq$ 1,000 mA g^{-1}) in the potential range of 4.0 to 1.5 V (vs. Na/Na^+) or at lower rates (down to 250 mA g^{-1}) in the range of

4.0 – 2.0 V (vs. Na/Na^+). This provides insights for further development of highly demanded stable SIB cathodes.

6.5 Acknowledgements

We would like to thank Ronald Rojeski of Catalyst Power Technologies Inc. for providing materials for this work, Prem Thapa and Maogang Gong of the University of Kansas for help in taking the TEM images, Qingfeng Liu for beneficial discussions of the XPS spectra, and Colleen Gura and Ian Andree of Kansas State University for their help with the XRD analyses. We would also like to thank Shah Valloppilly at the University of Nebraska Center for Materials for additional XRD analyses. This work was supported by NASA grant NNX13AD42A including the matching support by Kansas Board of Regents) and NSF grants CBET-1703263 and DMR-1707585. JW also acknowledges support from NSF-DMR-1508494 and ARO-W911NF-16-1-0029.

Chapter 7 - Future and Current Work

7.1: ALD of Al-Doped ZnO/HfO_2 Double layers on VACNFs

In a continuation of the conformal core−shell AZO/Al_2O_3/VACNF metal-insulator-metal work in chapter 2, we attempted to replicate the work using HfO_2 as the dielectric layer. Its reported that HfO_2 has a dielectric constant of ~25, which is significantly higher than the ~9.3 for Al_2O_3.[22-24] Though some material characterization work was done, we limit the discussion to the preliminary electrostatic characterization below.

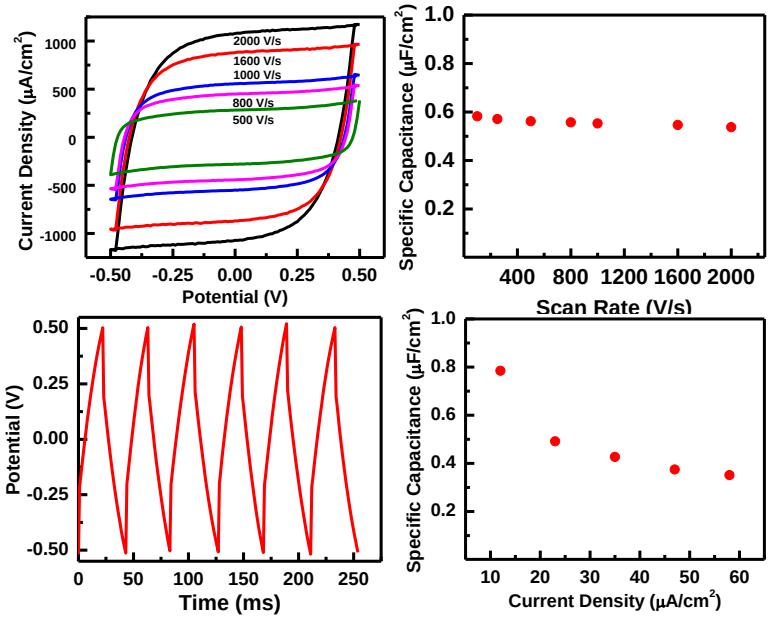

Figure 7.1 Electrical characterization of a planar capacitor. (a) I−V curves measured by cycling the bias voltage between −0.5 to +0.5 V at the rates of 500, 800, 1000, 1500 and 2000 V/s, respectively. (b) The area-specific capacitance vs the scan rate derived from the cycling I−V measurements. (c) Galvanostatic charge−discharge curve at a constant current density of 25 μA/cm^2. (d) Area-specific capacitance vs current density calculated from charge−discharge curves.

To assess the dielectric properties of ALD deposited HfO_2 we constructed an electrostatic planar capacitor of 2 mm x 2 mm lateral size with 20-nm HfO_2 dielectric layer deposited by ALD which was sandwiched between a 600-nm palladium top electrode and a 100-nm chromium bottom electrode on an n-doped silicon substrate as described in Chapter 2. Electrostatic characterization

was conducted to determine the specific capacitance of the planar electrode and the dielectric constants of the ALD deposited HfO_2. Figure 7.1a shows the cycling I-V curves of an annealed planar capacitor. The rectangular shapes indicate near ideal capacitive behavior. Both the charging and discharging curves are nearly horizontal indicating high Ohmic resistance across the thin HfO_2 dielectric film. The small rounded corners, along with the nearly vertical I-V curves at the voltage limits, indicate a low RC time constant, which is expected for an electrostatic capacitor. The value is nearly constant for scan rates from 500 V/s to 2000 V/s, indicating the capability of a high-power density, which is essential for an electrostatic capacitor as shown in Figure 7.1b. The area-specific capacitances of the planar capacitors were also determined by galvanostatic charge-discharge study at constant current densities. An ideal capacitor shows perfectly symmetric charging and discharging curves with identical time duration. A charge-discharge curve for the annealed planar capacitor at a current density of 25 $\mu A/cm^2$ is shown in Figure 7.1c with duration of ~25 milliseconds. A small IR drop can be seen at the beginning of each curve due to ESR (< 1 kΩ, mostly due to contact resistance) in the circuit. An area-specific capacitance value of ~0.4 $\mu F/cm^2$ is nearly consistent across all of the applied current densities as shown in Figure 7.1d. Unfortunately, a calculated dielectric value of ~11.3 was determined which is significantly lower than the reported values. Due to unavoidable circumstances, this project was put on hold in 2014.

7.2: Characterizing the Energy Storage Capability of Detonated Graphene as a Potential EDLC Material

In collaboration with Arjun Nepal and Dr. Chris Sorenson, the electrochemical characterization of a carbon aerosol gel (CAG) was evaluated as a potential EDLC. Briefly, the production of CAG involves a controlled detonation between acetylene (hydrocarbon) and oxygen (O_2) in a 16.6-liter cylindrical aluminum chamber.[398] The molar ratios of C_2H_2:O_2 were varied at

1:0.4, 1:0.5, 1:0.6, 1:0.7 and 1:0.8. During detonation, the hydrocarbon is first converted into nanometer size carbon monomers, which in turn quickly aggregated forming the CAG.[399] Once the detonation was complete, the chamber was cooled and the CAG powder was collected. For internal purposes, the CAG will be referred to as detonated graphene (DG) throughout the remainder of the section.

BET measurements confirm that the SSA lies in between 23 to 187 $m^2 g^{-1}$ as shown in Figure F.1. Interestingly, the lower oxygen ratios (0.4 and 0.5) have a significantly higher SSA than that of the higher oxygen ratios (0.6, 0.7, and 0.8). However, these values are significantly lower than the theoretical SSA of graphene (2600 $m^2 g^{-1}$). Electrochemical characterization was conducted in a two-electrode setup using the Swagelok apparatus discussed in Section 1.7. Briefly, a 9:1 mass ratio of DG to PVDF was mixed in a solution of NMP and dried at 100 °C for 18 hours under vacuum. The product was crushed and pressed in a KBr pellet press. Two DG pellets (electrodes) were separated by a polymer membrane separator soaked in an aqueous electrolyte (Na_2SO_4 or KOH). Electrochemical characterization was carried out using a 760E Bipotentiostat (CH Instruments Inc.).

The electrochemical performance was first evaluated using the 1:0.4 oxygen ratio DG in a 4.3 M KOH electrolyte as shown in Figure 7.2a. The near rectangular shape of the CV curves indicates good EDLC behavior with minimal rounding at the corners originating from the ESR. The mass-specific capacitance (C_o) was determined at each cycling rate using Equation 1.7, and is plotted in Figure 7.2b. The near horizontal trend at the high scan rates indicates a good power capability. The C_o was also determined by Galvanostatic charge-discharge at constant current densities as shown in Figure 7.2c. Both the charging and discharging curves are nearly symmetric

with a duration of ~150 seconds. The C_o was determined at each current density using Equation 1.8, and plotted in Figure 7.2d.

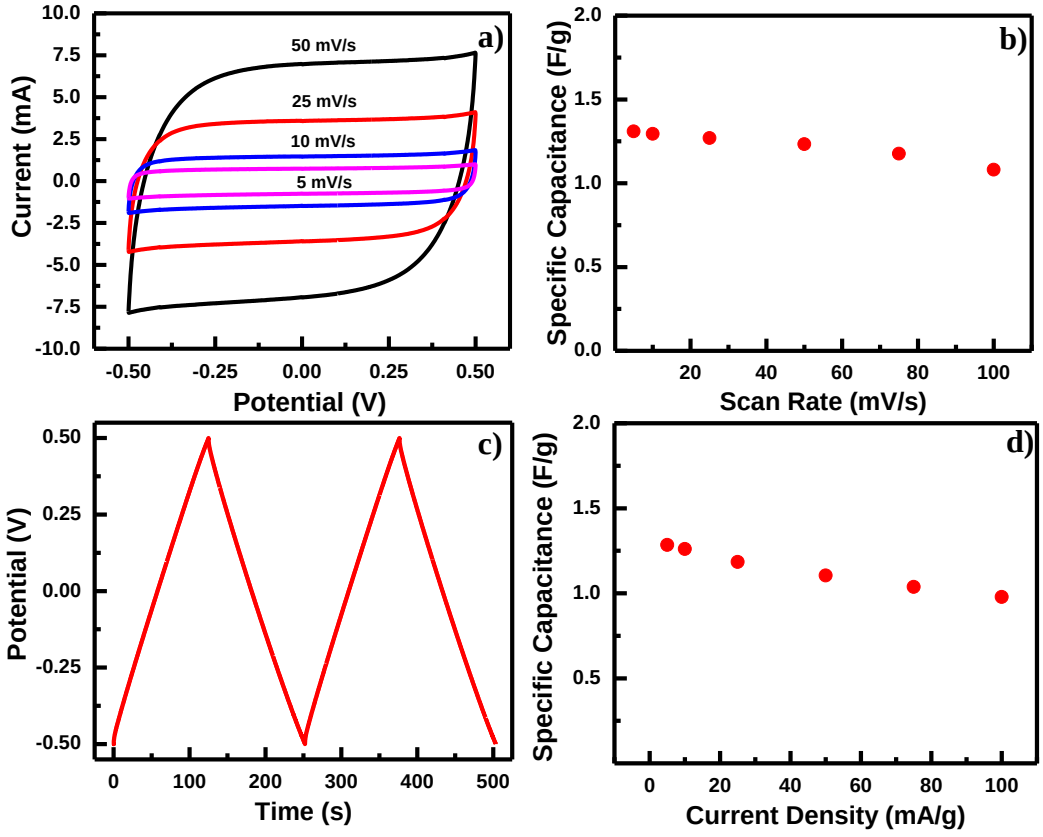

Figure 7.2 Electrochemical characterization of the detonated graphene in a Swagelok apparatus. (a) I−V curves measured by cycling the bias voltage between −0.5 to +0.5 V at the rates of 5, 10, 25 and 50 mV/s, respectively. (b) The mass-specific capacitance vs the scan rate derived from the cycling I−V measurements. (c) Galvanostatic charge−discharge curve at a constant current density of 20 mA/g. (d) mass-specific capacitance vs current density calculated from charge−discharge curves

The electrochemical performance was further evaluated for all five-oxygen ratio DGs using both a 1M Na_2SO_4 and 4.3 M KOH electrolyte solution. A plot of C_o values versus the different molar ratios for each electrolyte is shown in Figure F.2. As oxygen molar ratio decreased, the C_o increased owning to the increase in SSA. Interestingly, the 1:0.4 oxygen ratio DG did not follow this trend. The sudden drop in Co is likely due to the hydrophobicity of the DG coupled with the

larger SO_4^{-2} ion size and small pore size. The KOH solution has an increased capacitance over that of the Na_2SO_4 solution likely due to the increase in concentration.

The EDLC capability of DG was compared to the performance of commercially available carbon allotropes (MWCNTs, SWCNTs, and graphene (CG) with SSA of 370, 385, and 510 m^2/g, respectively), which were prepared and characterized in the same manner. The C_o values from the Galonstatic charge-discharge at a current density of 10 mA/g are plotted against the SSA values in Figure 7.3a. However, the plot illustrates the low C_o values owning to the low SSA of the DG. This is further illustrated in Figure 7.3b where the C_o values of the 1:0.4 oxygen ratio DG, MWCNTs, SWCNTs and CG are plotted against the applied scan rate. At 5 mV/s the 1:0.4 oxygen ratio DG had the lowest C_o value among all of carbon materials. Interestingly, as the scan rate increased, the C_o remained steady for the DG whereas the other carbon materials significantly decreased indicating potential as high-power EC. Ultimately, the low SSA of the DG hindered its use as a potential EDLC material. However, future work on this project involves the incorporation of a conductive polymer or metal oxide for a pseudocapacitive and LIB application.

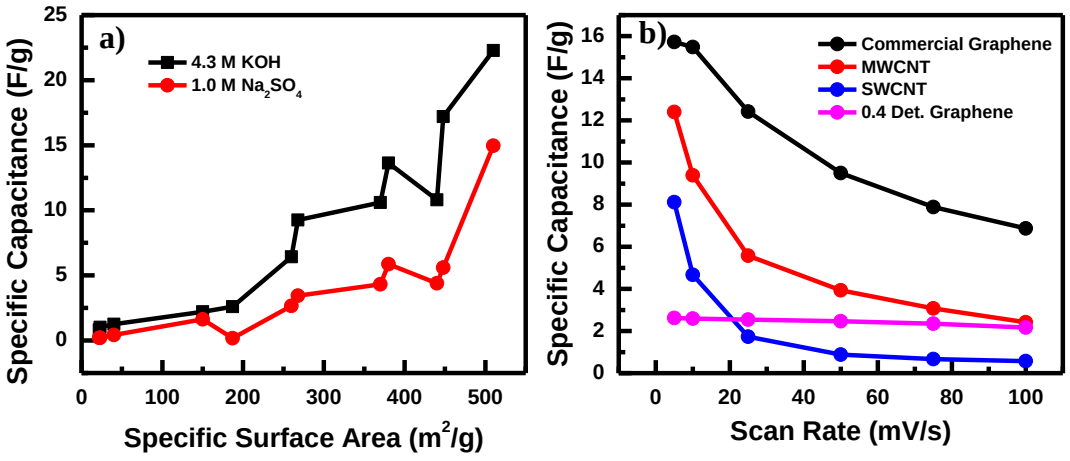

Figure 7.3 a) Mass-specific capacitance versus the specific surface area of the carbon electrodes. b) The mass-specific capacitance of the carbon electrodes versus the applied scan rates from the electrochemical characterization.

7.3: Pulsed Electrodeposition of Fe_3O_4 on VACNFs and CNFs for Pseudocapacitive Applications

The pseudocapacitive capability of Fe_3O_4 was first reported by N.L. Wu in 2002 where a Fe_3O_4-SnO_2 composite electrode exhibited a mass-specific capacitance of 33 F/g.[400] Early studies found that unlike most transition metal oxides, Fe_3O_4 operates in the negative potential range (-0.9 to 0.1 V vs. SCE) as a pseudocapacitive material. Moreover, it was found to be very sensitive to the anions (especially SO_3^{2-}) in the electrolyte solution whereas most metal oxides are only sensitive to the positive ions such as Na^+ or H^+.[401] The proposed charge storage mechanism is shown in Schematic 7.1:

$$(1)\ FeO + SO_3^{2-} \leftrightarrow FeSO_4 + 2e^-$$
$$(2)\ 2Fe^{II} + SO_3^{2-} \leftrightarrow (Fe^{III}O)^+SO_3^{2-}(Fe^{III}O)^+ + 2e^-$$

Schematic 7.1

where (1) is a surface adsorption reaction at the electrode electrolyte interface, and (2) is a redox reaction that occurs in the thin layers near the surface of the active material.[402] More recent reports have also proposed a similar mechanism for OH^-.[403-404]

Fe_3O_4 can achieve a theoretical capacitance of ~833 F/g, however, to the best of our knowledge this is yet to be reached; most reported values range from 100 to 200 F/g. Its electrical conductivity (10^2 S cm^{-1}) is relativity high compared to other pseudocapacitive metal oxides like MnO_2 and V_2O_5 with values of 10^{-5} – 10^{-6} and 10^{-3} – 10^{-5} S cm^{-1}, respectively.[405] However, it's still several orders of magnitude lower than most high SSA carbon materials. The low capacitance is most likely attributed to low ion diffusion coefficients. The SO_3^{2-} diffusion coefficient for Fe_3O_4 is yet to be determined, however, the Li^+ diffusion coefficient has recently been determined to have a low value of 7.15 x 10^{-14} cm^2 s^{-1}.[159] Given the fact that a SO_3^{2-} is significantly larger than a Li^+, it is not inconceivable to expect the SO_3^{2-} diffusion coefficient to be several orders of

magnitude smaller. To put this into perspective, a Li^+ will only diffuse ~60 nm through Fe_3O_4 during a 60 second charge duration. It's would not be unreasonable to expect the SO_3^{2-} to diffuse only several nm's under the same conditions.

To overcome the low ion diffusion coefficients various synthesis have been developed. H. Lee et al. reported the electrochemical deposition of green rust and its oxidation to form a nanosized cellular Fe_3O_4 thin film with average wall thicknesses on the order of ~60 nm.[406] Electrochemical characterization results reported a mass-specific capacitance of 105 F/g. J. Chen et al. reported the hydrothermal preparation of octadecahedron shaped Fe_3O_4 nanoparticles ranging in size from 10-50 nm with a mass-specific capacitance of ~118 F/g at 5 mV/s and a low mass-specific capacitance of ~50 F/g at 50 mV/s.[407] The large drop in capacitance is attributed to a poor electrical connection between the octadecahedron nanoparticles. L. Liu et al. reported the hydrothermal synthesis of MWCNTs with cubic Fe_3O_4 nanoparticles that reached mass-specific capacitance of ~130 F/g.[408] J. Mu et al. reported a core-shell structure with Fe_3O_4 nanosheets grown on randomly dispersed CNF. Electrochemical characterization revealed a mass-specific capacitance of 135 F/g at 10 mV/s.[409] Despite the efforts, the specific capacitance remains low due to the electrical connection between Fe_3O_4 nanoparticles and conductive additives. Here we aim to enhance the mass-specific capacitance with state-of-the-art core-shell structures using VACNFs and electrospun CNF membranes.

To accomplish this, we modified a reported a cathodic electrochemical deposition technique to develop a pulsed electrodeposition.[410] Briefly, iron(III)-triethanolamine (TEA) complex is reduced at the electrode surface to form a mesoporous film as shown in Schematic 7.2

$$(1)\quad [Fe(OH)_4TEA_2] + e^- \rightarrow Fe(TEA)_2^{2+} + 4OH^1$$
$$(2)\quad Fe(TEA)_2^{2+} + 2[Fe(OH)_4TEA_2]^- \rightarrow Fe_3O_4 + 6TEA + 4H_2O$$

Schematic 7.2

where $[Fe(OH)_4TEA_2]^-$ is reduced onto the electrode surface to form $Fe(TEA)_2^{2+}$ (1). The reaction continues where two more $[Fe(OH)_4TEA_2]^-$ in solution react with the deposited $Fe(TEA)_2^{2+}$ (2) to form Fe_3O_4. To explain the origin of the Fe_3O_4 stoichiometry, the initial $Fe(TEA)_2^{2+}$ provides the Fe^{2+} while the following two $[Fe(OH)_4TEA_2]^-$ provide the two Fe^{3+}. The reaction is repeated multiple times to form a thin mesoporous layer of Fe_3O_4. The reaction is complete when all of the $[Fe(OH)_4TEA_2]^-$ in solution is used up. A short summarization of the procedure is as follows: iron(III) sulfate hydrate ($Fe_2(SO_4)_3$) is dissolved in a 1M TEA solution. The resulting solution is then added to a 3.5 M NaOH solution and heated up to ~80 °C. Once the desired temperature is reached, the solution is deposited onto the VACNFs or CNFs via pulsed electrodeposition using a Pt counter electrode and a Hg/HgO reference electrode.

Initially we attempted to deposit Fe_3O_4 using a constant potential of -1.10 V vs. Ag/AgCl according at Switzer et al.[411] However, upon examination no Fe_3O_4 was observed. Interestingly, when the voltage was lowered to -1.30 V vs. Ag/AgCl a uniform Fe shell along the fibers was observed as shown in Figures 7.4a and b. The VACNF-Fe shell was then annealed in the presences of oxygen which resulted in a Fe_2O_3 shell as shown in the XRD spectrum in Figure 7.4c. However, when electrochemical characterization was conducted no capacity was observed. Thus, it was concluded that the Fe_2O_3 shell was not electrically connected to VACNFs. It's likely that during annealing the Fe shell was separated from the core during oxidation. Nevertheless, it was proven to be very difficult to optimize the deposition for Fe_3O_4. Aside from the challenges discussed in section 1.6.2.1, one of the major challenges was the heat required for the deposition which often destroyed the reference electrode after several depositions.

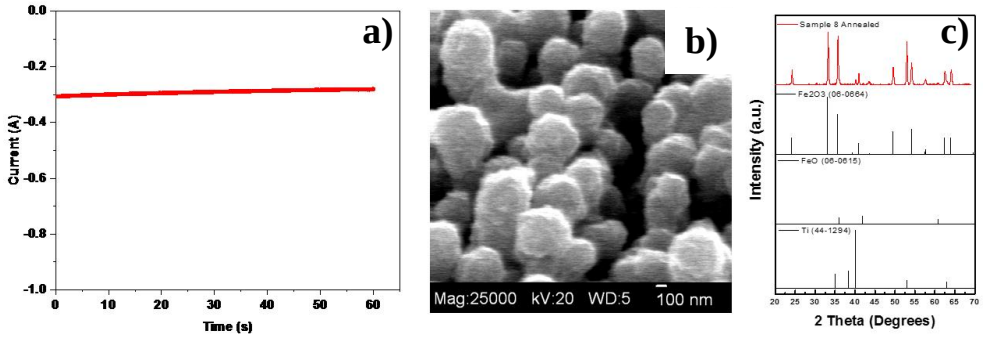

Figure 7.4 a) The amperometric curve for the Fe deposition, b) an SEM image of the VACNF-Fe core-shell structure, c) XRD spectrum of the Fe_2O_3 shell formed after annealing in the presences of oxygen.

To overcome these drawbacks the original deposition technique was modified for a pulse deposition technique. Moreover, the Ag/AgCl reference electrode was substituted out for a Hg/HgO electrode that not only works better at high temperatures, but more suitable for the high pH medium. The optimal potential was determined to be ~0.9 V vs Hg/HgO which was derived from the LSV curve in Figure 7.5a. A pulse was applied with an on time of 10 seconds and an off time of 10 seconds at -0.4 V vs Hg/HgO (or open circuit potential) as shown in Figure 7.5b.

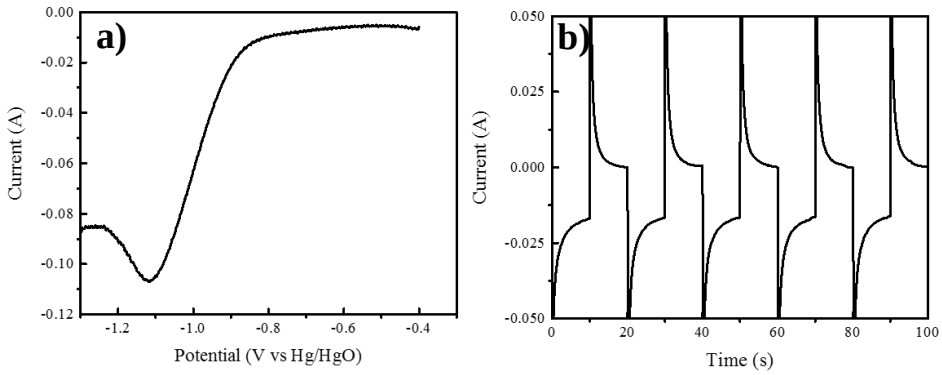

Figure 7.5 a) LSV curve of the Fe_3O_4 deposition on VACNF, b) the pulse deposition of Fe_3O_4 deposition on VACNFs at an on potential of -0.9 V (vs Hg/HgO)

After numerous trials, the parameters were optimized enough to obtain some iron oxide on the fibers as shown in the SEM images in Figure 7.6a. At high magnification, the Fe_3O_4 particles are observed along the fibers as shown in Figures 7.6b and c. However, a conformal shell was not achieved as illustrated by the "clumping" of the VACNFs due to a capillary affect in the

presence of aqueous solutions. This is a common occurrence when bare VACNFs are dried out after being exposed to an aqueous solution. Figure 7.6d shows the Fe_3O_4 nanoparticles along the clumped fibers further illustrating the non-uniform coating.

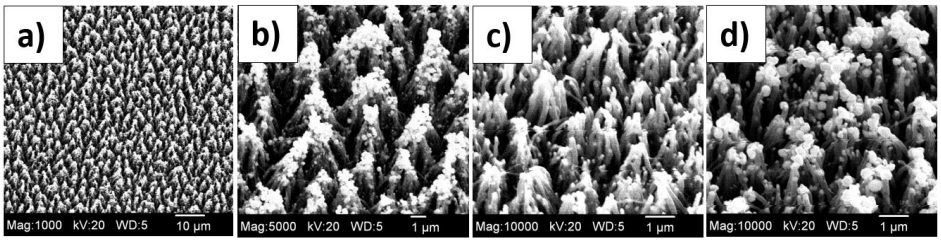

Figure 7.6 Low a) and high (b-d) SEM images of Fe_3O_4 deposited on VACNFs

Electrochemical characterization was conducted as shown in Figure 7.7. I-V cyclic measurements at scan rates of 10, 25, 50, 75, and 100 mV/s reveal near EDLC behavior in the potential range of -0.8 – 0.0 V (vs Ag/AgCl) with a small oxidation peak at -0.3 V as shown in Figure 7.7a. Charge-discharge curves further illustrate this behavior in Figure 7.7b. However, when compared with bare VACNFs (black curves) in Figures 7.7c and d it's clear that the contribution form Fe_3O_4 is quite low.

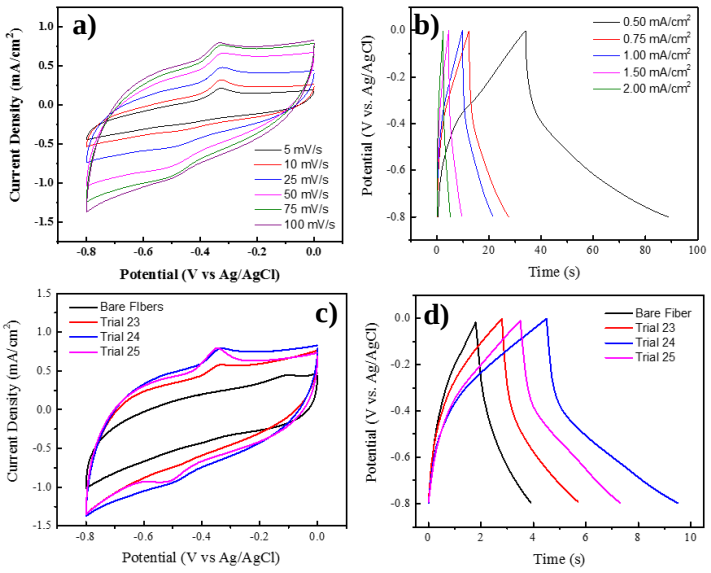

Figure 7.7 a) Cyclic I-V curves and b) charge-discharge curves of VACNF-Fe_3O_4 core-shell structure. A comparison of CV c) and charge-discharge curves d) with bare VACNFs

Despite the efforts, the deposition of Fe_3O_4 on VACNFs never panned out as expected. It's likely that the parameters need to be further optimized to accomplish the core-shell formation. Several avenues to focus on would be to optimize the temperature and pH of the deposition solution, as well as the deposition potential. However, we opted to take a different approach and perform the deposition on the electrospun CNFs as shown in Figure F.3a. Initial SEM images appear to show some coating on the CNFs, but the presences of Fe_3O_4 was not conclusive as shown in the EDS spectrum in Figure F.3b. Shortly thereafter, this project was temporarily shelved as the deposition of V_2O_5 (discussed in Chapter 4) took priority. The long-term goal of this project is to pair it with a MnO_2 or V_2O_5 core-shell structure for a Type III asymmetric pseudocapacitor as described in section 1.3.3. Moreover, we hope to be able to investigate its potential as a LIB and SIB anode in future work.

7.4: Pulsed Electrodeposition of Si onto CNFs for a LIB Anode

As discussed in section 1.4.1.2.2, Si has the highest theoretical capacity (4200 mAh/g) of any known LIB material. However, large volume expansion has prohibited its applicability. Previously, we reported a sputtered coated Si shell on VACNFs which allowed the large volume expansion without severe structural breakdown.[150-151] We extended this work by using a pulse electrodeposition technique to deposit Si onto the electrospun CNF mesoporous membrane. Briefly, 0.93 g of tetrabutylammonium chloride (TBACL) was dissolved in 40 g of propylene carbonate (PC) under nitrogen. While stirring 1.9 mL of silicon tetrachloride ($SiCl_4$) was added dropwise followed by a 10-minute purge. Under nitrogen a pulse electrodeposition technique was employed with a deposition potential of -2V (vs Ag/Ag^+ in 10 mM $AgNO_3$, 0.1 M TBACL) for 10 seconds and an off potential 1V for 20 seconds. Immediately after deposition the CNF-Si mesoporous core-shell structure was annealed for 1 hour at 400 °C under 2% hydrogen (98%

argon) to avoid SiO_2 formation. Preliminary electrochemical characterization is presented in Figure 7.8.

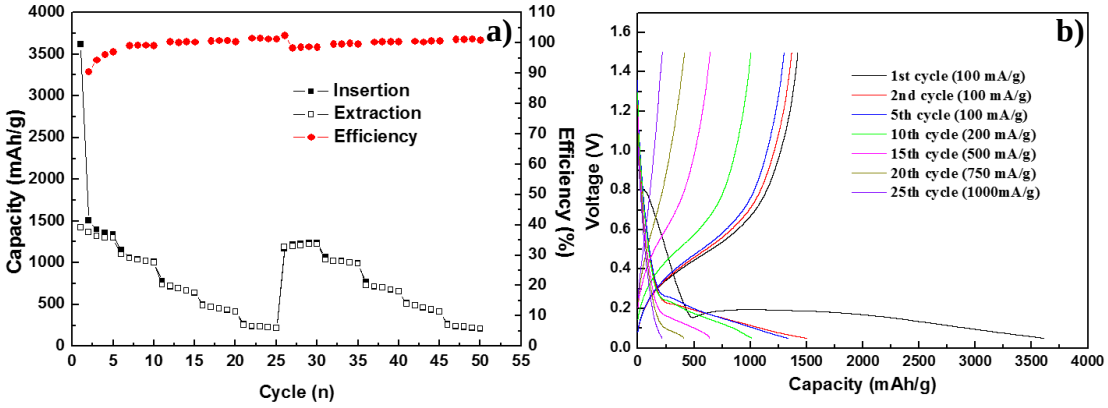

Figure 7.8 a) Rate-performance of the CNF-Si core-shell structure, b) charge-discharge curves from the rate-performance sequence.

A capacity of ~3650 mAh g^{-1} was achieved in the initial cycle at a rate of 100 mA g^{-1} as shown in the rate-performance test shown in Figure 7.8a. Capacity rapidly dropped in the second cycle to below 1500 mAh g^{-1} in cycle 2. Insertion capacities of 1000, 700, 450, and 200 mAh g^{-1} at rates of 200, 500, 750, and 1000 mA g^{-1}. When the sequence was repeated in cycle 26, a capacity of ~1250 mAh g^{-1} was achieved. The charge-discharge curves of cycles 1, 2, 5, 10, 15, 20, and 25 mA g^{-1} is shown in Figure 7.8b. These preliminary results are very encouraging; however, the capacities are still a low for Si after the initial cycle. Nevertheless, the electrospun CNFs appear to not only provide a good electrical conducting core but also allow for the large volume expansion owning to the voids throughout the mesoporous structure. This project is ongoing and we hope to complete the project in due time.

7.5: 3D Printed MoS_2-rGO on Nickel Foam for a SIB Anode

As discussed in section 1.4.2.1.4, MoS_2 is a layered metal sulfides that has been investigated as potential anode for SIBs owning to their large interlayer spacing which can

accommodate the Na^+ ion.[189] The Na^+ insertion mechanism occurs through a two-step process as shown in Schematic 7.3:

$$1)\ MoS_2 + xNa^+ + xe^- \leftrightarrow Na_xMoS_2\ (x < 2)$$

$$2)\ Na_xMoS_2 + (4-x)Na^+ + (4-x)e^- \leftrightarrow 2Na_2S + Mo$$

Schematic 7.3

The Na^+ ion first intercalates into MoS_2 to form an intermediate (Na_xMoS_2), which decomposes to Na_2S and Mo through a conversion reaction.[190] Unfortunately, the second step usually causes severe volume expansion and sluggish kinetics for Na^+ intercalation which results in rapid capacity fading.[191] To overcome this issue the second step can be restricted by limiting the cut voltage to ~0.4 V vs Na/Na^+. However, this strategy often limits the available capacity to ~300 mAh g^{-1}. The synthesis of unique MoS_2 architectures and the incorporation of carbon additives and have allowed the low voltage limit to be extended to 0.01 V vs Na/Na^+.

In collaboration with Dr. Pengli Yan and Dr. Dong Lin we aim to overcome the hurdles of the second step to enhance the insertion capacity with a high degree of stability at low potentials. Here, a newly developed 3D freeze assembling printing technique was employed for developing an MoS_2 anode for SIB applications. Briefly, an integrated drop-on-demand inkjet printing and freeze casting procedure was used.[412] For MoS_2 printing, a 1mg/1mL solution of ammonium thiomolybdate (ATM) was printed onto a cold block followed by a freeze-drying procedure. The resulting MoS_2 structure was annealed at 600 °C in the presences of 2% H_2 (98% argon). Interestingly, freeze casing directly aligns nanomaterials along the freezing direction to form delicate hierarchical microstructures that can be described as a light weight foam structure with large open pores suitable for Na^+ ion insertion and alloying as shown in the SEM image in Figure F.4.

The MoS_2 structure was first printed onto a copper substrate and annealed as described above. The Galvanostatic charge-discharge measurements are shown in Figure 7.9. A high insertion capacity of ~1150 mAh g^{-1} was achieved at a rate of 100 mA g^{-1} in the first cycle as shown in the rate-performance sequence in Figure 7.9a. However, after 10 cycles this the capacity dropped to ~200 mAh g^{-1} as shown in the charge-discharge cycles in Figure 7.9 b. When the rate was increased to 250, 500, 750, and 1000 mA g^{-1} the capacity faded to 75, 20, 5, and 2 mAh g^{-1}, respectively. Thus, we concluded that 1) there was severe structural collapse or 2) there was a poor electrical connection between the MoS_2 and the copper substrate.

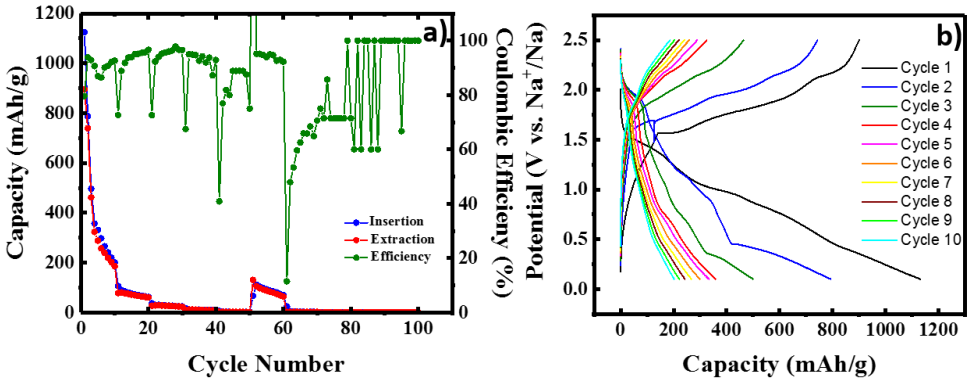

Figure 7.9 a) Galvanostatic charge-discharge rate performance of the MoS_2 printed on a copper substrate. b) first 10 cycles from the rate performance at a rate of 100 mA/g.

To further evaluate the MoS_2 traditional characterization techniques were employed. Briefly, the ATM precursor was freeze dried without any ink printing and mixed with carbon black and PVDF binder (70/20/10). The resulting mixture was casted onto a copper substrate and dried under vacuum for 48 hours prior to cell assembly. The galvanostatic charge-discharge rate performance test in Figure F.5 shows a great improvement over the printed structure. Thus, we concluded that the 3D printed structure was not electrically connected to the copper substrate. Furthermore, we determined that the 3D printed structure lacked in structural stability and

electrical conducting as a standalone material. To overcome these drawbacks rGO (10 mg/mL) was introduced to ink print mixture and printed onto a high surface area nickel foam.

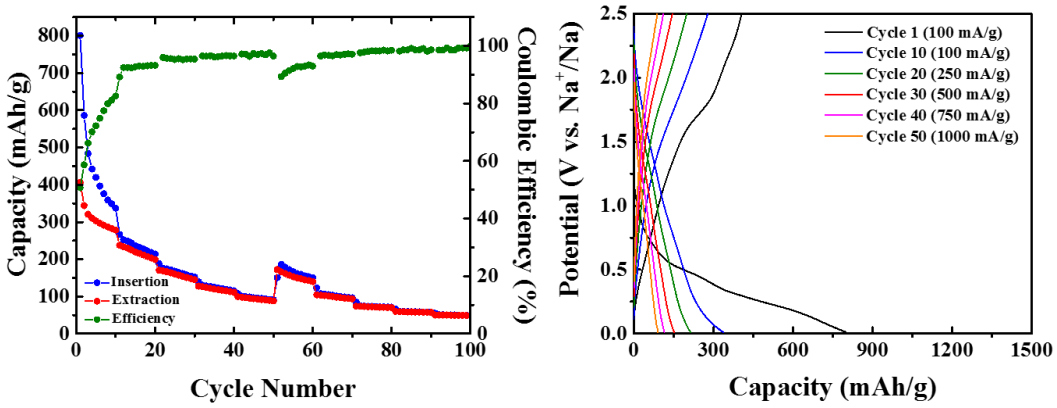

Figure 7.10 a) Galvanostatic charge-discharge rate performance of MoS_2-rGO printed on nickel foam, and b) charge-discharge curves from the rate-performance sequence.

The galvanostatic charge-discharge rate performance of the MoS_2-rGO structure printed on nickel foam is presented in Figure 7.10a. A high insertion capacity of 800 mAh g^{-1} was achieved in the initial cycle at a rate of 100 mA g^{-1} which faded to 350 mAh g^{-1} after 10 cycles as shown in the charge-discharge curves in Figure 7.10b. Last cycle insertion capacities of 200, 125, 115, and 100 mAh g^{-1} were achieved at rates of 250, 500, 750, and 1000 mA g^{-1}. Clearly, the mixing of rGO and the printing on nickel foam outperformed for the MoS_2 structure. All capacities were based on the mass of MoS_2 obtained from TGA measurements as shown in Figure F.6. It should be noted that this is short synopsis of the project. Some details were left out for the purposes of confidentiality as this is an ongoing project that we hope to complete in the near future.

Chapter 8 - Conclusions

In chapter 2 a high-aspect-ratio, VACNFs were conformally coated with Al_2O_3 and AZO using atomic layer deposition ALD to produce a three-dimensional array of metal−insulator−metal core−shell nanostructures. Prefunctionalization before ALD, as required for initiating covalent bonding on a carbon nanotube surface, was eliminated on VACNFs due to the graphitic edges along the surface of each CNF. The graphitic edges provided ideal nucleation sites under sequential exposures of H_2O and trimethylaluminum to form an Al_2O_3 coating up to 20 nm in thickness. HRTEM and scanning electron microscopy images confirmed the conformal core−shell AZO/Al_2O_3/CNF structures while energy-dispersive X-ray spectroscopy verified the elemental composition of the different layers. HRTEM selected area electron diffraction revealed that the as-made Al_2O_3 by ALD at 200 °C was amorphous, and then, after annealing in air at 450 °C for 30 min, was converted to polycrystalline form. Nevertheless, comparable dielectric constants of 9.3 were obtained in both cases by cyclic voltammetry at a scan rate of 1000 V s^{-1}. The conformal core−shell AZO/Al_2O_3/VACNF array structure demonstrated in this work provides a promising three-dimensional architecture toward applications of solid-state capacitors with large surface area having a thin, leak-free dielectric.

In chapter 3 the energy storage properties of $Pb_{0.92}La_{0.08}Zr_{0.52}Ti_{0.48}O_3$ (PLZT) films grown via PLD were evaluated at variable film thickness of 125, 250, 500, and 1000 nm. These films show high dielectric permittivity up to ~1200. Cyclic I-V measurements were used to evaluate the dielectric properties of these thin films, which not only provides the total electric displacement, but also separates contributions from each of the relevant components including electric conductivity (D1), dielectric capacitance (D2), and relaxor-ferroelectric domain switching polarization (P). The results show that, as the film thickness increases, the material transits from

a linear dielectric to nonlinear relaxor-ferroelectric. While the energy storage per volume increases with the film thickness, the energy storage efficiency drops from ~80% to ~30%. The PLZT films can be optimized for different energy storage applications by tuning the film thickness to optimize between the linear and nonlinear dielectric properties and energy storage efficiency.

In chapter 4 an approach to achieving stable 2 and 3 Li^+ insertion into V_2O_5 as a LIB cathode using a core-shell structure fabricated on electrospun CNF membranes was discussed. Uniform coaxial V_2O_5 shells are coated onto CNF cores via pulsed electrodeposition. The materials analyses confirm that the V_2O_5 shell after 4 hours of thermal annealing is a partially hydrated amorphous structure. SEM and TEM images indicate that the uniform 30 to 50 nm thick V_2O_5 shell forms an intimate interface with the CNF core. Lithium insertion capacities up to 291 and 429 mAh g^{-1} are achieved in the voltage ranges of 4.0 – 2.0 V and 4.0 – 1.5 V, respectively, which are in good agreement with the theoretical values of 294 mAh g^{-1} for 2 Li^+/V_2O_5 insertion and 441 mAh g^{-1} for 3 Li^+/V_2O_5 insertion into crystalline V_2O_5 materials. Moreover, after 100 cycles, remarkable retention rates of 97 and 70% are obtained for 2 Li^+/V_2O_5 and 3 Li^+/V_2O_5 insertion, respectively. These results reveal that the core-shell structure is an effective approach to breaking the intrinsic limits of V_2O_5 and enabling this high-capacity cathode materials for future LIBs.

In chapter 5 an alternative approach to achieving stable 3 Li^+ insertion into Vanadium pentoxide (V_2O_5) by implementing a three-dimensional (3D) core-shell structure consisting of coaxial V_2O_5 shells sputter-coated on VACNF cores was discussed. The hydrated amorphous microporous structure in the "as-deposited" V_2O_5 shells and the particulated nano-crystalline V_2O_5 structure formed by thermal annealing are compared. The former provides remarkably high capacity of 360 and 547 mAh g^{-1} in the voltage range of 4.0 – 2.0 V and 4.0 – 1.5 V, respectively, far exceeding values in current oxide-based LIB cathodes and even the corresponding theoretical

values of 294 mAh g^{-1} for 2 Li^+/V_2O_5 insertion and 441 mAh g^{-1} for 3 Li^+/V_2O_5 insertion into crystalline V_2O_5 materials. This is attributed to the additional reactions with the hydrated amorphous structure. After 100 cycles of 3 Li^+/V_2O_5 insertion/extraction at 0.20 A g^{-1} (~ C/3), ~ 84% of the initial capacity is retained. After thermal annealing, the core-shell structure presents a capacity of 294 and 390 mAh g^{-1}, matching well with the theoretical values for 2 and 3 Li^+/V_2O_5 insertion. The annealed sample shows further improved stability, with remarkable capacity retention of ~100% and ~88% for 2 and 3 Li^+/V_2O_5 insertion/extraction.

In chapter 6 the same approach was implemented to achieving high coulombic efficiency and Na^+ insertion/extraction capacity in vanadium pentoxide (V_2O_5) at high applied current rates The hydrated amorphous microporous structure in the "as-deposited" V_2O_5 shells is characterized in four potential ranges of 3.5 – 1.0, 4.0 – 1.5, , 4.0 – 1.0, and 4.0 – 2.0 V (vs Na/Na^+). An insertion capacity of 196 mAh g^{-1} is achieved in the potential range of 3.5 – 1.0 V (vs Na/Na^+) at a rate of 250 mA g^{-1}. Moreover, an insertion capacity of 78 mAh g^{-1} is retained when the rate is increased to 1500 mA g^{-1} with a coulombic efficiency of ~95%. When the potential window is shifted upwards to 4.0 – 1.5 V (vs Na/Na^+) an insertion capacity of 145 mAh g^{-1} is achieved. Moreover, a coulombic efficiency of ~98% is attained at a rate of 1500 mA g^{-1}. To enhance the energy density of the VACNF-V_2O_5 core-shell structures, the window is expanded to 4.0 – 1.0 V (vs Na/Na^+). An initial insertion capacity of 277 mAh g^{-1} is achieved at rate of 250 mA g^{-1}. However, rapid capacity fading and poor stability plagues the core-shell structures. Five strategies are briefly discussed to improve overall performance, but no improvements are observed. To further evaluate the stability of the Na^+ insertion the potential window was restricted to 4.0 – 2.0 V (vs Na/Na^+). Low capacities are observed but with a coulombic efficiency reaching 99%.

References

1. Luo, X.; Wang, J.; Dooner, M.; Clarke, J. C., Overview of Current Development in Electrical Energy Storage Technologies and the Application Potential in Power System Operation. *Appl. Energy* **2015,** *137*, 511–536.

2. Díaz-González, F.; Sumper, A.; Gomis-Bellmunt, O.; Villafáfila-Robles, R., A Review of Energy Storage Technologies for Wind Power Applications. *Renew. Sustainable Energy Rev.* **2012,** *16*, 2154– 2171.

3. Zhao, H.; Wu, Q.; Hu, S.; Xu, H.; Rasmussen, C. N., Review of Energy Storage System for Wind Power Integration Support. *Appl. Energy* **2015,** *137*, 545–553.

4. Thackeray, M. M.; Wolverton, C.; Isaacs, E. D., Electrical Energy Storage for Transportation-Approaching the Limits of, and Going Beyond, Lithium-Ion Batteries. *Energy Environ. Sci.* **2012,** *5*, 7854–7863.

5. Agrawal, A.; Kumar, M.; Prajapati, D. K., Smart Public Transit System Using an Energy Storage System and Its Coordination With a Distribution Grid. *IEEE Trans. Intell. Transp. Syst.* **2014,** *15* (4), 1622 - 1632.

6. Brecher, A., Transit Bus Applications of Lithium Ion Batteries: Progress and Prospects. Administration, F. T., Ed. Office of Research, Demonstration and Innovation, 2012.

7. Abdallah, T., *Sustainable Mass Transit: Challenges and Opportunities in Urban Public Transportation*. Elsevier: 2017.

8. Robyns, B.; Saudemont, C.; Hissel, D.; Roboam, X.; Sareni, B.; Pouget, J., *Electrical Energy Storage in Transportation Systems*. 2016.

9. Biryukov, V. V.; Kulekina, A. V., The Calculation Features of the Electrical Energy Storage Devices Parameters in Transport. In *Strategic Technology (IFOST), 2016 11th International Forum on*, IEEE: Novosibirsk, Russia, 2016.

10. Lukatskaya, M. R.; Dunn, B.; Gogotsi, Y., Multidimensional Materials and Device Architectures for Future Hybrid Energy Storage. *Nat. Commun.* **2016,** *7* (12647).

11. Whittingham, M. S. In *History, Evolution, and Future Status of Energy Storage*, IEEE, 2012.

12. Banerjee, P.; Perez, I.; Henn-Lecordier, L.; Lee, S. B.; Rubloff, G. W., Nanotubular Metal–Insulator–Metal Capacitor Arrays for Energy Storage. *Nat. Nanotechnol.* **2009,** *4*, 292 - 296.

13. Zhang, G.; Wu, H.; Chen, C.; Wang, T.; Wu, W.; Yue, J.; Liu, C., Transparent Nanotubular Capacitors Based On Transplanted Anodic Aluminum Oxide Templates. *ACS Appl. Mater. Interface* **2015,** *7* (9), 5522-5527.

14. Han, F.; Meng, G.; Zhou, F.; Song, L.; Li, X.; Hu, X.; Zhu, X.; Wu, B.; Wei, B., Dielectric Capacitors with Three-Dimensional Nanoscale Interdigital Electrodes for Energy Storage. *Science Advances* **2015,** *1* (9).

15. Kemell, M.; Ritala, M.; Leskelä, M.; Ossei-Wusu, E.; Carstensen, J.; Föll, H., $Si/Al_2O_3/ZnO:Al$ Capacitor Arrays Formed in Electrochemically Etched Porous Si by Atomic Layer Deposition. *Microelectron. Eng.* **2007,** *84* (2), 313-318.

16. Klootwijk, J. H.; Jinesh, K. B.; Dekkers, W.; Verhoeven, J. F.; van den Heuvel, F. C.; Kim, H. D.; Blin, D.; Verheijen, M. A.; Weemaes, R. G. R.; Kaiser, M.; Ruigrok, J. J. M.; Roozeboom, F., Ultrahigh Capacitance Density for Multiple ALD-Grown MIM Capacitor Stacks in 3-D Silicon. *IEEE Electron Device Lett.* **2008,** *29* (7), 740-742.

17. Peterson, K. L.; Johnson, W. L.; Kim, S. A.; Heyliger, P. R., Vibrational Modes of Multilayered Ceramic Capacitors. *Finite Elem. Anal. Des.* **2016,** *116* (Supplement C), 1-11.

18. Yu, B.-Y.; Wei, W.-C. J., Defects of Base Metal Electrode Layers in Multi-Layer Ceramic Capacitor. *J. Am. Ceram. Soc.* **2005,** *88* (8), 2328-2331.

19. Wu, Y.-H.; Kao, C.-K.; Chen, B.-Y.; Lin, Y.-S.; Li, M.-Y.; Wu, H.-C., High Density Metal-Insulator-Metal Capacitor based on $ZrO_2/Al_2O_3/ZrO_2$ Laminate Dielectric. *Appl. Phys. Lett.* **2008,** *93* (3), 033511.

20. Kim, J. B.; Kwon, D. R.; Chakrabarti, K.; Lee, C.; Oh, K. Y.; Lee, J. H., Improvement in Al_2O_3 Dielectric Behavior by using Ozone as an Oxidant for the Atomic Layer Deposition Technique. *J. Appl. Phys.* **2002,** *92* (11), 6739-6742.

21. Meng, S.; Basceri, C.; Busch, B. W.; Derderian, G.; Sandhu, G., Leakage Mechanisms and Dielectric Properties of Al_2O_3/TiN-based Metal-Insulator-Metal Capacitors. *Appl. Phys. Lett.* **2003,** *83* (21), 4429-4431.

22. Shi-Jin, D.; David Wei, Z.; Li-Kang, W., Atomic-Layer-Deposited Al_2O_3-HfO_2 Laminated and Sandwiched Dielectrics for Metal–Insulator–Metal Capacitors. *J. Phys. D: Appl. Physics* **2007,** *40* (4), 1072.

23. Perng, T.-H.; Chien, C.-H.; Chen, C.-W.; Lehnen, P.; Chang, C.-Y., High-Density MIM Capacitors with HfO_2 Dielectrics. *Thin Solid Films* **2004,** *469* (Supplement C), 345-349.

24. Hu, H.; Zhu, C.; Lu, Y. F.; Li, M. F.; Cho, B. J.; Choi, W. K., A High Performance MIM Capacitor Using HfO_2 Dielectrics. *IEEE Electron Device Lett.* **2002,** *23* (9), 514-516.

25. Alers, G. B.; Werder, D. J.; Chabal, Y.; Lu, H. C.; Gusev, E. P.; Garfunkel, E.; Gustafsson, T.; Urdahl, R. S., Intermixing at the Tantalum Oxide/Silicon Interface in Gate Dielectric Structures. *Appl. Phys. Lett.* **1998,** *73* (11), 1517-1519.

26. Kamiyama, S.; Lesaicherre, P. Y.; Suzuki, H.; Sakai, A.; Nishiyama, I.; Ishitani, A., Ultrathin Tantalum Oxide Capacitor Dielectric Layers Fabricated Using Rapid Thermal Nitridation prior to Low Pressure Chemical Vapor Deposition. *J. Electrochem. Soc.* **1993,** *140* (6), 1617-1625.

27. Cross, L. E., Relaxor Ferroelectrics In *Piezoelectricity*, Springer Berlin Heidelberg: 2008; Vol. 114, pp 131-155.

28. Mao, D.; Mejia, I.; Stiegler, H.; Gnade, B. E.; Quevedo-Lopez, M. A., Polarization Behavior of Poly(vinylidene fluoride-trifluoroethylene) Copolymer Ferroelectric Thin Film Capacitors for Nonvolatile Memory Application in Flexible Electronics. *J. Appl. Phys.* **2010,** *108* (9), 094102.

29. Li, M.; Wondergem, H. J.; Spijkman, M.-J.; Asadi, K.; Katsouras, I.; Blom, P. W. M.; de Leeuw, D. M., Revisiting the δ-Phase of Poly(vinylidene fluoride) for Solution-Processed Ferroelectric Thin Films. *Nat. Mater.* **2013,** *12* (5), 433-438.

30. Hong-ming, C.; Sheng-wei, T.; Joseph Ya-min, L., Leakage Current Characteristics of Lead-Zirconate-Titanate Thin Film Capacitors for Memory Device Applications. *Jpn. J. Appl. Phys.* **1998,** *37* (7R), 4056.

31. Kingon, A. I.; Srinivasan, S., Lead Zirconate Titanate Thin Films Directly on Copper Electrodes for Ferroelectric, Dielectric and Piezoelectric Applications. *Nat. Mater.* **2005,** *4* (3), 233-237.

32. Tombak, A.; Maria, J.-P.; Ayguavives, F.; Jin, Z.; Stauf, G. T.; Kingon, A. I.; Mortazawi, A., Tunable Barium Strontium Titanate Thin Film Capacitors for RF and Microwave Applications. *IEEE Microw. Compon. Lett.* **2002,** *12* (1), 3-5.

33. Cuniot-Ponsard, M., Strontium Barium Niobate Thin Films for Dielectric and Electro-Optic Applications. In *Ferroelectrics - Material Aspects*, Lallart, M., Ed. InTech: Rijeka, 2011; p Ch. 23.

34. Baginsky, I. L.; Kostsov, E. G.; Sterelykhina, L. N., Electronic Devices Based on Niobate Barium-Strontium Thin Film In *IEEE 7th International Symposium on*, IEEE: Urbana-Champaign, IL, USA, 1990; pp 302-305.

35. Reynolds, G. J.; Kratzer, M.; Dubs, M.; Felzer, H.; Mamazza, R., Sputtered Modified Barium Titanate for Thin-Film Capacitor Applications. *Materials* **2012,** *5* (4), 575-589.

36. Sakamoto, W.; Yogo, T.; Kikuta, K.; Ogiso, K.-j.; Kawase, A.; Hirano, S.-i., Synthesis of Strontium Barium Niobate Thin Films through Metal Alkoxide. *J. Am. Ceram. Soc.* **1996,** *79* (9), 2283-2288.

37. Li, C.; Guo, R.; Bhalla, A. S., Optical Frequency Dispersion Near Ferroelectric Relaxor Phase Transition in Lead Barium Niobate Crystal. *Ferroelectrics* **2006,** *339* (1), 103-113.

38. Zhao, J.; Zhang, Q. M.; Kim, N.; Shrout, T., Electromechanical Properties of Relaxor Ferroelectric Lead Magnesium Niobate-Lead Titanate Ceramics. *Jpn. J. Appl. Phys.* **1995,** *34* (10R), 5658.

39. Viehland, D.; Jang, S.; Cross, L. E.; Wuttig, M., The Dielectric Relaxation of Lead Magnesium Niobate Relaxor Ferroelectrics. *Philos. Mag. B* **1991,** *64* (3), 335-344.

40. Chu, F.; Reaney, I. M.; Setter, N., Role of Defects in the Ferroelectric Relaxor Lead Scandium Tantalate. *J. Am. Ceram. Soc.* **1995,** *78* (7), 1947-1952.

41. Bursill, L. A.; JuLin, P.; Hua, Q.; Setter, N., Relationship Between Nanostructure and Dielectric Response of Lead Scandium Tantalate -(I) Structure and Domain Textures. *Physica B: Condensed Matter* **1995,** *205* (3), 305-326.

42. Chen, W.; Yao, X.; Wei, X., Tunability and Ferroelectric Relaxor Properties of Bismuth Strontium Titanate Ceramics. *Appl. Phys. Lett.* **2007,** *90* (18), 182902.

43. Hou, R. Z.; Chen, X. M.; Zeng, Y. W., Diffuse Ferroelectric Phase Transition and Relaxor Behaviors in Ba-Based Bismuth Layer-Structured Compounds and La-Substituted $SrBi_4Ti_4O_{15}$. *J. Am. Ceram. Soc.* **2006,** *89* (9), 2839-2844.

44. Liu, S. Y.; Chua, L.; Tan, K. C.; Valavan, S. E., Novel Ferroelectric Capacitor for Non-Volatile Memory Storage and Biomedical Tactile Sensor Applications. *Thin Solid Films* **2010,** *518* (24), e152-e155.

45. Wang, Z. J.; Cao, Z. P.; Otsuka, Y.; Yoshikawa, N.; Kokawa, H.; Taniguchi, S., Low-Temperature Growth of Ferroelectric Lead Zirconate Titanate Thin Films Using the Magnetic Field of Low Power 2.45 GHz Microwave Irradiation. *Appl. Phys. Lett.* **2008,** *92* (22), 222905.

46. Shung, K. K.; Cannata, J. M.; Zhou, Q. F., Piezoelectric Materials for High Frequency Medical Imaging Applications: A Review. *J. Electroceram.* **2007,** *19* (1), 141-147.

47. Zhao, X.-Y.; Cao, J.-P.; Morishita, K.; Ozaki, J.-i.; Takarada, T., Electric Double-Layer Capacitors from Activated Carbon Derived from Black Liquor. *Energy & Fuels* **2010,** *24* (3), 1889-1893.

48. Kwon, S. H.; Lee, E.; Kim, B.-S.; Kim, S.-G.; Lee, B.-J.; Kim, M.-S.; Jung, J. C., Activated Carbon Aerogel as Electrode Material for Coin-type EDLC Cell in Organic Electrolyte. *Curr. Appl. Phys.* **2014,** *14* (4), 603-607.

49. Kanninen, P.; Luong, N. D.; Sinh, L. H.; Anoshkin, I. V.; Tsapenko, A.; Seppälä, J.; Nasibulin, A. G.; Kallio, T., Transparent and Flexible High-Performance Supercapacitors based on Single-Walled Carbon Nanotube Films. *Nanotechnology* **2016,** *27* (23), 235403.

50. Li, X.; Rong, J.; Wei, B., Electrochemical Behavior of Single-Walled Carbon Nanotube Supercapacitors under Compressive Stress. *ACS Nano* **2010,** *4* (10), 6039-6049.

51. Pandey, G. P.; Hashmi, S. A.; Kumar, Y., Multiwalled Carbon Nanotube Electrodes for Electrical Double Layer Capacitors with Ionic Liquid Based Gel Polymer Electrolytes. *J. Electrochem. Soc.* **2010,** *157* (1), A105-A114.

52. Dulyaseree, P.; Jarernboon, W.; Wongwiriyapan, W., Supercapacitor based on Multi-walled Carbon Nanotubes/Carbon Black Composites-coated Wooden Sheet. *Energy Procedia* **2014,** *56* (Supplement C), 481-486.

53. Moon, J. S.; Kim, H.; Lee, D.-C.; Lee, J. T.; Yushin, G., Increasing Capacitance of Zeolite-Templated Carbons in Electric Double Layer Capacitors. *J. Electrochem. Soc.* **2015,** *162* (5), A5070-A5076.

54. Portet, C.; Yang, Z.; Korenblit, Y.; Gogotsi, Y.; Mokaya, R.; Yushin, G., Electrical Double-Layer Capacitance of Zeolite-Templated Carbon in Organic Electrolyte. *J. Electrochem. Soc.* **2009,** *156* (1), A1-A6.

55. Ke, Q.; Wang, J., Graphene-based Materials for Supercapacitor Electrodes-A Review. *J. Materiomics* **2016,** *2* (1), 37-54.

56. Stoller, M. D.; Park, S.; Zhu, Y.; An, J.; Ruoff, R. S., Graphene-Based Ultracapacitors. *Nano Lett.* **2008,** *8* (10), 3498-3502.

57. Barranco, V.; Lillo-Rodenas, M. A.; Linares-Solano, A.; Oya, A.; Pico, F.; Ibañez, J.; Agullo-Rueda, F.; Amarilla, J. M.; Rojo, J. M., Amorphous Carbon Nanofibers and Their Activated Carbon Nanofibers as Supercapacitor Electrodes. *J. Phys. Chem. C* **2010,** *114* (22), 10302-10307.

58. Kim, C.; Yang, K. S., Electrochemical Properties of Carbon Nanofiber Web as an Electrode for Supercapacitor Prepared by Electrospinning. *Appl. Phys. Lett.* **2003,** *83* (6), 1216-1218.

59. Beguin, F.; Frackowiak, E., General Properties of Electrochemical Capacitors. In *Supercapacitors Materials, Systems, and Applications* Lu, M. G. Q., Ed. Wiley-VCH: Weinheim, Germany, 2013; pp 80-82.

60. Rennie, A. J. R.; Martins, V. L.; Torresi, R. M.; Hall, P. J., Ionic Liquids Containing Sulfonium Cations as Electrolytes for Electrochemical Double Layer Capacitors. *J. Phys. Chem. C* **2015,** *119* (42), 23865-23874.

61. Nishida, T.; Tashiro, Y.; Yamamoto, M., Physical and Electrochemical Properties of 1-alkyl-3-Methylimidazolium Tetrafluoroborate for Electrolyte. *J. Fluorine Chem.* **2003,** *120* (2), 135-141.

62. Osaka, T.; Liu, X.; Nojima, M.; Momma, T., An Electrochemical Double Layer Capacitor Using an Activated Carbon Electrode with Gel Electrolyte Binder. *J. Electrochem. Soc.* **1999,** *146* (5), 1724-1729.

63. Simon, P.; Gogotsi, Y., Materials for Electrochemical Capacitors. *Nat. Mater.* **2008,** *7* (11), 845-854.

64. Juodkazis, K.; Juodkazytė, J.; Šukienė, V.; Grigucevičienė, A.; Selskis, A., On the Charge Storage Mechanism at RuO_2/0.5 M H_2SO_4 Interface. *J. Solid State Electrochem.* **2008,** *12* (11), 1399-1404.

65. Huang, M.; Li, F.; Dong, F.; Zhang, Y. X.; Zhang, L. L., MnO_2-based Nanostructures for High-Performance Supercapacitors. *J. Mater. Chem. A* **2015,** *3* (43), 21380-21423.

66. Yang, Y.-Y.; Hu, Z.-A.; Zhang, Z.-Y.; Zhang, F.-H.; Zhang, Y.-J.; Liang, P.-J.; Zhang, H.-Y.; Wu, H.-Y., Reduced Graphene Oxide–Nickel Oxide Composites with High Electrochemical Capacitive Performance. *Mater. Chem. Phys.* **2012,** *133* (1), 363-368.

67. Pandey, G. P.; Liu, T.; Brown, E.; Yang, Y.; Li, Y.; Sun, X. S.; Fang, Y.; Li, J., Mesoporous Hybrids of Reduced Graphene Oxide and VanadiumPentoxide for Enhanced Performance in Lithium-Ion Batteries and Electrochemical Capacitors. *ACS applied materials & interfaces* **2016,** *8*, 9200-9210.

68. Wang, L.; Wang, D.; Zhu, J.; Liang, X., Preparation of Co_3O_4 Nanoplate/Graphene Sheet Composites and Their Synergistic Electrochemical Performance. *Ionics* **2013,** *19* (2), 215-220.

69. Wang, D.; Li, Y.; Wang, Q.; Wang, T., Nanostructured Fe_2O_3–Graphene Composite as a Novel Electrode Material for Supercapacitors. *J. Solid State Electrochem.* **2012,** *16* (6), 2095-2102.

70. Wang, Q.; Jiao, L.; Du, H.; Wang, Y.; Yuan, H., Fe_3O_4 Nanoparticles Grown on Graphene as Advanced Electrode Materials for Supercapacitors. *J. Power Sources* **2014,** *245* (Supplement C), 101-106.

71. Hu, C.-C.; Chang, K.-H.; Lin, M.-C.; Wu, Y.-T., Design and Tailoring of the Nanotubular Arrayed Architecture of Hydrous RuO_2 for Next Generation Supercapacitors. *Nano Lett.* **2006,** *6* (12), 2690-2695.

72. Klankowski, S. A.; Pandey, G. P.; Malek, G.; Thomas, C. R.; Bernasek, S. L.; Wu, J.; Li, J., Higher-Power Supercapacitor Electrodes Based on Mesoporous Manganese Oxide Coating on Vertically Aligned Carbon Nanofibers. *Nanoscale* **2015,** *7* (18), 8485-94.

73. Pandey, G. P.; Fang, Y.; Li, J., Advanced Materials for Supercapacitors. In *Electrochemical Energy*, CRC Press: 2015; pp 423-449.

74. Sathiya, M.; Prakash, A. S.; Ramesha, K.; Tarascon, J. M.; Shukla, A. K., V_2O_5-Anchored Carbon Nanotubes for Enhanced Electrochemical Energy Storage. *J. Am. Chem. Soc.* **2011,** *133* (40), 16291-16299.

75. Pan, X.; Ren, G.; Hoque, M. N. F.; Bayne, S.; Zhu, K.; Fan, Z., Fast Supercapacitors Based on Graphene-Bridged V_2O_3/VO_x Core–Shell Nanostructure Electrodes with a Power Density of 1 MW kg^{-1}. *Adv. Mater. Interfaces* **2014,** *1* (9), 1400398-n/a.

76. Mastragostino, M.; Arbizzani, C.; Soavi, F., Polymer-based Supercapacitors. *J. Power Sources* **2001,** *97* (Supplement C), 812-815.

77. Rudge, A.; Davey, J.; Raistrick, I.; Gottesfeld, S.; Ferraris, J. P., Conducting Polymers as Active Materials in Electrochemical Capacitors. *J. Power Sources* **1994,** *47* (1), 89-107.

78. Fang, Y.; Liu, J.; Yu, D. J.; Wicksted, J. P.; Kalkan, K.; Topal, O.; Flanders, B. N.; Wu, J.; Li, J., Self-supported Supercapacitor Membranes: Polypyrrole-coated Multi-walled Carbon Nanotube Networks Enabled by Pulsed Electrodeposition. *J. Power Sources* **2010,** *195* (2), 674-679.

79. Sharma, R. K.; Rastogi, A. C.; Desu, S. B., Pulse Polymerized Polypyrrole Electrodes for High Energy Density Electrochemical Supercapacitor. *Electrochem. Commun.* **2008,** *10* (2), 268-272.

80. Singh, A.; Chandra, A., Graphite Oxide/Polypyrrole Composite Electrodes for Achieving High Energy Density Supercapacitors. *J. Appl. Electrochem.* **2013,** *43* (8), 773-782.

81. Wang, H.; Lin, J.; Shen, Z. X., Polyaniline (PANi) Based Electrode Materials for Energy Storage and Conversion. *J. Sci.: Adv. Mater. Devices* **2016,** *1* (3), 225-255.

82. Wu, G.; Tan, P.; Wang, D.; Li, Z.; Peng, L.; Hu, Y.; Wang, C.; Zhu, W.; Chen, S.; Chen, W., High-performance Supercapacitors Based on Electrochemical-induced Vertical-aligned Carbon Nanotubes and Polyaniline Nanocomposite Electrodes. *Sci. Rep.* **2017,** *7*, 43676.

83. Liu, Y.; Weng, B.; Razal, J. M.; Xu, Q.; Zhao, C.; Hou, Y.; Seyedin, S.; Jalili, R.; Wallace, G. G.; Chen, J., High-Performance Flexible All-Solid-State Supercapacitor from Large Free-Standing Graphene-PEDOT/PSS Films. *Sci. Rep.* **2015,** *5*, 17045.

84. Acharya, S.; Santino, L. M.; Lu, Y.; Anandarajah, H.; Wayne, A.; D'Arcy, J. M., Ultrahigh stability of high-power nanofibrillar PEDOT supercapacitors. *Sustainable Energy & Fuels* **2017,** *1* (3), 482-491.

85. Brousse, T.; Bélanger, D.; Long, J. W., To Be or Not To Be Pseudocapacitive? *J. Electrochem. Soc.* **2015,** *162* (5), A5185-A5189.

86. Simon, P.; Gogotsi, Y.; Dunn, B., Where Do Batteries End and Supercapacitors Begin? *Science* **2014,** *343* (6176), 1210-1211.

87. Pell, W. G.; Conway, B. E., Peculiarities and Requirements of Asymmetric Capacitor Devices Based on Combination of Capacitor and Battery-type Electrodes. *J. Power Sources* **2004,** *136* (2), 334-345.

88. Chae, J. H.; Ng, K. C.; Chen, G. Z., Nanostructured Materials for the Construction of Asymmetrical Supercapacitors. *Proceedings of the Institution of Mechanical Engineers, Part A: Journal of Power and Energy* **2010,** *224* (4), 479-503.

89. Gao, H.; Xiao, F.; Ching, C. B.; Duan, H., High-Performance Asymmetric Supercapacitor Based on Graphene Hydrogel and Nanostructured MnO2. *ACS Appl. Mater. Interface* **2012,** *4* (5), 2801-2810.

90. Wang, Y.-G.; Wang, Z.-D.; Xia, Y.-Y., An Asymmetric Supercapacitor using RuO_2/TiO_2 Nanotube Composite and Activated Carbon Electrodes. *Electrochimica Acta* **2005,** *50* (28), 5641-5646.

91. Fan, Z.; Yan, J.; Wei, T.; Zhi, L.; Ning, G.; Li, T.; Wei, F., Asymmetric Supercapacitors Based on Graphene/MnO_2 and Activated Carbon Nanofiber Electrodes with High Power and Energy Density. *Adv. Funct. Mater.* **2011,** *21* (12), 2366-2375.

92. Khomenko, V.; Raymundo-Piñero, E.; Béguin, F., Optimisation of an Asymmetric Manganese Oxide/Activated Carbon Capacitor Working at 2V in Aqueous Medium. *J. Power Sources* **2006,** *153* (1), 183-190.

93. Du Pasquier, A.; Plitz, I.; Menocal, S.; Amatucci, G., A Comparative Study of Li-ion Battery, Supercapacitor and Nonaqueous Asymmetric Hybrid Devices for Automotive Applications. *J. Power Sources* **2003,** *115* (1), 171-178.

94. Dighe, A. B.; Dubal, D. P.; Holze, R., Screen Printed Asymmetric Supercapacitors based on $LiCoO_2$ and Graphene Oxide*. *Z. Anorg. Allg. Chem.* **2014,** *640* (14), 2852-2857.

95. Brousse, T.; Bélanger, D., A Hybrid Fe_3O_4 - MnO_2 Capacitor in Mild Aqueous Electrolyte. *Electrochem. Solid-State Lett.* **2003,** *6* (11), A244-A248.

96. Ng, K. C.; Zhang, S.; Chen, G. Z., An Asymmetrical Supercapacitor Based on CNTs/SnO_2 and CNTs/MnO_2 Nanocomposites Working at 1.7 V in Aqueous Electrolyte. *ECS Trans.* **2008,** *16* (1), 153-162.

97. Chang, J.; Jin, M.; Yao, F.; Kim, T. H.; Le, V. T.; Yue, H.; Gunes, F.; Li, B.; Ghosh, A.; Xie, S.; Lee, Y. H., Asymmetric Supercapacitors Based on Graphene/MnO_2 Nanospheres and Graphene/MoO_3 Nanosheets with High Energy Density. *Adv. Funct. Mater.* **2013,** *23* (40), 5074-5083.

98. Goodenough, J. B., Evolution of Strategies for Modern Rechargeable Batteries. *Acc. Chem. Res.* **2013,** *46* (5), 1053-1061.

99. Whittingham, M. S., Lithium Batteries and Cathode Materials. *Chem. Rev.* **2004,** *104* (10), 4271-4302.

100. Nichelson, A.; Karthickprabhu, S.; Karuppasamy, K.; Hirankumar, G.; Sahaya Shajan, X., A Brief Review on Integrated (Layered and Spinel) and Olivine Nanostructured Cathode Materials for Lithium Ion Battery Applications. *Materials Focus* **2016,** *5* (4), 324-334.

101. Li, S.; Li, C.; Fan, Y.; Xu, J.; Wang, T.; Yang, S., Electrochemical performance of $LiFePO_4$ cathode material for Li-ion battery. *Rare Metals* **2006,** *25* (6, Supplement 1), 62-66.

102. Zhang, X.; van Hulzen, M.; Singh, D. P.; Brownrigg, A.; Wright, J. P.; van Dijk, N. H.; Wagemaker, M., Direct View on the Phase Evolution in Individual $LiFePO_4$ Nanoparticles during Li-ion Battery Cycling. *Nat. Commun.* **2015,** *6*, 8333.

103. Oh, S.-M.; Oh, S.-W.; Yoon, C.-S.; Scrosati, B.; Amine, K.; Sun, Y.-K., High-Performance Carbon-$LiMnPO_4$ Nanocomposite Cathode for Lithium Batteries. *Adv. Funct. Mater.* **2010,** *20* (19), 3260-3265.

104. Gu, H. B.; Jin, B.; Jun, D. K.; Han, Z., Improved Electrochemical Performance of $LiCoPO_4$ Nanoparticles for Lithium Ion Batteries. *J. Nanosci. Nanotechnol.* **2007,** *7* (11), 4037-40.

105. Julien, M. C.; Mauger, A.; Trottier, J.; Zaghib, K.; Hovington, P.; Groult, H., Olivine-Based Blended Compounds as Positive Electrodes for Lithium Batteries. *Inorganics* **2016,** *4* (2).

106. Feng, Y.; Zhang, H.; Fang, L.; Ouyang, Y.; Wang, Y., Designed Synthesis of a Unique Sngle-Crystal Fe-doped $LiNiPO_4$ Nanomesh as an Enhanced Cathode for Lithium Ion Batteries. *J. Mater. Chem. A* **2015,** *3* (31), 15969-15976.

107. Gao, T.; Wang, B.; Fang, H.; Liu, C.; Wang, L.; Liu, G.; Liu, T.; Wang, D., $Li_3V_2(PO_4)_3$ as a Cathode Additive for the Over-Discharge Protection of Lithium Ion Batteries. *RSC Adv.* **2016,** *6* (80), 76933-76937.

108. Kreder, K. J.; Manthiram, A., Vanadium-Substituted $LiCoPO_4$ Core with a Monolithic $LiFePO_4$ Shell for High-Voltage Lithium-Ion Batteries. *ACS Energy Lett.* **2017,** *2* (1), 64-69.

109. Sickafus, K. E.; Wills, J. M.; Grimes, N. W., Structure of Spinel. *J. Am. Ceram. Soc.* **1999,** *82* (12), 3279-3292.

110. Wu, H. M.; Tu, J. P.; Chen, X. T.; Li, Y.; Zhao, X. B.; Cao, G. S., Electrochemical Study on $LiMn_2O_4$ as Cathode Material for Lithium Ion Batteries. *J. Electroanal. Chem.* **2006,** *586* (2), 180-183.

111. Wang, H.-Q.; Lai, F.-Y.; Li, Y.; Zhang, X.-H.; Huang, Y.-G.; Hu, S.-J.; Li, Q.-Y., Excellent Stability of Spinel $LiMn_2O_4$-based Cathode Materials for Lithium-Ion Batteries. *Electrochimica Acta* **2015,** *177* (Supplement C), 290-297.

112. Kim, J. H.; Myung, S. T.; Yoon, C. S.; Kang, S. G.; Sun, Y. K., Comparative Study of $LiNi_{0.5}Mn_{1.5}O_4$-δ and $LiNi_{0.5}Mn_{1.5}O_4$ Cathodes Having Two Crystallographic Structures: $Fd\bar{3}m$ and $P4_332$. *Chem. Mater.* **2004,** *16* (5), 906-914.

113. Mukai, K.; Uyama, T., Toward Positive Electrode Materials with High-Energy Density: Electrochemical and Structural Studies on $LiCoxMn_{2-x}O_4$ with $0 \leq x \leq 1$. *ACS Omega* **2017,** *2* (8), 5142-5149.

114. Manthiram, A.; Chemelewski, K.; Lee, E.-S., A Perspective on the High-voltage $LiMn_{1.5}Ni_{0.5}O_4$ Spinel Cathode for Lithium-ion Batteries. *Energy Environ. Sci.* **2014,** *7* (4), 1339-1350.

115. Xu, B.; Qian, D.; Wang, Z.; Meng, Y. S., Recent Progress in Cathode Materials Research for Advanced Lithium Ion Batteries. *Mater. Sci. Eng. R-Rep.* **2012,** *73* (5), 51-65.

116. Zhong, S.-w.; Zhao, Y.-j.; Lian, F.; Li, Y.; Hu, Y.; Li, P.-z.; Mei, J.; Liu, Q.-g., Characteristics and Electrochemical Performance of Cathode Material Co-coated $LiNiO_2$ for Li-ion Batteries. *Trans. Nonferrous Met. Soc. China* **2006,** *16* (1), 137-141.

117. Zhou, H.; Li, Y.; Zhang, J.; Kang, W.; Yu, D. Y. W., Low-temperature Direct Synthesis of Layered m-$LiMnO_2$ for Lithium-ion Battery Applications. *J. Alloys Compd.* **2016,** *659* (Supplement C), 248-254.

118. Meng, X.; Dou, S.; Wang, W.-l., High Power and High Capacity Cathode Material $LiNi_{0.5}Mn_{0.5}O_2$ for Advanced Lithium-ion Batteries. *J. Power Sources* **2008,** *184* (2), 489-493.

119. Liu, Y.; Chen, B.; Cao, F.; Zhao, X.; Yuan, J., Synthesis of Nanoarchitectured $LiNi_{0.5}Mn_{0.5}O_2$ Spheres for High-performance Rechargeable Lithium-ion Batteries via an In Situ Conversion Route. *J. Mater. Chem.* **2011,** *21* (28), 10437-10441.

120. Rao, C. V.; Reddy, A. L. M.; Yasuyuki, I.; Ajayan, P. M., $LiNi_{1/3}Co_{1/3}Mn_{1/3}O_2$–Graphene Composite as a Promising Cathode for Lithium-Ion Batteries. *ACS Appl. Mater. Interface* **2011,** *3* (8), 2966-2972.

121. Yang, C.; Zhang, X.; Huang, M.; Huang, J.; Fang, Z., Preparation and Rate Capability of Carbon Coated $LiNi_{1/3}Co_{1/3}Mn_{1/3}O_2$ as Cathode Material in Lithium Ion Batteries. *ACS Appl. Mater. Interface* **2017,** *9* (14), 12408-12415.

122. Oh, P.; Ko, M.; Myeong, S.; Kim, Y.; Cho, J., A Novel Surface Treatment Method and New Insight into Discharge Voltage Deterioration for High-Performance $0.4Li_2MnO_3$–$0.6LiNi_{1/3}Co_{1/3}Mn_{1/3}O_2$ Cathode Materials. *Adv. Energy Mater.* **2014,** *4* (16), 1400631-n/a.

123. Wang, M.; Chen, Y.; Luo, M.; Chen, L., Nanosized $0.3Li_2MnO_3 \cdot 0.7LiNi_{1/3}Mn_{1/3}Co_{1/3}O_2$ Synthesized by CNTs-assisted Hydrothermal Method as Cathode Material for Lithium Ion Battery. *J. Appl. Electrochem.* **2016,** *46* (9), 907-915.

124. Whittingham, M. S., Ultimate Limits to Intercalation Reactions for Lithium Batteries. *Chem. Rev.* **2014,** *114*, 11414-11440.

125. Whittingham, M. S.; Song, Y.; Lutta, S.; Zavalij, P. Y.; Chernova, N. A., Some Transition metal (oxy)Phosphates and Vanadium Oxides for Lithium Batteries. *J. Mater. Chem.* **2005,** *15*, 3362–3379.

126. Liu, Q.; Li, Z.-F.; Liu, Y.; Zhang, H.; Ren, Y.; Sun, C.-J.; Lu, W.; Zhou, Y.; Stanciu, L.; Stach, E. A.; Xie, J., Graphene-Modified Nanostructured Vanadium Pentoxide Hybrids with Extraordinary Electrochemical Performance for Li-Ion Batteries. *Nat. Commun.* **2015,** *6*, 1-10.

127. Liu, Y.; Uchaker, E.; Zhou, N.; Li, J.; Zhanga, Q.; Cao, G., Facile Synthesis of Nanostructured Vanadium Oxide as Cathode Materials for Efficient Li-ion Batteries. *J. Mater. Chem.* **2012,** *22*, 24439-24445.

128. Tan, H. T.; Rui, X.; Sun, W.; Yan, Q.; Lim, T. M., Vanadium-Based Nanostructure Materials for Secondary Lithium Battery Applications. *Nanoscale* **2015,** *7*, 14595-14607.

129. Lin, D.; Liu, Y.; Cui, Y., Reviving the Lithium Metal Anode for High-energy Batteries. *Nat Nano* **2017,** *12* (3), 194-206.

130. Goriparti, S.; Miele, E.; De Angelis, F.; Di Fabrizio, E.; Proietti Zaccaria, R.; Capiglia, C., Review on Recent Progress of Nanostructured Anode Materials for Li-ion Batteries. *J. Power Sources* **2014,** *257* (Supplement C), 421-443.

131. Park, T.-H.; Yeo, J.-S.; Seo, M.-H.; Miyawaki, J.; Mochida, I.; Yoon, S.-H., Enhancing the Rate Performance of Graphite Anodes Through Addition of Natural Graphite/Carbon Nanofibers in Lithium-ion Batteries. *Electrochimica Acta* **2013,** *93* (Supplement C), 236-240.

132. Fujimoto, H.; Tokumitsu, K.; Mabuchi, A.; Chinnasamy, N.; Kasuh, T., The Anode Performance of the Hard Carbon for the Lithium Ion Battery Derived from the Oxygen-containing Aromatic Precursors. *J. Power Sources* **2010,** *195* (21), 7452-7456.

133. Yang, J.; Zhou, X.-y.; Li, J.; Zou, Y.-l.; Tang, J.-j., Study of Nano-porous Hard Carbons as Anode Materials for Lithium Ion Batteries. *Mater. Chem. Phys.* **2012,** *135* (2), 445-450.

134. Ng, S. H.; Wang, J.; Guo, Z. P.; Chen, J.; Wang, G. X.; Liu, H. K., Single Wall Carbon Nanotube Paper as Anode for Lithium-ion Battery. *Electrochimica Acta* **2005,** *51* (1), 23-28.

135. Xiong, Z.; Yun, Y. S.; Jin, H.-J., Applications of Carbon Nanotubes for Lithium Ion Battery Anodes. *Materials* **2013,** *6* (3), 1138-1158.

136. Landi, B. J.; DiLeo, R. A.; Schauerman, C. M.; Cress, C. D.; Ganter, M. J.; Raffaelle, R. P., Multi-walled Carbon Nanotube Paper Anodes for Lithium Ion Batteries. *J. Nanosci. Nanotechnol.* **2009,** *9* (6), 3406-10.

137. Lu, X. Y.; Jin, X. H.; Sun, J., Advances of Graphene Application in Electrode Materials for Lithium Ion Batteries. *Sci. China Tech. Sci.* **2015,** *58* (11), 1829-1840.

138. Liu, Y.; Artyukhov, V. I.; Liu, M.; Harutyunyan, A. R.; Yakobson, B. I., Feasibility of Lithium Storage on Graphene and Its Derivatives. *J. Phys. Chem. Lett.* **2013,** *4* (10), 1737-1742.

139. Hwang, H. J.; Koo, J.; Park, M.; Park, N.; Kwon, Y.; Lee, H., Multilayer Graphynes for Lithium Ion Battery Anode. *J. Phys. Chem. C* **2013,** *117* (14), 6919-6923.

140. Pan, D.; Wang, S.; Zhao, B.; Wu, M.; Zhang, H.; Wang, Y.; Jiao, Z., Li Storage Properties of Disordered Graphene Nanosheets. *Chem. Mater.* **2009,** *21* (14), 3136-3142

.

141. Han, F.-D.; Yao, B.; Bai, Y.-J., Preparation of Carbon Nano-Onions and Their Application as Anode Materials for Rechargeable Lithium-Ion Batteries. *J. Phys. Chem. C* **2011,** *115* (18), 8923-8927.

142. Yu, Y.; Liu, Y.; Yang, X., Carbon Nanofiber-Based Materials as Anode Materials for Lithium-Ion Batteries. In *Alkali-ion Batteries*, Yang, D., Ed. InTech: Rijeka, 2016; p Ch. 01.

143. Huang, Q.; Wang, S.; Zhang, Y.; Yu, B.; Hou, L.; Su, G.; Ma, S.; Zou, J.; Huang, H., Hollow Carbon Nanospheres with Extremely Small Size as Anode Material in Lithium-Ion Batteries with Outstanding Cycling Stability. *J. Phys. Chem. C* **2016,** *120* (6), 3139-3144.

144. Wu, H. B.; Chen, J. S.; Hng, H. H.; Lou, W. X., Nanostructured Metal Oxide-based Materials as Advanced Anodes for Lithium-ion Batteries. *Nanoscale* **2012,** *4* (8), 2526-2542.

145. Yi, T.-F.; Jiang, L.-J.; Shu, J.; Yue, C.-B.; Zhu, R.-S.; Qiao, H.-B., Recent Development and Application of $Li_4Ti_5O_{12}$ as Anode Material of Lithium Ion Battery. *J. Phys. Chem. Solids* **2010,** *71* (9), 1236-1242.

146. Hao, Y.-J.; Lai, Q.-Y.; Lu, J.-Z.; Wang, H.-L.; Chen, Y.-D.; Ji, X.-Y., Synthesis and Characterization of Spinel $Li_4Ti_5O_{12}$ Anode Material by Oxalic Acid-assisted Sol–gel Method. *J. Power Sources* **2006,** *158* (2), 1358-1364.

147. Liu, Y.; Yang, Y., Recent Progress of TiO_2-Based Anodes for Li Ion Batteries. *J. Nanomaterials* **2016,** *2016*, 15.

148. Guler, M. O.; Cevher, O.; Cetinkaya, T.; Tocoglu, U.; Akbulut, H., High Capacity TiO_2 Anode Materials for Li-ion Batteries. *Energy Convers. Manag.* **2013,** *72* (Supplement C), 111-116.

149. Chan, C. K.; Peng, H.; Liu, G.; McIlwrath, K.; Zhang, X. F.; Huggins, R. A.; Cui, Y., High-performance Lithium Battery Anodes using Silicon Nanowires. *Nat. Nano.* **2008,** *3* (1), 31-35.

150. Klankowski, S. A.; Rojeski, R. A.; Cruden, B. A.; Liu, J.; Wu, J.; Li, J., A High-Performance Lithium-Ion Battery Anode Based on the Core-Shell Heterostructure of Silicon-Coated Vertically Aligned Carbon Nanofibers. *J. Mater. Chem. A* **2013,** *1* (4), 1055-1064.

151. Klankowski, S. A.; Pandey, G. P.; Cruden, B. A.; Liu, J.; Wu, J.; Rojeski, R. A.; Li, J., Anomalous Capacity Increase at High-Rates in Lithium-ion Battery Anodes Based on Silicon-Coated Vertically Aligned Carbon Nanofibers. *J. Power Sources* **2015,** *276* (Supplement C), 73-79.

152. Miyachi, M.; Yamamoto, H.; Kawai, H.; Ohta, T.; Shirakata, M., Analysis of SiO Anodes for Lithium-Ion Batteries. *J. Electrochem. Soc.* **2005,** *152* (10), A2089-A2091.

153. Song, K.; Yoo, S.; Kang, K.; Heo, H.; Kang, Y.-M.; Jo, M.-H., Hierarchical SiO_x Nanoconifers for Li-ion Battery Anodes with Structural Stability and Kinetic Enhancement. *J. Power Sources* **2013,** *229* (Supplement C), 229-233.

154. Park, C.-M.; Choi, W.; Hwa, Y.; Kim, J.-H.; Jeong, G.; Sohn, H.-J., Characterizations and Electrochemical Behaviors of Disproportionated SiO and its Composite forRechargeable Li-ion Batteries. *J. Mater. Chem.* **2010,** *20* (23), 4854-4860.

155. Liu, J.; Song, K.; Zhu, C.; Chen, C.-C.; van Aken, P. A.; Maier, J.; Yu, Y., Ge/C Nanowires as High-Capacity and Long-Life Anode Materials for Li-Ion Batteries. *ACS Nano* **2014,** *8* (7), 7051-7059.

156. Liang, J.; Li, X.; Hou, Z.; Zhang, T.; Zhu, Y.; Yan, X.; Qian, Y., Honeycomb-like Macro-Germanium as High-Capacity Anodes for Lithium-Ion Batteries with Good Cycling and Rate Performance. *Chem. Mater.* **2015,** *27* (11), 4156-4164.

157. Lee, S.-Y.; Park, K.-Y.; Kim, W.-S.; Yoon, S.; Hong, S.-H.; Kang, K.; Kim, M., Unveiling Origin of Additional Capacity of SnO_2 Anode in Lithium-ion Batteries by Realistic ex situ TEM Analysis. *Nano Energy* **2016,** *19* (Supplement C), 234-245.

158. Wang, D.; Dong, H.; Zhang, H.; Zhang, Y.; Xu, Y.; Zhao, C.; Sun, Y.; Zhou, N., Enabling a High Performance of Mesoporous α-Fe_2O_3 Anodes by Building a Conformal Coating of Cyclized-PAN Network. *ACS Appl. Mater. Interface* **2016,** *8* (30), 19524-19532.

159. Jiang, Y.; Jiang, Z.-J.; Yang, L.; Cheng, S.; Liu, M., A high-Performance Anode for Lithium Ion Batteries: Fe_3O_4 Microspheres Encapsulated in Hollow Graphene Shells. *J. Mater. Chem. A* **2015,** *3* (22), 11847-11856.

160. Huang, G.; Xu, S.; Lu, S.; Li, L.; Sun, H., Micro-/Nanostructured Co_3O_4 Anode with Enhanced Rate Capability for Lithium-Ion Batteries. *ACS Appl. Mater. Interface* **2014,** *6* (10), 7236-7243.

161. Rai, A. K.; Anh, L. T.; Gim, J.; Kim, J., One-step Synthesis of CoO Anode Material for Rechargeable Lithium-ion Batteries. *Cer. Int.* **2013,** *39* (8), 9325-9330.

162. Reddy, M. V.; Subba Rao, G. V.; Chowdari, B. V. R., Metal Oxides and Oxysalts as Anode Materials for Li Ion Batteries. *Chem. Rev.* **2013,** *113* (7), 5364-5457.

163. Slater, M. D.; Kim, D.; Lee, E.; Johnson, C. S., Sodium-Ion Batteries. *Adv. Funct. Mater.* **2013,** *23* (8), 947-958.

164. Xu, J.; Wang, M.; Wickramaratne, N. P.; Jaroniec, M.; Dou, S.; Dai, L., High-Performance Sodium Ion Batteries Based on a 3D Anode from Nitrogen-Doped Graphene Foams. *Adv. Mater.* **2015,** *27* (12), 2042-2048.

165. Zhu, K.; Zhang, C.; Guo, S.; Yu, H.; Liao, K.; Chen, G.; Wei, Y.; Zhou, H., Sponge-Like Cathode Material Self-Assembled from Two-Dimensional V_2O_5 Nanosheets for Sodium-Ion Batteries. *Chem. Electro. Chem* **2015,** *2* (11), 1660-1664.

166. Seh, Z. W.; Sun, J.; Sun, Y.; Cui, Y., A Highly Reversible Room-Temperature Sodium Metal Anode. *ACS Cent. Sci.* **2015,** *1* (8), 449-455.

167. Wen, Y.; He, K.; Zhu, Y.; Han, F.; Xu, Y.; Matsuda, I.; Ishii, Y.; Cumings, J.; Wang, C., Expanded Graphite as Superior Anode for Sodium-ion Batteries. *Nat. Commun.* **2014,** *5*, 4033.

168. Kang, H.; Liu, Y.; Cao, K.; Zhao, Y.; Jiao, L.; Wang, Y.; Yuan, H., Update on Anode Materials for Na-ion Batteries. *J. Mater. Chem. A* **2015,** *3* (35), 17899-17913.

169. Wang, Y.-X.; Chou, S.-L.; Liu, H.-K.; Dou, S.-X., Reduced Graphene Oxide with Superior Cycling Stability and Rate Capability for Sodium Storage. *Carbon* **2013,** *57* (Supplement C), 202-208.

170. Suresh Babu, R.; Pyo, M., Hard Carbon and Carbon Nanotube Composites for the Improvement of Low-Voltage Performance in Na Ion Batteries. *J. Electrochem. Soc.* **2014,** *161* (6), A1045-A1050.

171. Zhou, X.; Guo, Y.-G., Highly Disordered Carbon as a Superior Anode Material for Room-Temperature Sodium-Ion Batteries. *Chem. Electro. Chem.* **2014,** *1* (1), 83-86.

172. Liu, Y.; Fan, F.; Wang, J.; Liu, Y.; Chen, H.; Jungjohann, K. L.; Xu, Y.; Zhu, Y.; Bigio, D.; Zhu, T.; Wang, C., In Situ Transmission Electron Microscopy Study of Electrochemical Sodiation and Potassiation of Carbon Nanofibers. *Nano Letters* **2014,** *14* (6), 3445-3452.

173. Xu, G.-L.; Chen, Z.; Zhong, G.-M.; Liu, Y.; Yang, Y.; Ma, T.; Ren, Y.; Zuo, X.; Wu, X.-H.; Zhang, X.; Amine, K., Nanostructured Black Phosphorus/Ketjenblack–Multiwalled Carbon Nanotubes Composite as High Performance Anode Material for Sodium-Ion Batteries. *Nano Letters* **2016,** *16* (6), 3955-3965.

174. Zhu, Y.; Wen, Y.; Fan, X.; Gao, T.; Han, F.; Luo, C.; Liou, S.-C.; Wang, C., Red Phosphorus–Single-Walled Carbon Nanotube Composite as a Superior Anode for Sodium Ion Batteries. *ACS Nano* **2015,** *9* (3), 3254-3264.

175. Webb, S. A.; Baggetto, L.; Bridges, C. A.; Veith, G. M., The Electrochemical Reactions of Pure Indium with Li and Na: Anomalous Electrolyte Decomposition, Benefits of FEC Additive, Phase Transitions and Electrode Performance. *J. Power Sources* **2014,** *248* (Supplement C), 1105-1117.

176. Li, Z.; Ding, J.; Mitlin, D., Tin and Tin Compounds for Sodium Ion Battery Anodes: Phase Transformations and Performance. *Acc. Chem. Res.* **2015,** *48* (6), 1657-1665.

177. Farbod, B.; Cui, K.; Kalisvaart, W. P.; Kupsta, M.; Zahiri, B.; Kohandehghan, A.; Lotfabad, E. M.; Li, Z.; Luber, E. J.; Mitlin, D., Anodes for Sodium Ion Batteries Based on Tin–Germanium–Antimony Alloys. *ACS Nano* **2014,** *8* (5), 4415-4429.

178. Liang, L.; Xu, Y.; Wang, C.; Wen, L.; Fang, Y.; Mi, Y.; Zhou, M.; Zhao, H.; Lei, Y., Large-scale Highly Ordered Sb Nanorod Array Anodes with High Capacity and Rate Capability for Sodium-ion Batteries. *Energy Environ. Sci.* **2015,** *8* (10), 2954-2962.

179. Li, D.; Zhou, J.; Chen, X.; Song, H., Amorphous Fe_2O_3/Graphene Composite Nanosheets with Enhanced Electrochemical Performance for Sodium-Ion Battery. *ACS Appl. Mater. Interface* **2016,** *8* (45), 30899-30907.

180. Fu, F.; Li, J.; Yao, Y.; Qin, X.; Dou, Y.; Wang, H.; Tsui, J.; Chan, K.-Y.; Shao, M., Hierarchical $NiCo_2O_4$ Micro- and Nanostructures with Tunable Morphologies as Anode Materials for Lithium- and Sodium-Ion Batteries. *ACS Appl. Mater. Interface* **2017,** *9* (19), 16194-16201.

181. Fan, M.; Yu, H.; Chen, Y., High-Capacity Sodium Ion Battery Anodes based on CuO Nanosheets and Carboxymethyl Cellulose Binder. *Mater. Technol.* **2017,** *32* (10), 598-605.

182. Mei, Y.; Huang, Y.; Hu, X., Nanostructured Ti-based Anode Materials for Na-ion Batteries. *J. Mater. Chem. A* **2016,** *4* (31), 12001-12013.

183. Deng, Q.; Wang, L.; Li, J., Electrochemical Characterization of Co_3O_4/MCNTs Composite Anode Materials for Sodium-ion Batteries. *J. Mater. Sci.* **2015,** *50* (11), 4142-4148.

184. Tang, J.; Ni, S.; Chen, Q.; Han, W.; Yang, X.; Zhang, L., The Electrochemical Performance of NiO Nanowalls/Ni Anode in Half-cell and Full-cell Sodium Ion Batteries. *Mater. Lett.* **2017,** *195* (Supplement C), 127-130.

185. Zhang, X.; Fu, C.; Li, J.; Yao, C.; Lu, T.; Pan, L., MoO_3/Reduced Graphene Oxide Composites as Anode Material for Sodium ion Batteries. *Cer. Int.* **2017,** *43* (4), 3769-3773.

186. Zhang, Z.; Zhao, X.; Li, J., Facile Synthesis of Nanostructured MnO_2 as Anode Materials for Sodium-Ion Batteries. *ChemNanoMat* **2016,** *2* (3), 196-200.

187. Lu, Y. C.; Ma, C.; Alvarado, J.; Kidera, T.; Dimov, N.; Meng, Y. S.; Okada, S., Electrochemical Properties of Tin Oxide Anodes for Sodium-ion Batteries. *J. Power Sources* **2015,** *284*, 287-295.

188. Li, K.; Liu, H.; Wang, G., Sb_2O_3 Nanowires as Anode Material for Sodium-Ion Battery. *AJSE* **2014,** *39* (9), 6589-6593.

189. Hu, Z.; Wang, L.; Zhang, K.; Wang, J.; Cheng, F.; Tao, Z.; Chen, J., MoS_2 Nanoflowers with Expanded Interlayers as High-Performance Anodes for Sodium-Ion Batteries. *Angewandte Chemie* **2014,** *126* (47), 13008-13012.

190. Sahu, T. S.; Mitra, S., Exfoliated MoS_2 Sheets and Reduced Graphene Oxide-An Excellent and Fast Anode for Sodium-ion Battery. *Nat. Commun.* **2015,** *5*, 12571.

191. Wang, J.; Luo, C.; Gao, T.; Langrock, A.; Mignerey, A. C.; Wang, C., An Advanced MoS_2/Carbon Anode for High-Performance Sodium-Ion Batteries. *Small* **2015,** *11* (4), 473-481.

192. Xiang, X.; Zhang, K.; Chen, J., Recent Advances and Prospects of Cathode Materials for Sodium-Ion Batteries. *Adv. Mater.* **2015,** *27* (36), 5343-5364.

193. Kosova, N. V.; Podugolnikov, V. R.; Devyatkina, E. T.; Slobodyuk, A. B., Structure and Electrochemistry of $NaFePO_4$ and Na_2FePO_4F Cathode Materials Prepared via Mechanochemical Route. *Materials Research Bulletin* **2014,** *60* (Supplement C), 849-857.

194. Gao, R.; Tan, R.; Han, L.; Zhao, Y.; Wang, Z.; Yang, L.; Pan, F., Nanofiber Networks of $Na_3V_2(PO_4)_3$ as a Cathode Material for High Performance all-solid-state Sodium-ion Batteries. *J. Mater. Chem. A* **2017,** *5* (11), 5273-5277.

195. Clark, J. M.; Barpanda, P.; Yamada, A.; Islam, M. S., Sodium-ion Battery Cathodes $Na_2FeP_2O_7$ and $Na_2MnP_2O_7$: Diffusion Behaviour for High Rate Performance. *J. Mater. Chem. A* **2014,** *2* (30), 11807-11812.

196. Wood, S. M.; Eames, C.; Kendrick, E.; Islam, M. S., Sodium Ion Diffusion and Voltage Trends in Phosphates $Na_4M_3(PO_4)_2P_2O_7$ (M = Fe, Mn, Co, Ni) for Possible High-Rate Cathodes. *J. Phys. Chem. C* **2015,** *119* (28), 15935-15941.

197. Ellis, B. L.; Makahnouk, W. R. M.; Rowan-Weetaluktuk, W. N.; Ryan, D. H.; Nazar, L. F., Crystal Structure and Electrochemical Properties of A_2MPO_4F Fluorophosphates (A = Na, Li; M = Fe, Mn, Co, Ni). *Chem. Mater.* **2010,** *22* (3), 1059-1070.

198. Shakoor, R. A.; Seo, D.-H.; Kim, H.; Park, Y.-U.; Kim, J.; Kim, S.-W.; Gwon, H.; Lee, S.; Kang, K., A Combined First Principles and Experimental Study on $Na_3V_2(PO_4)_2F_3$ for Rechargeable Na Batteries. *J. Mater. Chem.* **2012,** *22* (38), 20535-20541.

199. Barpanda, P.; Oyama, G.; Nishimura, S.-i.; Chung, S.-C.; Yamada, A., A 3.8-V Earth-Abundant Sodium Battery Electrode. *Nat. Commun.* **2014,** *5*, 4358.

200. Yue, Y.; Binder, A. J.; Guo, B.; Zhang, Z.; Qiao, Z.-A.; Tian, C.; Dai, S., Mesoporous Prussian Blue Analogues: Template-Free Synthesis and Sodium-Ion Battery Applications. *Angew. Chem. Int. Ed.* **2014,** *53* (12), 3134-3137.

201. Lu, Y.; Wang, L.; Cheng, J.; Goodenough, J. B., Prussian Blue: a New Framework of Electrode Materials for Sodium Batteries. *Chem. Commun.* **2012,** *48* (52), 6544-6546.

202. You, Y.; Wu, X.-L.; Yin, Y.-X.; Guo, Y.-G., High-quality Prussian Blue Crystals as Superior Cathode Materials for Room-Temperature Sodium-ion Batteries. *Energy Environ. Sci.* **2014,** *7* (5), 1643-1647.

203. Yang, D.; Xu, J.; Liao, X.-Z.; He, Y.-S.; Liu, H.; Ma, Z.-F., Structure Optimization of Prussian blue Analogue Cathode Materials for Advanced Sodium Ion Batteries. *Chem. Commun.* **2014,** *50* (87), 13377-13380.

204. Lee, H.-W.; Wang, R. Y.; Pasta, M.; Woo Lee, S.; Liu, N.; Cui, Y., Manganese Hexacyanomanganate Open Framework as a High-capacity Positive Electrode Material for Sodium-ion Batteries. **2014,** *5*, 5280.

205. Shibata, T.; Fukuzumi, Y.; Kobayashi, W.; Moritomo, Y., Fast Discharge Process of Layered Cobalt Oxides due to High Na^+ Diffusion. *Nat. Commun.* **2015,** *5*, 9006.

206. Rai, A. K.; Anh, L. T.; Gim, J.; Mathew, V.; Kim, J., Electrochemical Properties of Na_xCoO_2 (x~0.71) Cathode for Rechargeable Sodium-ion Batteries. *Cer. Int.* **2014,** *40* (1, Part B), 2411-2417.

207. Bucher, N.; Hartung, S.; Nagasubramanian, A.; Cheah, Y. L.; Hoster, H. E.; Madhavi, S., Layered Na_xMnO_2+z in Sodium Ion Batteries–Influence of Morphology on Cycle Performance. *ACS Appl. Mater. Interface* **2014,** *6* (11), 8059-8065.

208. Lee, E.; Brown, D. E.; Alp, E. E.; Ren, Y.; Lu, J.; Woo, J.-J.; Johnson, C. S., New Insights into the Performance Degradation of Fe-Based Layered Oxides in Sodium-Ion Batteries: Instability of $Fe3^+/Fe4^+$ Redox in α-$NaFeO_2$. *Chem. Mater.* **2015,** *27* (19), 6755-6764.

209. Yu, C.-Y.; Park, J.-S.; Jung, H.-G.; Chung, K.-Y.; Aurbach, D.; Sun, Y.-K.; Myung, S.-T., $NaCrO_2$ Cathode for High-rate Sodium-ion batteries. *Energy Environ. Sci.* **2015,** *8* (7), 2019-2026.

210. Vassilaras, P.; Ma, X.; Li, X.; Ceder, G., Electrochemical Properties of Monoclinic $NaNiO_2$. *J. Electrochem. Soc.* **2013,** *160* (2), A207-A211.

211. Su, D.; Wang, G., Single-Crystalline Bilayered V_2O_5 Nanobelts for High-Capacity Sodium-Ion Batteries. *ACS Nano* **2013,** *7* (12), 11218-11226.

212. Su, D. W.; Dou, S. X.; Wang, G. X., Hierarchical Orthorhombic V_2O_5 Hollow Nanospheres as High Performance Cathode Materials for Sodium-Ion Batteries. *J. Mater. Chem. A* **2014,** *2*, 11185-11194.

213. Zhu, K.; Wei, Y.; Zhang, C.; Guo, S.; Yu, H.; Liao, K.; Chen, G.; Zhou, H., Sponge-Like Cathode Material Self-Assembled from Two-Dimensional V_2O_5 Nanosheets for Sodium-Ion Batteries. *Chem. Electro. Chem.* **2015,** *2*, 1660-1664.

214. Li, H.-Y.; Yang, C.-H.; Tseng, C.-M.; Lee, S.-W.; Yang, C.-C.; Wu, T.-Y.; Chang, J.-K., Electrochemically Grown Nanocrystalline V_2O_5 as High-Performance Cathode for Sodium-Ion Batteries. *J. Power Sources* **2015,** *285*, 418-424.

215. Tepavcevic, S.; Xiong, H.; Stamenkovic, V.; Zuo, X.; Balasubramanian, M.; Prakapenka, V.; Johnson, C.; Rajh, T., Nanostructured Bilayered Vanadium Oxide Electrodes for Rechargeable Sodium-Ion Batteries. *ACS Nano* **2012,** *6* (1), 530-538.

216. Uchaker, E.; Zheng, Y. Z.; Li, S.; Candelaria, S. L.; Hu, S.; Cao, G. Z., Better than Crystalline: Amorphous Vanadium Oxide for Sodium-Ion Batteries. *J. Mater. Chem. A* **2014,** *2* (43), 18208-18214.

217. Liu, S.; Tong, Z.; Zhao, J.; Liu, X.; Wang, J.; Ma, X.; Chi, C.; Yang, Y.; Liu, X.; Li, Y., Rational Selection of Amorphous or Crystalline V_2O_5 Cathode for Sodium-Ion Batteries. *Phys. Chem. Chem. Phys.* **2016,** *18*, 25645-25654.

218. Moretti, A.; Maroni, F.; Osada, I.; Nobill, F.; Passerini, S., V_2O_5 Aerogel as aVersatile Cathode Material for Lithium and Sodium Batteries. *Chem. Electro. Chem.* **2015,** *2* (529-537).

219. Chen, D.; Quan, H.; Luo, S.; Luo, X.; Deng, F.; Jiang, H., Reduced Graphene Oxide Enwrapped Vanadium Pentoxide Nanorods as Cathode Materials for Lithium-ion Batteries. *Physica E* **2014,** *56*, 231–237.

220. Yang, S.; Gong, Y.; Liu, Z.; Zhan, L.; Hashim, D. P.; Ma, L.; Vajtai, R.; Ajayan, P. M., Bottom-up Approach toward Single-Crystalline VO2-Graphene Ribbons as Cathodes for Ultrafast Lithium Storage. *Nano Letters* **2013,** *13* (4), 1596-1601.

221. Kavan, L., Lithium Insertion into TiO_2 (Anatase): Electrochemistry, Raman Spectroscopy, and Isotope Labeling. *J. Solid State Electrochem.* **2014,** *18* (8), 2297-2306.

222. Liwei Su, Y. J., Zhen Zhou, Li ion battery materials with core–shell nanostructures. *Nanoscale* **2011,** *3*, 3967-3983.

223. Mohamedi, M.; Lee, S.-J.; Takahashi, D.; Nishizawa, M.; Itoh, T.; Uchida, I., Amorphous Tin Oxide Films: Preparation and Characterization as an Anode Active Material for Lithium ion Batteries. *Electrochimica Acta* **2001,** *46* (8), 1161-1168.

224. Jian, Z.; Zhao, L.; Pan, H.; Hu, Y.-S.; Li, H.; Chen, W.; Chen, L., Carbon Coated $Na_3V_2(PO_4)_3$ as Novel Electrode Material for Sodium Ion Batteries. *Electrochem. Commun.* **2012,** *14*, 86–89.

225. Su, L.; Winnick, J.; Kohl, P., Sodium Insertion into Vanadium Pentoxide in Methanesulfonyl Chloride-Aluminum Chloride Ionic Liquid. *J. Power Sources* **2001,** *101*, 226-230.

226. Wu, G.-M.; Wang, A.-R.; Zhang, M.-X.; Yang, H.-Y.; Zhou, B.; Shen, J., Investigation on Properties of V_2O_5–MWCNTs Composites as Cathode Materials. *J Sol-Gel Sci Technol* **2008,** *46*, 79–85.

227. Zhu, Y.-J.; Chen, F., Microwave-Assisted Preparation of Inorganic Nanostructures in Liquid Phase. *Chem. Rev.* **2014,** *114* (12), 6462-6555.

228. Liu, N.; Wu, H.; McDowell, M. T.; Yao, Y.; Wang, C.; Cui, Y., A Yolk-Shell Design for Stabilized and Scalable Li-Ion Battery Alloy Anodes. *Nano Letters* **2012,** *12* (6), 3315-3321.

229. Wang, Y.; Wang, Y.; Hosono, E.; Wang, K.; Zhou, H., The Design of a $LiFePO_4$/Carbon Nanocomposite With a Core–Shell Structure and Its Synthesis by an In Situ Polymerization Restriction Method. *Ang. Chem. Int. Ed.* **2008,** *47* (39), 7461-7465.

230. Chao, D.; Xia, X.; Liu, J.; Fan, Z.; Ng, C. F.; Lin, J.; Zhang, H.; Shen, Z. X.; Fan, H. J., A V_2O_5/Conductive-Polymer Core/Shell Nanobelt Array on Three-Dimensional Graphite Foam: A High-Rate, Ultrastable, and Freestanding Cathode for Lithium-Ion Batteries. *Adv. Mater.* **2014,** *26* (33), 5794-5800.

231. Chen, X.; Zhu, H.; Chen, Y.-C.; Shang, Y.; Cao, A.; Hu, L.; Rubloff, G. W., MWCNT/V_2O_5 Core/Shell Sponge for High Areal Capacity and Power Density Li-Ion Cathodes. *ACS Nano* **2012,** *6*, 7948–7955.

232. Zussman, E.; Chen, X.; Ding, W.; Calabri, L.; Dikin, D. A.; Quintana, J. P.; Ruoff, R. S., Mechanical and Structural Characterization of Electrospun PAN-derived Carbon Nanofibers. *Carbon* **2005,** *43* (10), 2175-2185.

233. Melechko, A. V.; Merkulov, V. I.; McKnight, T. E.; Guillorn, M. A.; Klein, K. L.; Lowndes, D. H.; Simpson, M. L., Vertically Aligned Carbon Nanofibers and Related Structures: Controlled Synthesis and Directed Assembly. *J. Appl. Phys.* **2005,** *97*, 041301.

234. Cruden, B. A.; Cassell, A. M.; Ye, Q.; Meyyappan, M., Reactor Design Considerations in the Hot Filament/Direct Current Plasma Synthesis of Carbon Nanofibers. *J. Appl. Phys.* **2003,** *94*, 4070-4078.

235. Liu, J.; Essner, J.; Li, J., Hybrid Supercapacitor Based on Coaxially Coated Manganese Oxide on Vertically Aligned Carbon Nanofiber Arrays. *Chem. Mater.* **2010,** *22*, 5022–5030.

236. Kelly, P. J.; Arnell, R. D., Magnetron Sputtering: a Review of Recent Developments and Applications. *Vacuum* **2000,** *56* (3), 159-172.

237. Pulsed Laser Deposition of Thin Films. 1st Edition ed.; Chrisey, D. B.; Hubler, G. K., Eds. Wiley-Interscience: 1994.

238. Johnson, R. W.; Hultqvist, A.; Bent, S. F., A Brief Review of Atomic Layer Deposition: from Fundamentals to Applications. *Mater. Today* **2014,** *17* (5), 236-246.

239. Schwarzacher, W., Electrodeposition: A Technology for the Future. *Electrochem. Soc. Int. Spring* **2006**, 32-35.

240. Kanani, N., Chapter 1 - Metal Finishing — A Key Technology? In *Electroplating*, Elsevier: Oxford, 2004; pp 1-19.

241. Bard, A.; Faulkner, L., *Electrochemical Methods: Fundamentals and Applications*. John Wiley & Sons, Inc: 2001.

242. Instruments, G. Testing Electrochemical Capacitors Part 1: CV, EIS, and Leakage Current. https://www.gamry.com/application-notes/battery-research/testing-electrochemical-capacitors-cyclic-voltammetry-leakage-current/.

243. Mattelaer, F.; Geryl, K.; Rampelberg, G.; Dendooven, J.; Detavernier, C., Amorphous and Crystalline Vanadium Oxides as High-Energy and High-Power Cathodes for Three-Dimensional Thin-Film Lithium Ion Batteries. *ACS applied materials & interfaces* **2017,** *9*, 13121−13131.

244. Jiang, H.; Lee, P. S.; Li, C., 3D Carbon Based Nanostructures for Advanced Supercapacitors. *Energy Environ. Sci.* **2013,** *6* (41), 41–53.

245. Zhang, L. L.; Zhao, X. S., Carbon-Based Materials as Supercapacitor Electrodes. *Chem. Soc. Rev.* **2009,** *38*, 2520–2531.

246. Lytle, J. C.; Wallace, J. M.; Sassin, M. B.; Barrow, A. J.; Long, J. W.; Dysart, J. L.; Renninger, C. H.; Saunders, M. P.; Brandell, N. L.; Rolison, D. R., The Right Kind of Interior for Multifunctional Electrode Architectures: Carbon Nanofoam Papers with Aperiodic Submicrometre Pore Networks Interconnected in 3D. *Energy Environ. Sci.* **2011,** *4*, 1913–1925.

247. Liu, J.; Kuo, Y.-T.; Klabunde, K. J.; Rochford, C.; Wu, J.; Li, J., Novel Dye-Sensitized Solar Cell Architecture Using TiO_2-Coated Vertically Aligned Carbon Nanofiber Arrays. *ACS Appl. Mater. Interface* **2009,** *1* (8), 1645–1649.

248. George, S. M., Atomic Layer Deposition: An Overview. *Chem. Rev.* **2010,** *110*, 111–131.

249. Hirsch, A., Functionalization of Single-Walled Carbon Nanotubes. *Angew. Chem. Int. Ed.* **2002,** *41* (11), 1853-1859.

250. Banerjee, S.; Hemraj-Benny, T.; Wong, S. S., Covalent Surface Chemistry of Single-Walled Carbon Nanotubes. *Adv. Mater.* **2005,** *17* (1), 17-29.

251. Farmer, D. B.; Gordon, R. G., Atomic Layer Deposition on Suspended Single-Walled Carbon Nanotubes via Gas-Phase Noncovalent Functionalization. *Nano Lett.* **2006,** *6* (4), 699-703.

252. Klein, K. L.; Melechko, A. V.; McKnight, T. E.; Retterer, S. T.; Rack, P. D.; Fowlkes, J. D.; Joy, D. C.; Simpson, M. L., Surface Characterization and Functionalization of Carbon Nanofibers. *J. Appl. Phys.* **2008,** *103*, 061301.

253. Lee, J. S.; Min, B.; Cho, K.; Kim, S.; Park, J.; Lee, Y. T.; Kim, N. S.; Lee, M. S.; Park, S. O.; Moon, J. T., Al_2O_3 Nanotubes and Nanorods Fabricated by Coating and Filling of Carbon Nanotubes with Atomic-Layer Deposition. *J. Cryst. Growth* **2003,** *254* (3-4), 443-448.

254. Herrmann, C. F.; Fabreguette, F. H.; Finch, D. S.; R., G.; George, S. M., Multilayer and Functional Coatings on Carbon Nanotubes using Atomic Layer Deposition. *Appl. Phys. Lett.* **2005,** *87*, 123110.

255. Dhindsa, M. S.; Smith, N. R.; Heikenfeld, J., Reversible Electrowetting of Vertically Aligned Superhydrophobic Carbon Nanofibers. *Langmuir* **2006,** *22*, 9030-9034.

256. Ngo, Q.; Yamada, T.; Suzuki, M.; Ominami, Y.; Cassell, A. M.; Li, J.; Meyyappan, M.; Yang, C. Y., Structural and Electrical Characterization of Carbon Nanofibers for Interconnect via Applications. *IEEE Trans. Nanotechnol.* **2007,** *6* (6), 688-695.

257. Elam, J. W.; Groner, M. D.; George, S. M., Viscous Flow Reactor with Quartz Crystal Microbalance for Thin Film Growth by Atomic Layer Deposition. *Rev. Sci. Instrum.* **2002,** *73* (8), 2981-2987.

258. Groner, M. D.; Elam, J. W.; Fabreguette, F. H.; George, S. M., Electrical Characterization of Thin Al_2O_3 Films Grown by Atomic Layer Deposition on Silicon and Various Metal Substrates. *Thin Solid Films* **2002,** *413* (1-2), 186-197.

259. Elliot, A. J.; Malek, G.; Wille, L.; Lu, R.; Han, S.; Wu, J.; Talvacchio, J.; Lewis, R. M., Probing the Nucleation of Al_2O_3 in Atomic Layer Deposition on Aluminum for Ultrathin Tunneling Barriers in Josephson Junctions. *IEEE Trans. Appl. Supercond.* **2013,** *23* (3), 1101405.

260. Lu, R.; Elliot, A. J.; Wille, L.; Mao, B.; Han, S.; Wu, J.; Talvacchio, J.; Schulze, H. M.; Lewis, R. M.; Ewing, D. J.; Yu, H. F.; Xue, G. M.; Zhao, S. P., Fabrication of $Nb/Al_2O_3/Nb$ Josephson Junctions using *in situ* Magnetron Sputtering and Atomic Layer Deposition. *IEEE Trans. Appl. Supercond.* **2013,** *23* (3), 1-5.

261. Miikkulainen, V.; Leskelä, M.; Ritala, M.; Puurunen, R. L., Crystallinity of Inorganic Films Grown by Atomic Layer Deposition: Overview and General Trends. *J. Appl. Phys.* **2013,** *113*, 021301.

262. Kong, B. H.; Choi, M. K.; Cho, H. K.; Kim, J. H.; Baek, S.; Lee, J.-H., Conformal Coating of Conductive ZnO:Al Films as Transparent Electrodes on High Aspect Ratio Si Microrods. *Electrochem. Solid-State Lett.* **2010,** *13* (2), K12-K14.

263. Elam, J. W.; Routkevitch, D.; George, S. M., Properties of $ZnO/A_{l2}O_3$ Alloy Films Grown Using Atomic Layer Deposition Techniques. *J. Electrochem. Soc.* **2003,** *150* (6), G339-G347.

264. Elam, J. W.; George, S. M., Growth of ZnO/Al_2O_3 Alloy Films Using Atomic Layer Deposition Techniques. *Chem. Mater.* **2013,** *15*, 1020-1028.

265. Banerjee, P.; Lee, W.-J.; Bae, K.-R.; Lee, S. B.; Rubloff, G. W., Structural, Electrical, and Optical Properties of Atomic Layer Deposition Al-doped ZnO Films. *J. Appl. Phys.* **2010,** *108*, 043504.

266. Rochford, C.; Li, Z.-Z.; Baca, J.; Liu, J.; Li, J.; Wu, J., The Effect of Annealing on the Photoconductivity of Carbon Nanofiber/TiO_2 Core-Shell Nanowires for use in Dye-Sensitized Solar Cells. *Appl. Phys. Lett.* **2010,** *97*, 043102

267. Lide, D. R., CRC Handbook of Chemistry and Physics. 85 ed.; CRC Press: Boca Raton, FL, 2004.

268. Yao, K.; Chen, S.; Rahimabady, M.; Mirshekarloo, M. S.; Yu, S.; Tay, F. E. H.; Sritharan, T.; Lu, L., Nonlinear Dielectric Thin Films for High-Power Electric Storage with Energy Density Comparable with Electrochemical Capacitors. *IEEE Trans. Ultrason., Ferroelect., Freq. Control* **2011,** *58* (9), 1968-1974.

269. Ogihara, H.; Randall, C. A.; Trolier-McKinstry, S., High-Energy Density Capacitors Utilizing $0.7BaTiO_3$-$0.3BiScO_3$ Ceramics. *J. Am. Ceram. Soc.* **2009,** *92* (8), 1719-1724.

270. Tong, S.; Ma, B.; Narayanan, M.; Liu, S.; Koritala, R.; Balachandran, U.; Shi, D., Lead Lanthanum Zirconate Titanate Ceramic Thin Films for Energy Storage. *ACS applied materials & interfaces* **2013,** *5* (4), 1474-80.

271. Dang, Z.-M.; Lin, Y.-H.; Nan, C.-W., Novel Ferroelectric Polymer Composites with High Dielectric Constants. *Adv. Mater.* **2003,** *15* (19), 1625-1629.

272. Poulsen, M.; Ducharme, S., Why Ferroelectric Polyvinylidene Fluoride is Special. *IEEE Trans. Dielectr. Electr. Insul.* **2010,** *17* (4), 1028-1035.

273. Zhu, L.; Wang, Q., Novel Ferroelectric Polymers for High Energy Density and Low Loss Dielectrics. *Macromolecules* **2012,** *45* (7), 2937-2954.

274. Damjanovic, D., Hysteresis in Piezoelectric and Ferroelectric Materials. In *The Science of Hysteresis*, Bertotti, G.; Mayergoyz, I., Eds. Elsevier: 2005; Vol. 3.

275. Tang, X.; Dai, J.; Zhu, X.; Lin, J.; Chang, Q.; Wu, D.; Song, W.; Sun, Y.; Tan, X., Thickness-Dependent Dielectric, Ferroelectric, and Magnetodielectric Properties of $BiFeO_3$ Thin Films Derived by Chemical Solution Deposition. *J. Am. Ceram. Soc.* **2012,** *95* (2), 538-544.

276. Ortega, N.; Kumar, A.; Scott, J. F.; Chrisey, D. B.; Tomazawa, M.; Kumari, S.; Diestra, D. G.; Katiyar, R. S., Relaxor-Ferroelectric Superlattices: High Energy Density Capacitors.

Journal of physics. Condensed matter : an Institute of Physics journal **2012,** *24* (44), 445901.

277. Hao, X., A Review on the Dielectric Materials for High Energy-Storage Application. *J. Adv. Dielectr.* **2013,** *03* (01), 1330001.

278. Hao, X.; Wang, Y.; Yang, J.; An, S.; Xu, J., High Energy-Storage Performance in $Pb_{0.91}La_{0.09}(Ti_{0.65}Zr_{0.35})O_3$ Relaxor Ferroelectric Thin Films. *J. Appl. Phys.* **2012,** *112* (11), 114111.

279. Ma, B.; Narayanan, M.; Liu, S.; Chao, S.; U., B., Ferroelectric PLZT Films Grown on Metal Foils for Power Electronics Applications.pdf. Energy Systems Division, A. N. L., Ed. Argonne, IL.

280. Scarisoreanu, N.; Dinescu, M.; Craciun, F.; Verardi, P.; Moldovan, A.; Purice, A.; Galassi, C., Pulsed Laser Deposition of Perovskite Relaxor Ferroelectric Thin Films. *Appl. Surf. Sci.* **2006,** *252* (13), 4553-4557.

281. Tyunina, M.; Levoska, J.; Sternberg, A.; Leppävuori, S., Relaxor Behavior of Pulsed Laser Deposited Ferroelectric $(Pb_{1-x}La_x)(Zr_{0.65}Ti_{0.35})O_3$ Films. *J. Appl. Phys.* **1998,** *84* (12), 6800.

282. Ma, C.; Ma, B.; Mi, S.-B.; Lui, M.; Wu, J., Enhanced Dielectric Nonlinearity in Epitaxial $Pb_{0.92}La_{0.08}Zr_{0.52}Ti_{0.48}O_3$ Thin Films. *Appl. Phys. Lett.* **2014,** *104* (16), 162902-5.

283. Lee, K.; Rhee, B. R., Leakage Current-Voltage Characteristics of Ferroelectric Thin Film Capacitors. *J. Korean Phys. Soc.* **2001,** *38* (6), 723-8.

284. Meyer, R.; Waser, R.; Prume, K.; Schmitz, T.; Tiedke, S., Dynamic Leakage Current Compensation in Ferroelectric Thin-Film Capacitor Structures. *Appl. Phys. Lett.* **2005,** *86* (14), 142907.

285. Yan, H.; Inam, F.; Viola, G.; Ning, H.; Zhang, H.; Jiang, Q.; Zeng, T. A. O.; Gao, Z.; Reece, M. J., The Contribution of Electrical Conductivity, Dielectric Permittivity and Domain Switching in Ferroelectric Hysteresis Loops. *J. Adv. Dielectr.* **2011,** *01* (01), 107-118.

286. Bobnar, V.; Uršič, H.; Casar, G.; Drnovšek, S., Distinctive Contributions to Dielectric Response of Relaxor Ferroelectric Lead Scandium Niobate Ceramic System. *Phys. Status Solidi (b)* **2013,** *250* (10), 2232-2236.

287. Pike, G. E.; Warren, W. L.; Dimos, D.; Tuttle, B. A.; Ramesh, R.; Lee, J.; Keramidas, V. G.; Evans, J. T., Voltage Offsets in (Pb,La)(Zr,Ti)O_3 thin films. *Appl. Phys. Lett.* **1995,** *66* (4), 484.

288. Zheng, Y.; Wang, B.; Woo, C. H., Effects of Strain Gradient on Charge Offsets and Pyroelectric Properties of Ferroelectric Thin Films. *Appl. Phys. Lett.* **2006,** *89* (6), 062904.

289. Karden, E.; Ploumen, S.; Frickea, B.; Miller, T.; Snyder, K., Energy Storage Devices for Future Hybrid Electric Vehicles. *J. Power Sources* **2007,** *168*, 2-11.

290. Armand, M.; Tarascon, J. M., Building Better Batteries. *Nature* **2008,** *451*, 652-657.

291. Scrosati, B.; Garche, J., Lithium Batteries: Status, Prospects and Future. *J. Power Sources* **2010,** *195*, 2419–2430.

292. Yoo, H. D.; Markevich, E.; Salitra, G.; Sharon, D.; Aurbach, D., On the Challenge of Developing Advanced Technologies for Electrochemical Energy Storage and Conversion. *Mater. Today* **2014,** *17*, 110-121.

293. Szczech, J. R.; Jin, S., Nanostructured Silicon for High Capacity Lithium Battery Anodes. *Energy Environ. Sci.* **2011,** *4* (1), 56-72.

294. Chan, C. K.; Peng, H. L.; Liu, G.; McIlwrath, K.; Zhang, X. F.; Huggins, R. A.; Cui, Y., High-Performance Lithium Battery Anodes Using Silicon Nanowires. *Nat. Nanotechnol.* **2008,** *3* (1), 31-35.

295. Xu, J.; Dou, S.; Liu, H.; Dai, L., Cathode Materials for Next Generation Lithium Ion Batteries. *Nano Energy* **2013,** *2*, 439-442.

296. Fergus, J. W., Recent Developments in Cathode Materials for Lithium Ion Batteries. *J. Power Sources* **2010,** *195*, 939-954.

297. Yue, Y.; Liang, H., Micro- and Nano-Structured Vanadium Pentoxide (V_2O_5) for Electrodes of Lithium-Ion Batteries. *Adv. Energy Mater.* **2017**, 1602545.

298. Cheng, J.; Wang, B.; Xin, H. L.; Yang, G.; Cai, H.; Niea, F.; Huang, H., Self-Assembled V_2O_5 Nanosheets/Reduced Graphene Oxide Hierarchical Nanocomposite as a High-Performance Cathode Material for Lithium Ion Batteries. *J. Mater. Chem. A* **2013,** *1*, 10814–10820.

299. Moretti, A.; Passerini, S., Bilayered Nanostructured $V_2O_5{\cdot}nH_2O$ for Metal Batteries. *Adv. Energy Mater.* **2016**, 1600868.

300. Huang, X.; Rui, X.; Hng, H. H.; Yan, Q., Vanadium Pentoxide-Based Cathode Materials for Lithium-Ion Batteries: Morphology Control, Carbon Hybridization, and Cation Doping. *Part. Part. Syst. Char.* **2015,** *32* (3), 276-294.

301. Afyon, S.; Krumeich, F.; Mensing, C.; Borgschulte, A.; Nesper, R., New High Capacity Cathode Materials for Rechargeable Li-ion Batteries: Vanadate-Borate Glasses. *Sci. Rep.* **2014,** *4*, 7113.

302. Liu, Y.; Uchaker, E.; Zhou, N.; Li, J.; Zhanga, Q.; Cao, G., Facile Synthesis of Nanostructured Vanadium Oxide as Cathode Materials for Efficient Li-ion Batteries. *J. Mater. Chem.* **2012,** *22*, 24439-24445.

303. Wang, C.; Cao, Y.; Luo, Z.; Li, G.; Xu, W.; Xiong, C.; He, G.; Wang, Y.; Li, S.; Liu, H.; Fang, D., Flexible Potassium Vanadate Nanowires on Ti Fabric as a Binder-Free Cathode for High-Performance Advanced Lithium-Ion Battery. *Chem. Eng. J.* **2017,** *307*, 382–388.

304. Fang, D.; Li, L.; Xu, W.; Li, G.; Luo, Z.; Liang, C.; Ji, Y.; Xu, J.; Xiong, C., Self-Assembled Hairy Ball-Like V_2O_5 Nanostructures for Lithium Ion Batteries. *RSC Adv.* **2014,** *4*, 25205.

305. Cao, Y.; Fang, D.; Wang, C.; Li, L.; Xu, W.; Luo, Z.; Liu, X.; Xiong, C.; Liu, S., Novel Aligned Sodium Vanadate Nanowire Arrays for High-Performance Lithium-Ion Battery Electrodes. *RSC Adv.* **2015,** *5*, 42955.

306. Cao, Y.; Fang, D.; Liu, R.; Jiang, M.; Zhang, H.; Li, G.; Luo, Z.; Liu, X.; Xu, J.; Xu, W.; Xiong, C., Three-Dimensional Porous Iron Vanadate Nanowire Arrays as a High Performance Lithium-Ion Battery. *ACS Appl. Mater. Interface* **2015,** *7*, 27685−27693.

307. Zhang, C.; Chen, Z.; Guo, Z.; Lou, X. W., Additive-free synthesis of 3D porous V_2O_5 hierarchical microspheres with enhanced lithium storage properties. *Energy Environ. Sci.* **2013,** *6* (3), 974-978.

308. Sun, B.; Huang, K.; Qi, X.; Wei, X.; Zhong, J., Rational Construction of a Functionalized V_2O_5 Nanosphere/MWCNT Layer-by-Layer Nanoarchitecture as Cathode for Enhanced Performance of Lithium-Ion Batteries. *Adv. Funct. Mater.* **2015,** *25*, 5633–5639.

309. Lee, J. H.; Kim, J.-M.; Kim, J.-H.; Jang, Y.-R.; Kim, J. A.; Yeon, S.-H.; Lee, S.-Y., Toward Ultrahigh-Capacity V_2O_5 Lithium-Ion Battery Cathodes via One-Pot Synthetic Route from Precursors to Electrode Sheets. *Adv. Mater. Interfaces* **2016,** *3*, 1600173.

310. Yu, R.; Zhang, C.; Meng, Q.; Chen, Z.; Liu, H.; Guo, Z., Facile Synthesis of Hierarchical Networks Composed of Highly Interconnected V_2O_5 Nanosheets Assembled on Carbon Nanotubes and Their Superior Lithium Storage Properties. *ACS Appl. Mater. Interfaces* **2013,** *5* (23), 12394-12399.

311. Seng, K. H.; Liu, J.; Guo, Z. P.; Chen, Z. X.; Jia, D.; Liu, H. K., Free-Standing V_2O_5 Electrode for Flexible Lithium Ion Batteries. *Electrochem. Commun.* **2011,** *13* (5), 383-386.

312. Yang, Y.; Li, L.; Fei, H.; Peng, Z.; Ruan, G.; Tour, J. M., Graphene Nanoribbon/V_2O_5 Cathodes in Lithium-Ion Batteries. *ACS applied materials & interfaces* **2014,** *9*, 9590−9594.

313. Choi, S. H.; Kang, Y. C., Uniform Decoration of Vanadium Oxide Nanocrystals on Reduced Graphene-Oxide Balls by an Aerosol Process for Lithium-Ion Battery Cathode Material. *Chem. Eur. J.* **2014,** *20*, 6294 – 6299.

314. Zhao, H.; Pan, L.; Xing, S.; Luo, J.; Xu, J., Vanadium Oxides-Reduced Graphene Oxide Composite for lLithium-ion Batteries and Supercapacitors with Improved Electrochemical Performance. *J. Power Sources* **2013,** *22*, 21-31.

315. Pham-Cong, D.; Ahn, K.; Hong, S. W.; Jeong, S. Y.; Choi, J. H.; Doh, C. H.; Jin, J. S.; Jeong, E. D.; Cho, C. R., Cathodic Performance of V_2O_5 Nanowires and Reduced Graphene Oxide Composites for Lithium ion Batteries. *Curr. Appli. Phys.* **2014,** *14*, 215-221.

316. Cao, Y.; Chai, D.; Luo, Z.; Jiang, M.; Xu, W.; Xiong, C.; Li, S.; Liu, H.; Fang, D., Lithium Vanadate Nanowires@Reduced Graphene Oxide Nanocomposites on Titanium Foil with Super High Capacities for Lithium-Ion Batteries. *J. Colloid Interface Sci.* **2017,** *498*, 210–216.

317. Brown, E.; Acharya, J.; Pandey, G. P.; Wu, J.; Li, J., Highly Stable Three Lithium Insertion in Thin V_2O_5 Shells on Vertically Aligned Carbon Nanofiber Arrays for Ultrahigh-Capacity Lithium Ion Battery Cathodes. *Adv. Mater. Interfaces* **2016**, 1600824.

318. Park, S.-H.; Lee, W.-J., Hierarchically Mesoporous Carbon Nanofiber/Mn_3O_4 Coaxial Nanocables as Anodes in Lithium Ion Batteries. *J. Power Sources* **2015,** *281*, 301-309.

319. Park, S.-H.; Lee, W.-J., Hierarchically Mesoporous CuO/Carbon Nanofiber Coaxial Shell-Core Nanowires for Lithium Ion Batteries. *Sci. Rep.* **2015,** *5*, 9754.

320. Liu, J.; Essner, J.; Li, J., Hybrid Supercapacitor Based on Coaxially Coated Manganese Oxide on Vertically Aligned Carbon Nanofiber Arrays. *Chem. Mater.* **2010,** *22* (17), 5022-5030.

321. Singh, T.; Wang, S.; Aslam, N.; Zhang, H. Z.; Hoffmann-Eifert, S.; Mathur, S., Atomic Layer Deposition of Transparent VO_x Thin Films for Resistive Switching Applications. *Chem. Vap. Deposition* **2014,** *20*, 291–297.

322. Baddour-Hadjean, R.; Smirnov, M. B.; Smirnov, K. S.; Kazimirov, V. Y.; Gallardo-Amores, J. M.; Amador, U.; Arroyo-de Dompablo, M. E.; Pereira-Ramos, J. P., Lattice Dynamics of β-V_2O_5: Raman Spectroscopic Insight into the Atomistic Structure of a High-Pressure Vanadium Pentoxide Polymorph. *Inorg. Chem.* **2012,** *51*, 3194−3201.

323. Su, Q.; Liu, X. Q.; Ma, H. L.; Guo, Y. P.; Wang, Y. Y., Raman Spectroscopic Characterization of the Microstructure of V_2O_5 Films. *J Solid State Electrochem.* **2008,** *12*, 919–923.

324. Moretti, A.; Maroni, F.; Osada, I.; Nobili, F.; Passerini, S., V_2O_5 Aerogel as a Versatile Cathode Material for Lithium and Sodium Batteries. *Chem Electrochem* **2015,** *2*, 529–537.

325. Lee, J.; Urban, A.; Li, X.; Su, D.; Hautier, G.; Ceder, G., Unlocking the Potential of Cation-Disordered Oxides for Rechargeable Lithium Batteries. *Science* **2014,** *343* (6170), 519-522.

326. Passerini, S.; Le, D. B.; Smyrl, W. H.; Berrettoni, M.; Tossici, R.; Marassi, R.; Giorgetti, M., XAS and Electrochemical Characterization of Lithiated High Surface Area V_2O_5 Aerogels. *Solid State Ion.* **1997,** *104*, 195-204.

327. Takahashi, K.; Wang, Y.; Cao, G., Ni−V_2O_5·nH_2O Core−Shell Nanocable Arrays for Enhanced Electrochemical Intercalation. *J. Phys. Chem. B* **2005,** *109* (1), 48-51.

328. Rui, X.; Lu, Z.; Yu, H.; Yang, D.; Hng, H. H.; Lim, T. M.; Yan, Q., Ultrathin V_2O_5 Nanosheet Cathodes: Realizing Ultrafast Reversible Lithium Storage. *Nanoscale* **2013,** *5* (2), 556-560.

329. Hu, Y.-S.; Liu, X.; Müller, J.-O.; Schlögl, R.; Maier, J.; Su, D. S., Synthesis and Electrode Performance of Nanostructured V_2O5 by Using a Carbon Tube-in-Tube as a Nanoreactor and an Efficient Mixed-Conducting Network. *Angew. Chem. Int. Ed.* **2009,** *48* (1), 210-214.

330. Noorden, R. V., A Better Battery. *Nature* **2014,** *507*, 26-28.

331. Zhu, C.; Shu, J.; Wu, X.; Li, P.; Li, X., Electrospun V_2O_5 Micro/Nanorods as Cathodematerials for Lithium Ion Battery. *J. Electroanal. Chem.* **2015,** *759*, 184–189.

332. Yu, D.; Chen, C.; Xie, S.; Liu, Y.; Park, K.; Zhou, X.; Zhang, Q.; Lic, J.; Cao, G., Mesoporous Vanadium Pentoxide Nanofibers with Significantly Enhanced Li-ion Storage Properties by Electrospinning. *Energy Environ. Sci.* **2011,** *4*, 858–861.

333. Chan, C. K.; Peng, H. L.; Twesten, R. D.; Jarausch, K.; Zhangn, X. F.; Cui, Y., Fast, Completely Reversible Li Insertion in Vanadium Pentoxide Nanoribbons. *Nano Lett.* **2007,** *2*, 490–495.

334. Wang, H.; Huang, K.; Huang, C.; Liu, S.; Ren, Y.; Huang, X., $(NH_4)_{0.5}V_2O_5$ Nanobelt with Good Cycling Stability as Cathode Material for Li-ion Battery. *J. Power Sources* **1011,** *196*, 5645–5650.

335. Mai, L.; Xu, L.; Han, C.; Xu, X.; Luo, Y.; Zhao, S.; Zhao, Y., Electrospun Ultralong Hierarchical Vanadium Oxide Nanowires with High Performance for Lithium Ion Batteries. *Nano Lett.* **2010,** *10*, 4750–4755.

336. Rui, X.; Lu, Z.; Yu, H.; Yang, D.; Hng, H. H.; Lim, T. M.; Yan, Q., Ultrathin V_2O_5 Nanosheet Cathodes: Realizing Ultrafast Reversible Lithium Storage. *Nanoscale* **2013,** *5*, 556–560.

337. Wang, H.-E.; Chen, D.-S.; Cai, Y.; Zhang, R.-L.; Xu, J.-M.; Deng, Z.; Zheng, X.-F.; Li, Y.; Bello, I.; Su, B.-L., Facile Synthesis of Hierarchical and Porous V_2O_5 Microspheres as Cathode Materials for Lithium Ion Batteries. *J. Colloid Interface Sci.* **2014,** *418*, 74–80.

338. Zhang, C.; Chen, Z.; Guo, Z.; Lou, X. W., Additive-Free Synthesis of 3D Porous V_2O_5 Hierarchical Microspheres with Enhanced Lithium Storage Properties. *Energy Environ. Sci.* **2013,** *6*, 974-978.

339. Bai, H.; Liu, Z.; Sun, D. D.; Chan, S. H., Hierarchical 3D Micro-/Nano-V_2O_5 (vanadium pentoxide) Spheres as Cathode Materials for High-Energy and High-Power Lithium Ion-Batteries. *Energy* **2014,** *76*, 607e613.

340. Tang, Y.; Rui, X.; Zhang, Y.; Lim, T. M.; Dong, Z.; Hng, H. H.; Chen, X.; Yan, Q.; Che, Z., Vanadium Pentoxide Cathode Materials for High-Performance Lithium-ion Batteries Enabled by a Hierarchical Nanoflower Structure via an Electrochemical Process. *J. Mater. Chem. A* **2013,** *1*, 82-88.

341. Mai, L.; An, Q.; Wei, Q.; Fei, J.; Zhang, P.; Xu, X.; Zhao, Y.; Yan, M.; Wen, W.; Xu, L., Nanoflakes-Assembled Three-Dimensional Hollow-Porous V_2O_5 as Lithium Storage Cathodes with High-Rate Capacity. *Small* **2014,** *10*, 3032–3037.

342. Wang, S.; Li, S.; Sun, Y.; Feng, X.; Chen, C., Three-Dimensional Porous V_2O_5 Cathode with Ultra High Rate Capability. *Energy Environ. Sci.* **2011,** *4*, 2854-2857.

343. An, Q.; Wei, Q.; Zhang, P.; Sheng, J.; Hercule, K. M.; Lv, F.; Wang, Q.; Wei, X.; Mai, L., Three-Dimensional Interconnected Vanadium Pentoxide Nanonetwork Cathode for High-Rate Long-Life Lithium Batteries. *Small* **2015,** *11*, 2654–2660.

344. Li, Z.-F.; Zhang, H.; Liu, Q.; Liu, Y.; Stanciu, L.; Xie, J., Hierarchical Nanocomposites of Vanadium Oxide Thin Film Anchored on Graphene as High-Performance Cathodes in Li-Ion Batteries. *ACS Appl. Mater. Interface* **2014,** *6*, 18894−18900.

345. Wang, Y.; Takahashi, K.; Lee, K.; Cao, G., Nanostructured Vanadium Oxide Electrodes for Enhanced Lithium-Ion Intercalation. *Adv. Funct. Mater.* **2006,** *16*, 1133–1144.

346. Lu, W.; Goering, A.; Quy, L.; Dai, L., Lithium-ion Batteries Based on Vertically-Aligned Carbon Nanotube Electrodes and Ionic Liquid Electrolytes. *Phys. Chem. Chem. Phys.* **2012,** *14*.

347. Cheah, Y. L.; Aravindan, V.; Madhavi, S., Electrochemical Lithium Insertion Behavior of Combustion Synthesized V_2O_5 Cathodes for Lithium-Ion Batteries. *J. Electrochem. Soc.* **2012,** *159*, A273-A280.

348. Messier, R.; Giri, A. P.; Roy, R. A., Revised Structure Zone Model for Thin Film Physical Structure. *J. Vac. Sci. Technol.* **1984,** *2*, 500-503.

349. Chen, X.-B., Assignment of the Raman Modes of VO_2 in the Monoclinic Insulating Phase. *J. Korean Phys. Soc.* **2011,** *58*, 100-104.

350. Sanchez, C.; Livage, J.; Lucazeau, G., Infrared and Raman Study of Amorphous V_2O_5. *J. Raman Spectrosc.* **1982,** *12*, 68.

351. Xie, S.; Iglesia, E.; Bell, A. T., Effects of Hydration and Dehydration on the Structure of Silica-Supported Vanadia Species. *Langmuir* **2000,** *16*, 7162-7167.

352. Pan, X.; Zhao, Y.; Ren, G.; Fan, Z., Highly conductive VO_2 treated with hydrogen for supercapacitors. *Chem. Commun.* **2013,** *49*, 3943.

353. Lu, X.; Wang, G.; Zhai, T.; Yu, M.; Gan, J.; Tong, Y.; Li, Y., Hydrogenated TiO_2 Nanotube Arrays for Supercapacitors. *Nano Lett.* **2012,** *12*, 1690.

354. Long, J. W.; Swider, K. E.; Merzbacher, C. I.; Rolison, D. R., Voltammetric Characterization of Ruthenium Oxide-Based Aerogels and Other RuO_2 Solids: The Nature of Capacitance in Nanostructured Materials. *Langmuir* **1999,** *15*, 780.

355. Armand, M.; Tarascon, J. M., Building better batteries. *Nature* **2008,** *451* (7179), 652-657.

356. Tarascon, J. M., Is Lithium the New Gold? *Nat. Chem.* **2010,** *2*, 510.

357. Slater, M. D.; Kim, D.; Lee, E.; Johnson, C. S., Sodium-Ion Batteries. *Adv. Funct. Mater.* **2013,** *23*, 947–958.

358. Xu, G.-L.; Amine, R.; Abouimrane, A.; Che, H.; Dahbi, M.; Ma, Z.-F.; Saadoune, I.; Alami, J.; Mattis, W. L.; Pan, F.; Chen, Z.; Amine, K., Challenges in Developing Electrodes, Electrolytes, and Diagnostics Tools to Understand and Advance Sodium-Ion Batteries. *Adv. Energy Mater.* **2018**, 1702403.

359. Ohzuku, T.; Iwakoshi, Y.; Sawai, K., Formation of Lithium-Graphite Intercalation Compounds in Nonaqueous Electrolytes and Their Application as a Negative Electrode for a Lithium Ion (Shuttlecock) Cell. *J. Electrochem. Soc.* **1993,** *140* (9), 2490-2498.

360. Xu, J.; Dou, Y.; Wei, Z.; Ma, J.; Deng, Y.; Li, Y.; Liu, H.; Dou, S., Recent Progress in Graphite Intercalation Compounds for Rechargeable Metal (Li, Na, K, Al)-Ion Batteries. *Adv. Sci.* **2017,** *4* (10), 1700146-n/a.

361. Wen, Y.; He, K.; Zhu, Y.; Han, F.; Xu, Y.; Matsuda, I.; Ishii, Y.; Cumings, J.; Wang, C., Expanded Graphite as Superior Anode for Sodium-Ion Batteries. *Nat. Commun.* **2014,** *5*, 1-10.

362. Xu, J.; Wang, M.; Wickramaratne, N. P.; Jaroniec, M.; Dou, S.; Dai, L., High-Performance Sodium Ion Batteries Based on a 3D Anode from Nitrogen-Doped Graphene Foams. *Adv. Mater.* **2015,** *27*, 2042–2048.

363. Yun, Y. S.; Park, Y.-U.; Chang, S.-J.; Kim, B. H.; Choi, J.; Wang, J.; Zhang, D.; Braun, P. V.; Jin, H.-J.; Kang, K., Crumpled Graphene Paper for High Power Sodium Battery Anode. *Carbon* **2016,** *99*, 658-664.

364. Xiang, X.; Zhang, K.; Chen, J., Recent Advances and Prospects of Cathode Materials for Sodium-Ion Batteries. *Advanced Materials* **2015,** *27* (36), 5343-5364.

365. Reddy, B.; Ravikumar, R.; Nithya, C.; Gopukumar, S., High Performance Na_xCoO_2 as a Cathode Material for Rechargeable Sodium Batteries. *J. Mater. Chem. A* **2015,** *3*, 18059–18063.

366. Rai, A. K.; Anh, T.; Gim, J.; Mathew, V.; Kim, J., Electrochemical Properties of Na_xCoO_2 (x~0.71) Cathode for Rechargeable Sodium-Ion Batteries. *Ceram. Int.* **2014,** *40*, 2411–2417.

367. Rahman, M.; Sultana, I.; Mateti, S.; Liu, J.; Sharma, N.; Chen, Y., Maricite $NaFePO_4$/C/Graphene: A Novel Hybrid Cathode for Sodium-Ion Batteries. *J. Mater. Chem. A* **2017,** *5*, 16616–16621.

368. Ali, G.; Lee, J.-H.; Susanto, D.; Choi, S.-W.; Cho, B. W.; Nam, K.-W.; Chung, K. Y., Polythiophene-Wrapped Olivine $NaFePO_4$ as a Cathode for Na-Ion Batteries. *ACS applied materials & interfaces* **2016,** *8*, 15422−15429.

369. Guo, S.; Yu, H.; Liu, D.; Tian, W.; Liu, X.; Hanada, N.; Ishida, M.; Zhou, H., A novel tunnel $Na_{0.61}Ti_{0.48}Mn_{0.52}O_2$ cathode material for sodium-ion batteries. *Chem. Comm.* **2014,** *50*, 7998-8001.

370. Yuan, D. D.; Wang, Y. X.; Cao, Y. L.; Ai, X. P.; Yan, H. X., Improved Electrochemical Performance of Fe-Substituted $NaNi_{0.5}Mn_{0.5}O_2$ Cathode Materials for Sodium-Ion Batteries. *ACS applied materials & interfaces* **2015,** *7*, 8585−8591.

371. Yoshida, H.; Yabuuchi, N.; Komaba, S., $NaFe_{0.5}Co_{0.5}O_2$ as High Energy and Power Positive Electrode for Na-Ion Batteries. *Electrochem. Commun.* **2013,** *34*, 60-63.

372. Minowa, H.; Yui, Y.; One, Y.; Hayashi, M.; Hayashi, K.; Kobayashi, R.; Takahashi, K. I., Characterization of Prussian Blue as Positive Electrode Materials for Sodium-Ion Batteries. *Solid State Ion.* **2014,** *262*, 216-219.

373. You, Y.; Wu, X.-L.; Yin, Y.-X.; Guo, Y.-G., High-Quality Prussian Blue Crystals as Superior Cathode Materials for Room-Temperature Sodium-Ion Batteries. *Energy Environ. Sci.* **2014,** *7*, 1643–1647.

374. Raju, V.; Rains, J.; Gates, C.; Luo, W.; Wang, X.; Stickle, W.; Stucky, G.; Ji, X., Superior Cathode of Sodium-Ion Batteries: Orthorhombic V_2O_5 Nanoparticles Generated in Nanoporous Carbon by Ambient Hydrolysis Deposition. *Nano Lett.* **2014,** *14*, 4119-4124.

375. Wang, H.; Gao, X.; Feng, J.; Xiong, S., Nanostructured V_2O_5 Arrays on Metal Substrate as Binder Free Cathode Materials for Sodium-Ion Batteries. *Electrochim. Acta* **2015,** *182*, 769-774.

376. Ali, G.; Lee, J.-H.; Oh, S. H.; Cho, B. W.; Nam, K.-W.; Chung, K. Y., Investigation of the Na Intercalation Mechanism into Nanosized V_2O_5/C Composite Cathode Material for Na-Ion Batteries. *ACS applied materials & interfaces* **2016,** *8*, 6032-6039.

377. Uchaker, E.; Zheng, Y. Z.; Li, S.; Candelaria, S. L.; Hu, S.; Cao, G. Z., Better Than Crystalline: Amorphous Vanadium Oxide for Sodium-Ion Batteries. *J. Mater. Chem. A* **2014,** *2*, 18208-18214.

378. Wei, Q.; Liu, J.; Feng, W.; Sheng, J.; Tian, X.; He, L.; Anb, Q.; Mai, L., Hydrated Vanadium Pentoxide with Superior Sodium Storage Capacity. *J. Mater. Chem. A* **2015,** *3*, 8070–8075.

379. Lee, J. H.; Kim, J.-M.; Kim, J.-H.; Jang, Y.-R.; Kim, J. A.; Yeon, S.-H.; Lee, S.-Y., Toward Ultrahigh-Capacity V_2O_5 Lithium-Ion Battery Cathodes via One-Pot Synthetic Route from Precursors to Electrode Sheets. *Adv. Mater. Interfaces* **2016**, n/a-n/a.

380. Li, Z.-F.; Zhang, H.; Liu, Q.; Liu, Y.; Stanciu, L.; Xie, J., Hierarchical Nanocomposites of Vanadium Oxide Thin Film Anchored on Graphene as High-Performance Cathodes in Li-Ion Batteries. *ACS Appl. Mater. Interfaces* **2014,** *6*, 18894−18900.

381. Pandey, G. P.; Liu, T.; Brown, E.; Yang, Y.; Li, Y.; Sun, X. S.; Fang, Y.; Li, J., Mesoporous Hybrids of Reduced Graphene Oxide and Vanadium Pentoxide for Enhanced Performance in Lithium-Ion Batteries and Electrochemical Capacitors. *ACS Appl. Mater. Interfaces* **2016,** *8*, 9200-9210.

382. Lu, W.; Goering, A.; Quy, L.; Dai, L., Lithium-ion Batteries Based on Vertically-Aligned Carbon Nanotube Electrodes and Ionic Liquid Electrolytes. *Phys. Chem. Chem. Phys.* **2012,** *14*, 12099–12104.

383. Chen, X.; Pomerantseva, E.; Banerjee, P.; Gregorczyk, K.; Ghodssi, R.; Rubloff, G., Ozone-Based Atomic Layer Deposition of Crystalline V2O5 Films for High Performance Electrochemical Energy Storage. *Chem. Mater.* **2012,** *24*, 1255–1261.

384. Liu, C.; Gillette, E. I.; Chen, X.; Pearse, A. J.; Kozen, A. C.; Schroeder, M. A.; Gregorczyk, K. E.; Lee, S.; Rubloff, G., An All-In-One Nanopore Battery Array. *Nat. Nanotechnol.* **2014,** *9*, 1031-1039.

385. Melechko, A. V.; Merkulov, V. I.; McKnight, T. E.; Guillorn, M. A.; Klein, K. L.; Lowndes, D. H.; Simpson, M. L., Vertically Aligned Carbon Nanofibers and Related Structures: Controlled Synthesis and Directed Assembly. *J. Appl. Phys.* **2005,** *97*, 041301-1.

386. Brown, E.; Acharya, J.; Pandey, G. P.; Wu, J.; Li, J., Highly Stable Three Lithium Insertion in Thin V_2O_5 Shells on Vertically Aligned Carbon Nanofiber Arrays for Ultrahigh-Capacity Lithium Ion Battery Cathodes. *Adv. Mater. Interfaces* **2016,** *3* (23), 1600824.

387. Klankowski, S. A.; Pandey, G. P.; Cruden, B. A.; Liu, J.; Wu, J.; Rojeski, R. A.; Li, J., Anomalous Capacity Increase at High-Rates in Lithium-ion Battery Anodes Based on Silicon-Coated Vertically Aligned Carbon Nanofiber. *J. Power Sources* **2015,** *276*, 73-79.

388. Klankowski, S. A.; Rojeski, R. A.; Cruden, B. A.; Liu, J.; Wu, J.; Li, J., A High-Performance Lithium-ion Battery Anode Based on the Core–Shell Heterostructure of Silicon-Coated Vertically Aligned Carbon Nanofibers. *J. Mater. Chem. A* **2013,** *1*, 1055-1064.

389. Singh, T.; Wang, S.; Aslam, N.; Zhang, H.; Hoffmann-Eifert, S.; Mathur, S., Atomic Layer Deposition of Transparent VOx Thin Films for Resistive Switching Applications. *Chem. Vap. Deposition* **2014,** *20*, 291.

390. Baddour-Hadjean, R.; Smirnov, M. B.; Smirnov, K. S.; Kazimirov, V. Y.; Gallardo-Amores, J. M.; Amador, U.; Dompablo, M. E. A.-d.; Pereira-Ramos, J. P., Lattice Dynamics of β-V_2O_5: Raman Spectroscopic Insight into the Atomistic Structure of a High-Pressure Vanadium Pentoxide Polymorph. *Inorg. Chem.* **2012,** *51*, 3194.

391. Su, Q.; Liu, X. Q.; Ma, H. L.; Guo, Y. P.; Wang, Y. Y., Raman spectroscopic characterization of the microstructure of V_2O_5 films. *J Solid State Electrochem* **2008,** *12*, 919.

392. Schreckenbach, J. P.; Witke, K.; Butte, D.; Marx, G., Characterization of Thin Metastable Vanadium Oxide Films by Raman Spectroscopy. *Fresenius J. Anal. Chem.* **1999,** *363* (2), 211-214.

393. Moretti, A.; Passerini, S., Bilayered Nanostructured $V_2O_5{\cdot}nH_2O$ for Metal Batteries. *Adv. Energy Mater.* **2016,** *6* (23), 1600868-n/a.

394. Jung, S. C.; Kim, H.-J.; Choi, J. W.; Han, Y.-K., Sodium Ion Diffusion in Al_2O_3: A Distinct Perspective Compared with Lithium Ion Diffusion. *Nano Lett.* **2014,** *14*, 6559-6563.

395. Han, X.; Liu, Y.; Jia, Z.; Chen, Y.-C.; Wan, J.; Weadock, N.; Gaskell, K. J.; Li, T.; Hu, L., Atomic-Layer-Deposition Oxide Nanoglue for Sodium Ion Batteries. *Nano Lett.* **2014,** *14*, 139-147.

396. Zhang, X.; Belharouak, I.; Li, L.; Lei, Y.; Elam, J. W.; Nie, A.; Chen, X.; Yassar, R. S.; Axelbaum, R. L., Structural and Electrochemical Study of Al_2O_3 and TiO_2 Coated $Li_{1.2}Ni_{0.13}Mn_{0.54}Co_{0.13}O_2$ Cathode Material Using ALD. *Adv. Energy Mater.* **2013,** *3*, 1299-1307.

397. Acharya, J.; Wilt, J.; Liu, B.; Wu, J., Probing the Dielectric Properties of Ultrathin $Al/Al_2O_3/Al$ Trilayers Fabricated Using in Situ Sputtering and Atomic Layer Deposition. *ACS Appl. Mater. Interfaces* **2018,** *10* (3), 3112-3120.

398. Nepal, A.; Singh, G., P; Flanders, B., N. ; Sorensen, C. M., One-step Synthesis of Graphene via Catalyst-free Gas-phase Hydrocarbon Detonation. *Nanotechnology* **2013,** *24* (24), 245602.

399. Nepal, A.; Chiu, G.; Xie, J.; Singh, G. P.; Ploscariu, N.; Klankowski, S.; Sung, T.; Li, J.; Flanders, B. N.; Hohn, K. L.; Sorensen, C. M., Highly Oxidized Graphene Nanosheets via the Oxidization of Detonation Carbon. *Appl. Phys. A* **2015,** *120* (2), 543-549.

400. Wu, N.-L., Nanocrystalline oxide supercapacitors. *Mater. Chem. Phys.* **2002,** *75* (1), 6-11.

401. Lih-Ren, S.; Nae-Lih, W.; Dien-Shi, W.; Chieng-Wen, C.; Yi-Ping, L. Electrochemical capacitor with electrode material for energy storage 2002.

402. Wang, S.-Y.; Ho, K.-C.; Kuo, S.-L.; Wu, N.-L., Investigation on Capacitance Mechanisms of Fe_3O_4 Electrochemical Capacitors. *J. Electrochem. Soc.* **2006,** *153* (1), A75-A80.

403. Shi, W.; Zhu, J.; Sim, D. H.; Tay, Y. Y.; Lu, Z.; Zhang, X.; Sharma, Y.; Srinivasan, M.; Zhang, H.; Hng, H. H.; Yan, Q., Achieving High Specific Charge Capacitances in Fe_3O_4/Reduced Graphene Oxide Nanocomposites. *J. Mater. Chem.* **2011,** *21* (10), 3422-3427.

404. Du, X.; Wang, C.; Chen, M.; Jiao, Y.; Wang, J., Electrochemical Performances of Nanoparticle Fe_3O_4/Activated Carbon Supercapacitor Using KOH Electrolyte Solution. *J. Phys. Chem. C* **2009,** *113* (6), 2643-2646.

405. Rolison, D. R.; Long, J. W.; Lytle, J. C.; Fischer, A. E.; Rhodes, C. P.; McEvoy, T. M.; Bourg, M. E.; Lubers, A. M., Multifunctional 3D Nanoarchitectures for Energy Storage and Conversion. *Chem. Soc. Rev.* **2009,** *38* (1), 226-252.

406. Chung, K. W.; Kim, K. B.; Han, S.-H.; Lee, H., Novel Synthesis and Electrochemical Characterization of Nano-sized Cellular Fe_3O_4 Thin Film. *Electrochem. Solid-State Lett.* **2005,** *8* (5), A259-A262.

407. Chen, J.; Huang, K.; Liu, S., Hydrothermal Preparation of Octadecahedron Fe_3O_4 Thin Film for use in an Electrochemical Supercapacitor. *Electrochimica Acta* **2009,** *55* (1), 1-5.

408. Guan, D.; Gao, Z.; Yang, W.; Wang, J.; Yuan, Y.; Wang, B.; Zhang, M.; Liu, L., Hydrothermal Synthesis of Carbon Nanotube/Cubic Fe_3O_4 Nanocomposite for Enhanced Performance Supercapacitor Electrode Material. *Mater. Sci. Eng. B* **2013,** *178* (10), 736-743.

409. Mu, J.; Chen, B.; Guo, Z.; Zhang, M.; Zhang, Z.; Zhang, P.; Shao, C.; Liu, Y., Highly Dispersed Fe_3O_4 Nanosheets on One-Dimensional Carbon Nanofibers: Synthesis, Formation Mechanism, and Electrochemical Performance as Supercapacitor Electrode Materials. *Nanoscale* **2011,** *3* (12), 5034-5040.

410. Kothari, H. M.; Kulp, E. A.; Limmer, S. J.; Poizot, P.; Bohannan, E. W.; Switzer, J. A., Electrochemical Deposition and Characterization of Fe_3O_4 Films Produced by the Reduction of Fe(III)-Triethanolamine. *J. Mater. Res.* **2006,** *21* (1), 293-301.

411. Kulp, E. A.; Kothari, H. M.; Limmer, S. J.; Yang, J.; Gudavarthy, R. V.; Bohannan, E. W.; Switzer, J. A., Electrodeposition of Epitaxial Magnetite Films and Ferrihydrite Nanoribbons on Single-Crystal Gold. *Chem. Mater.* **2009,** *21* (21), 5022-5031.

412. Yan, P.; Brown, E.; Su, Q.; Li, J.; Wang, J.; Xu, C.; Zhou, C.; Lin, D., 3D Printing Hierarchical Silver Nanowire Aerogel with Highly Compressive Resilience and Tensile Elongation through Tunable Poisson's Ratio. *Small* **2017,** *13* (38), 1701756-n/a.

Appendix A - Supplementary Information of Chapter 2

Theoretical Capacitance Calculation

The specific capacitance of the optimized 3D, solid-state VACNF array capacitor utilizing ALD Al_2O_3 is calculated as follows:

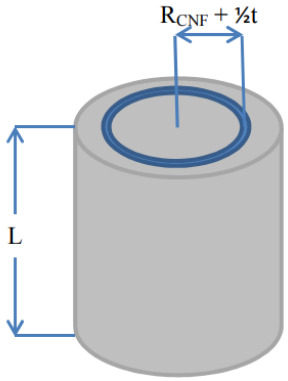

R_{CNF} = 50 nm

Al_2O_3 thickness (t) = 6.7 nm

$R_{area\ calculation} = 50\ nm + \frac{6.7\ nm}{2} = 53.35\ nm$

L = 10 μm

k = 9.3

Maximum areal density = $2x10^9$ CNFs/cm^2

Area per CNF = $2\pi(53.35nm)(10\mu m) = 3.35x10^{-8}\ cm^2$

Actual area per 1 cm^2 CNFs = ($3.35x10^{-8}\ cm^2$) x ($2x10^9$ CNFs/cm^2) + 1 cm^2 = 68 cm^2

Area-specific capacitance scaled to 6.7 nm Al_2O_3 = 0.41 μF/cm^2 x (20 nm/6.7 nm) = 1.22 μF/cm^2

Capacitance = (1.22 μF/cm^2)(68 cm^2) = 83 μF per cm^2 CNFs

The energy per unit area can be calculated by the following equation:

$$\text{Energy per unit area} = \frac{1}{2}C_0V^2$$

where C_0 is the area-specific capacitance and V the operating voltage. When compared to electric double layer capacitors, the area-specific capacitance value of the nanostructured electrostatic capacitor is still over 2 orders of magnitude less, but the voltage window can be extended to >8 V which partially compensates for the low C_0 value to raise the energy density. The high power density (as indicated by the high working frequency up to 100 kHz) is the main advantage of this 3D, solid-state design.

Figure A.1 Theoretical capacitance of the VACNF-Al_2O_3 array. (Reprinted with permission from ACS Appl. Mater. Interface, 2014, 6, 6865-6871)

Appendix B - Supplementary Information for Chapter 3

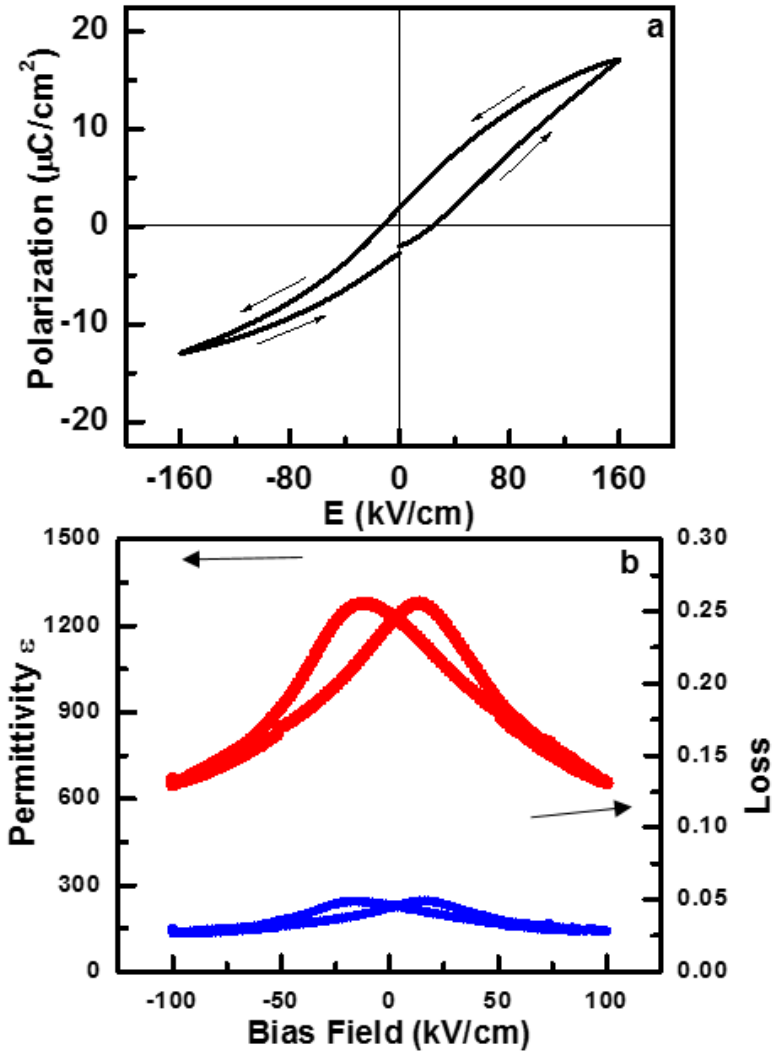

Figure B.1 (a) The *P-E* hysteresis loop measured with a conventional Radiant Premier II tester at 100 Hz. (b) The dielectric property of the 500-nm PLZT film by pulsed laser deposition as a function of bias electric field. (Reprinted with permission from ACS Appl. Mater. Interface, 2014, 6, 22417-22422)

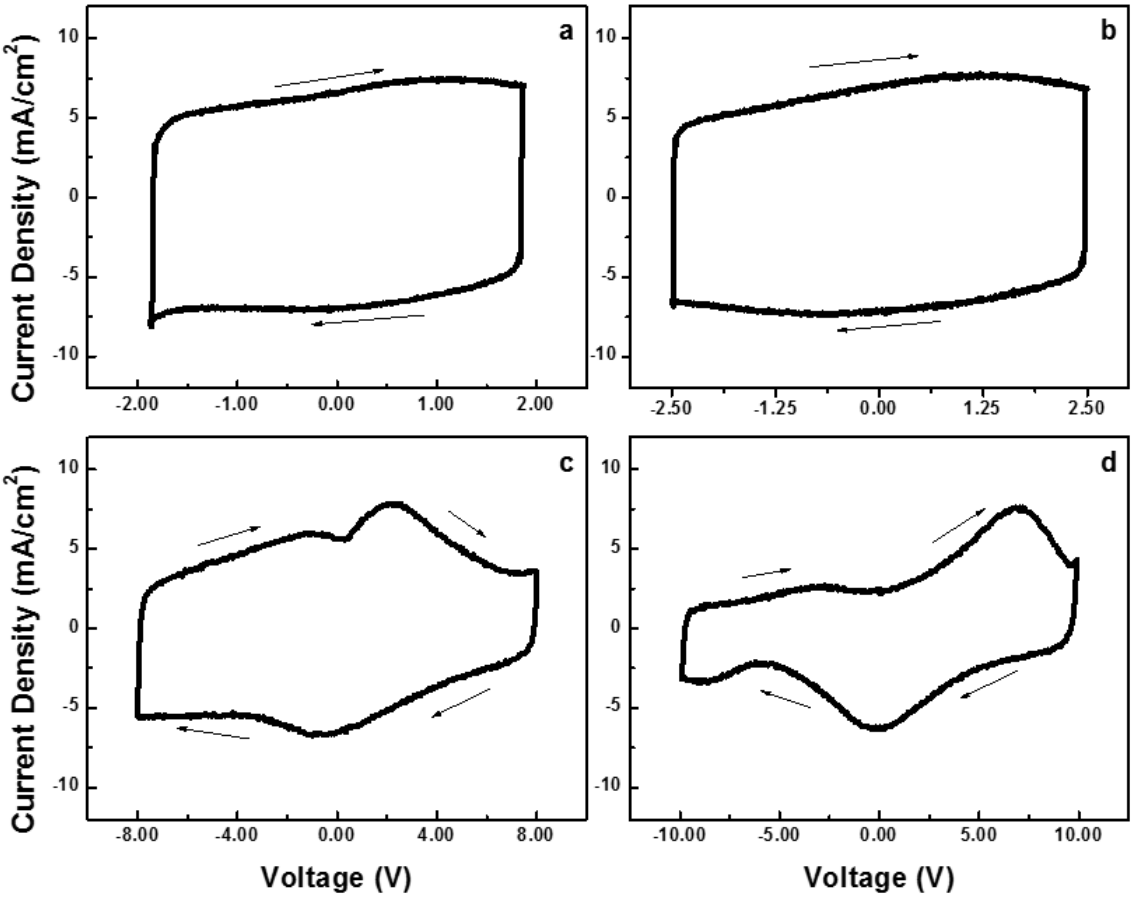

Figure B.2 Representative I-V curves measured at a cycling rate of 2000 Vs^{-1} for (a) 125 nm, (b) 250 nm, (c) 500 nm, and (d) 1000 nm PLZT film thickness. (Reprinted with permission from ACS Appl. Mater. Interface, 2014, 6, 22417-22422)

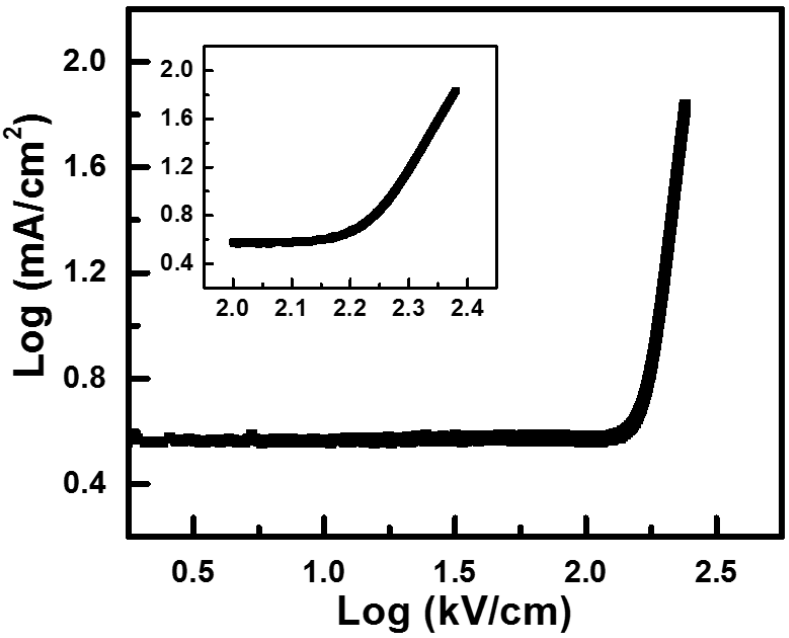

Figure B.3 *I-V* curve of the 125-nm PLZT films in wider range of electric field *E*. The leakage current dramatically increases as *E* exceeds 160 kV cm^{-1} (corresponding to the breakdown field E_b). The inset is the enlarged curve at high *E*. (Reprinted with permission from ACS Appl. Mater. Interface, 2014, 6, 22417-22422)

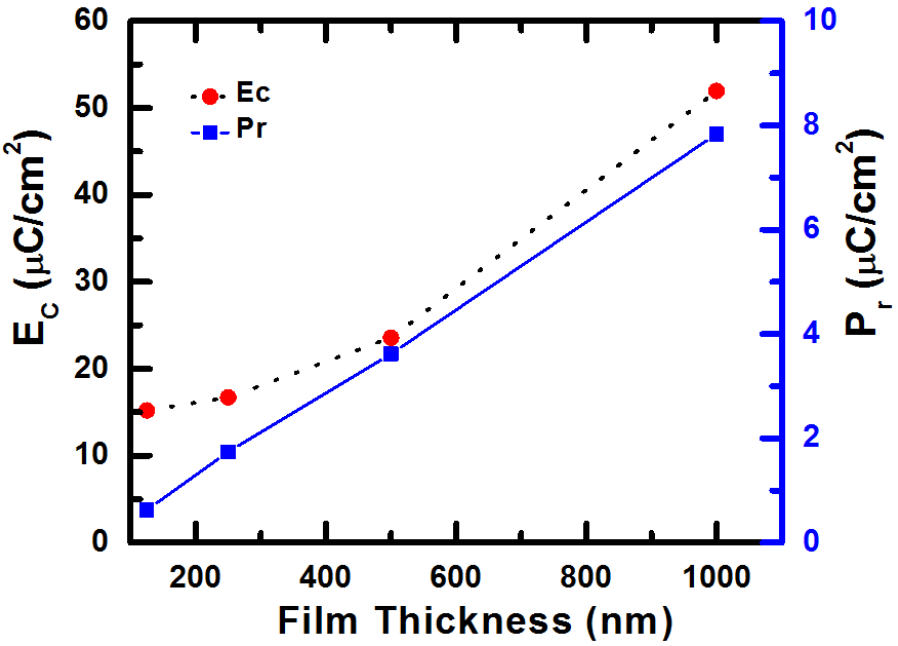

Figure B.4 The characteristic values for remnant polarization P_r and coersive electric field E_c of PLZT films at 125, 250, 500 and 1000 nm thickness measured by *I-V* measurements. All values are normalized to those at a maximum electric field strength of 160 kV cm^{-1}. (Reprinted with permission from ACS Appl. Mater. Interface, 2014, 6, 22417-22422)

Appendix C - Supplementary Information for Chapter 4

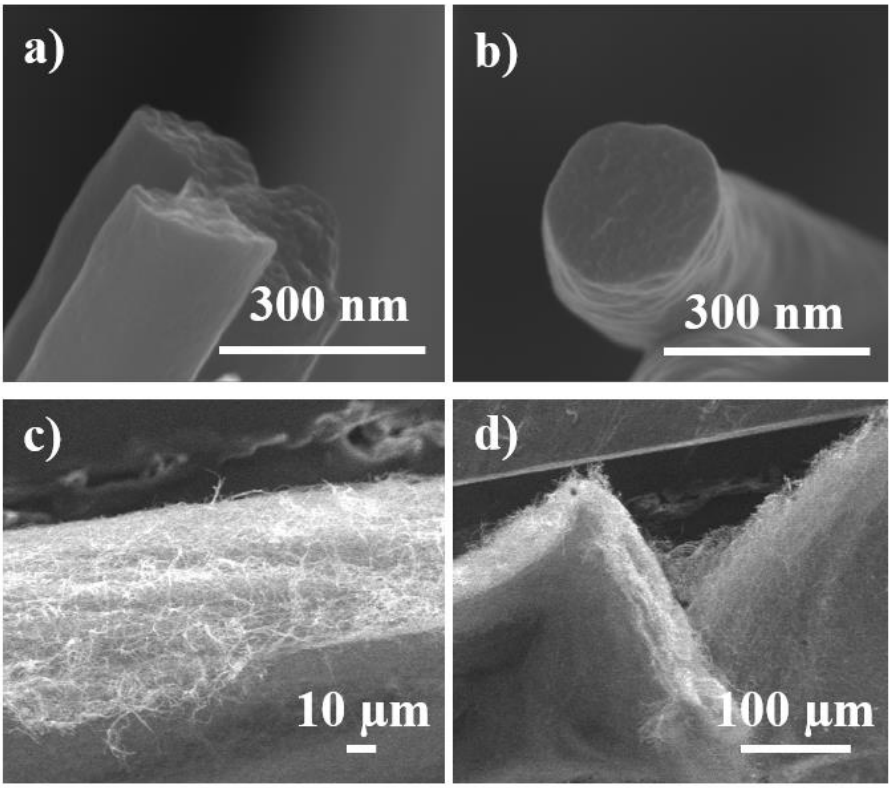

Figure C.1 High magnification SEM image of a) the side and b) cross-section of a bare CNFs. c) High- and d) low- magnification SEM images of the cross-sectional cut of a bare CNF membrane.

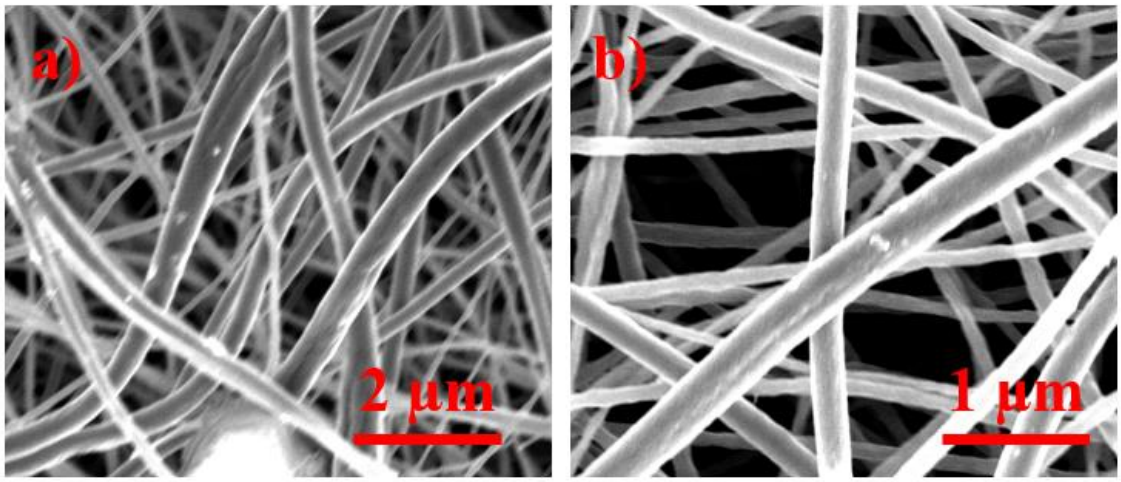

Figure C.2 a) Low- and b) high- magnification SEM images of the CNF-V_2O_5 core-shell structure at an accelerating voltage of 3kV.

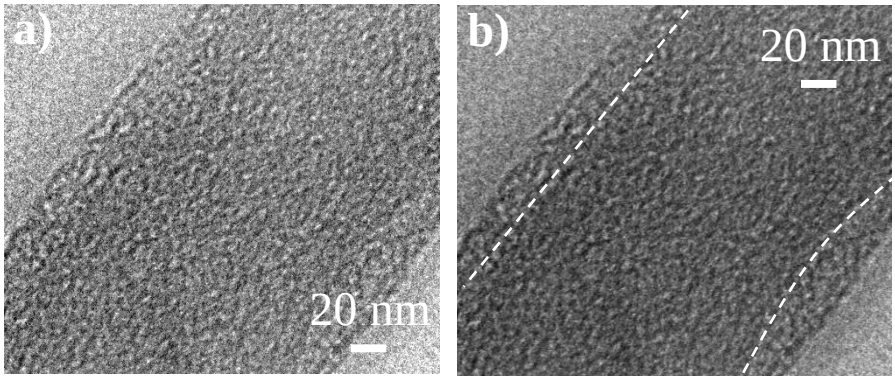

Figure C.3 HRTEM images of a CNF-V_2O_5 core-shell nanofiber. The white dash lines in b) are visual guides to indicate the inner CNF core and the outer V_2O_5 shell.

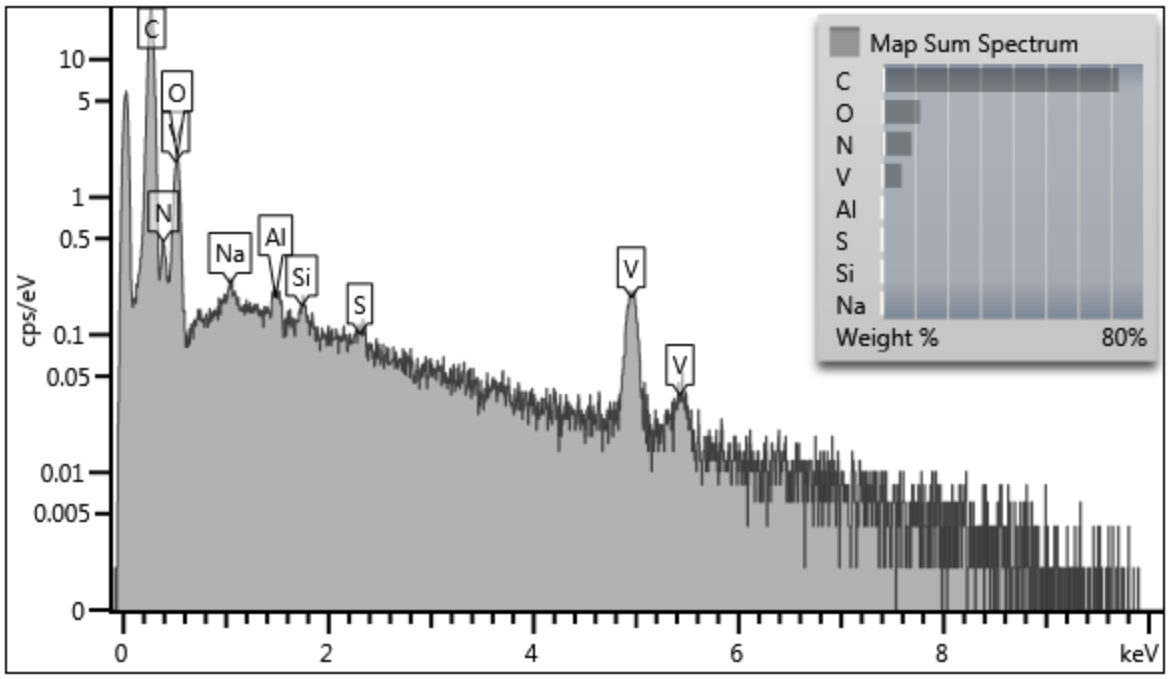

Figure C.4 : EDS spectrum of the CNF-V_2O_5 core-shell structure.

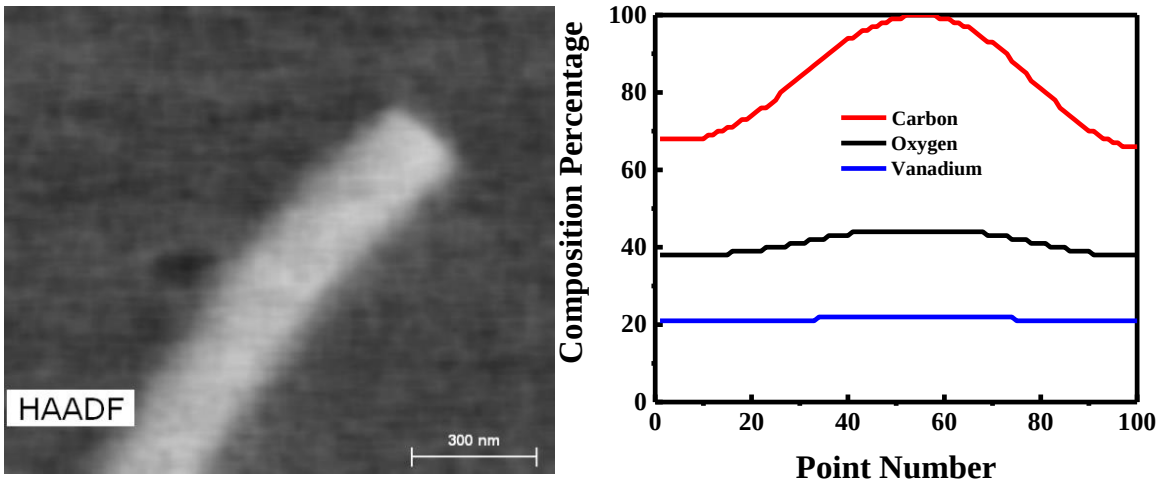

Figure C.5 : a) A HAADF STEM image of the CNF-V_2O_5 core-shell structure. b) The EDS lines of carbon, oxygen and vanadium elements scanned over the region illustrated by the yellow line in panel (a). Note: The oxygen and vanadium scans have been increased by 30 and 20%, respectively for visual purposes.

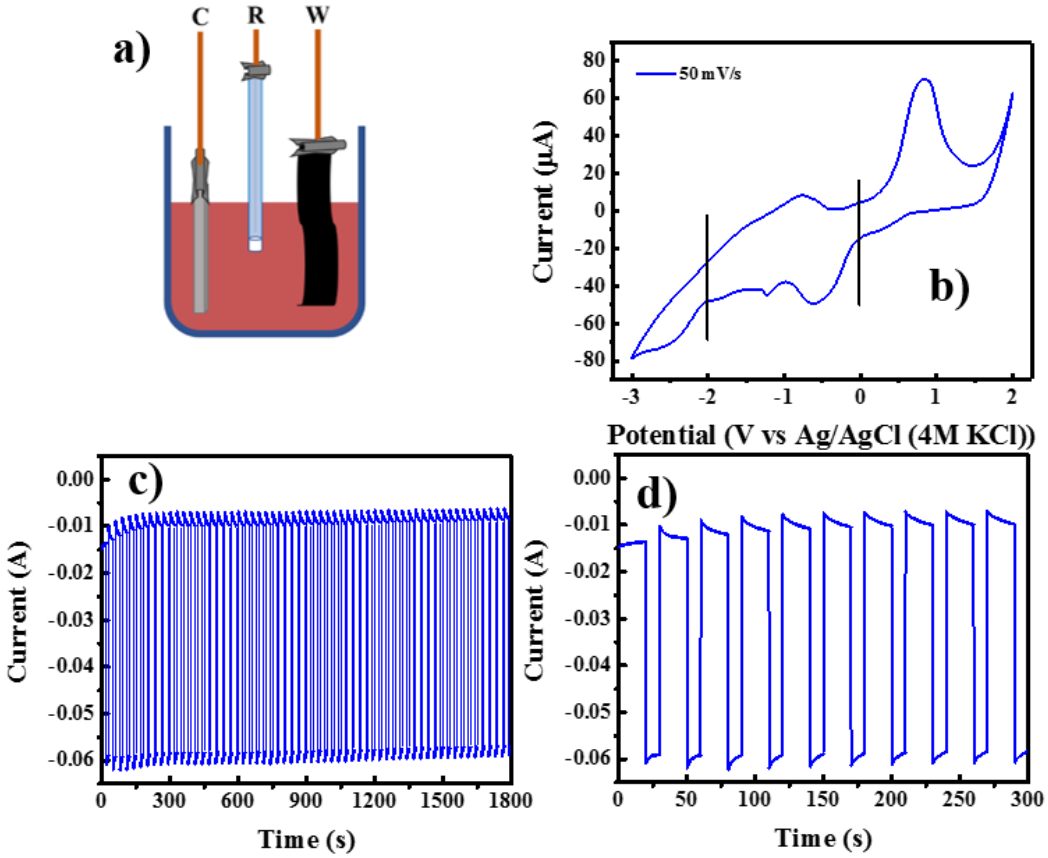

Figure C.6 a) The experimental setup, b) cyclic voltammogram, and the current profiles of c) the full 60 cycles and d) the first 300 seconds of the pulse electrodeposition of V_2O_5 on the CNF membrane.

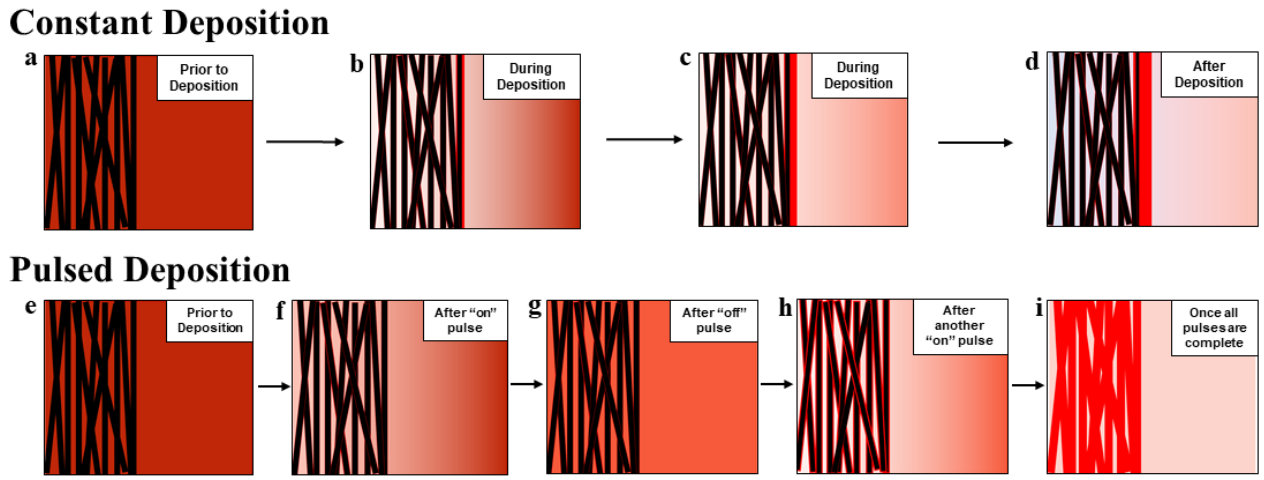

Figure C.7 Illustration of pulsed electrodeposition of V_2O_5 on CNF

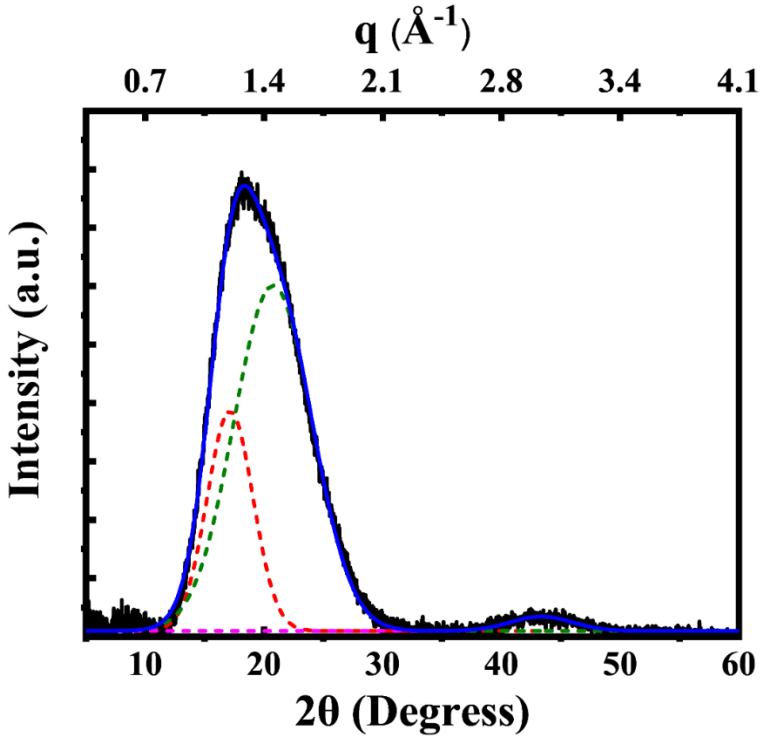

Figure C.8 The zoom-in deconvoluted XRD peak of the CNF-V_2O_5 core-shell structure after thermal annealing at 300° C for 4 hrs.

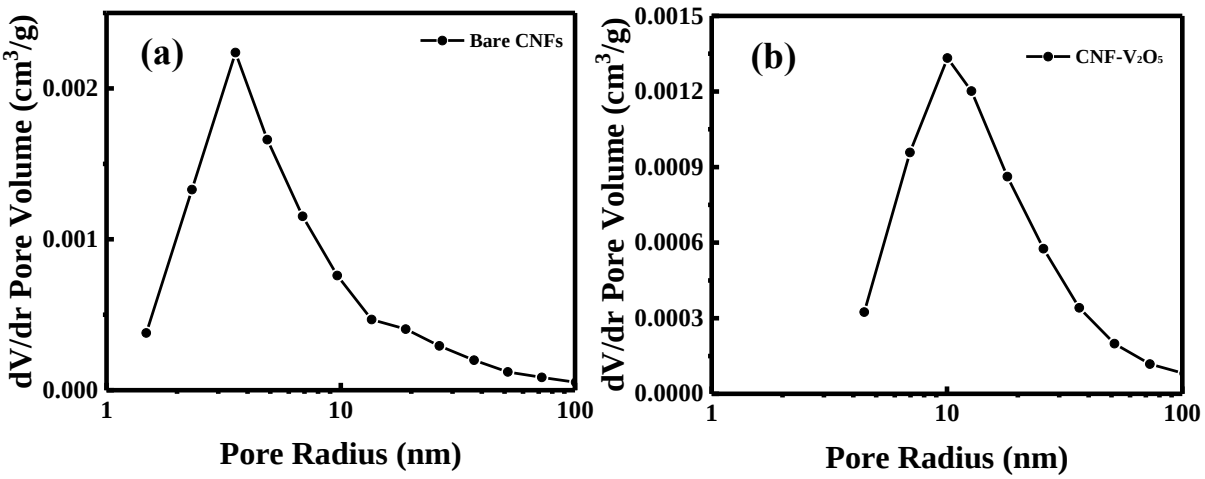

Figure C.9 The pore size distribution of a) bare CNFs and b) CNF-V_2O_5 core-shell materials derived from BET surface analyses.

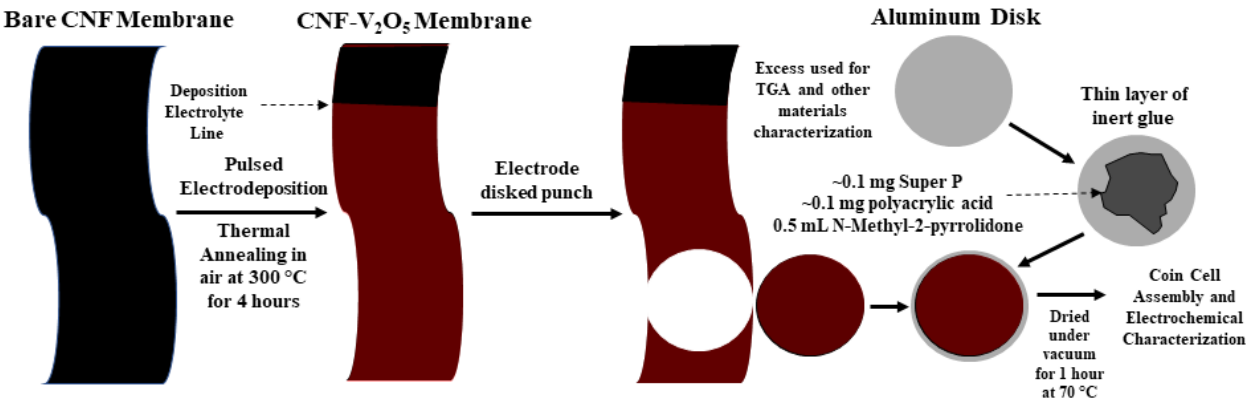

Figure C.10 Illustration of CNF-V_2O_5 membrane preparation for electrochemical characterization

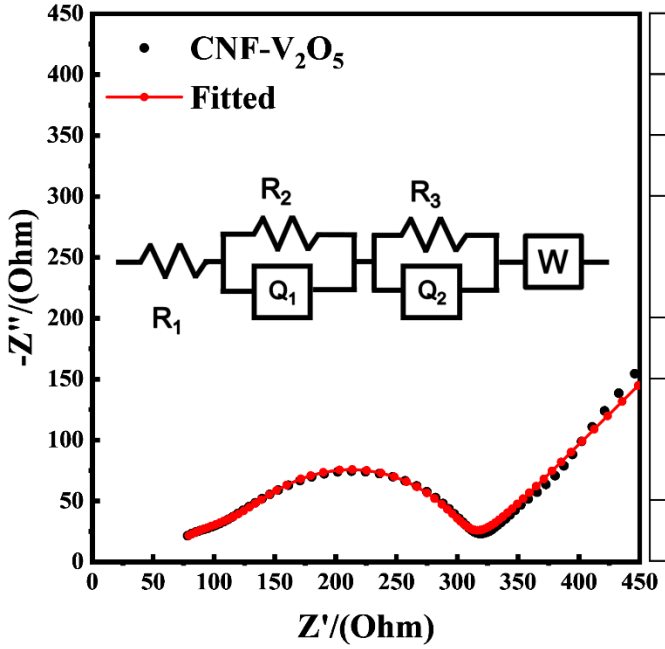

Element	Value	
R_1	53.33 Ω	
R_2	80.18 Ω	
CPE_1	C_1	8.82×10^{-6} F
	n_1	0.60
R_3	170.8 Ω	
CPE_2	C_2	4.55×10^{-6} F
	n_2	0.84
W	$\sigma = 0.0035$ Ω ($s^{-1/2}$)	

Figure C.11 Nyquist plot from the electrochemical impedance spectroscopy measurement (EIS) of the CNF-V_2O_5 core-shell structure at the charged state (~4.0 V) after completing 5 cyclic voltammetry cycles (1 mV/s) shown in Fig. S12 and the fitting parameters based on the equivalent circuit shown in the inset. The presented EIS data are in the range of 100 kHz to 0.22 Hz. The symbol R stands for a resistor, Q for a constant phase element (CPE) with $Z_{CPE} = (1/C\omega^n)e^{-\pi nj/2}$ and W for Warburg element ($Z_w=(\sigma/\omega^{1/2}) - (j\sigma/\omega^{1/2})$). The fitting was done with ZSimpWin (Princeton Applied Research, Oak Ridge, TN).

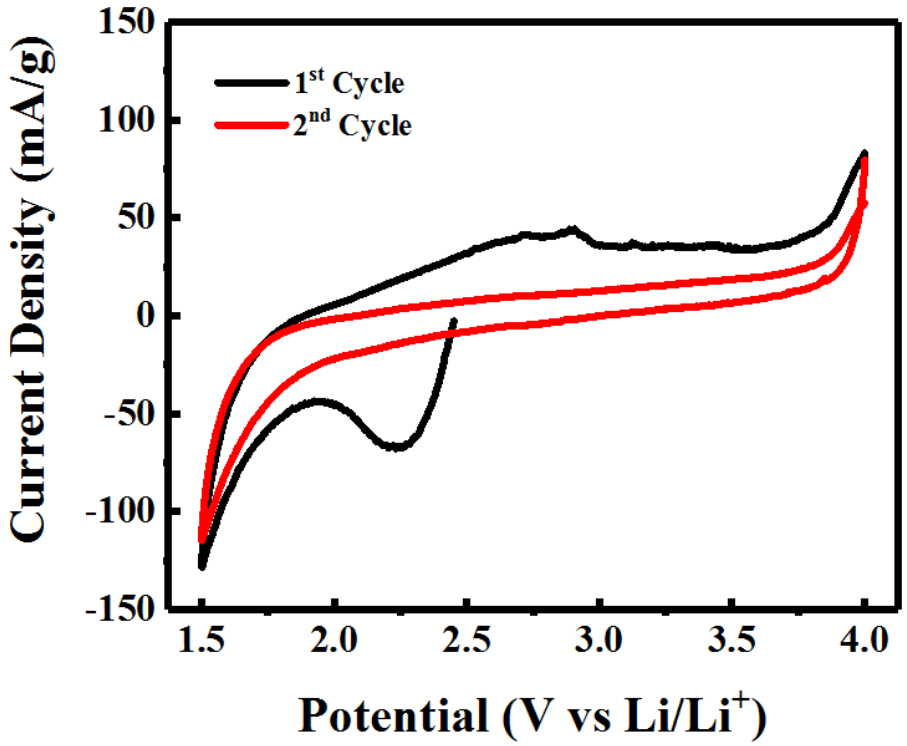

Figure C.12 First and second cycle CV curves for 3 Li^+/V_2O_5 insertion/extraction at a scan rate of 0.1 mV s^{-1} in the potential range of 4.0 – 1.5 V (vs Li/Li^+)

Material	Capacity ($mAh\ g^{-1}$)	Synthesis Method	Electrolyte	Additives	Ref
V_2O_5-rGO	235 (20 mA g^{-1})	Hydrothermal	$LiPF_6$	1:1:1 (EC:DMC:DEC)	1.
V_2O_5-Graphene	243 (50 mA g^{-1})	Slow Hydrolysis	1.2 M $LiPF_6$	3:7 (EC:EMC)	2.
V_2O_5/rGO	211 (190 mA g^{-1})	Solvothermal	1 M $LiPF_6$	1:1 (EC:DMC)	3.
V_2O_5-Graphene Nanoribbons	278 (C/10)	Synthetic Reaction	1 M $LiPF_6$	1:1:1 (EC:DEC:DMC)	4.
Graphene Oxide Coated V_2O_5	240 (100 mA g^{-1})	Hydrothermal	1 M $LiPF_6$	1:1:1 (EC:DEC:DMC)	5.
rGO-Enwrapped V_2O_5 Nanorods	287 (100 mA g^{-1})	Hydrothermal followed by Reflux	1 M $LiPF_6$	1:1 (EC:DMC)	6.
V_2O_5 Nanocrystals on rGO Balls	280 (300 mA g^{-1})	Spray Pyrolysis	1 M $LiPF_6$	1:1 (EC:DMC)	7.
V_2O_5 Nanowires-rGO Composites	225 (C/5)	Electrospinning	1 M $LiPF_6$	1:1 (EC:DMC)	8.
rGO-V_2O_5	295 (31.3 mA g^{-1})	Solvothermal	1 M $LiPF_6$	1:1:1 (EC:DMC:DEC)	9.
V_2O_5/MWCNT sponge	816 μAh cm^{-2} 1C	ALD	1 M LiPF6	1:1 (EC:DEC)	10.
VACNF-V_2O_5	360 (as-dep.) 294 (annealed) (200 mA g^{-1})	PECVD /RF Sputtering	1 M $LiPF_6$	1:1:1 (EC:EMC:DMC)	20.
CNF-V_2O_5 Core-shell	**292 (100 mA g^{-1}) (~C/2.9)**	**Electrospinning/ Pulse Electrodeposition**	**1 M $LiPF_6$**	**1:1:1 (EC:EMC:DMC)**	**This Study**

Table C.1 Comparison of the 2 Li^+/V_2O_5 insertion/extraction performance of this study with literature.

Material	Capacity ($mAh\ g^{-1}$)	Synthesis Method	Electrolyte	Additives	Ref
V_2O_5-Graphene (2% Graphene)	438 (C/20)	Sol-gel	1.2 M $LiPF_6$	3:7 (EC:EMC)	11.
V_2O_5 Nanobelts	288 0.2 mA cm^{-2}	Synthesis	1M $LiPF_6$	1:1 (EC:DMC)	12.
V_2O_5 Nanowires	351 (50 mA g^{-1})	Hydrothermal	1M $LiClO_4$	1:1 (EC:DMC)	13.
V_2O_5 Nanowire (85% Graphene)	400 (100 mA g^{-1})	Hydrothermal	1M $LiPF_6$	1:1 (EC:DMC)	14.
V_2O_5 Aerogel	423 (C/8)	Sol-gel/Freeze Dry	1M $LiClO_4$	1:1 (EC:DMC)	15.
V_2O_5-Carbon (3:1)	320 (C/10)	Combustion/ ball milling of Carbon	1M $LiPF_6$	1:1 (EC:DMC)	16.
V_2O_5 - $LiBO_2$ glass with rGO	400 (50 mA g^{-1})	Glass forming/ball milling of rGO	1M $LiPF_6$	1:1 (EC:DMC)	17.
V_2O_5	350 (C/10)	Aerogel	1M $LiClO_4$	PC	18.
V_2O_5-VACNT Array	368 C/4	CVD /Electrodeposition	1 M LiTFSI	20% EC /[EDMMEA] [TFSI]	19.
VACNF-V_2O_5	547 (as-dep.) 390 (annealed) (200 mA g^{-1})	PECVD /RF Sputtering	1 M $LiPF_6$	1:1:1 (EC:EMC:DMC)	20.
CNF-V_2O_5 Core-shell	**442 (100 mA g^{-1}) (~C/4.4)**	**Electrospinning/ Pulse Electrodeposition**	**1 M $LiPF_6$**	**1:1:1 (EC:EMC:DMC)**	**This Study**

Table C.2 Comparison of the 3 Li^+/V_2O_5 insertion/extraction performance of this study with literature.

1. H. Zhao, L. Pan, S. Xing, J. Luo, J. Xu, Vanadium Oxides–Reduced Graphene Oxide Composite for Lithium-ion Batteries and Supercapacitors with Improved Electrochemical Performance *J. Power Sources.* **2013**, 222, 21-31.

2. Z. Li, H. Zhang, Q. Liu, Y. Liu, L. Stanciu, J. Xie, Hierarchical Nanocomposites of Vanadium Oxide Thin Film Anchored on Graphene as High-Performance Cathodes in Li-Ion Batteries, *ACS Appl. Mater. Interfaces.* **2014**, 6 (21), 18894–18900.

3. X. Rui, J. Zhu, D. Sim, C. Xu, Y. Zeng, H. H. Hng, T. M. Lim, Q. Yan, Reduced Graphene Oxide Supported Highly Porous V_2O_5 Spheres as a High-Power Cathode Material for Lithium Ion Batteries, *Nanoscale* **2011**, 3, 4752-4758.

4. Y. Yang, L. Li, H. Fei, Z. Peng, R. Gedeng, J. M. Tour, Graphene Nanoribbon/V_2O_5 Cathodes in Lithium-Ion Batteries, *ACS Appl. Mater. Interfaces* **2014**, 6 (12), 9590–9594.

5. V. S. R. Channu, D. Ravichandran, B. Rambabu, R. Holze, Carbon and Functionalized Graphene Oxide Coated Vanadium Oxide Electrodes for Lithium Ion Batteries, *Appl. Surf. Sci*. **2014**, 305, 596-602.

6. D. Chen, O. Quan, S. Luo, X. Luo, F. Deng, H. Jiang, Reduced Graphene Oxide Enwrapped Vanadium Pentoxide Nanorods as Cathode Materials for Lithium-ion Batteries, *Physica E* **2014**, 56, 231-237.

7. S. H. Choi, Y. C. Kang, Uniform Decoration of Vanadium Oxide Nanocrystals on Reduced Graphene-Oxide Balls by an Aerosol Process for Lithium-Ion Battery Cathode Material, *Chem. Eur. J*. **2014**, 20 (21), 6294-6299.

8. D. Pham-Cong, K. Ahn, S. W. Hong, S. Y. Jeong, J. H. Choi, C. H. Doh, J. S. Jin, E. D. Jeong, C. R. Cho, Cathodic Performance of V_2O_5 Nanowires and Reduced Graphene Oxide Composites for Lithium Ion Batteries, *Curr. Appl. Phys*. **2014**, 14, 215-221.

9. G. P. Pandey, T. Liu, E. Brown, Y. Yang, Y. Li, X. S. Sun, Y. Fang, J. Li, Mesoporous Hybrids of Reduced Graphene Oxide and Vanadium Pentoxide for Enhanced Performance in Lithium-Ion Batteries and Electrochemical Capacitors *ACS Appl. Mater. Interfaces* **2016**, 8, 9200–9210.

10. C. Xinyi, H. Zhu, Y. C. Chen, Y. Shang, A. Cao, L. Hu, G. W. Rubloff, MWCNT/V_2O_5 Core/Shell Sponge for High Areal Capacity and Power Density Li-Ion Cathodes *ACS Nano* **2012**, 6 (9), 7948–7955.

11. Q. Liu, Z. F. Li, Y. Liu, H. Zhang, Y. Ren, C. J. Sun, W. Lu, Y. Zhou, L. Stanciu, E. A. Stach, J. Xie, Graphene-Modified Nanostructured Vanadium Pentoxide Hybrids with Extraordinary Electrochemical Performance for Li-ion Batteries, *Nat. Commun*. **2014**, 6, 1-10.

12. G. Li, S. Pang, L. Jiang, Z. Guo, Z. Zhang, Environmentally Friendly Chemical Route to Vanadium Oxide Single-Crystalline Nanobelts as a Cathode Material for Lithium-Ion Batteries, *J. Phys. Chem. B,* **2006**, 110 (19), 9383-9386.

13. T. Zhai, H. Liu, H. Li,X. Fang, M. Liao, L. Li, H. Zhou, Y. Koide, Y. Bando, D. Golberg, Centimeter-long V_2O_5 Nanowires: from Synthesis to Field-Emission, Electrochemical, Electrical Transport, and Photoconductive Properties, *Adv. Mater*. **2010**, 22 (23), 2547-2552.

14. J. W. Lee, S. Y.Lim, H. M. Jeong, T. H. Hwang, J. K. Kang, J. W. Choi, Extremely Stable Cycling of Ultra-Thin V_2O_5 Nanowire–Graphene Electrodes for Lithium Rechargeable Battery Cathodes, *Energy Environ. Sci*. **2012**, 5, 9889-9894.

15. H. Li, P. He, Y. Wang, E. Hosono, H. Zhou, High-Surface Vanadium Oxides with Large Capacities for Lithium-ion Batteries: from Hydrated Aerogel to Nanocrystalline VO_2(B), V_6O_{13} and V_2O_5, *J. Mater. Chem*. **2011**, 21, 10999-11009.

16. Y. L. Cheah, V. Aravindan, S. Madhavi, Electrochemical Lithium Insertion Behavior of Combustion Synthesized V_2O_5 Cathodes for Lithium-Ion Batteries, *J. Electrochem. Soc*. **2012**, 159, A273-A280.

17. S. Afyon, F. Krumeich, C. Mensing, A. Borgschulte, R. Nesper, New High Capacity Cathode Materials for Rechargeable Li-ion Batteries: Vanadate-Borate Glasses, *Sci. Rep*. **2014**, 4, 7113

18. A. Moretti, F. Maroni, I. Osada, F. Nobili, S. Passerini, V_2O_5 Aerogel as a Versatile Cathode Material for Lithium and Sodium Batteries, *Chem. Electrochem*. **2015**, 2, 529-537.

19. W. Lu, A. Goering, L. Quy, L. Dai, Lithium-ion Batteries based on Vertically-Aligned Carbon Nanotube Electrodes and Ionic Liquid Electrolytes, *Phys. Chem. Chem. Phys*. **2012**, 14, 12099-12104.

20. E. Brown, J. Acharya, G. Pandey, J. Wu, J. Li, Highly Stable Three Lithium Insertion in Thin V_2O_5 Shells on Vertically Aligned Carbon Nanofiber Arrays for Ultrahigh-Capacity Lithium Ion Battery Cathodes, *Adv. Mater. Interfaces* **2016**, 3 (23), 1600824

Appendix D - Supplementary Information for Chapter 5

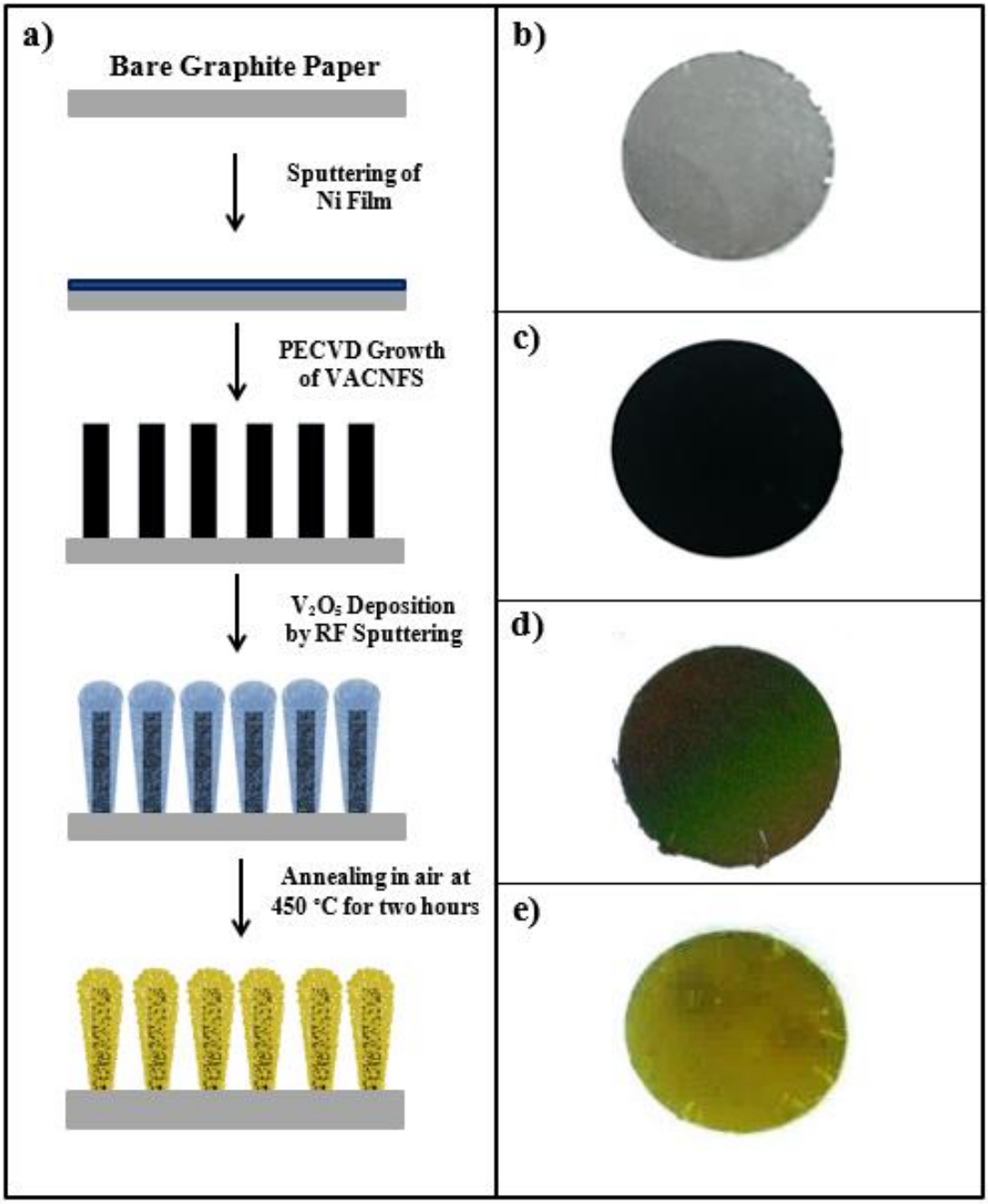

Figure D.1 A schematic illustration of the VACNF growth and V_2O_5 deposition a). Digital images at different stages of the core-shell construction process including bare graphite paper b), bare VACNFs grown on the graphite paper c), as-deposited V_2O_5 on VACNFs d), and annealed V_2O_5 on VACNFs e). (Reprinted with permission from Adv. Mater. Interfaces 2016, 3, 1600824)

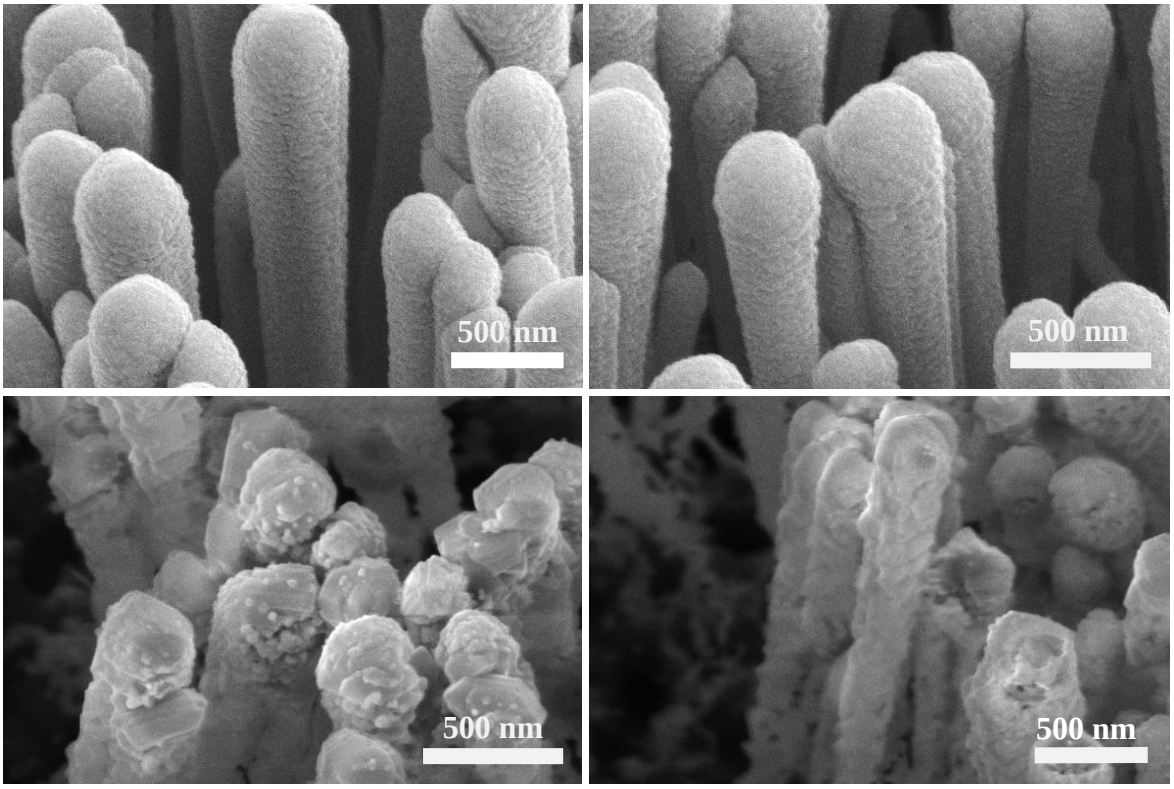

Figure D.2 SEM images of the as-deposited (a-b) and annealed (c-d) VACNF-V_2O_5 core-shell structures. (Reprinted with permission from Adv. Mater. Interfaces 2016, 3, 1600824)

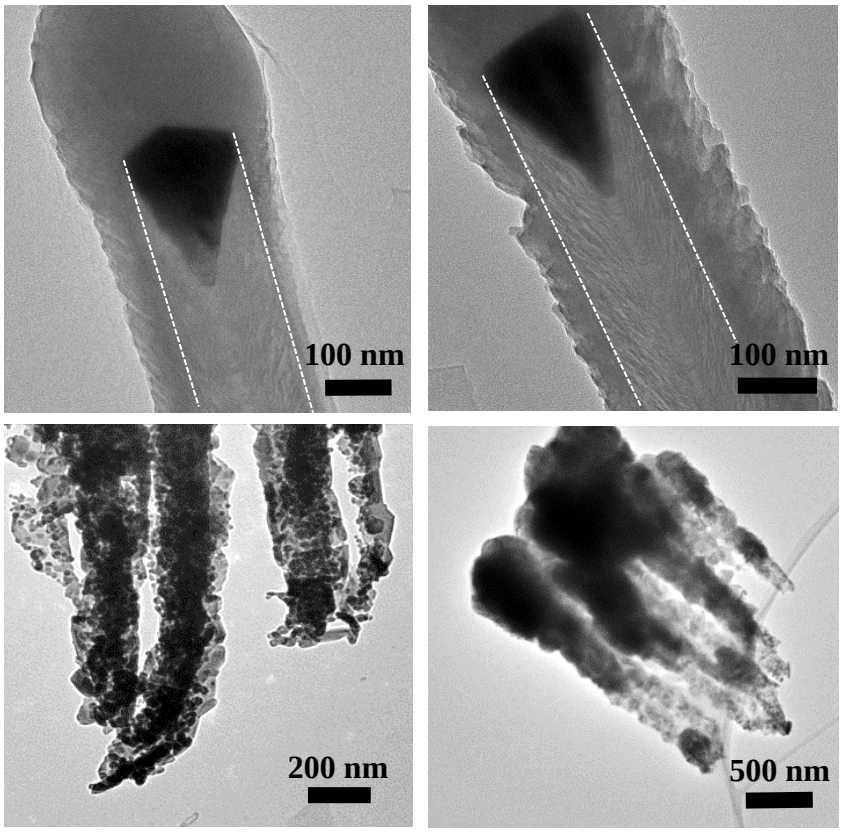

Figure D.3 TEM images of the as-deposited (a-b) and annealed (c-d) VACNF-V_2O_5 core-shell structures. White dashed lines have been inserted to indicate the contour of the VACNF surface. (Reprinted with permission from Adv. Mater. Interfaces 2016, 3, 1600824)

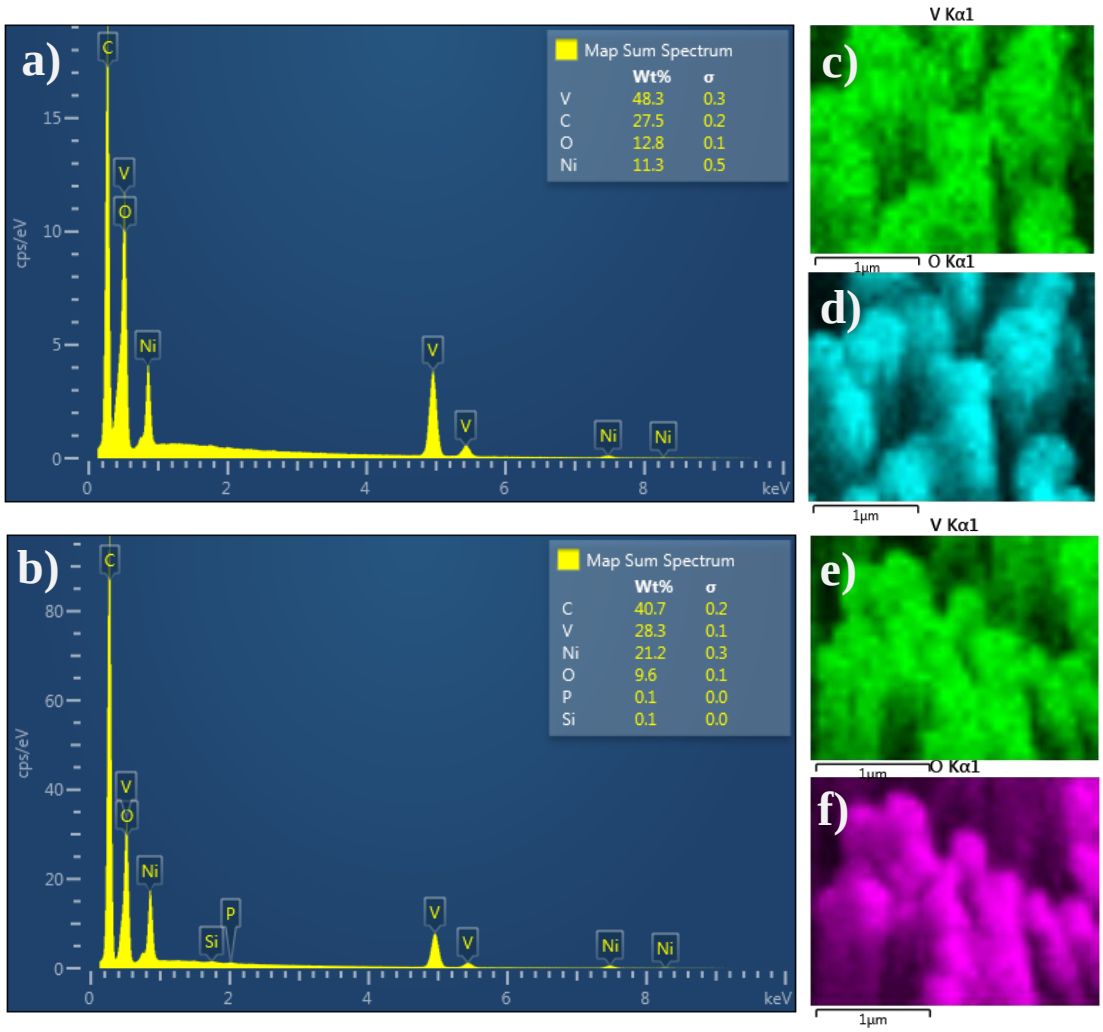

Figure D.4 EDS spectra of the as-deposited a) and annealed b) VACNF-V_2O_5 core-shell structures and EDS maps of the as-deposited (c-d) and annealed (e-f) core-shell structure. (Reprinted with permission from Adv. Mater. Interfaces 2016, 3, 1600824)

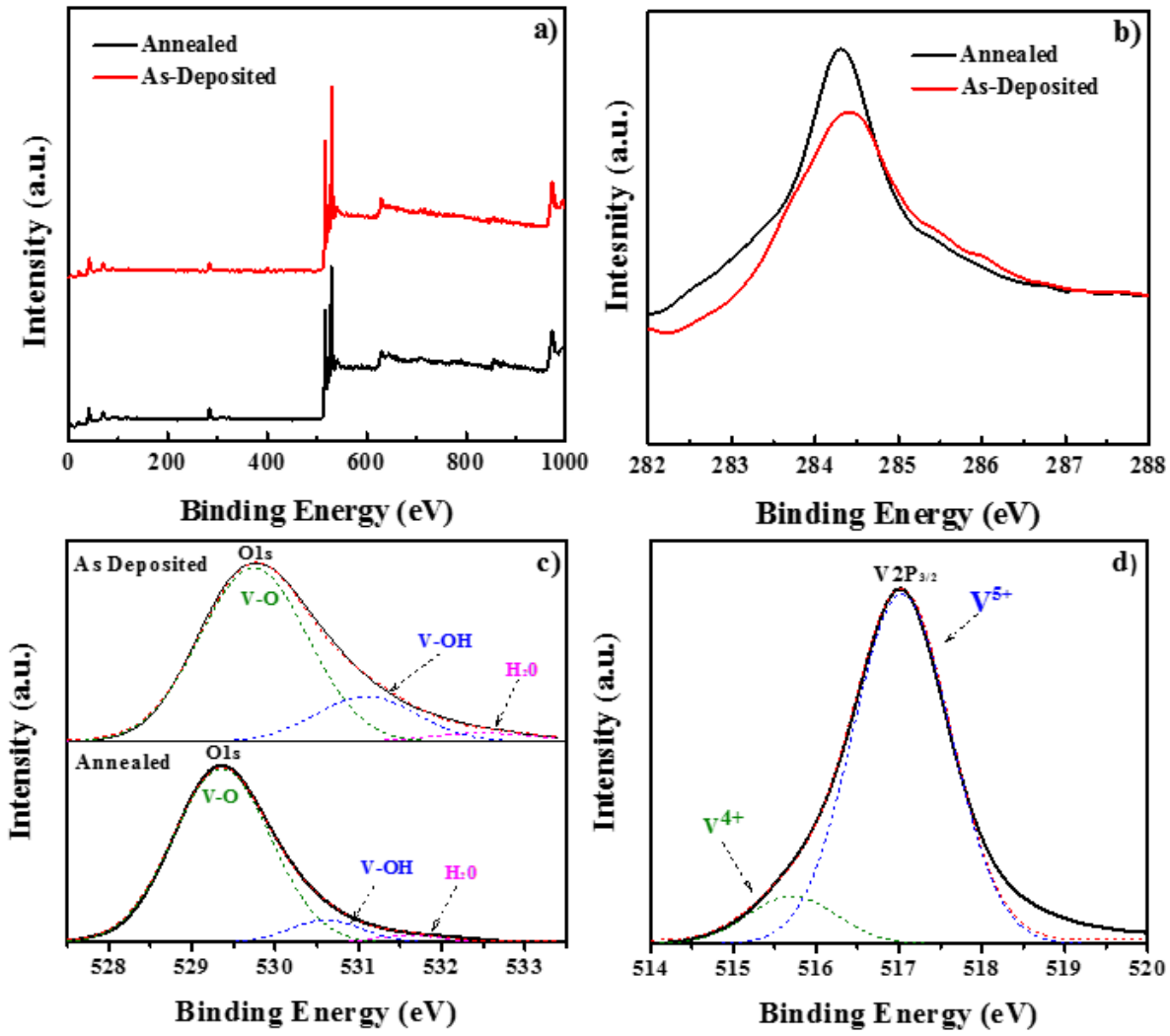

Figure D.5 Wide-scan XPS spectra a) and high-resolution C1s spectra b) of both as-deposited and annealed VACNF-V_2O_5 core-shell structures. Deconvoluted XPS core level spectra of O1s c) of both structures and $V2p_{3/2}$ of the as-deposited VACNF-V_2O_5 core-shell structure d). (Reprinted with permission from Adv. Mater. Interfaces 2016, 3, 1600824)

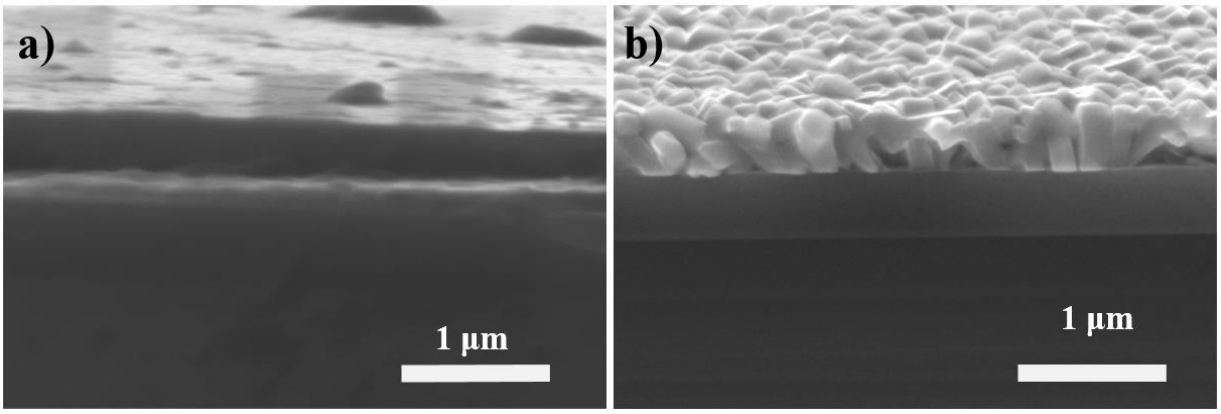

Figure D.6 Cross-sectional SEM images to determine the nominal thicknesses and morphology of as-deposited a) and annealed b) V_2O_5 on silicon. (Reprinted with permission from Adv. Mater. Interfaces 2016, 3, 1600824)

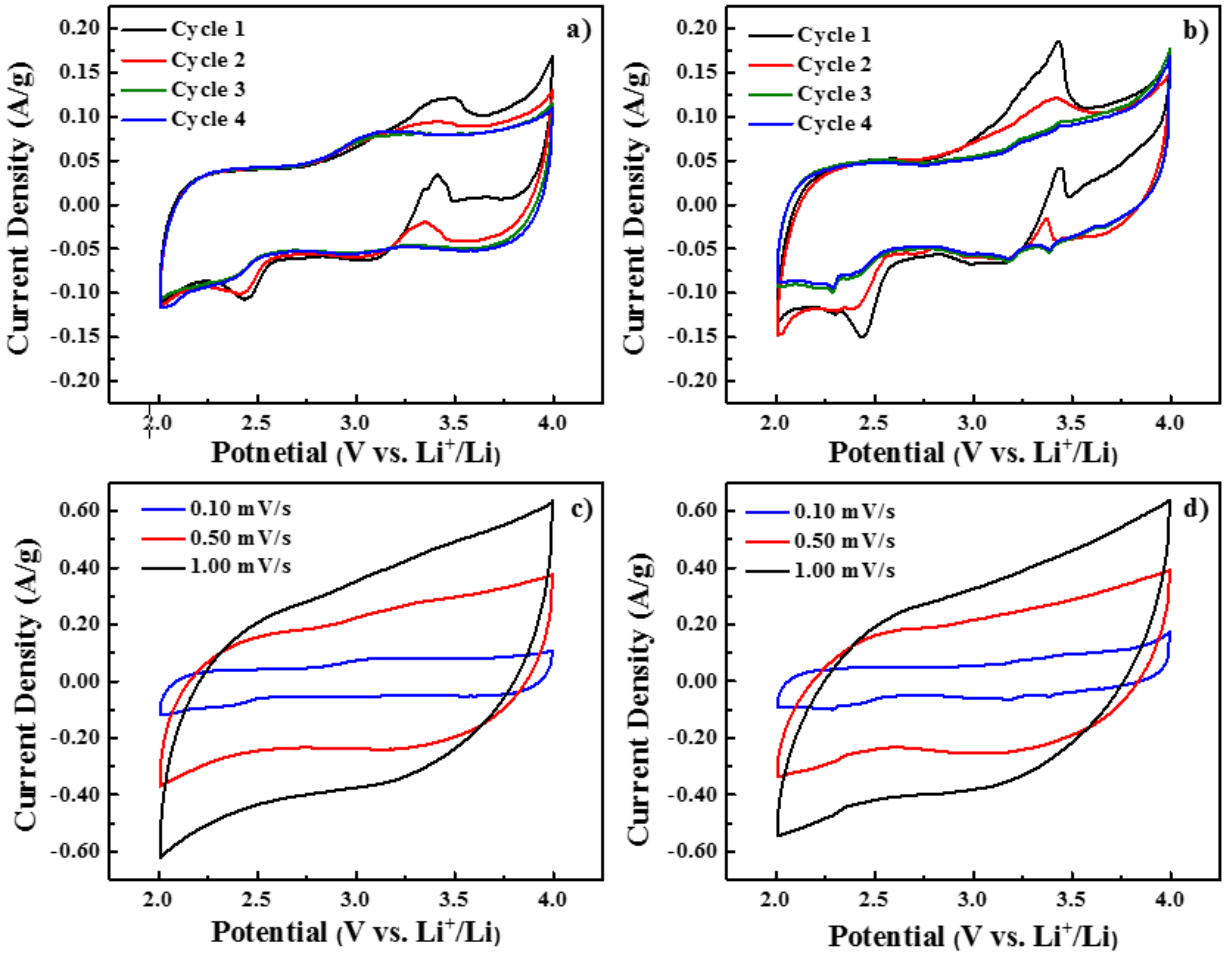

Figure D.7 First four cyclic voltammetry measurements at 0.10 mV/s for the as-deposited a) and annealed b) VACNF-V_2O_5 core-shell structures. Further cyclic voltammetry measurements at 0.10, 0.50, and 1.00 mV/s for the as-deposited c) and annealed d) VACNF-V_2O_5 core-shell structures. (Reprinted with permission from Adv. Mater. Interfaces 2016, 3, 1600824)

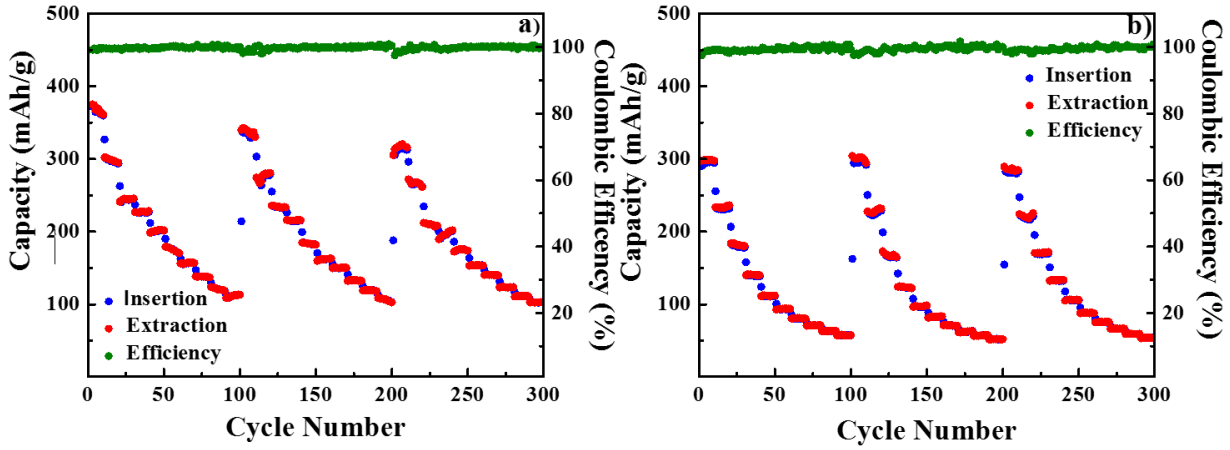

Figure D.8 Three hundred cycles of rate performance measurements of the as-deposited a) and annealed b) VACNF-V_2O_5 core-shell structure in the potential range of 4.0 – 2.0 V. Each rate test sequence consists of 10 galvanic charge-discharge cycles at each of the 10 different current density values (0.20, 0.35, 0.50, 0.60, 0.75, 0.90, 1.00, 1.20, 1.35, and 1.50 A g^{-1}). The sequence is repeated 3 times. (Reprinted with permission from Adv. Mater. Interfaces 2016, 3, 1600824)

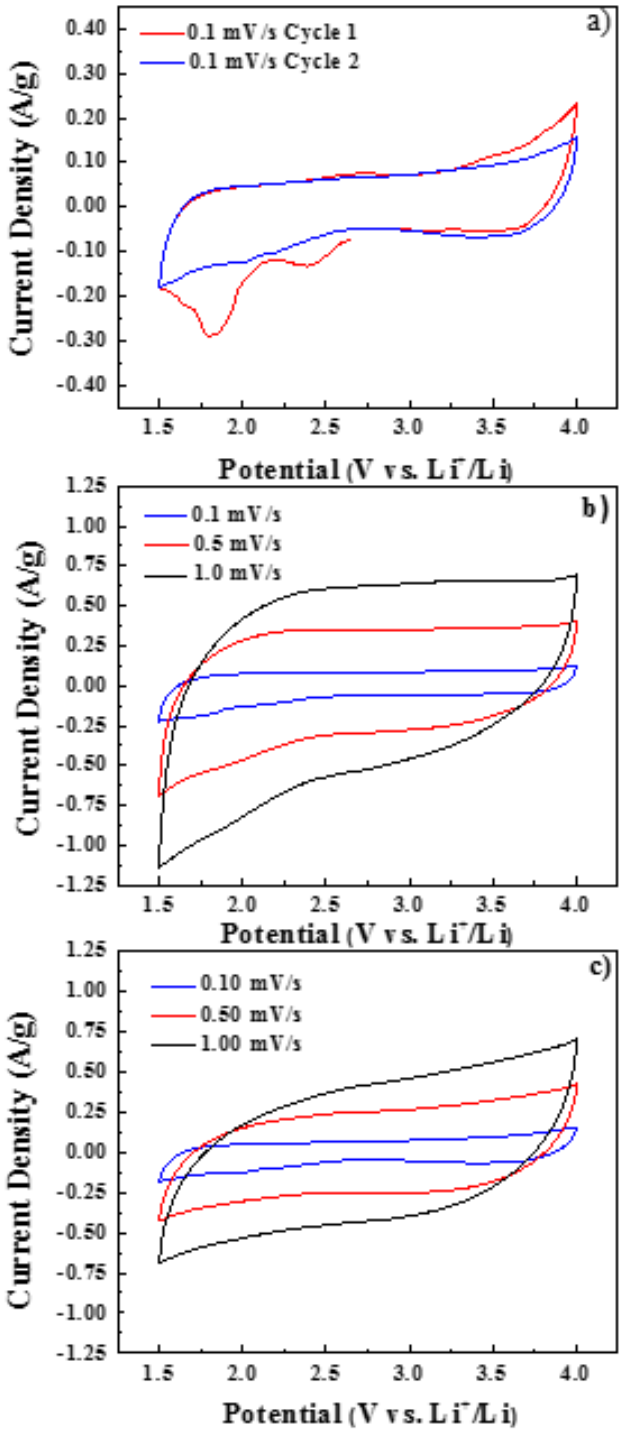

Figure D.9 First two cyclic voltammetry measurements at 0.10 mV/s for the annealed a) VACNF-V_2O_5 core-shell structures in the voltage range of 4.0 – 1.5 V. Further cyclic voltammetry measurements at 0.10, 0.50, and 1.00 mV/s for the as-deposited b) and annealed c) VACNF-V_2O_5 core-shell structures in the voltage range of 4.0 – 2.0 V. (Reprinted with permission from Adv. Mater. Interfaces 2016, 3, 1600824)

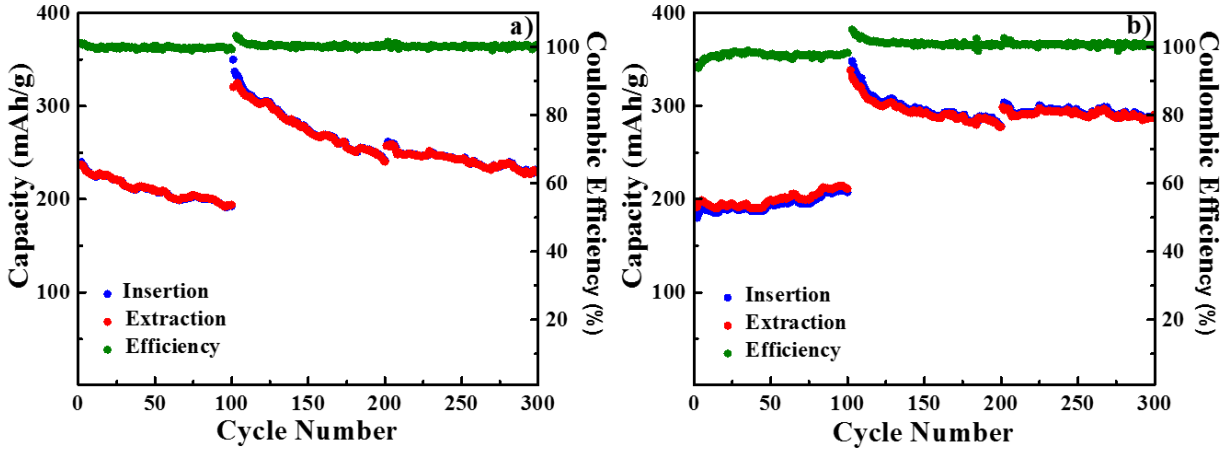

Figure D.10 Long-term cycling performance of the as-deposited a) and annealed b) VACNF-V_2O_5 core-shell structures at a rate of 0.50 A g^{-1}. The first 100 cycles were conducted in the potential range of 4.0 – 2.0 V and the last 200 cycles were conducted in the range of 4.0 – 1.5 V. (Reprinted with permission from Adv. Mater. Interfaces 2016, 3, 1600824)

Material	Capacity ($mAh\ g^{-1}$)	Synthesis Method	Electrolyte	Additives	Ref.
V_2O_5-rGO	235 (20 $mA\ g^{-1}$)	Hydrothermal	$LiPF_6$	1:1:1 (EC:DMC:DEC)	1.
V_2O_5-Graphene	243 (50 $mA\ g^{-1}$)	Slow Hydrolysis	1.2 M $LiPF_6$	3:7 (EC:EMC)	2.
V_2O_5/rGO	211 (190 $mA\ g^{-1}$)	Solvothermal	1 M $LiPF_6$	1:1 (EC:DMC)	3.
V_2O_5-Graphene Nanoribbons	278 (C/10)	Synthetic Reaction	1 M $LiPF_6$	1:1:1 (EC:DEC:DMC)	4.
Graphene Oxide Coated V_2O_5	240 (100 $mA\ g^{-1}$)	Hydrothermal	1 M $LiPF_6$	1:1:1 (EC:DEC:DMC)	5.
rGO-Enwrapped V_2O_5 Nanorods	287 (100 $mA\ g^{-1}$)	Hydrothermal followed by Reflux	1 M $LiPF_6$	1:1 (EC:DMC)	6.
V_2O_5 Nanocrystals on rGO Balls	280 (300 $mA\ g^{-1}$)	Spray Pyrolysis	1 M $LiPF_6$	1:1 (EC:DMC)	7.
V_2O_5 Nanowires-rGO Composites	225 (C/5)	Electrospinning	1 M $LiPF_6$	1:1 (EC:DMC)	8.
rGO-V_2O_5	295 (31.3 $mA\ g^{-1}$)	Solvothermal	1 M $LiPF_6$	1:1:1 (EC:DMC:DEC)	9.
V_2O_5/MWCNT sponge	816 $\mu Ah\ cm^{-2}$ 1C	ALD	1 M LiPF6	1:1 (EC:DEC)	10.
VACNF-V_2O_5	**360 (as-dep.) 294 (annealed) (200 $mA\ g^{-1}$)**	**PECVD /RF Sputtering**	**1 M $LiPF_6$**	**1:1:1 (EC:EMC:DMC)**	

Table D.1 Comparison of the 2 Li^+/V_2O_5 insertion/extraction performance of this study with literature. (Reprinted with permission from Adv. Mater. Interfaces 2016, 3, 1600824)

Material	Capacity ($mAh\ g^{-1}$)	Synthesis Method	Electrolyte	Additives	Ref
V_2O_5-Graphene (2% Graphene)	438 (C/20)	Sol-gel	1.2 M $LiPF_6$	3:7 (EC:EMC)	11.
V_2O_5 Nanobelts	288 0.2 mA cm^{-2}	Synthesis	1M $LiPF_6$	1:1 (EC:DMC)	12.
V_2O_5 Nanowires	351 (50 mA g^{-1})	Hydrothermal	1M $LiClO_4$	1:1 (EC:DMC)	13.
V_2O_5 Nanowire (85% Graphene)	400 (100 mA g^{-1})	Hydrothermal	1M $LiPF_6$	1:1 (EC:DMC)	14.
V_2O_5 Aerogel	423 (C/8)	Sol-gel/Freeze Dry	1M $LiClO_4$	1:1 (EC:DMC)	15.
V_2O_5-Carbon (3:1)	320 (C/10)	Combustion/ ball milling of Carbon	1M $LiPF_6$	1:1 (EC:DMC)	16.
V_2O_5 - $LiBO_2$ glass with rGO	400 (50 mA g^{-1})	Glass forming/ball milling of rGO	1M $LiPF_6$	1:1 (EC:DMC)	17.
V_2O_5	350 (C/10)	Aerogel	1M $LiClO_4$	PC	18.
V_2O_5-VACNT Array	368 C/4	CVD /Electrodeposition	1 M LiTFSI	20% EC /[EDMMEA] [TFSI]	19.
VACNF-V_2O_5	**547 (as-dep.) 390 (annealed) (200 mA g^{-1})**	**PECVD /RF Sputtering**	**1 M $LiPF_6$**	**1:1:1 (EC:EMC:DMC)**	

Table D.2 Comparison of the 3 Li^+/V_2O_5 insertion/extraction performance of this study with literature. (Reprinted with permission from Adv. Mater. Interfaces 2016, 3, 1600824)

1. H. Zhao, L. Pan, S. Xing, J. Luo, J. Xu, Vanadium Oxides–Reduced Graphene Oxide Composite for Lithium-ion Batteries and Supercapacitors with Improved Electrochemical Performance *J. Power Sources.* **2013**, 222, 21-31.

2. Z. Li, H. Zhang, Q. Liu, Y. Liu, L. Stanciu, J. Xie, Hierarchical Nanocomposites of Vanadium Oxide Thin Film Anchored on Graphene as High-Performance Cathodes in Li-Ion Batteries, *ACS Appl. Mater. Interfaces.* **2014**, 6 (21), 18894–18900.

3. X. Rui, J. Zhu, D. Sim, C. Xu, Y. Zeng, H. H. Hng, T. M. Lim, Q. Yan, Reduced Graphene Oxide Supported Highly Porous V_2O_5 Spheres as a High-Power Cathode Material for Lithium Ion Batteries, *Nanoscale* **2011**, 3, 4752-4758.

4. Y. Yang, L. Li, H. Fei, Z. Peng, R. Gedeng, J. M. Tour, Graphene Nanoribbon/V_2O_5 Cathodes in Lithium-Ion Batteries, *ACS Appl. Mater. Interfaces* **2014**, 6 (12), 9590–9594.

5. V. S. R. Channu, D. Ravichandran, B. Rambabu, R. Holze, Carbon and Functionalized Graphene Oxide Coated Vanadium Oxide Electrodes for Lithium Ion Batteries, *Appl. Surf. Sci*. **2014**, 305, 596-602.

6. D. Chen, O. Quan, S. Luo, X. Luo, F. Deng, H. Jiang, Reduced Graphene Oxide Enwrapped Vanadium Pentoxide Nanorods as Cathode Materials for Lithium-ion Batteries, *Physica E* **2014**, 56, 231-237.

7. S. H. Choi, Y. C. Kang, Uniform Decoration of Vanadium Oxide Nanocrystals on Reduced Graphene-Oxide Balls by an Aerosol Process for Lithium-Ion Battery Cathode Material, *Chem. Eur. J*. **2014**, 20 (21), 6294-6299.

8. D. Pham-Cong, K. Ahn, S. W. Hong, S. Y. Jeong, J. H. Choi, C. H. Doh, J. S. Jin, E. D. Jeong, C. R. Cho, Cathodic Performance of V_2O_5 Nanowires and Reduced Graphene Oxide Composites for Lithium Ion Batteries, *Curr. Appl. Phys*. **2014**, 14, 215-221.

9. G. P. Pandey, T. Liu, E. Brown, Y. Yang, Y. Li, X. S. Sun, Y. Fang, J. Li, Mesoporous Hybrids of Reduced Graphene Oxide and Vanadium Pentoxide for Enhanced Performance in Lithium-Ion Batteries and Electrochemical Capacitors *ACS Appl. Mater. Interfaces* **2016**, 8, 9200–9210.

10. C. Xinyi, H. Zhu, Y. C. Chen, Y. Shang, A. Cao, L. Hu, G. W. Rubloff, MWCNT/V_2O_5 Core/Shell Sponge for High Areal Capacity and Power Density Li-Ion Cathodes *ACS Nano* **2012**, 6 (9), 7948–7955.

11. Q. Liu, Z. F. Li, Y. Liu, H. Zhang, Y. Ren, C. J. Sun, W. Lu, Y. Zhou, L. Stanciu, E. A. Stach, J. Xie, Graphene-Modified Nanostructured Vanadium Pentoxide Hybrids with Extraordinary Electrochemical Performance for Li-ion Batteries, *Nat. Commun*. **2014**, 6, 1-10.

12. G. Li, S. Pang, L. Jiang, Z. Guo, Z. Zhang, Environmentally Friendly Chemical Route to Vanadium Oxide Single-Crystalline Nanobelts as a Cathode Material for Lithium-Ion Batteries, *J. Phys. Chem. B,* **2006**, 110 (19), 9383-9386.

13. T. Zhai, H. Liu, H. Li,X. Fang, M. Liao, L. Li, H. Zhou, Y. Koide, Y. Bando, D. Golberg, Centimeter-long V_2O_5 Nanowires: from Synthesis to Field-Emission, Electrochemical, Electrical Transport, and Photoconductive Properties, *Adv. Mater*. **2010**, 22 (23), 2547-2552.

14. J. W. Lee, S. Y.Lim, H. M. Jeong, T. H. Hwang, J. K. Kang, J. W. Choi, Extremely Stable Cycling of Ultra-Thin V_2O_5 Nanowire–Graphene Electrodes for Lithium Rechargeable Battery Cathodes, *Energy Environ. Sci*. **2012**, 5, 9889-9894.

15. H. Li, P. He, Y. Wang, E. Hosono, H. Zhou, High-Surface Vanadium Oxides with Large Capacities for Lithium-ion Batteries: from Hydrated Aerogel to Nanocrystalline VO_2(B), V_6O_{13} and V_2O_5, *J. Mater. Chem*. **2011**, 21, 10999-11009.

16. Y. L. Cheah, V. Aravindan, S. Madhavi, Electrochemical Lithium Insertion Behavior of Combustion Synthesized V_2O_5 Cathodes for Lithium-Ion Batteries, *J. Electrochem. Soc*. **2012**, 159, A273-A280.

17. S. Afyon, F. Krumeich, C. Mensing, A. Borgschulte, R. Nesper, New High Capacity Cathode Materials for Rechargeable Li-ion Batteries: Vanadate-Borate Glasses, *Sci. Rep*. **2014**, 4, 7113

18. A. Moretti, F. Maroni, I. Osada, F. Nobili, S. Passerini, V_2O_5 Aerogel as a Versatile Cathode Material for Lithium and Sodium Batteries, *Chem. Electrochem*. **2015**, 2, 529-537.

19. W. Lu, A. Goering, L. Quy, L. Dai, Lithium-ion Batteries based on Vertically-Aligned Carbon Nanotube Electrodes and Ionic Liquid Electrolytes, *Phys. Chem. Chem. Phys*. **2012**, 14, 12099-12104.

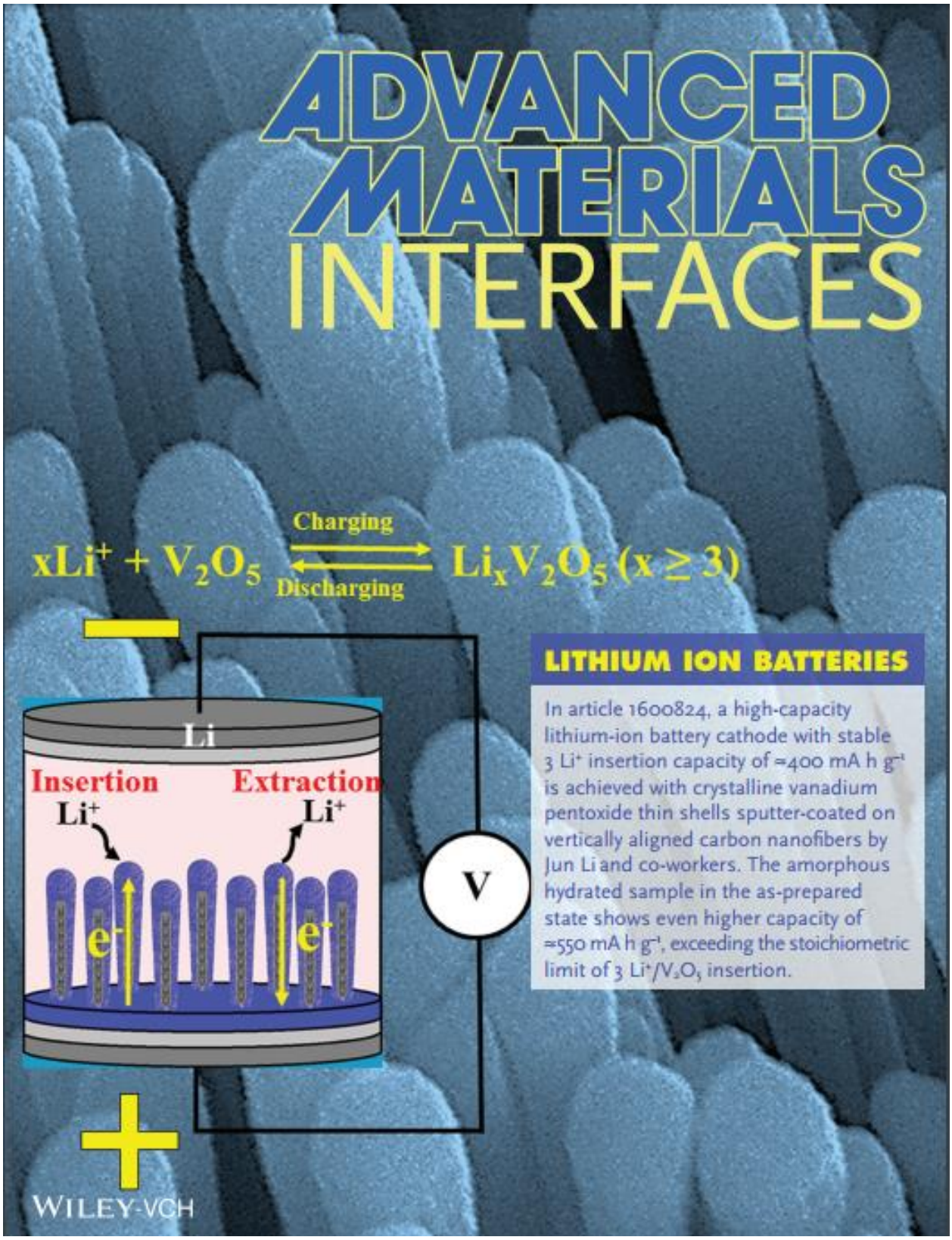

Figure D.11 Frontpiece from Highly Stable Three Lithium Insertion in Thin V_2O_5 Shells on Vertically Aligned Carbon Nanofiber Arrays for Ultrahigh-Capacity Lithium Ion Battery Cathodes. (Reprinted with permission from Adv. Mater. Interfaces 2016, 3, 1600824)

Appendix E - Supplementary Information for Chapter 6

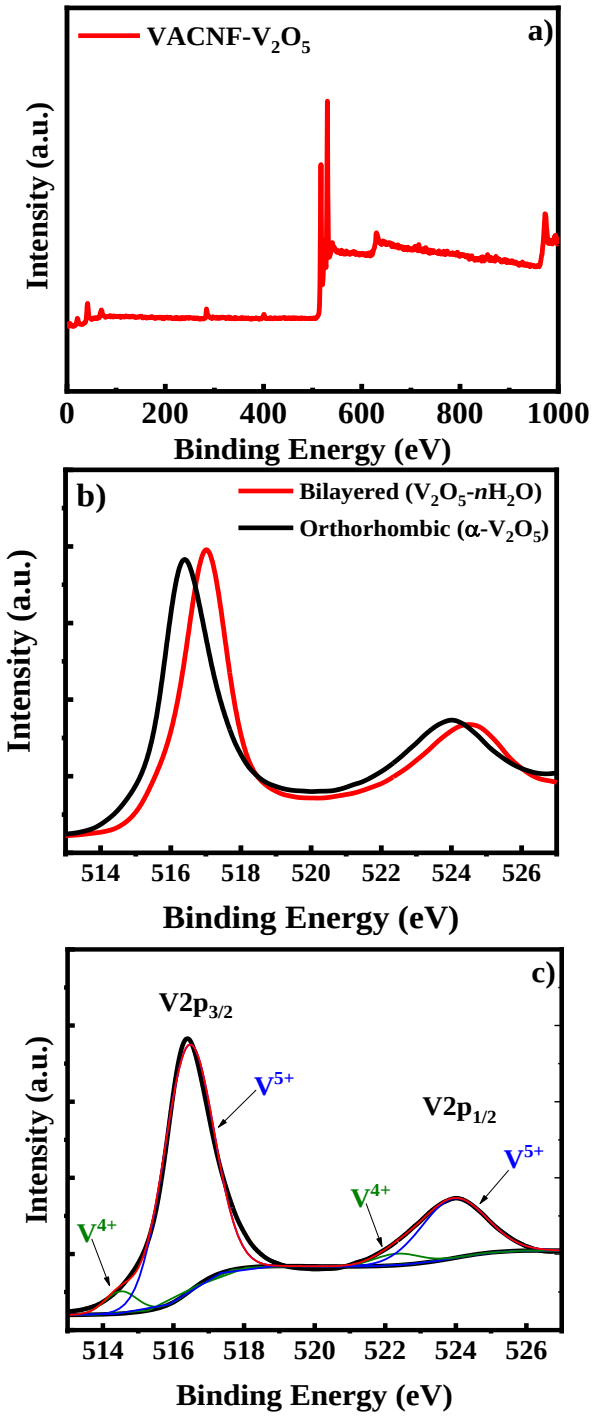

Figure E.1 . a) The wide-scan, b) high-resolution V2p$_{3/2}$, V2p$_{1/2}$, and O1s peaks of the XPS spectrum of the as-deposited (red) and annealed (black) VACNF-V$_2$O$_5$ core-shell structures, and c) the deconvoluted XPS core level spectra V2p$_{3/2}$ of the annealed VACNF-V$_2$O$_5$ core-shell structure.

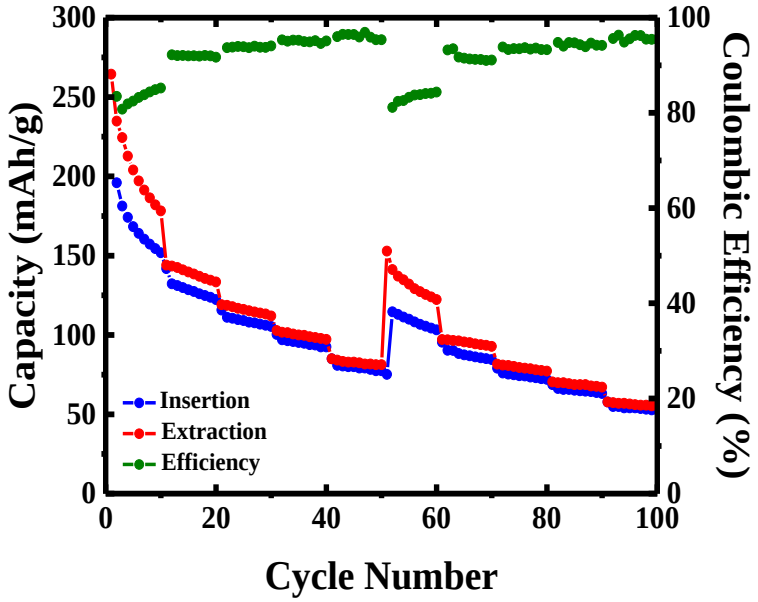

Figure E.2 Electrochemical characterization of the Na^+/V_2O_5 insertion/extraction properties of the as-deposited VACNF-V_2O_5 core-shell structure in the potential range of 3.5 – 1.0 V (vs. Na/Na^+). Rate performance is assessed at 5 different current density values (250, 500, 750, 1000, and 1500 mA g^{-1}), each for 10 charge-discharge cycles.

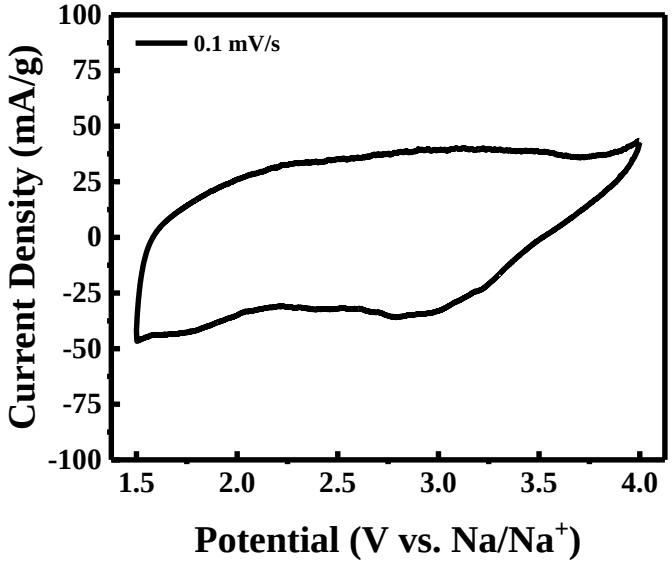

Figure E.3 Cyclic voltammetry curve of the as-deposited VACNF-V_2O_5 core-shell structure at the scan rate of 0.1 mV s^{-1} in the potential window of 4.0 – 1.5 V (vs Na/Na^+).

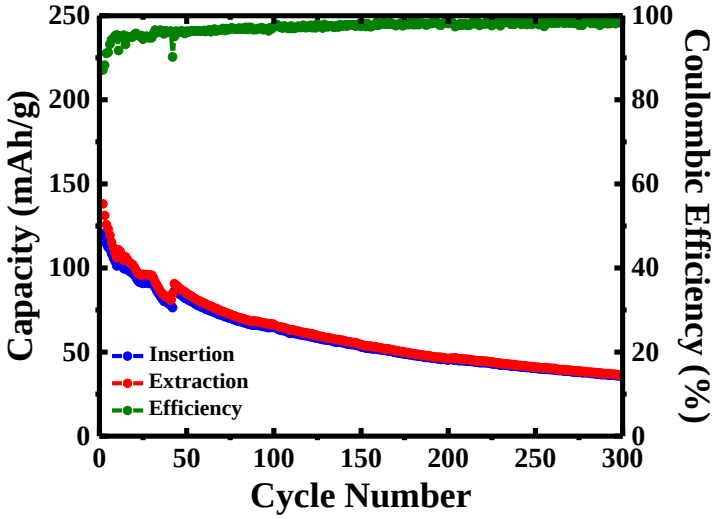

Figure E.4 Extended long-term cycling of the as-deposited VACNF-V_2O_5 core-shell structure at a rate of 625 mA g^{-1} in the potential window of 4.0 – 1.5 V (vs. Na/Na^+). Note: the jump at cycle 42 was due to a power surge that interrupted the long cycling.

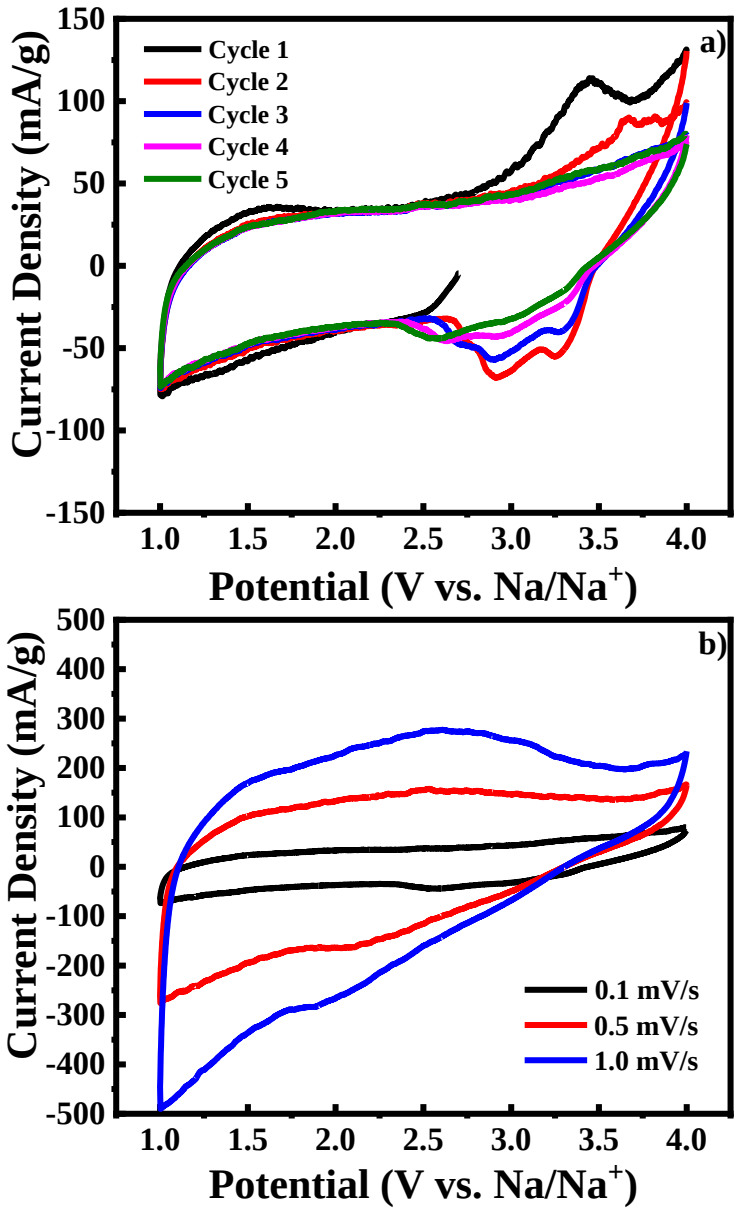

Figure E.5 a) First five CV curves at a scan rate of 0.1 mV s^{-1} of the as-deposited VACNF-V_2O_5 core-shell structure. b) Cyclic voltammetry curves at 0.1 (black), 0.5 (red) and 1.0 (blue) mV s^{-1} in the potential range of 4.0 – 1.0 V (vs. Na/Na^+).

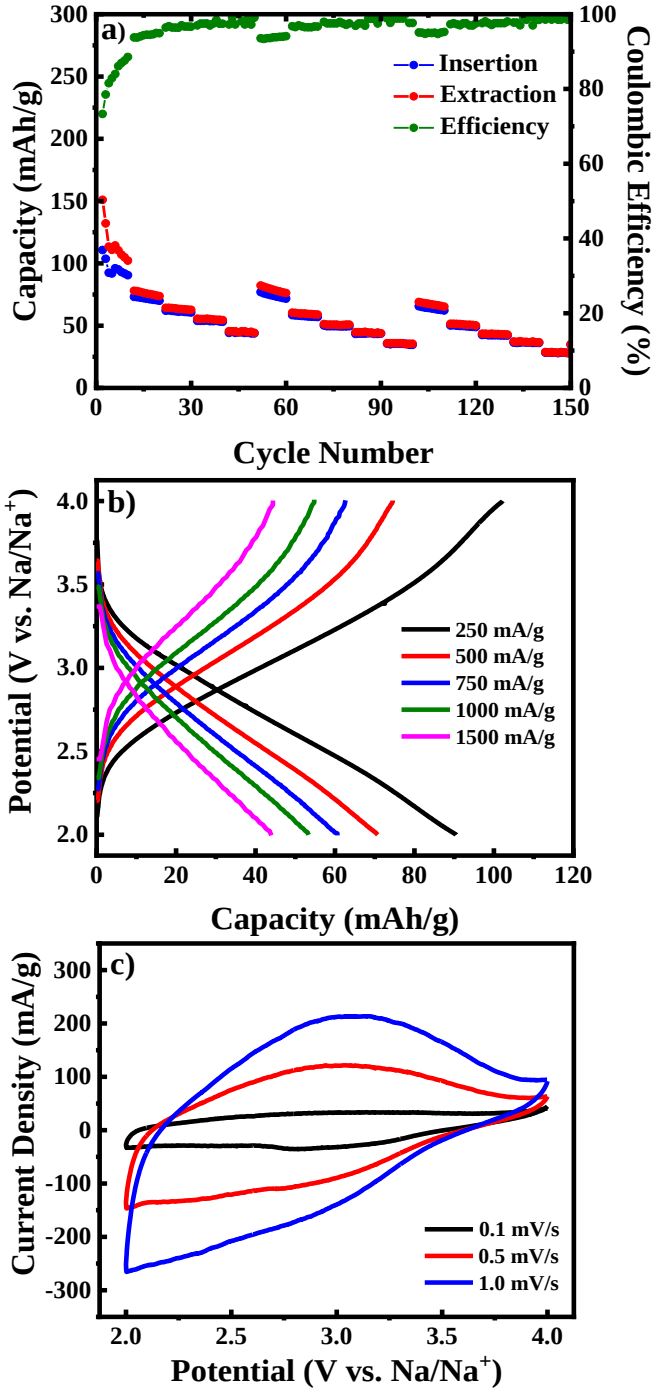

Figure E.6 Electrochemical characterization of the Na^+/V_2O_5 insertion/extraction of the as-deposited VACNF-V_2O_5 core-shell structure in the potential range of 4.0 – 2.0 V (vs. Na/Na^+). a) Three consecutive sets of rate performance at 5 different current density values (250, 500, 750, 1000, and 1500 mA g^{-1}), each for 10 charge-discharge cycles. b) The galvanostatic charge-discharge profiles at the last cycle at each current density in the rate performance. c) Cyclic voltammetry curves at 0.1 (black), 0.5 (red) and 1.0 (blue) mV s^{-1}.

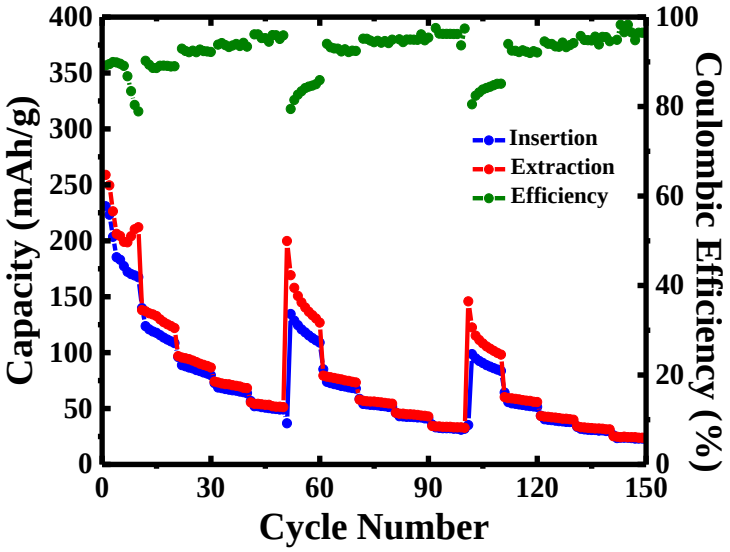

Figure E.7 Rate performance of the VACNF-V_2O_5 core-shell structure using a 1M $NaClO_4$ in EC/DEC 1:1 (V/V) electrolyte a) in the potential range of 4.0 – 1.0 V (vs. Na/Na^+) at 5 different current density values (250, 500, 750, 1000, and 1500 mA g^{-1}), each for 10 charge-discharge cycles.

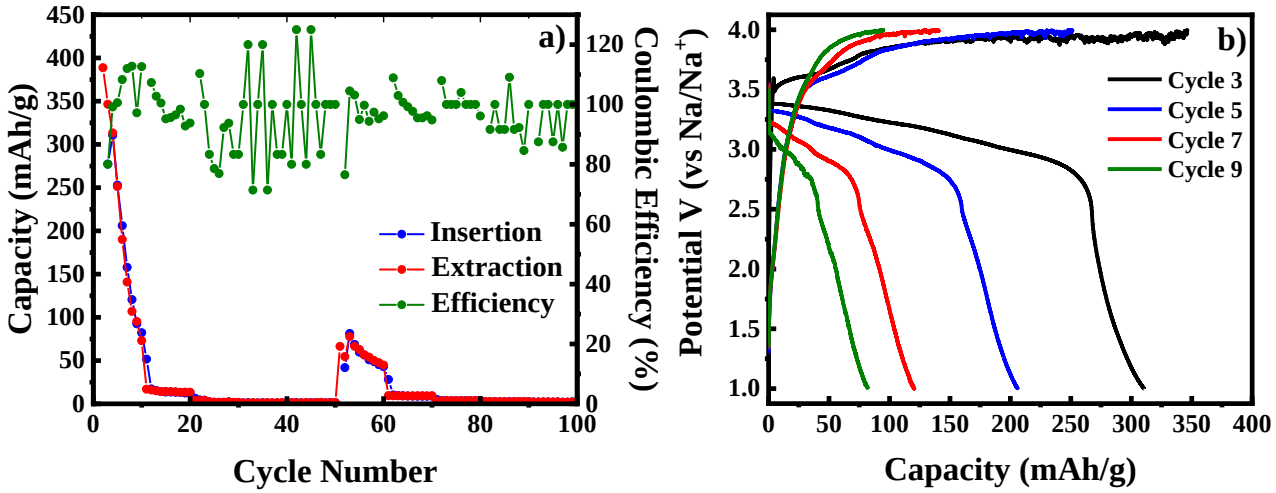

Figure E.8 The rate performance test of a VACNF-V_2O_5 core-shell structure annealed at 450 °C in the air for 2 hours in the potential range of 4.0 – 1.0 V (vs. Na/Na^+) at 5 different current density values (250, 500, 750, 1000, and 1500 mA g^{-1}), each for 10 charge-discharge cycles. b) Representative charge-discharge curves for cycles 3, 5, 7, and 9.

The VACNF-V_2O_5 core-shell structure was annealed at 450 °C in air for two hours as was done in our previous study to form an orthorhombic crystalline shell. The first few cycles are very unstable. An initial insertion capacity of ~800 mAh g^{-1} (not shown) was achieved in the first cycle at a rate of 250 mAh g^{-1} but rapidly faded to 310 mAh g^{-1} in cycle 3 and then continuously dropped to 82 mAh g^{-1} in cycle 10 as shown in Figure S8a. After 10 cycles the capacity dropped below ~15 mAh g^{-1} due to structural collapse owing to the small inter layer d-spacing of orthorhombic V_2O_5. The charge-discharge curves in the first few cycles indeed show long plateaus corresponding to Na^+ insertion into crystalline V_2O_5 but are very unstable. The poor stability was also reflected in the largely varied coulombic efficiency over the cycling.

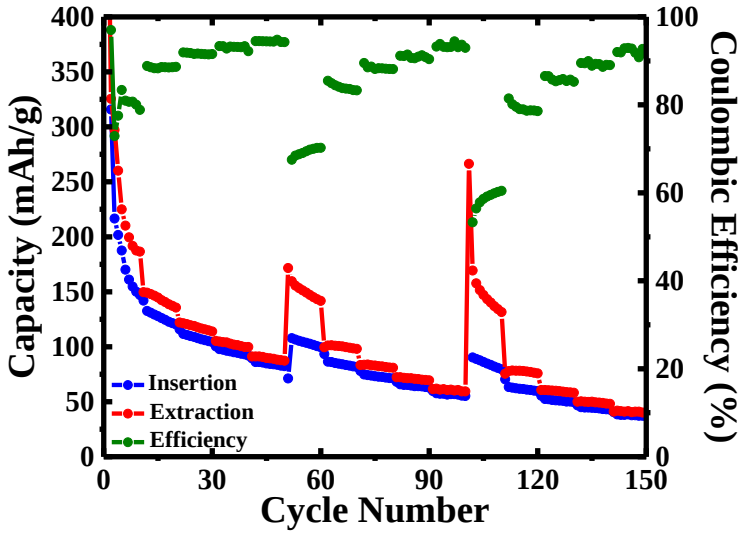

Figure E.9 Rate performance of the VACNF-V_2O_5 core-shell structure annealed in air at 250 °C for two hours in the potential range of 4.0 – 1.0 V (vs. Na/Na^+) at 5 different current density values (250, 500, 750, 1000, and 1500 mA g^{-1}), each for 10 charge-discharge cycles.

Annealing was reduced to 250 °C for two hours in air in order to optimize the annealing conditions. Three galvanostatic charge-discharge rate performance sequences were conducted as shown in Figure S9. An initial insertion capacity of 316 mAh g^{-1} was achieved at a rate of 250 mA g^{-1} which faded to 147 mAh g^{-1} (1.7C) in cycle 10. Insertion capacities of 120, 104, 92, and 82 mAh g^{-1} were achieved at rates of 500, 750, 1000, and 1500 mA g^{-1}, respectively, corresponding to 4.2C, 7.2C, 10.9C, and 18.3 C. When compared to the as-deposited core-shell structure, the capacities increased at the higher rates. This pattern is consistent in the second and third rate performance sequences. However, the last cycle coulombic efficiency only reached 94% at a rate of 1500 mA g^{-1} in the first-rate performance sequence and dropped to 93 and 92% in the second and third rate sequences, respectively. Moreover, the last cycle coulombic efficiency only reached 80% at the rate of 250 mA g^{-1} in the first-rate sequence which dropped dramatically to ~70% and ~60% in the second and third sequences, respectively. Hence, capacity increased at the expense of coulombic efficiency and cell stability.

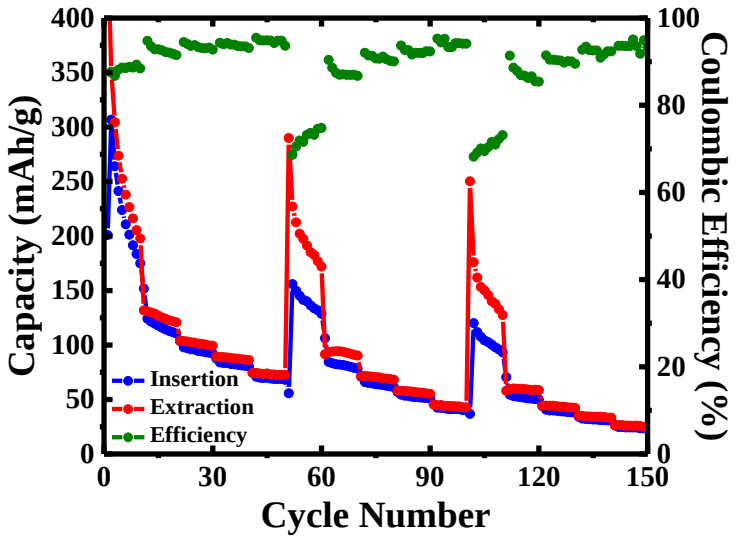

Figure E.10 Rate performance of the VACNF-V_2O_5 core-shell structure annealed under vacuum at 120 °C for 20 hours in the potential range of 4.0 – 1.0 V (vs. Na/Na^+) at 5 different current density values (250, 500, 750, 1000, and 1500 mA g^{-1}), each for 10 charge-discharge cycles.

Tepavcevic et al. reported a bilayered V_2O_5 nanostructure with an interlayer d-spacing of 13.5 Å.[215] Following their work, the VACNF-V_2O_5 core-shell structure was annealed at 120 °C under vacuum for 20 hours. Three galvanostatic charge-discharge rate performance sequences were conducted as shown in Figure S10. An initial insertion capacity of 307 mAh g^{-1} was achieved at a rate of 250 mA g^{-1} which faded to 174 mAh g^{-1} in cycle 10. Insertion capacities of 110, 92, 80, and 68 mAh g^{-1} were achieved at rates of 500, 750, 1000, and 1500 mA g^{-1}, respectively. When the rate performance was repeated insertion capacities of 129, 78, 61, 51, and 40 mAh g^{-1} were achieved at the respective current rates. The decay of insertion capacities continued in the third-rate performance with values of 93, 50, 38, 31, and 24 mAh g^{-1} at the respective current rates. The capacity values are slightly higher than those observed in the as-deposited core-shell structure especially at the higher rates. However, the coulombic efficiency only reached a maximum value of 94% at the rate of 1500 mA g^{-1}. Moreover, the coulombic efficiency reached 88% at the low rate of 250 mA g^{-1} in the first-rate performance which rapidly decreased to 75 and 73% in the

second and third rate sequences, respectively. It's clear that these annealing strategies aid in improving the overall insertion capacity especially at high rates. However, coulombic efficiency remains an issue especially at the low rates which overall reduces its long-term stability. It's likely that the performance of the VACNF-V_2O_5 core-shell structure could be optimized with proper thermal annealing.

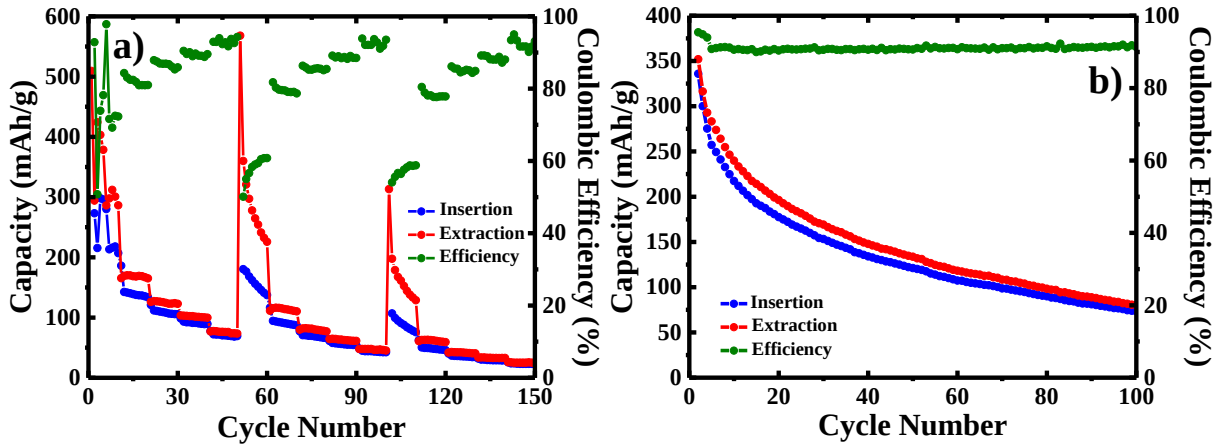

Figure E.11 Rate performance of the VACNF-V_2O_5 core-shell structure with a 5.5 nm of Al_2O_3 protective layer in the potential range of 4.0 – 1.0 V (vs. Na/Na^+) at 5 different current density values (250, 500, 750, 1000, and 1500 mA g^{-1}), each for 10 charge-discharge cycles. Long term cycling of the VACNF-V_2O_5-Al_2O_3 core-shell structure b) at a rate of 625 mA g^{-1} in the potential range of 4.0 – 1.0 V (vs. Na/Na^+).

` Several reports have shown improved performances with a thin protective layer of Al_2O_3 along the surface of the active material. A 5.5 nm thick Al_2O_3 film was deposited along on the VACNF-V_2O_5 core-shell structure using atomic layer deposition. Three galvanostatic charge-discharge rate performance sequences were conducted as shown in Figure S11a. An insertion capacity of 273 mAh g^{-1} was achieved in the 2nd cycle, however, the first 10 cycles were unstable contrary to expectations. Insertion capacities of 134, 105, 90, and 69 mAh g^{-1} were achieved in the first-rate performance sequence at rates of 500, 750, 1000, and 1500 mA g^{-1}, respectively. However, coulombic efficiency reached a max value of only 93% at the rate of 1500 mA g^{-1}. Insertion capacities in the second/third rate performance sequence rapidly faded to 137/75, 87/46, 66/34, 54/29, and 42/23 mAh g^{-1} at the respected rates. Moreover, coulombic efficiencies decreased to ~60% at the rate of 250 mA g^{-1} in second and third-rate performances. Long term cycling at 625 mAh g^{-1} in Figure S11b shows moderate improvement over the as-deposited core-shell structure in terms of capacity. A high initial insertion capacity of 335 mAh g^{-1} was achieved but dropped to 72 mAh g^{-1} after 100 cycles. It could be argued that the increase in capacity could

be attributed to Al_2O_3 contribution. Moreover, coulombic efficiency remained steady at ~91% throughout cycling duration which is consistent with the as-deposited core-shell structure. Overall, no significant improvement is observed in terms of overall performance with a thin Al_2O_3 protective layer.

Element	LIB		NIB
R_s	12.08 Ω		68.6 Ω
R_{ct1}	68.35 Ω		2.818×10^{7} Ω
CPE_1	C_1	2.786×10^{-3} F	1.739×10^{-3} F
	n_1	0.8028	0.1602
R_{ct2}	106.2 Ω		573 Ω
CPE_2	C_2	1.387×10^{-4} F	7.064×10^{-6} F
	n_2	0.5571	0.8975
W	$\sigma = 3.875 \times 10^{-3}$ Ω ($s^{-1/2}$)		$\sigma = 1.138 \times 10^{-3}$ Ω ($s^{-1/2}$)

Table E.1 The fitting parameters of the as-deposited VACNF-V_2O_5 electrode in the coin cell at open circuit potentials of ~2.35 V (vs Na/Na^+) and ~3.00 V (vs Li/Li^+) for the SIB and LIB, respectively, based on the equivalent circuit shown in inset of Figure 6.7.

\

Appendix F - Supplementary Information for Chapter 7

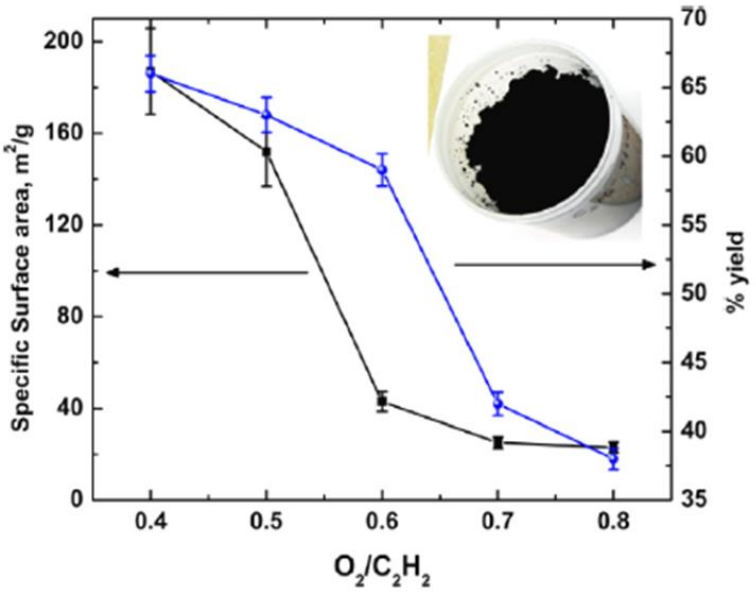

Figure F.1 Specific surface area derived from BET measurements of the various oxygen ratios detonated graphene.

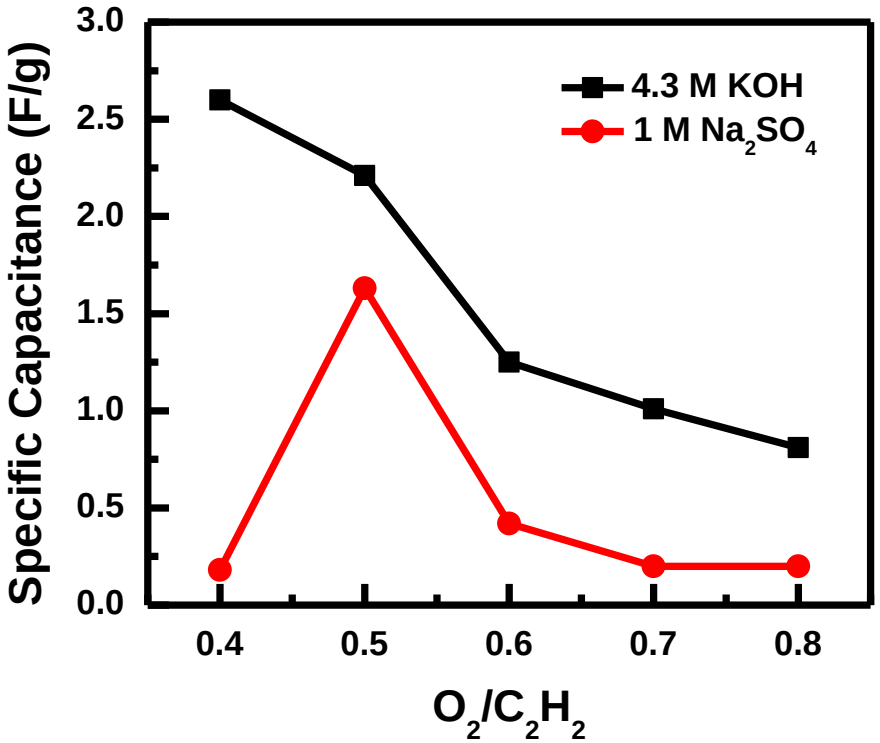

Figure F.2 Mass-specific capacitance of the different oxygen ratios of detonated graphene using 4.3 M KOH (black) and 1 M Na_2SO_4 (red) as electrolyte.

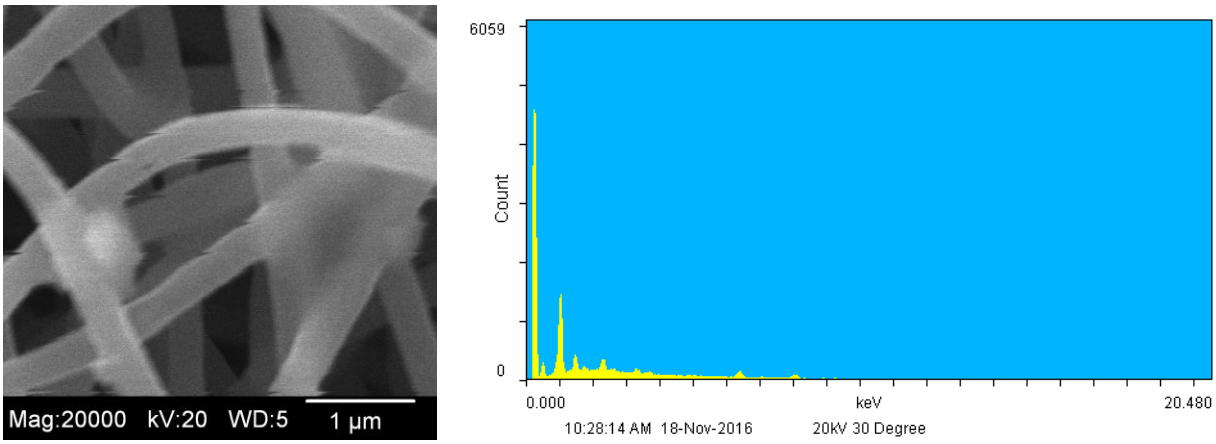

Figure F.3 a) An SEM image of Fe_3O_4 coated CNF fibers. b) The EDS spectrum indicating minimal Fe content.

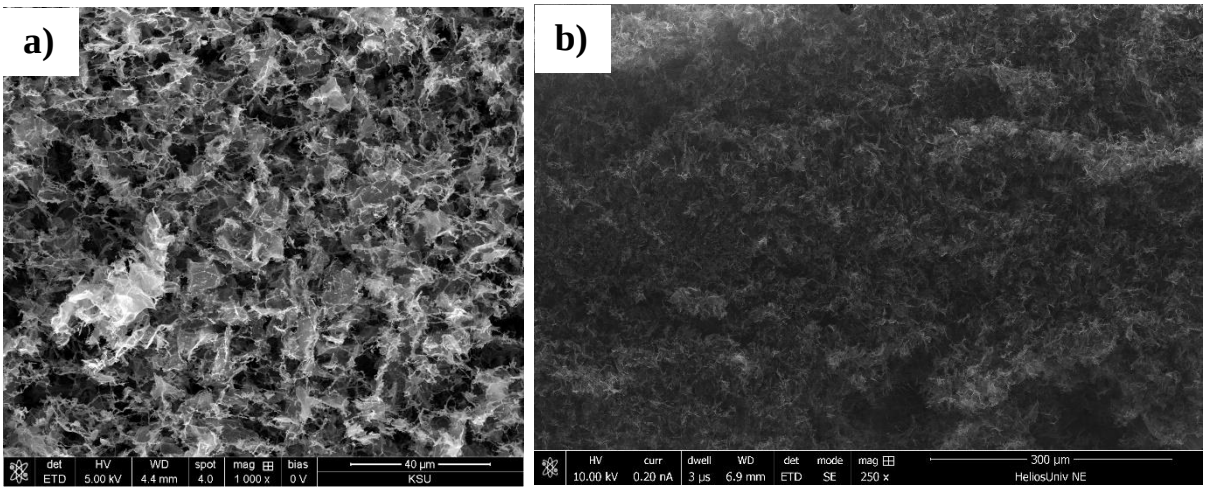

Figure F.4 SEM images of the 3D printed MoS_2-rGO structure on Nickel foam from the top a) and side view b).

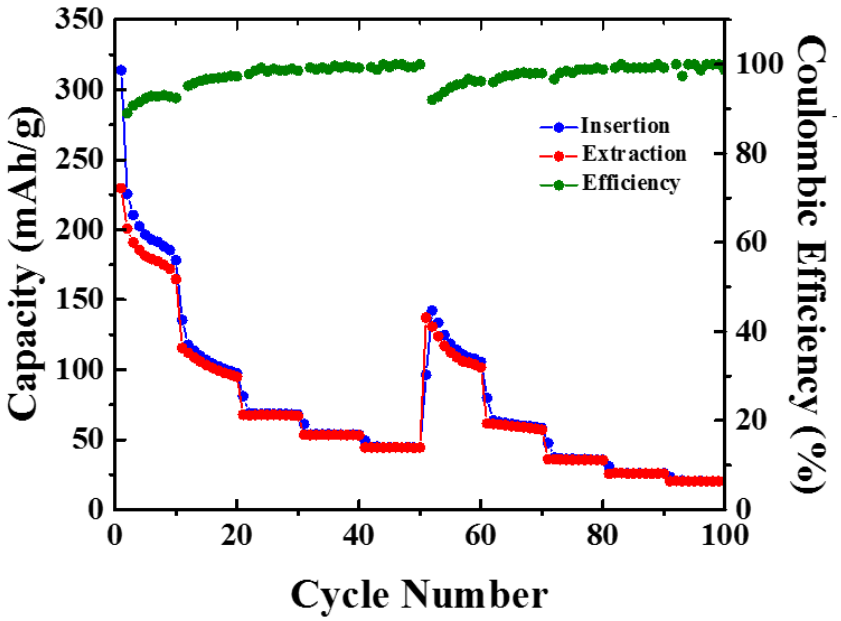

Figure F.5 Galvanostatic charge-discharge rate performance of MoS_2 mixed with carbon black and PVDF casted onto a copper substrate

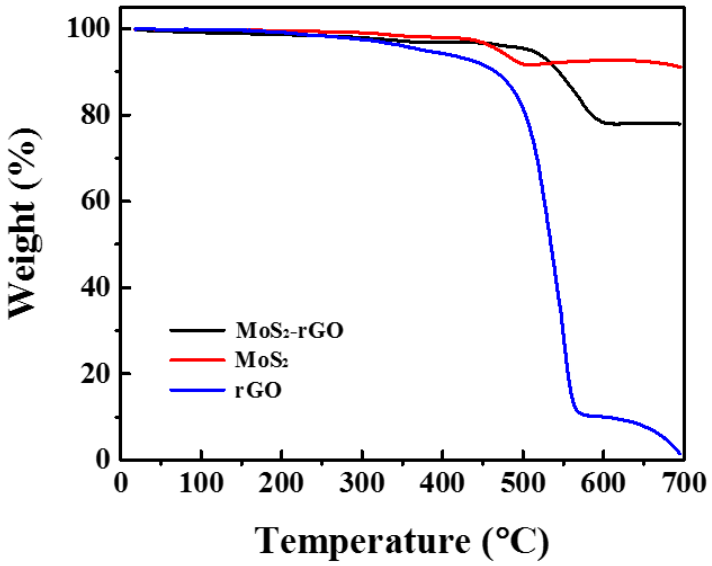

Figure F.6 TGA measurements of MoS_2, MoS_2-rGO, and rGO under air

Appendix G - List of Publication and Presentations

Publications

- **Emery Brown**, Pengli Yan, Halil Tekik, Ayyappan Elangovan, Jun Li, Dong Lin, 3D Printed hybrid MoS_2-rGO aerogel for a Highly Stable Sodium Ion Battery Anode, ***Under Preparation***

- **Emery Brown**, Jagaran Acharya, Ayyappan Elangovan, Gaind P. Pandey, Judy Wu, Jun Li, Enabling Stable Sodium Ion Battery Cathodes with a Hybrid Structure of Disordered Bilayered $V_2O_5 \cdot nH_2O$ Shells Deposited on Vertically Aligned Carbon Nanofiber Arrays, ***Submitted to ACS Applied Materials and Interfaces***

- **Emery Brown**, Seok-Hwan Park, Ayyappan Elangovan, Yue Yuan, Jooyoun Kim, Xiuzhi Susan Sun, Xiaoming Zhang, Guohong Wang, Jun Li, Facilitating High-Capacity V_2O_5 Cathodes with Stable Two and Three Li^+ Insertion Using a Hybrid Membrane Structure Consisting of Amorphous V_2O_5 Shells Coaxially Deposited on Electrospun Carbon Nanofibers, ***Electrochimica Acta***, 2018, 269, 144-154

- Pengli Yan, **Emery Brown**, Qing Su, Jun Li, Jian Wang, Changxue Xu, Chi Zhou, Dong Li, 3D Printing Hierarchical Silver Nanowire Aerogel with Highly Compressive Resilience and Tensile Elongation Through Tunable Poisson's Ratio, ***Small***, 2017, 1701756

- **Emery Brown**, Jagaran Acharya, Gaind P. Pandey, Judy Wu, Jun Li, Highly Stable Three Lithium Insertion in Thin V_2O_5 Shells on Vertically Aligned Carbon Nanofiber Arrays for Ultrahigh-Capacity Lithium Ion Battery Cathodes, ***Advanced Materials Interfaces***, 2016, 3, 16000824

- Gaind P. Pandey, Tao Liu, **Emery Brown**, Yiqun Yang, Yonghui Li, Xiuzhi Susan Sun, Yueping Fang, Jun Li, Mesoporous Hybrids of Reduced Graphene Oxide and Vanadium Pentoxide for Enhanced Performance in Lithium-Ion Batteries and Electrochemical Capacitors, ***ACS Applied Materials and Interfaces***, 2016, 8, 9200–9210

- Jagaran Acharya, Chunrui Ma, **Emery Brown**, Jun Li, Judy Wu, Probing Effect of Temperature on Energy Storage Properties of Relaxor-Ferroelectric Epitaxial $Pb_{0.92}La_{0.08}Zr_{0.52}Ti_{0.48}O_3$ Thin Film Capacitors, ***Thin Solid Films***, 2016, 616, 711-716

- Chunrui Ma, Youpin Gong, Rongtao Lu, **Emery Brown**, Beihai Ma, Jun Li, Judy Wu, Detangling Extrinsic and Intrinsic Hysteresis for Detecting Dynamic Switch of Electric Dipoles Using Graphene Field-Effect Transistors on Ferroelectric Gates, ***Nanoscale***, 2015, 44, 18347 to 18828

- Xunfu Zhou, Weijian Liu, Xiaoyuan Yu, Yingiu Liu, Yueping Fang, Steven Klankowski, Yiqun Yang, **Emery Brown**, Jun Li, Tin Dioxide@Carbon Core-Shell Nanoarchitectures Anchored on Wrinkled Graphene for Ultrafast and Stable Lithium Storage, ***ACS Applied Materials and Interfaces***, 2014, 7434-7443

- **Emery Brown**, Chunrui Ma, Jagaran Acharya, Beihai Ma, Judy Wu, Jun Li, Controlling Dielectric and Relaxor-Ferroelectric Properties for Energy Storage by Tuning $Pb_{0.92}La_{0.08}Zr_{0.52}Ti_{0.48}O_3$ Film Thickness***, ACS Applied Materials and Interfaces***, 2014, 6, 22417–22422

- Gary Malek, **Emery Brown**, Steven Klankowski, Jianwei Liu, Alan Elliot, Rongtao Lu, Jun Li, Judy Wu, Atomic Layer Deposition of Al-doped ZnO/Al_2O_3 Double Layers on Vertically Aligned Carbon Nanofiber Arrays, ***ACS Applied Materials and Interfaces***, 2014, 6, 6865–6871

- **Emery Brown**, Russell Baughman, 2-Methyl-4,4-dioxo-*N*-phenyl-5,6-dihydro-1,4-oxathiine-3-carboxamide (Oxycarboxin), ***Acta Crystallographica Section E***, 2010, E66, o2654

- **Emery Brown**, Russell Baughman, *N*-Ethyl-6-ethylamino-4-oxo-1,3,5-triazin-2-aminium chloride (Oxysimazine·HCl), ***Acta Crystallographica Section E***, 2010, E66, o2418

Presentations

- **Emery Brown**, Seok-Hwan Park, Ayyappan Elangovan, Yue Yuan, Jooyoun Kim, Xiuzhi Susan Sun, Xiaoming Zhang, Guohong Wang, Jun Li, "Highly Stable Two and Three Lithium Insertion in Amorphous V_2O_5 Shells Coaxially Deposited on Electrospun Carbon Nanofibers: a Self-supported Membrane for High-capacity Lithium Ion Battery Cathodes", 255th ACS National Meeting, New Orleans, LA (2018)

- **Emery Brown**, Seok-Hwan Park, Ayyappan Elangovan, Yue Yuan, Jooyoun Kim, Xiuzhi Susan Sun, Xiaoming Zhang, Guohong Wang, Jun Li, "Highly Stable Two and Three Lithium Insertion in Amorphous V_2O_5 Shells Coaxially Deposited on Electrospun Carbon Nanofibers: a Self-supported Membrane for High-capacity Lithium Ion Battery Cathodes", 52nd ACS Regional Meeting, Lawrence, KS (2017)

- **Emery Brown**, Jagaran Acharya, Gaind P. Pandey, Judy Wu, Jun Li, "Highly Stable Three Lithium Insertion in Thin V_2O_5 Shells on Vertically Aligned Carbon Nanofiber Arrays for Ultrahigh-Capacity Lithium Ion Battery Cathodes" 51st ACS Midwest Regional Meeting, Manhattan, KS (2016)

- **Emery Brown**, Viktor Chikan, "Formation of Ag Doped CdTe Quantum Dots for Thin Film Photovoltaics, Kansas EPSCOR Meeting, Lawrence KS (2013)

- **Emery Brown**, Minh Ho, Richard Knopik, Patrick Kilgore, Brian Lamp, David McCurdy, "Atomic Absorption Determination of Mercury in Local Freshwater Fish Using a Home-Built Cold Vapor Generator" 24th National Conference for Undergraduate Research, Missoula MT (2010)

- **Emery Brown**, Russell Baughman, "Crystal and 3-Dimensional Molecular Structures of Pesticides", 43rd ACS Midwest Regional Meeting, Kearney, NE (2008)

Awards and Scholarships

- Ohno Award for outstanding graduate research in Chemistry (2017)

- Melan Award in recognition of outstand graduate research in Analytical Chemistry (2016)

- Dan Hansen Foundation Summer Graduate Fellowship (2014)

- Timothy R. Donoghue Graduate Scholarship (2014)

- Timothy R. Donoghue Graduate Scholarship (2013)